

DISSERTATION

STRUCTURE OF THE MADDEN-JULIAN OSCILLATION IN COUPLED AND
UNCOUPLED VERSIONS OF THE SUPERPARAMETERIZED COMMUNITY
ATMOSPHERE MODEL

Submitted by

James J. Benedict

Department of Atmospheric Science

In partial fulfillment of the requirements

For the Degree of Doctor of Philosophy

Colorado State University

Fort Collins, Colorado

Spring 2010

COLORADO STATE UNIVERSITY

NOVEMBER 16, 2009

WE HEREBY RECOMMEND THAT THE DISSERTATION PREPARED UNDER OUR SUPERVISION BY JAMES JOSEPH BENEDICT ENTITLED STRUCTURE OF THE MADDEN-JULIAN OSCILLATION IN COUPLED AND UNCOUPLED VERSIONS OF THE SUPERPARAMETERIZED COMMUNITY ATMOSPHERE MODEL BE ACCEPTED AS FULFILLING IN PART REQUIREMENTS FOR THE DEGREE OF DOCTOR OF PHILOSOPHY.

Committee on Graduate Work

Eric D. Maloney

Jorge A. Ramirez

Wayne H. Schubert

David W. J. Thompson

David A. Randall, Advisor

Richard H. Johnson, Department Head

ABSTRACT OF DISSERTATION

STRUCTURE OF THE MADDEN-JULIAN OSCILLATION IN COUPLED AND UN- COUPLED VERSIONS OF THE SUPERPARAMETERIZED COMMUNITY ATMOS- PHERE MODEL

The Madden-Julian Oscillation (MJO), an eastward-propagating atmospheric disturbance resembling a transient Walker cell, dominates intraseasonal (20-100 days) variability in the tropical Indian and West Pacific Ocean regions. The phenomenon is most active during the Northern Hemisphere winter and is characterized by cyclic periods of suppressed (dry phase) and active (wet phase) cloudiness and precipitation. Numerous complexities—multi-scale interactions of moist convection and large-scale wave dynamics, air-sea fluxes and feedbacks, topographical impacts, and tropical-extratropical interactions—challenge our ability to fully understand the MJO and result in its poor representation in most current general circulation models (GCMs).

This study examines the representation of the MJO in a modified version of the NCAR Community Atmosphere Model (CAM). The modifications involve substituting conventional boundary layer, turbulence, and cloud parameterizations with a configuration of cloud-resolving models (CRMs) embedded into each GCM grid cell in a technique termed “superparameterization” (SP). Unlike many GCMs including the standard CAM, the SP-CAM displays robust intraseasonal convective variability. Two SP-CAM

simulations are utilized in this study: one forced by observed sea-surface temperatures (SSTs; “uncoupled”) and a second identical to the first except for a new treatment of tropical SSTs in which a simplified mixed-layer ocean model is used to predict SST anomalies that are coupled to the atmosphere (“coupled”).

Key physical features of the MJO are captured in the uncoupled SP-CAM. Ahead (east) of the disturbance there is meridional boundary layer moisture convergence and a vertical progression of warmth, moisture, and convective heating from the lower to upper troposphere. The space-time dynamical response to convective heating is also reproduced, especially the vertical structure of anomalous westerly wind and its migration into the region of heavy rainfall as the disturbance propagates eastward. Advective drying processes in the MJO wake are also represented well.

The coupled SP-CAM shows more realistic MJO eastward propagation, signal coherence and spatial structure relative to the uncoupled SP-CAM. The improvement varies with longitude but generally stems from better space-time relationships among MJO convective heating, its dynamical response, SSTs, surface fluxes, boundary layer properties, and vertical moisture structure. Coupled MJO events in the Indian Ocean display more realistic intensity; in the West Pacific, the coupled SP-CAM overestimates convective strength but shows an improved vertical structure relative to the uncoupled SP-CAM.

Biases related to MJO convection are also examined. Overestimated convective intensity in the West Pacific appears to be linked to basic state biases, Maritime Continent topographical impacts, unrealistic convection-wind-evaporation feedbacks, and the ne-

glect of convective momentum transport in the model. Phase errors between observed and simulated boundary layer moisture appear to stem from an unrealistic representation of shallow cumuli.

James J. Benedict
Department of Atmospheric Science
Colorado State University
Fort Collins, CO 80523
Spring 2010

ACKNOWLEDGEMENTS

I am very grateful for the guidance and support of my advisor, Dr. David A. Randall. This dissertation could not have been written without his expertise and encouragement. I am lucky to have had numerous opportunities to travel around the world to learn more about the MJO and present my findings to others in the scientific community. It is truly an honor to work with someone such as Dave. I would also like to thank Drs. Eric D. Maloney, Jorge A. Ramirez, Wayne H. Schubert, and David W. J. Thompson for their active participation on my doctoral committee.

Special thanks is owed to the Randall research group, in particular Marat Khairoutdinov for running the AMIP SP-CAM simulation; Mark Branson for organizing the coupled SP-CAM simulation; Cindy Carrick and Connie Hale for coordinating travel and funding; and Tak Yamaguchi and Luke Van Roekel for their hours of conversation related to my research ideas and problems. I would also like to my parents, family, friends, and former teachers, who made completing this dissertation significantly easier.

This project was supported by the National Science Foundation Science and Technology Center for Multi-Scale Modeling of Atmospheric Processes (CMMAP), managed by Colorado State University under cooperative agreement No. ATM-0425247. Funding also came from NASA contract NNG04GI25G, Development of Methods for Data Assimilation with Advanced Models and Advanced Data Sources.

TABLE OF CONTENTS

SIGNATURE PAGE	ii
ABSTRACT OF DISSERTATION	iii
ACKNOWLEDGEMENTS	vi
TABLE OF CONTENTS	vii
LIST OF TABLES	x
LIST OF FIGURES	xi
Chapter 1: Introduction	1
Chapter 2: MJO Structure in an Uncoupled Version of the Superparameterized CAM.....	8
2.1. Introduction.....	8
2.2. Data Sources	12
2.2.a. AMIP simulation with the SP-CAM	12
2.2.b. Observations and reanalysis.....	14
2.3. Methodology.....	16
2.4. Results.....	19
2.4.a. Boreal winter mean state	19
2.4.b. MJO events	22

2.4.c. Time-height structure of basic variables	24
2.4.d. Structure of derived quantities	30
2.4.e. Longitudinal dependence of MJO structure	36
2.4.f. Composite maps	39
2.5. Discussion and Conclusions	42
2.5.a. The West Pacific MJO intensity bias	42
2.5.b. Summary	49

Chapter 3: Modifications to the MJO in a Coupled Version of the

Superparameterized CAM	52
3.1. Introduction: Air-sea Interaction and the MJO	53
3.1.a. Observations	53
3.1.b. Theoretical modeling studies	56
3.1.c. Numerical modeling studies	58
3.2. Data Sources	64
3.3. Methodology	68
3.3.a. Climatological total and filtered variance	68
3.3.b. Decile averaging	69
3.3.c. Zonal wavenumber-frequency analysis	69
3.3.d. Longitude-time analysis	70
3.3.e. Lag correlation	70
3.3.f. Lag regression	71
3.3.g. Compositing	72

3.4. Results.....	72
3.4.a. Energy budget	72
3.4.b. Climatology: Mean state.....	74
3.4.c. Climatology: Variance.....	84
3.4.d. Decile averages	93
3.4.e. Zonal wavenumber-frequency analysis.....	101
3.4.f. Longitude-time analysis	107
3.4.g. Lag correlations	110
3.4.h. Lagged linear regression analysis	117
3.4.i. Composite analysis of filtered fields	141
3.5. Discussion and Conclusions	146
3.5.a. Overview: CTL–SOM comparison.....	146
3.5.b. Mechanisms: Why has the MJO in the coupled model changed?.....	149
3.5.c. Comments on the simulated boundary layer heat and moisture biases	158
Chapter 4: Conclusions	165
APPENDIX A: List of Acronyms	175
APPENDIX B: Coupling Between the CRM and GCM	178
REFERENCES.....	180

LIST OF TABLES

TABLE 2.2.1: Primary data sources used in Chapter 2	15
TABLE 2.4.1: The number of MJO events recorded in each longitudinal sector.....	36
TABLE 3.4.1: Global mean energy budgets at the top of the atmosphere (TOA) and Earth surface (SFC) for the standard Community Atmosphere Model version 3.0 (CAM), the control SP-CAM simulation (CTL), the slab-ocean SP-CAM simulation (SOM), and the best current observational estimates	73
TABLE 3.4.2: Ratios of eastward to westward MJO spectral power for the control SP-CAM simulation (CTL), the SP-CAM with slab ocean (SOM), and observations (OBS)	107

LIST OF FIGURES

FIG. 1.1: Schematic diagram of basic MJO structure and propagation.....	2
FIG. 2.2.1: Schematic diagram of the coupling between the GCM and CRM in super- parameterized models	13
FIG. 2.4.1: November-March mean fields of total rainfall, OLR, precipitable water (PW), 600 hPa specific humidity (q_{600}), 850 hPa zonal wind (u_{850}), and 200 hPa zonal wind (u_{200}).....	20, 21
FIG. 2.4.2: Time and longitude information of all identified MJO events from (a) GPCP and (b) SP-CAM rainfall.....	23
FIG. 2.4.3: Composite time-height plots of anomalous zonal wind u' , specific humidity q' , and air temperature T' based on ERA-40 data and SP-CAM output.....	25
FIG. 2.4.4: As in Fig. 2.4.3, but for equivalent potential temperature θ_e' for (a) ERA-40 and (b) the SP-CAM	29
FIG. 2.4.5: Timeseries of (a) precipitable water PW' and (b) OLR' during the MJO life cycle	30
FIG. 2.4.6: Longitudinal cross section of anomalous apparent convective heat source Q_1' , averaged between 10°S–5°N, at fixed time corresponding to maximum MJO- related rainfall at 160°E for (a) ERA-40 and (b) SP-CAM	31

FIG. 2.4.7: As in Fig. 2.4.6, but for zonal divergence, meridional divergence, and total horizontal divergence.....	33
FIG. 2.4.8: As in Fig. 2.4.4, but for horizontal moisture transport.....	35
FIG. 2.4.9: A comparison between ERA-40 and SP-CAM composite anomalous zonal wind u' for the Indian (50°E–100°E), Maritime Continent (100°E–145°E), and West Pacific sectors (145°E–170°W).....	37
FIG. 2.4.10: A comparison between ERA-40 and SP-CAM anomalous zonal winds at 925 hPa for the longitudinal sectors examined in Fig. 2.4.9.....	38
FIG. 2.4.11: Composite plots of anomalous 850 hPa wind, precipitable water, and SST for simulated and observed MJO events with rainfall maxima at 90°E.....	39
FIG. 2.4.12: As in Fig. 2.4.11, but for MJO events with rainfall maxima at 160°E.....	40
FIG. 2.5.1: Composite timeseries of boundary layer fields during the life cycle of MJO disturbances in the Indian Ocean and West Pacific.....	44
FIG. 3.4.1: Mean zonal wind at 850 hPa for all months and winter months.....	75
FIG. 3.4.2: As in Fig. 3.4.1, but for precipitation.....	77
FIG. 3.4.3: As in Fig. 3.4.1, but for SST.....	79
FIG. 3.4.4: As in Fig. 3.4.1, but for OLR.....	80
FIG. 3.4.5: As in Fig. 3.4.1, but for surface latent heat flux.....	82
FIG. 3.4.6: As in Fig. 3.4.1, but for vertical wind shear, defined as the difference between zonal wind at 850 hPa and 200 hPa (U850–U200).....	83

FIG. 3.4.7: 850 hPa zonal wind total winter variance, 20-100-day filtered winter variance, and the 20-100-day winter variance as a percent of total winter variance for the CTL, SOM, observations	85
FIG. 3.4.8: As in Fig. 3.4.7, but for precipitation.....	87
FIG. 3.4.9: As in Fig. 3.4.7, but for SST.....	88
FIG. 3.4.10: As in Fig. 3.4.7, but for OLR.....	90
FIG. 3.4.11: As in Fig. 3.4.7, but for surface latent heat flux.....	92
FIG. 3.4.12: Total precipitation, SST, surface latent heat flux, and boundary layer wind magnitude binned based on deciles of total precipitation for all ocean grid points within the region 60°E-180° and 10°S-10°N, for all seasons.....	93
FIG. 3.4.13: 20-100-day filtered SST, surface latent heat flux, boundary layer specific humidity, and boundary layer equivalent potential temperature binned based on deciles of 20-100-day filtered precipitation for all ocean grid points within the region 60°E-180° and 10°S-10°N, for all seasons.....	96
FIG. 3.4.14: Cross section differences of anomalous longwave heating and apparent convective moisture sink between the SOM and CTL, binned based on deciles of anomalous precipitation for all ocean grid points within the region 60°E-180° and 10°S-10°N, for all seasons	99
FIG. 3.4.15: Ratios of antisymmetric and symmetric spectral power to a smoothed background power for zonal wind at 850 hPa.....	102
FIG. 3.4.16: As in Fig. 3.4.15, but for precipitation.....	104
FIG. 3.4.17: As in Fig. 3.4.15, but for OLR.....	106

FIG. 3.4.18: Longitude-time plots of anomalous and filtered precipitation from observations , the CTL, and the SOM.....	108
FIG. 3.4.19: Lag autocorrelation of 20-100-day filtered OLR at 90°E, averaged between 10°S-5°N, for the CTL, SOM, and observations	110
FIG. 3.4.20: Lag correlation of 20-100-day filtered 850 hPa zonal wind with 20-100-day filtered precipitation at 90°E, averaged between 10°S-5°N, for the CTL, SOM, and observations.....	112
FIG. 3.4.21: As in Fig. 3.4.20, but for a base longitude of 150°E.....	112
FIG. 3.4.22: Lag correlation of 20-100-day filtered SST with 20-100-day filtered precipitation, averaged between 10°S-5°N, for the CTL, SOM, and observations .	113
FIG. 3.4.23: As in Fig.3.4.22, but for 20-100-day filtered 850 hPa zonal wind lag correlated with 20-100-day filtered precipitation.....	113
FIG. 3.4.24: As in Fig.3.4.22, but for 20-100-day filtered surface latent heat flux lag correlated with 20-100-day filtered precipitation	115
FIG. 3.4.25: As in Fig. 3.4.22, but for 20-100-day filtered 925 hPa equivalent potential temperature lag correlated with 20-100-day filtered precipitation	115
FIG. 3.4.26: Lag regressions of observed 20-100-day filtered OLR and 20-100-day filtered 850 hPa winds onto a base timeseries of 20-100-day filtered precipitation at 90°E.....	118
FIG. 3.4.27: As in Fig. 3.4.26, but for the CTL	119
FIG. 3.4.28: As in Fig. 3.4.26, but for the SOM.....	121

FIG. 3.4.29: Lag regressions of observed 20-100-day filtered SSTs and 20-100-day filtered boundary layer averaged wind magnitudes onto a base timeseries of 20-100-day filtered precipitation at 90°E	123
FIG. 3.4.30: As in Fig. 3.4.29, but for the CTL	124
FIG. 3.4.31: As in Fig. 3.4.29, but for the SOM	126
FIG. 3.4.32: Lag regressions of observed 20-100-day filtered downward surface short-wave radiation and 20-100-day filtered surface air pressure onto a base timeseries of 20-100-day filtered precipitation at 90°E	128
FIG. 3.4.33: As in Fig. 3.4.32, but for the CTL	130
FIG. 3.4.34: As in Fig. 3.4.32, but for the SOM	131
FIG. 3.4.35: Lag regressions of observed 20-100-day filtered surface latent heat flux and 20-100-day filtered boundary layer averaged winds onto a base timeseries of 20-100-day filtered precipitation at 90°E.....	133
FIG. 3.4.36: As in Fig. 3.4.35, but for the CTL	134
FIG. 3.4.37: As in Fig. 3.4.35, but for the SOM	135
FIG. 3.4.38: Lagged linear regressions of 20-100-day filtered anomalous horizontal divergence onto an index timeseries of 20-100-day filtered anomalous precipitation at 90°E for the CTL, SOM, and observations.....	136
FIG. 3.4.39: As in Fig. 3.4.38, but for the precipitation index timeseries at 150°E.....	136
FIG. 3.4.40: As in Fig. 3.4.38, but for 20-100-day filtered anomalous convective heating regressed onto the precipitation index at 90°E.....	138
FIG. 3.4.41: As in Fig. 3.4.40, but for the precipitation index timeseries at 150°E.....	138

FIG. 3.4.42: As in Fig. 3.4.38, but for 20-100-day filtered anomalous specific humidity regressed onto the precipitation index at 90°E.....	140
FIG. 3.4.43: MJO composite timeseries of anomalous filtered horizontal divergence, specific humidity, and vertical moisture transport at 90°E.....	143
FIG. 3.4.44: As in Fig. 3.4.44, but for a base longitude of 150°E.....	145
FIG. 3.5.1: Timeseries of lagged regression values based on a one standard deviation change in an index timeseries of precipitation at 90°E.....	151
FIG. 3.5.2: As in Fig. 3.5.1, but for a base longitude of 150°E.....	156
FIG. 3.5.3: Temporal cross sections of specific humidity, temperature, and equivalent potential temperature linearly regression onto an index timeseries of precipitation at 90°E.....	160
FIG. 3.5.4: As in Fig. 3.5.3, but for a base longitude of 150°E.....	162
FIG. 4.1: Longitudinal cross section of the interaction between MJO structure and basic state circulation when the MJO convective center is in the West Pacific and Indian Ocean regions.....	171

Chapter 1

INTRODUCTION

Tropical weather and climate play an integral role in the global energy budget and circulation patterns. Although the equatorial belt receives substantially more insolation than the higher latitudes, low-latitude temperature and pressure gradients are weak due to the small effect that the Earth's rotation has on air parcels in that region. These weak gradients result in a far-reaching dynamical response to localized heating perturbations through the effect of equatorial waves. In the Tropics, latent heating associated with cloud and precipitation formation is of primary importance. This heating drives multi-scale circulations—both locally and remotely—and is balanced locally by adiabatic cooling and globally by radiative cooling. The dynamical response to equatorial heating can influence midlatitude and tropical circulation regimes and can even alter the heating patterns themselves, thereby affecting the equatorial wave propagation characteristics.

The most dominant feature of the equatorial atmosphere on intraseasonal time scales (20-100 days) is the Madden-Julian Oscillation (MJO¹), sometimes called the intraseasonal oscillation (ISO). Discovered in the early 1970s (Madden and Julian 1971), the MJO is an eastward-propagating disturbance most active during the boreal winter months and across the equatorial Indian and West Pacific Oceans (see Fig. 1.1). It involves multi-scale cloud and precipitation processes and is manifested in numerous at-

¹ A list of selected acronyms appears in Appendix A.

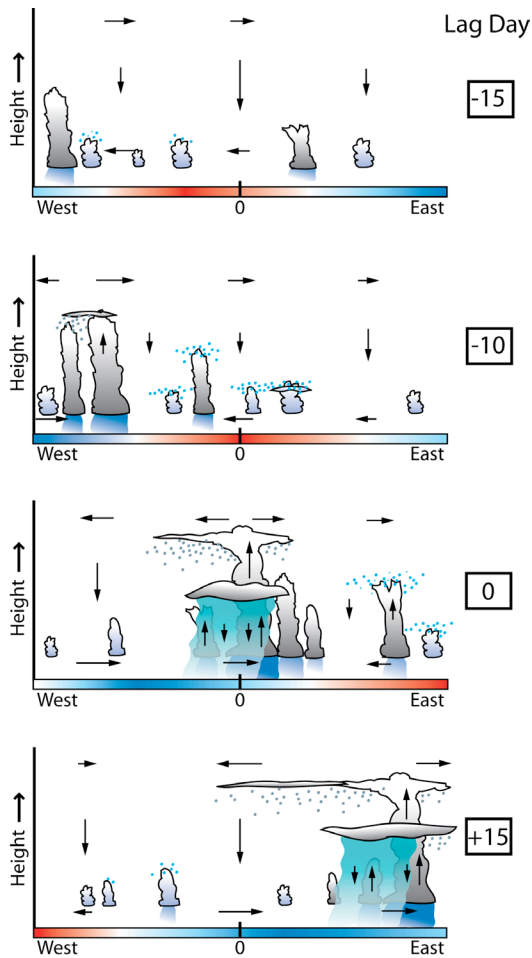


Fig. 1.1. Schematic diagram of MJO structure and propagation. Lag days relative to maximum rainfall at point “0” appear at right. Red (blue) color shading along the x-axis indicates high (low) SST anomalies, and arrows are anomalies of horizontal winds and vertical motion. Convective (stratiform) clouds have a large vertical (horizontal) extent and dark (light) blue rain shafts. Blue (gray) dots represent moistening via cloud-top detrainment (ice crystal fallout).

atmospheric and oceanic variables. At the time of its discovery, a framework of linear wave types had been established (Matsuno 1966) but did not include the MJO due to its lack of linear mathematical roots. Subsequent observational studies revealed that the MJO involves a transient Walker cell circulation (Madden and Julian 1972), displays complex cloud properties (Gruber 1974, Nakazawa 1988, Salby and Hendon 1994) and a characteristic life cycle (Hendon and Salby 1994), resembles a coupled Kelvin-Rossby mode (Gill 1980), and includes important atmosphere-ocean interactions (Krishnamurti et al. 1988, Zhang and McPhaden 1995).

Several theories have been proposed in an attempt to explain the generation, maintenance, and propagation characteristics of MJO disturbances. The theory of conditional instability of the second kind applied to large-scale equatorial waves (wave-CISK; Hayashi 1970, Lindzen 1974) suggests an instability that results from a mutual positive feedback between localized convective heating and the environmental large-scale circula-

tion. Importantly, the interactions between convection and its dynamical response—referred to as “convective coupling”—act to slow Kelvin-like waves to phase speeds of 15–20 m s⁻¹ [c.f. uncoupled, dry Kelvin wave speed of 30–40 m s⁻¹ (Wheeler et al. 2000)]. The original wave-CISK theory predicts wave speeds that are still unrealistically fast compared to observations, however. Modified versions of wave-CISK, which include a frictional boundary layer that allows for low-level moisture convergence/divergence, result in a substantially more realistic depiction of convectively coupled disturbances (Wang 1988, Salby et al. 1994). The stratiform instability mechanism states that wave growth can occur due to fluctuations in convective inhibition (CIN) driven by a positive correlation between second-mode temperature and stratiform heating profiles (Mapes 2000). Although intraseasonal disturbances predicted by the stratiform instability mechanism show upper-level heating leading deep convection (it coincides with deep convection in observations; Straub and Kiladis 2003), this mechanism may play a role in prolonging the MJO wet phase once it develops (Benedict and Randall 2007). A third theory, the discharge-recharge hypothesis (Bladé and Hartmann 1993), states that the time scale of the MJO is determined by the speed with which the atmosphere becomes “pre-conditioned.” The development and deepening of cumuli warm the lower troposphere and moisten the dry middle levels, resulting in an environment that promotes the development of future deep convection. It has also been theorized that the time scale of pre-conditioning is affected by radiative effects (Hu and Randall 1994) and more complex interactions between the hydrologic cycle and SSTs (Stephens et al. 2004).

Yet another theory of MJO energetics involves the role of air-sea interactions. The possible importance of such interactions and their influence on the MJO was first investigated in the mid-1980s. The convection-wind-evaporation feedback mechanism, or wind-induced surface heat exchange (WISHE), was originally developed by Emanuel (1987) and Neelin et al. (1987). The proposed WISHE theory states that increases in low-level entropy (i.e., equivalent potential temperature) mainly driven by enhanced surface fluxes are redistributed throughout the atmospheric column by convection and ultimately fuel equatorial wave growth. A more detailed discussion of WISHE theory is presented in Section 3.1.b. Although required features of the WISHE mechanism such as low-level mean easterly winds and strong (weak) evaporative fluxes leading (lagging) the convective center often do not match observations (e.g., Jones and Weare 1996), feedbacks among convection, dynamics, and surface latent heat fluxes have been shown to impact the MJO in many ways and may not necessarily require mean tropical easterlies to act (Maloney and Sobel 2004, Sobel et al. 2008).

Our understanding of the intraseasonal oscillation remains inadequate, and accurately simulating its many features is extremely challenging. Physical processes involving multi-scale and subgrid-scale cloud systems, the interactions of moist convection and dynamics on a wide range of space-time scales, heat and moisture fluxes and distributions within the atmospheric and oceanic mixed-layers, and the tropical-extratropical connection can all impact the MJO and should be accurately represented. Modeling issues related to horizontal and vertical grid resolution; convection, radiation, and microphysical parameterizations; and air-sea coupling must also be addressed. Faced with this daunting

task and our lack of understanding of several MJO mechanisms, it is no surprise that many general circulation models (GCMs) have a poor representation of intraseasonal variability. Common GCM deficiencies related to the MJO include unrealistically weak intraseasonal convective variability, convective activity that shows no seasonality, lack of coherent eastward propagation, phase speeds that are too fast, and even an unrealistic mean state, which has been shown to strongly impact the MJO (Slingo et al. 1996, Slingo 2005, Lin et al. 2006, Kim et al. 2009).

A recently developed version of the National Center for Atmospheric Research (NCAR) Community Atmosphere Model (CAM; Collins et al. 2006) involves substituting conventional boundary layer, moist convection, and cloud parameterizations with a configuration of cloud-resolving models (CRMs) embedded into each CAM grid cell (Khairoutdinov and Randall 2001). Through the implementation of this technique, termed *superparameterization*, intraseasonal variability in the modified CAM (the “SP-CAM”) increases markedly over the standard CAM whose variability, like many GCMs, remains unrealistically weak (Khairoutdinov et al. 2008, hereafter KDR08). The findings of KDR08 suggest that simulated MJO representation may be improved with a more realistic treatment of subgrid-scale processes. Khairoutdinov and Randall (2001) and all subsequent studies of intraseasonal variability in the SP-CAM up to this point have used prescribed SSTs, but numerous studies have demonstrated that robust interactions between the atmospheric and oceanic mixed layers exist and strongly impact MJO simulations (Lau and Sui 1997, Flatau et al. 1997, Waliser et al. 1999, Inness and Slingo 2003, Sperber et al. 2005, Zhang et al. 2006).

The purpose of this study is to comprehensively analyze many aspects of the MJO simulated by the SP-CAM. We first analyze the detailed space-time structure of the MJO in a 19-year simulation forced by observed monthly mean SSTs. This Atmospheric Modeling Intercomparison Project (AMIP; Gates 1992) run is one of the longest SP-CAM simulations to date and provides the opportunity to examine a statistically robust composite MJO of approximately 50 events. Our analyses build off of previous studies such as KDR08, who only investigated limited spectral characteristics and intraseasonal variance spatial distributions. In this study, we present a more extensive analysis of MJO representation in the SP-CAM, including its detailed space-time structure, the mean states in which it operates, the fundamental impacts of convective and advective processes, the longitudinal dependence of the dynamical response to convective heating, and a discussion of convection intensity biases.

In the second half of the study, we examine results from a five-year simulation in which the SP-CAM is coupled to an idealized slab ocean model that allows ocean surface temperatures to respond to anomalous surface heat fluxes in a more natural manner. To our knowledge, this five-year simulation is the first in which the SP-CAM is coupled to a slab ocean model. Another simulation recently conducted by C. Stan at the Center for Ocean-Land-Atmosphere Studies (COLA) uses a superparameterized version of the Community Climate System Model version 3 (CCSM; Collins et al. 2006). The preliminary results from C. Stan's simulation show a marked improvement of the MJO representation (among other features) compared to a CCSM run using conventional parameterizations, but physical mechanisms related to the improvement have not been examined and

the results have yet to be published. We investigate changes to the MJO structure and intensity, propagation, and signal coherence between our uncoupled and coupled versions of the SP-CAM. We propose mechanisms that explain why such changes occur and discuss biases seen in the SP-CAM that are not alleviated by the atmosphere-ocean coupling.

A comparison of MJO structures between the 19-year SP-CAM AMIP simulation and observations is presented in Chapter 2. A more detailed introduction of superparameterization and the primary goals of Chapter 2 are provided in Section 2.1. A review of the SP-CAM configuration and the observational datasets appear in Section 2.2, followed by a description of the technique used to isolate MJO events in Section 2.3. Results showing the MJO space-time structures are presented in Section 2.4. Comments on the results and a discussion of SP-CAM biases are provided in Section 2.5.

Chapter 3 presents MJO representation in the coupled SP-CAM and compares those results to the uncoupled version of that model. We provide a historical review of observational and modeling studies that have investigated the impacts of air-sea interaction on the MJO in Section 3.1. Descriptions of the slab ocean model and observational datasets appear in Section 3.2, followed by an outline of the implemented statistical methods in Section 3.3. In Section 3.4 we present a comparison of the MJO structures from the uncoupled and coupled SP-CAM simulations as well as observations. We discuss these results and propose mechanisms that explain the observed changes in the MJO between the uncoupled and coupled SP-CAM simulations in Section 3.5.

Overall conclusions appear in Chapter 4.

Chapter 2

MJO STRUCTURE IN AN UNCOUPLED VERSION OF THE SUPERPARAMETERIZED CAM

The results presented in Khairoutdinov et al. (2005) and KDR08 suggest that basic characteristics of intraseasonal convective variability—power in the zonal wavenumber-frequency domain and the spatial distributions of filtered variance—are improved in the CAM¹ through the use of superparameterization. However, such metrics do not guarantee a realistic depiction of key physical features of the MJO such as low-level moisture convergence ahead of the disturbance and the advective drying structure in its wake. In this chapter, we examine in considerably greater detail the space-time structure of the MJO in the SP-CAM, with a particular focus on the interrelationships among convection, its dynamical response, and the thermodynamic and advective processes that modulate it.

2.1. Introduction

The MJO, the eastward-moving couplet of convectively active and suppressed atmospheric conditions in the Indian and West Pacific Ocean regions, is the leading mode

¹ A list of selected acronyms appears in Appendix A.

of tropical variability on 20-100-day (intraseasonal) time scales. Since its discovery in the early 1970s (Madden and Julian 1971), a host of observational, theoretical, and modeling studies have gradually improved our understanding of the MJO but have also revealed its many complexities (e.g., Madden and Julian 2005, Zhang 2005). For example, we do not yet have adequate explanations of MJO convective initiation in the Indian Ocean, scale interactions linking individual cloud processes to planetary-scale waves, and the role of air-sea coupling. Because equatorial heating associated with organized convective systems such as the MJO has far-reaching impacts, an accurate representation of tropical variability in GCMs is critical for producing realistic patterns of global weather and climate. Unfortunately, most current GCMs do not simulate the MJO well, lacking sufficient variability on intraseasonal space-time scales (Lin et al. 2006).

The poor representation of the MJO is a well-documented deficiency plaguing many current GCMs (Slingo et al. 1996, Lin et al. 2006, Kim et al. 2009). Lin et al. (2006) present results from 14 coupled GCMs participating in the Intergovernmental Panel on Climate Change (IPCC) Fourth Assessment Report (AR4) and find that the magnitude of intraseasonal variability in 12 of those models was less than half of the observed value. Those authors conclude that improvements in the representation of subgrid-scale processes in the model (e.g., boundary layer and moist convective processes, saturated and unsaturated convective downdrafts, etc.) would lead to a more accurate MJO depiction.

Traditional GCMs have grid spacings of $O(100 \text{ km})$ and thus cannot accurately resolve subgrid-scale cloud and boundary layer processes without making some

assumptions about how such processes “behave.” Parameterizations are semiempirical theories that predict the statistical behavior of subgrid-scale processes and their physical interactions with each other and with resolved-scale phenomena. A major weakness of parameterizations is that they artificially separate subgrid-scale processes that are highly interactive in nature. One approach to bypassing this limitation is to replace certain conventional parameterizations with cloud resolving models (CRMs; Grabowski and Smolarkiewicz 1999, Grabowski 2001), a technique termed *superparameterization* (Khairoutdinov and Randall 2001). Replacing conventional cloud parameterizations with CRMs of horizontal resolution $O(1 \text{ km})$ allows cloud-scale dynamics, moist processes, and radiation to interact in a more natural manner (Grabowski 2001). Specific conventional parameterizations, including radiation and microphysics, are still implemented in superparameterized models; however, because such parameterizations are inherently limited by their input conditions to begin with, improvement of the input conditions through superparameterization contributes to further improvement in the results (Randall et al. 2003). Although great progress has been made in using a global CRM to produce a single but realistic MJO (e.g., Miura et al. 2007), simulations of sufficient duration to analyze systematic MJO behavior—ideally, multiple years—remain computationally prohibitive (KDR08). The method of superparameterization thus bridges the computational gap between conventionally parameterized GCMs and global CRMs.

The simulated data used in this study is taken from a superparameterized version of the National Center for Atmospheric Research (NCAR) Community Atmosphere

Model version 3.0 (CAM3.0; Collins et al. 2006), hereafter referred to as the SP-CAM. The SP-CAM simulation being analyzed is based on the Atmospheric Model Intercomparison Project (AMIP) protocol (Gates 1992) in that the model is forced by observed sea surface temperatures (SSTs). The current SP-CAM and previous versions of it demonstrate a remarkable increase in intraseasonal variability relative to the standard CAM (e.g., Randall et al. 2003). Using a suite of standardized diagnostics, Kim et al. (2009) find that the SP-CAM demonstrates good skill in representing the MJO relative to seven other GCMs, including versions of the CAM with updated parameterizations. Several explanations relating poor MJO depiction in the standard CAM and its intensified signal in superparameterized GCMs have been proposed recently. Thayer-Calder and Randall (2009) find that insufficient column moistening during convective development in CAM3.0 is related to the choice of deep convection parameterization. They conclude that this lack of moistening severely limits that model's intraseasonal variability. Zhu et al. (2009) compare CAM3.0 to the SP-CAM and discover that organized convection in the SP-CAM is delayed until a moister environment is achieved. The delayed initiation appears to result in an MJO wet phase with more vigorous convection, higher rain rates, and a stratiform heating profile that more closely resembles observations. Additionally, Luo and Stephens (2006), in their study of the Asian summer monsoon, postulate that convective enhancement in two superparameterized GCMs is related to an overly intense convection-wind-evaporation feedback augmented by the CRM's periodic boundary conditions. Our analysis provides additional insight of the MJO structure in the SP-CAM

and proposes an explanation regarding its more realistic but overly-intensified MJO convection.

Section 2.2 reviews the SP-CAM set-up and describes the simulated and observation-based datasets. MJO event selection and compositing techniques are discussed in Section 2.3. Results displaying the composite MJO space-time structure from the 19-year simulation forced by monthly mean SSTs are presented in Section 2.4, followed by a discussion and summary of these results in Section 2.5.

2.2. Data Sources

2.2.a. AMIP run with the SP-CAM

The NCAR CAM3.0 (Collins et al. 2006) acted as the host GCM. CAM3.0 has a $2.8^{\circ} \times 2.8^{\circ}$ horizontal grid (T42 spatial truncation), 30 levels up to 3.6 hPa, and a time step of 30 min. Embedded within each GCM grid cell is a 2D “curtain” of 32 CRM grid columns oriented in the north-south direction, with 4 km horizontal grid spacing, periodic boundary conditions, 28 levels collocated with the 28 lowest CAM levels, and a time step of 20 s. The 2D CRM replaces the CAM’s conventional parameterizations of moist physics, convection, turbulence, and boundary layer processes. As discussed in Khairoutdinov et al. 2005, momentum feedback from the CRM to the GCM is not allowed. Coupling between the surface and atmosphere is computed only on the GCM grid such that enhanced, localized surface fluxes that may arise from gust fronts are not

included. CRM-scale enhancements of surface drag related to localized gustiness of near-surface winds are explicitly included, however. Additional details of the SP-CAM AMIP simulation used in this study can be found in KDR08.

Figure 2.2.1 presents a simplified picture of the coupling between the host GCM and embedded CRMs. Further discussion of GCM-CRM coupling can be found in Khairoutdinov and Randall 2003, Khairoutdinov et al. 2005, and Appendix B. In Fig.

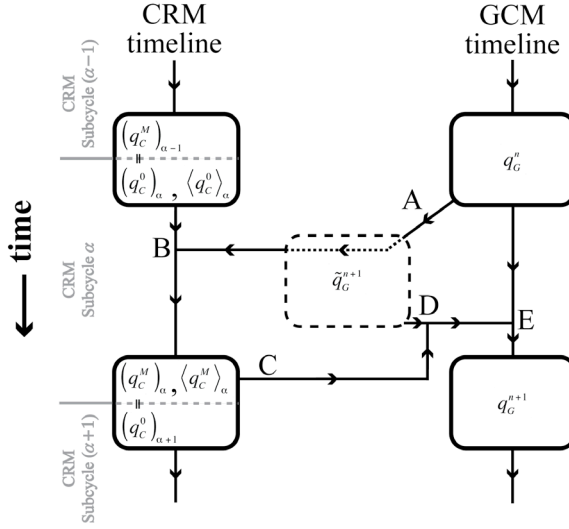


Fig. 2.2.1. Schematic diagram of the coupling between the GCM and CRM in superparameterized models. Time stepping n to $n+1$ in the GCM, a provisional value of a prognostic variable q is first computed using only non-CRM, large-scale advective tendencies (A). The CRM field q_c , initiated with the q field from the end of the previous CRM subcycle ($\alpha-1$) such that continuous integration occurs in the CRM, is time-stepped through subcycle α with CRM advection, CRM physics, and a relaxation term (B). The relaxation term prevents drift of CRM field q_c from GCM field q_G and involves CRM-domain-averaged q field from the start of the subcycle, $\langle q_c^0 \rangle$, along with \tilde{q}_G^{n+1} . During subcycle α , the CRM is integrated from $m=0$ to $m=M$ corresponding to GCM time steps n and $n+1$, respectively. At the end of subcycle α , the CRM-domain-averaged field $\langle q_c^M \rangle_\alpha = \langle q_c^{n+1} \rangle_\alpha$ (C) is combined with \tilde{q}_G^{n+1} (D) and non-CRM, large-scale advective tendencies (E) to arrive at q_G^{n+1} . A discussion is given in Appendix B.

2.2.1, q represents liquid water/ice moist static energy or total nonprecipitating water (i.e., a prognostic thermodynamic variable excluding total precipitating water).

Mathematically, the CRM is influenced by the GCM through a relaxation term that prevents drift of the CRM fields away from those of the GCM; simultaneously, the CRM is forced by the GCM's large-scale advection. The GCM, in turn, is modified by CRM-domain-averaged tendencies of temperature, water vapor, and nonprecipitating liquid arising from cloud processes on the CRM grid.

The AMIP simulation was conducted using prescribed monthly mean (interpolated to daily mean) SSTs and sea ice concentrations (Hurrell et al. 2008). The simulation produced 19 yr of global daily output spanning 1 Sep 1985–25 Sep 2004. Our analysis utilizes pentad-averaged SP-CAM fields interpolated to a $2.5^\circ \times 2.5^\circ$ horizontal grid (see Table 2.2.1 for a summary of data sources).

2.2.b. Observations and reanalysis

We compare the SP-CAM AMIP simulation results to a host of observation-based datasets. The aim of this study is to examine a large sample of MJO events with particular focus on their synoptic to planetary scale spatial features. To maximize the number of events, we seek observation-based datasets with a sufficiently long temporal range (at least 14 yr) and minimal missing data points. Owing to this limitation, a pentad-averaged version of ECMWF 40-yr Reanalyses (ERA-40, Uppala et al. 2005) is utilized as the observational basis for most dynamic and thermodynamic fields. ERA-40 has the advantage of complete data coverage in remote and data-sparse areas of the Indian and Pacific Oceans but is also subject to errors introduced by parameterizations, particularly in the boundary layer and aloft in highly convective situations (ECMWF

2003 and references therein). Despite the dependence of ERA-40 on parameterizations, previous studies suggest that the overall synoptic and mesoscale features associated with tropical intraseasonal disturbances in warm-ocean regions are well represented by ECMWF reanalyses [Lin and Johnson 1996a; Straub and Kiladis 2003; Sperber 2003; Kiladis et al. 2005 (hereafter KSH05)].

Table 2.2.1. Primary data sources used in Chapter 2.

	SP-CAM	ERA-40	GPCP	NVAP	ISCCP
Origin/ platform	Model	Radiosonde and satellite measurements, model forecasts	Satellite and rain gauge measurements	Satellite and radiosonde measurements	Satellite measurements
Horizontal resolution	2.5°x2.5° ^a	2.5°x2.5°	2.5°x2.5°	2.5°x2.5° ^c	2.5°x2.5°
Temporal resolution and domain	Pentad ^b ; 1 Sep 1985—25 Sep 2004	Pentad ^b ; 1 Jan 1984—31 Dec 2001	Pentad; 1 Jan 1984—31 Dec 2001	Pentad ^b ; 1 Jan 1988—31 Dec 2001	Pentad; 1 Jan 1984—31 Dec 2001
Vertical levels	30, 3.6 hPa top; 7 levels below 850 hPa	13; 1000, 925, 850, 775, 700, 600, 500, 400, 300, 250, 200, 150, 100 hPa	Surface	Column integration	Top of atmosphere
Selected variables	Dynamic and thermodynamic fields	Dynamic and thermodynamic fields	Total precipitation	Precipitable water	OLR

^a Interpolated from 2.8°x2.8° horizontal grid

^b 5-day averages calculated from daily data

^c Interpolated from 1°x1° horizontal grid

We use 19 years of pentad-averaged rain data from the Global Precipitation Climatology Project (GPCP). This version of pentad GPCP data is a companion dataset to the monthly GPCP archive (Adler et al. 2003), which merges rain gauge measurements with space-borne infrared and microwave retrievals on a 2.5°x2.5° grid. Remotely

sensed measurements of precipitable water are based on the NASA Water Vapor Project (NVAP; Randel et al. 1996). NVAP blends radiosonde, infrared, and microwave measurements to produce a comprehensive global dataset spanning 14 years (1 Jan 1988–31 Dec 2001). We use OLR measurements from the International Satellite Cloud Climatology Project (ISCCP; Zhang et al. 2004), and SSTs are taken from version 2 of the National Oceanic and Atmospheric Administration Optimal Interpolation SST (OISST2; Reynolds et al. 2002).

2.3. Methodology

Our approach to isolating and compositing MJO events is very similar to that described by Benedict and Randall (2007). Pentad GPCP rain is spectrally filtered to identify intraseasonal convective envelopes. Using the space-time coordinates of MJO-filtered convective activity, we then return to the *unfiltered* rain dataset to generate MJO event composites based on the longitude and pentad of maximum rain. In essence, we utilize spectrally filtered signals simply as a guide in our selection of intraseasonal convective events; the actual event selection and all subsequent analyses are based on *unfiltered* data. This procedure helps to maintain spatial and temporal fidelity of synoptic features which might be masked by the filtering process. Influences from high-frequency phenomena such as inertia-gravity waves are essentially eliminated through the use of pentad-averaged data. Evidence of mixed Rossby-gravity waves and tropical depressions may nevertheless arise in individual MJO events owing to the selection procedure. In a

composite of numerous MJO events, however, such features will tend to be eliminated by averaging.

At the beginning of the event-selection process, we subtract the mean and first three harmonics of the seasonal cycle from GPCP rainfall at each grid point. Following the methods of Wheeler and Kiladis (1999), we retain rain data only within the appropriate MJO spectral region (zonal wavenumbers +1 to +5, indicating eastward-propagating disturbances, and 20-100-day periods). A zonal wavenumber-frequency diagram of tropical rainfall (see Fig. 3.4.16) indicates that the eastward component of intraseasonal, planetary disturbances is substantial while the corresponding westward counterpart is small for both the model and observations (not shown). Thus, the influence of westward components that are coherent with eastward components is small (Hayashi 1979) and our method of filtering will accurately capture eastward propagating signals. The data are then averaged between 10°S-5°N, corresponding to the latitude band of greatest MJO variability in boreal winter (Wheeler and Kiladis 1999). We scan the MJO-filtered, pentad- and meridionally averaged GPCP rain field to locate broad convective envelopes, labeling them “events” if they pass a specific set of criteria based on spatial extent, temporal duration, and rain intensity (Benedict and Randall 2007). Only events occurring within 50°E-170°W during boreal non-summer months (15 September-31 May) are used. The time and longitude of maximum filtered rain for each MJO event are recorded. We return to the unfiltered, meridionally averaged version of GPCP rain and locate the recorded time and longitude. Often the time and longitude of rain maximum in the filtered field does not exactly match that of the unfiltered data, so

we scan a small area (± 1 pentad, $\pm 15^\circ$ longitude) in the unfiltered dataset to locate an updated temporal and spatial coordinate of rain maximum. This position in time t_o and space L^* of maximum rain in the unfiltered data field acts as the base point (day 0) upon which all other unfiltered variables are centered. With L^* fixed, we take a timeseries of any variable from 30 days prior to the most intense MJO-related rainfall ($t_o = -30$) to 20 days following it ($t_o = +20$). This timeseries essentially shows the temporal evolution, at L^* , of any unfiltered variable during an MJO event. By gathering the timeseries at all available pressure levels, we can generate time-height cross sections for any variable and any identified MJO event. We form a composite MJO by aligning the t_o values (lag day 0) of all events. In Section 2.4.e, we subdivide all MJO events based on the longitude at which their maximum rainfall is recorded; in this way, we can construct composites for the Indian Ocean, Maritime Continent, and West Pacific sectors.

It is important to note that L^* can be located anywhere within the equatorial Indian and West Pacific sectors. Therefore, departures from the calendar-day mean at L^* are used in the composite MJO cross sections (except where noted). One can think of this space-time anomaly as a departure from what would be expected at the time of year associated with t_o and at longitude L^* . This reduces the effects of the basic state differences in which the MJO operates, such as the change in climatological 850 hPa zonal winds from westerly over the Indian Ocean to easterly over the Date Line during boreal winter (Fig. 2.4.1r). An identical MJO event selection and compositing procedure is also applied to the SP-CAM data.

2.4. Results

2.4.a. Boreal winter mean state

Several studies have highlighted the seasonal-mean differences between CAM3.0 and a number of SP-CAM simulations (Khairoutdinov et al. 2005, KDR08). Examining the climatological background in which the MJO operates provides an understanding of some of the fundamental relationships between moisture, clouds, and convection on space-time scales larger than the MJO itself. Knowledge of climatological biases is also important regarding the interpretation of the composite anomaly plots shown later in this section.

November-March means and corresponding model biases based on all available years are displayed for selected variables in Fig. 2.4.1 (see Table 2.2.1 for dataset temporal ranges). Longitudinal cross sections of model biases averaged from 10°S-5°N are shown along the bottom row of Fig. 2.4.1. A comparison of total rainfall between the SP-CAM and GPCP observations (Fig. 2.4.1c) indicates simulated wet biases over the western Indian Ocean, the waters north of Australia, and the West Pacific. A dry bias is noted over Maritime Continent land masses and the eastern Indian Ocean. We can infer from biases in OLR (Fig. 2.4.1g) that simulated boreal winter deep convection and associated cirrus clouds are unrealistically widespread in the West Pacific warm pool region but lacking in coverage over the western Maritime Continent and eastern Indian Ocean.

Across a broad area of the Maritime Continent, simulated mean precipitable water values (PW, Fig. 2.4.1k) are lower than observed climatology. The largest PW difference

is collocated with the simulated dry rainfall and positive OLR biases. Weakly positive biases in SP-CAM PW appear in the far western Indian Ocean and near the International Date Line. Fig. 2.4.1o presents a dry bias pattern of simulated specific humidity at 600

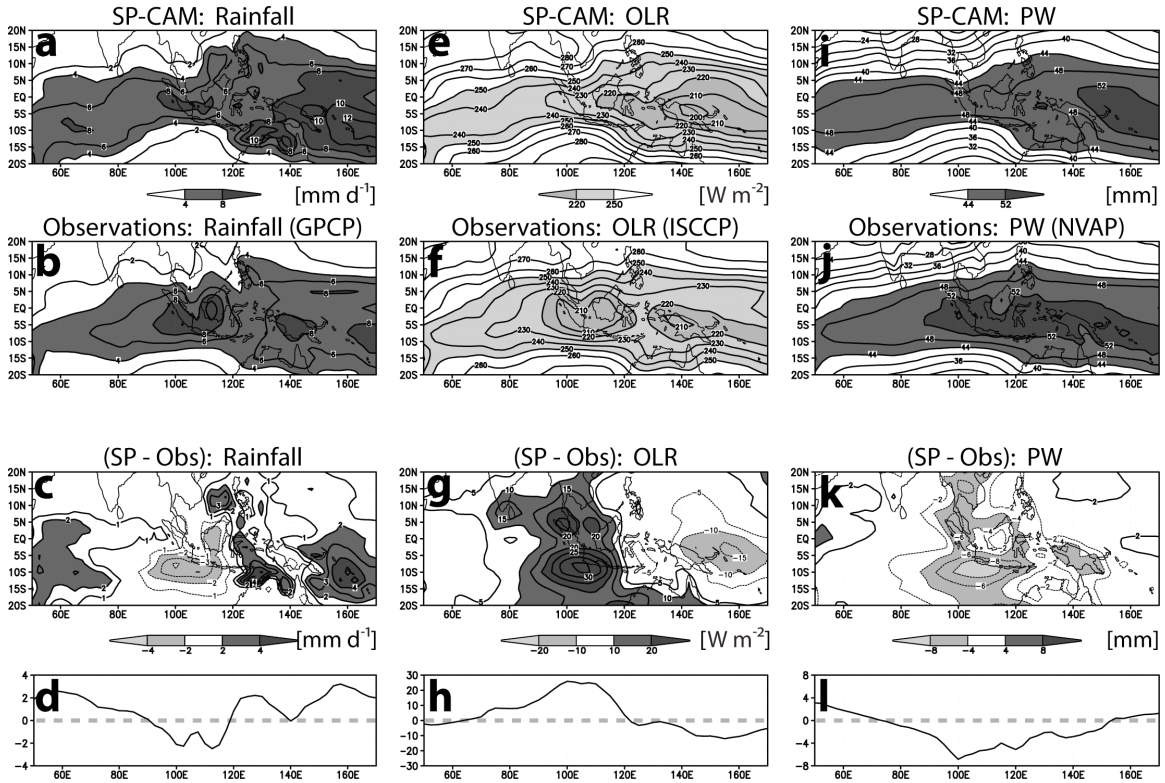


Fig. 2.4.1. November-March mean fields of total rainfall, OLR, precipitable water (PW), 600 hPa specific humidity (q_{600}), 850 hPa zonal wind (u_{850}), and 200 hPa zonal wind (u_{200}) based on all available years (see Table 2.2.1 for data temporal ranges). Mean fields corresponding to the SP-CAM, observations, their difference (SP-CAM—observations), and the meridional average (10°S – 5°N) of their difference are displayed from top to bottom.

hPa (q_{600}) that is similar to that of PW. The equatorial band of maximum q_{600} in the model is unrealistically dry and narrow over the western Maritime Continent compared to observations (Fig. 2.4.1n), while biases are nearly zero across much of the Indian and Pacific sectors. The SP-CAM also underestimates boundary layer moisture over land masses of the Maritime Continent (by 10% of climatology), northern Australia (20%),

and southeast Asia (25%) (not shown). Mirroring these dry biases in the SP-CAM, strong negative θ_e biases at 600 hPa and 925 hPa over Maritime Continent land masses are also apparent (not shown). Away from the Maritime Continent region, no substantial biases are observed in any of the thermodynamic variables discussed above.

In eastern Indonesia and the West Pacific, the SP-CAM exhibits a tendency for unrealistically strong low-level west winds but a nearly zero wind bias at upper levels

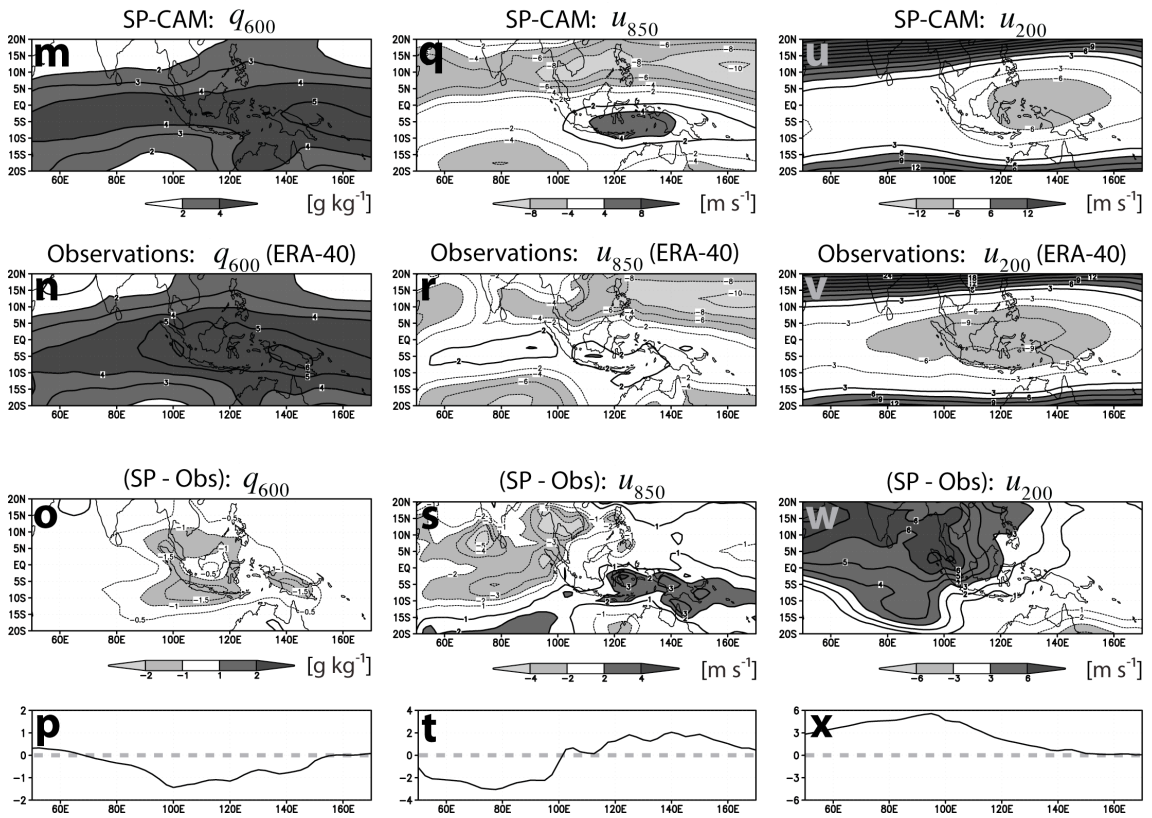


Fig. 2.4.1. *Continued.*

(Figs. 2.4.1t and 2.4.1x, respectively). In the Indian Ocean sector, climatological simulated low-level westerlies and upper-level easterlies are too weak compared to ERA-40. The structure of climatological low-level westerlies over the Indo-Pacific

region critically impacts MJO propagation (Inness et al. 2003). Together, panels q-x of Fig. 2.4.1 suggest greater convergence (divergence) of the simulated climatological zonal winds in the upper (lower) troposphere over the western Maritime Continent. Additionally, more intense low-level simulated zonal convergence in the West Pacific can be inferred from a comparison of Figs. 2.4.1q and 2.4.1r. These inferences agree nicely with bias plots of rainfall (Fig. 2.4.1d), OLR (2.4.1h), and PW (2.4.1i), indicating that climatological deep convection in the SP-CAM is overestimated in the West Pacific and underestimated in western Indonesia and the eastern Indian Ocean. The biases in Fig. 2.4.1 appear to resemble the phase of the MJO when convection is enhanced over the West Pacific and suppressed over the eastern Indian Ocean. Analysis of identified MJO disturbances indicates that simulated events in the region of the dry climatological bias (90°-110°E) have weaker convection than observed events, a deficiency also found in coupled simulations (Zhang et al. 2006). Given that the MJO is one of the larger contributors to boreal winter deep convection over the West Pacific (Wheeler and Kiladis 1999), the longitudinal bias profiles suggest that MJO-related convection in the West Pacific region might be unrealistically vigorous in the SP-CAM.

2.4.b. MJO events

We identified 46 MJO events in the GPCP dataset and 50 in the SP-CAM dataset. A summary of the temporal and spatial event locations is displayed in Fig. 2.4.2. This plot indicates the time t_o and longitude L^* (organized into monthly and 10°-wide bins, respectively) at which each identified MJO event was most intense as measured by

surface rainfall rate. Events based on observed precipitation (Fig. 2.4.2a) tend to have their maximum intensities clustered in two areas: the East Indian Ocean from November to January, and the West Pacific Ocean during boreal spring. To a lesser extent, there is also a cluster of events in the east-central Indian Ocean in April and May possibly tied to Asian monsoon activity (Jones et al. 2004).

It is less common for MJO events in nature to have their maximum intensity over the Maritime Continent between 110°E-140°E (Fig. 2.4.2a). In this region, the effects of an enhanced diurnal cycle and a disruption of low-level winds and surface heat fluxes by the terrain can weaken intraseasonal variability (e.g., Inness and Slingo 2006, Sobel et al. 2009). Events are often strongest during December with a secondary maximum in May. In the model (Fig. 2.4.2b), MJO events occur most frequently in December with a secondary maximum in May, mirroring nature.

Unlike observations, however, simulated events have peak intensities most frequently over the Maritime Continent (120°E-130°E) rather than the east Indian Ocean (although overall

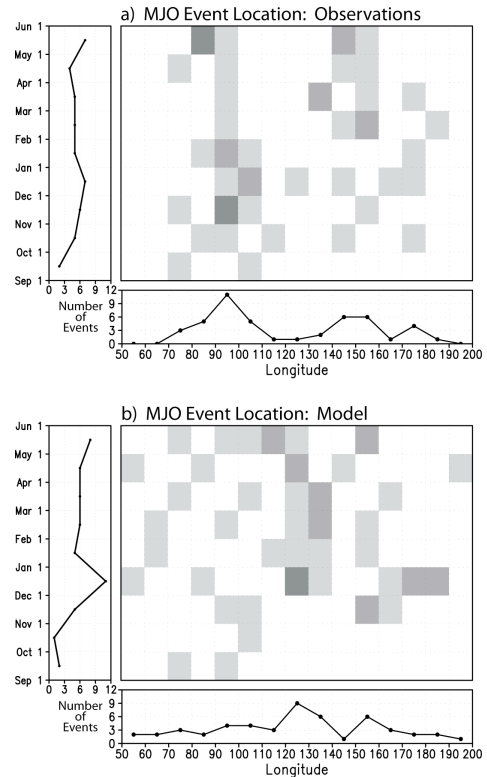


Fig. 2.4.2. Time and longitude information of all identified MJO events from (a) GPCP and (b) SP-CAM rainfall. Shaded squares in the grid represent the time and longitude (binned by month and 10° span) of maximum rainfall intensity associated with each MJO event. Lightest (darkest) shading represents 1 (3) event(s) occurring during that particular month and longitudinal bin. Horizontal and vertical line plots display cumulative event numbers based on longitude and month, respectively.

composite rainfall is greater for West Pacific events). This is consistent with Fig. 2.4.1c and with the finding by Khairoutdinov et al. 2005 that boreal winter rainfall over eastern Indonesia and northern Australia, a sizable portion of which is related to MJO activity, is substantially overestimated by the SP-CAM. The weaker secondary peak of simulated MJO disturbances occurs near 150°E-160°E and matches observations. There is an overall weaker event clustering in the model, with only a broad maximum over the Maritime Continent between December and May and a second isolated peak at the Date Line in December.

2.4.c. Time-height structure of basic variables

Observed time-height structures of the MJO life cycle have become increasingly well-documented in recent years (e.g., Woolnough et al. 2000, Kemball-Cook and Weare 2001, Sperber 2003, Myers and Waliser 2003, KSH05, Benedict and Randall 2007). Figure 2.4.3 displays composite MJO life cycles of several variables. Composites are based on all identified MJO events. In all figures, time is plotted from right to left to mimic a zonal cross section such that negative (positive) lag days correspond to positions east (west) of deep convection. Composites of total rainfall from GPCP, SP-CAM, and their difference (Fig. 2.4.3d, repeated in Fig. 2.4.3h) are also displayed.

A comparison of zonal wind anomalies in ERA-40 and SP-CAM (Figs. 2.4.3a and 2.4.3e, respectively) suggests that the SP-CAM results closely match the qualitative structural evolution of the MJO passage despite some differences in the magnitude of certain features. Specifically, the general baroclinic structure, the timing and vertical

structure of westerly onset, and the timing and magnitude of maximum westerlies following deep convection are well simulated by the model. The simulated magnitude and temporal extent of low-level easterly and upper-level westerly anomalies prior to maximum rainfall appear to be too large, however, suggesting an overly intensified

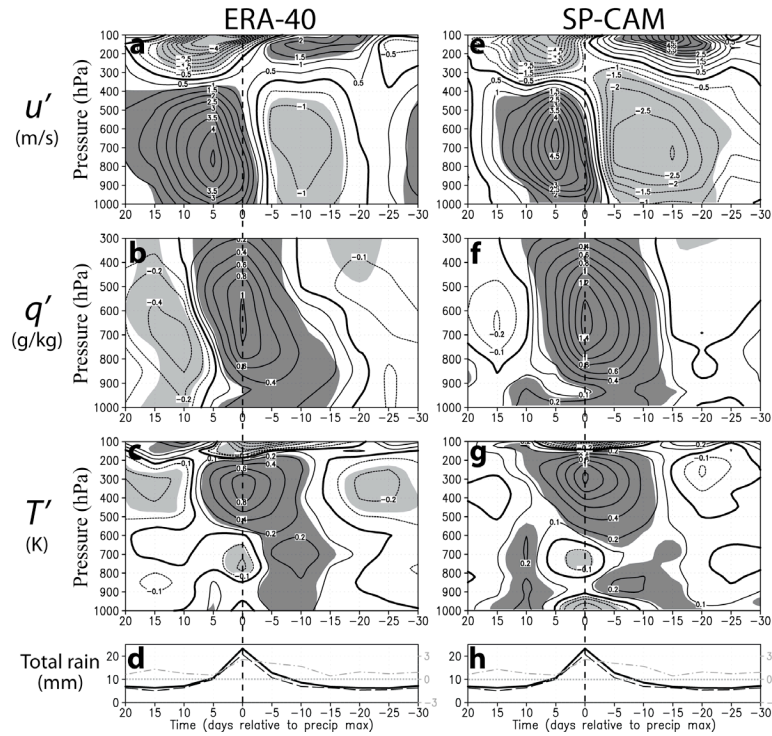


Fig. 2.4.3. Composite time-height plots of anomalous zonal wind u' (top row), specific humidity q' (second row), and air temperature T' (third row) based on ERA-40 data (left column) and SP-CAM output (right column). Composites contain all identified MJO events within their respective data sources. Thin solid (thin dashed, thick solid) lines display the positive (negative, zero) contours, and dark (light) shading indicates areas of statistical significance greater than 95% for positive (negative) anomalies. In the bottom row, composite timeseries of rainfall from GPCP (dashed black), SP-CAM (thick solid black) and their difference (SP-CAM-GPCP; dot-dash gray) are shown.

transient Walker-type circulation in the SP-CAM. KSH05 used data from several radiosonde stations to show that the development of significant low-level easterly winds prior to MJO deep convection tended to occur around Day -25, slightly earlier than the ERA-40 results might suggest and closer in line with the SP-CAM cross section.

Composite moisture profiles (Figs. 2.4.3b and 2.4.3f) indicate moistening of the initially dry free troposphere, first in the lower levels and then deepening to the upper levels as convection intensifies. This feature is seen in both ERA-40 and SP-CAM, as are Day-0 q' maxima at 650 hPa and drying following maximum rainfall. Whereas reanalysis has distinct dry periods throughout the entire troposphere before and after heaviest rains, the q' evolution in the model is shifted positively such that dry periods are less dry and wet periods are wetter. This discrepancy is particularly evident during the suppressed phase following deep convection (Days +5 to +20), at the Day-0 maximum q' (40% larger in SP-CAM), and in the persistent positive q' below 800 hPa throughout the model's MJO life cycle. As will be discussed in Section 2.5, an unrealistic feedback between convection, surface fluxes, and SSTs in the simulation set-up might contribute to this positive moisture bias. It is also possible that the fewer number of MJO events in the Indian Ocean region might suppress anomalous drying from Asia.

The fundamental elements of the evolving MJO temperature structure (Figs. 2.4.3c,g) are captured by the SP-CAM. In both composites, low-level warm anomalies lead heavy precipitation by one to two weeks. When rainfall is most intense near Day 0, upper-level T' is maximized as significant negative anomalies develop near the tropopause and below the tropical freezing level (550 hPa). Radiosonde-based studies (Lin and Johnson 1996a, Kemball-Cook and Weare 2001, KSH05) that diagnose the evolving vertical temperature structure during an MJO passage have shown that maximum upper-tropospheric warmth typically occurs within five days of the deepest convection, in concert with the simulated composite results here. Together, the

composite plots of T' (Figs. 2.4.3c,g) and q' (Figs. 2.4.3b,f) depict well-documented features of the MJO: low-level warming and moistening on Days -15 to -10 suggesting shallow convection development, deep-layer positive T' and q' on Days -10 to -5 reflecting deep convective processes, and “top-heavy” profiles of T' and q' on Days -5 to $+5$ indicating a transition to stratiform precipitation processes (e.g., KSH05).

Despite capturing many features of the observed MJO temperature structure, several model deficiencies exist. The SP-CAM has insufficient cooling in the middle to upper troposphere during the MJO suppressed phase (Fig. 2.4.3g). The model tends to redevelop significant low-level warm anomalies during the post-convective suppressed phase (Days $+7$ to $+16$), where no such warming is seen in observations. Additionally, the magnitude of simulated 300 hPa T' maximum on Day 0 is nearly 50% larger than in nature. Important boundary-layer features differ between the model and reanalysis as well. In the SP-CAM, low-level warmth prior to deep convection develops first within the boundary layer beginning near Day -20 , while in ERA-40 initial warmth is seen first at 700 hPa and significant boundary layer warming is delayed until about Day -12 . Also, the SP-CAM produces a well-developed boundary layer cold pool (near-surface $T' = -0.6$ K on Day 0, Fig. 2.4.3g), likely the result of vigorous convection and abundant boundary layer rain evaporation. Owing to its coarser vertical resolution and strong dependence on parameterizations over the open ocean, the reanalysis could have difficulty accurately capturing the low-level stratiform precipitation signature and evaporative cooling within the boundary layer. Radiosonde-based results show that Day-0 meridionally averaged boundary layer cooling does not exceed -0.4 K for the composite MJO (KSH05), further

suggesting an overestimation by the SP-CAM. Fluctuations of boundary layer moisture and temperature are an essential aspect of intraseasonal convective episodes (Wang 1988, Maloney and Hartmann 1998, Kemball-Cook and Weare 2001), and capturing such variability in GCMs is likely a critical step toward simulating a realistic MJO.

The composite timeseries of total rainfall for SP-CAM, GPCP, and their difference are shown in Fig. 2.4.3d (and repeated in Fig. 2.4.3h). For the composite of all MJO events, the SP-CAM consistently overestimates rainfall during all phases of the MJO by 1-2 mm d⁻¹. As we will see shortly, these biases are mainly associated with MJO disturbances whose peak rainfall intensities occur in the West Pacific rather than the Indian Ocean or Maritime Continent sectors. The greatest departures from observations occur during the 10 days leading up to deepest convection and at two weeks following heaviest rainfall as the suppressed phase emerges. When rainfall is most intense (Day 0, Fig. 2.4.3d), the SP-CAM out-precipitates GPCP by 20%. These overestimations of precipitation combined with the excessive warmth, moisture, and zonal circulation reflect the model's tendency to produce MJO convection that is too vigorous, particularly for West Pacific disturbances.

Cross sections of equivalent potential temperature θ_e' , which behaves similarly to moist static energy, are displayed in Figs. 2.4.4a,b for ERA-40 and SP-CAM, respectively. Positive departures of θ_e' develop first in the lower troposphere below about 800 hPa in both composites. Deepening convective clouds rooted in the boundary layer loft high- θ_e air into the free troposphere between Days -15 and -10 as θ_e' becomes negative near 100 hPa. The lofting of high- θ_e air near Day -10 is too rapid in the SP-

CAM (Fig. 2.4.4b) compared to reanalysis (Fig. 2.4.4a), suggesting a premature yet intense onset of MJO-related deep convection in the model that is confirmed by the

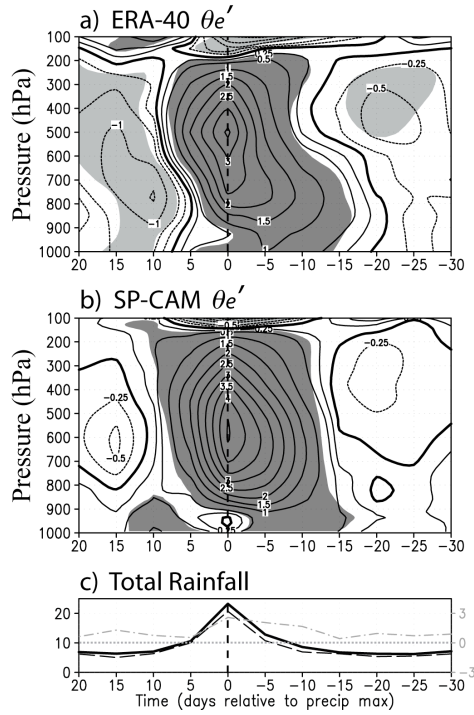


Fig. 2.4.4. As in Fig. 2.4.3, but for equivalent potential temperature θ_e' for (a) ERA-40 and (b) the SP-CAM.

rainfall bias in panel c. We see that θ_e' is also uniformly too positive in the SP-CAM, particularly below 800 hPa during the suppressed phase. This observation is consistent with the SP-CAM's positive biases of low-level T' and q' during the suppressed phase (Fig. 2.4.3). Additionally, simulated maximum perturbations of θ_e' on Day 0 are lower in altitude and greater in magnitude than those in nature.

Composite timeseries of simulated and observed precipitable water (PW) anomalies (Fig. 2.4.5a) indicate a gradual moistening during the two weeks preceding deep convection followed by a more rapid decline in moisture to below-climatological values after heaviest rainfall. Except for Day -15, simulated PW' is consistently 0.5-2.0 mm wetter than observations. This wet bias, which matches the q' plots of Fig. 2.4.3 along with the SP-CAM's persistent overestimation of precipitation (dashed line in the bottom panel of Fig. 2.4.5), is most notable one to two pentads prior to heaviest rainfall as well as during the drying phase of the MJO (Days +5 to +15). Despite these discrepancies, the time evolution of simulated

PW' closely follows observations and the magnitude of the maximum anomaly is only 10% larger than NVAP satellite-based measurements.

Simulated and remotely sensed OLR perturbations are displayed in Figure 2.4.5b and support the theme of unrealistically intense convection in the SP-CAM during the peak of the MJO wet phase. Composite OLR' based on all simulated MJO events is more negative than ISCCP-based composites, especially within two weeks before and after maximum MJO-related rainfall.

2.4.d. Structure of derived quantities

Convective heating and advective moisture transport are two complex yet fundamental processes associated with the MJO. Because such processes involve several dynamic and thermodynamic variables, their accurate representation is a critical test of the SP-CAM's ability to produce realistic MJO disturbances.

We examine the anomalous apparent convective heating Q_1' , representing both cumulus and stratiform heating and radiative effects, in pressure-longitude space rather

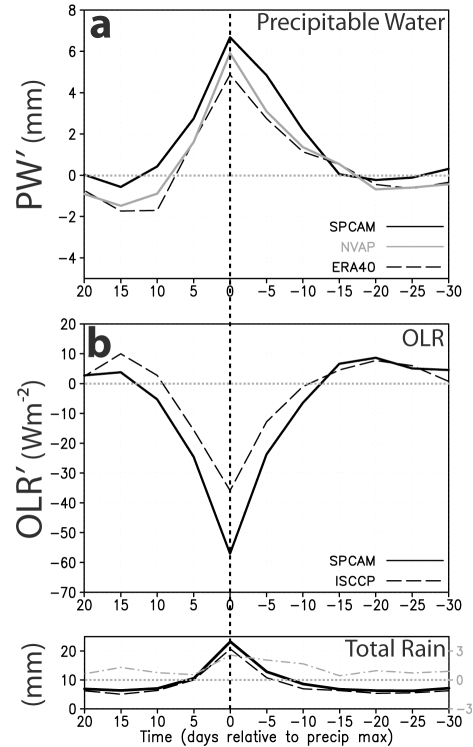


Fig. 2.4.5. Timeseries of (a) precipitable water PW' and (b) OLR' during the MJO life cycle. Data sources for PW' include SP-CAM (solid black), NVAP (solid gray), and ERA-40 (dashed black); OLR' sources include SP-CAM (solid black) and ISCCP (dashed black). Composites contain all identified MJO events within their respective data sources. Rainfall plot at bottom is identical to Fig. 2.4.4c.

than pressure-time space as in Figs. 2.4.3-2.4.5. Having longitude rather than time along the horizontal axis better illustrates the westward tilt of Q_1' with height (see Lin et al. 2004), a feature that was less clear using the coarser pentad time resolution from previous

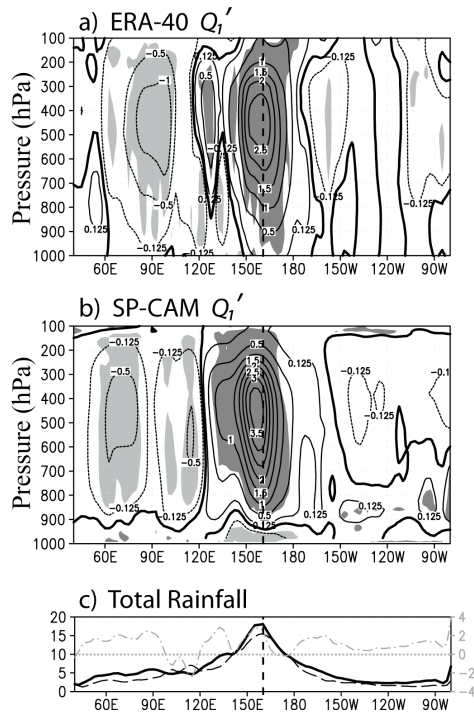


Fig. 2.4.6. Longitudinal cross section of anomalous apparent convective heat source Q_1' , averaged between 10°S - 5°N , at fixed time corresponding to maximum MJO-related rainfall at 160°E for (a) ERA-40 and (b) SP-CAM. Contours and significance shading are identical to Fig. 2.4.3. Corresponding longitudinal profile of rainfall (c) displays observed, simulated, and difference rainfall values as in Fig. 2.4.3.

plots. For Fig. 2.4.6, we again utilize MJO filtered signals as a guide to construct composites of the unfiltered field. For a given MJO disturbance (previously identified in Section 2.3), we scan the times during which its MJO convective envelope overlaps a chosen longitude (for Fig. 2.4.6, 160°E). We select the pentad corresponding to the maximum in unfiltered meridionally averaged rainfall at that chosen longitude, and call this the *base time*. We then composite the

unfiltered meridionally averaged Q_1' field in pressure-longitude space referenced to this base time. Figure 2.4.6 displays longitudinal cross sections of Q_1' and total rainfall averaged

between 10°S and 5°N . Both heating profiles

are qualitatively similar, with mid-level maxima near 450 hPa within 4 - 8° longitude [1-2 days, assuming a 5 m s^{-1} MJO phase speed (Woolnough et al. 2000)] of heaviest rainfall, lingering heating above 500 hPa to the west of the deep heating, and deep-layer negative

anomalies west of 120°E reflecting increased radiative cooling and decreased convective heating during the MJO suppressed phase. The model, however, tends to produce a maximum heating value that is larger than observed, does not produce as clear a mesoscale stratiform signal in the MJO wake (120°-140°E), and has weaker and westward-shifted suppressed-phase radiative cooling (negative Q_1') over the Indian Ocean. The SP-CAM fails to produce weak but significant negative Q_1' values in the middle troposphere prior to heaviest rainfall (near 160°W) and in the lower troposphere during the time when stratiform processes are active (near 130°E). At both of these longitudes, simulated rainfall is notably higher than observed rainfall. We can therefore infer that deep convective processes are not as weak as they should be at these locations relative to maximum MJO rainfall.

Returning to the pressure-time composite framework, we next examine horizontal divergence. Observed boundary layer convergence (Fig. 2.4.7c) develops approximately two weeks prior to heavy rainfall and is followed by stronger, deep-layer convergence on Day 0, lingering weaker convergence at mid levels through Day +10, and finally upper-level convergence after Day +10. A very similar vertically tilted structure is noted in the simulated divergence field (Fig. 2.4.7f), although maximum convergence (divergence) magnitudes at lower (upper) levels on Day 0 are substantially larger than those in Fig. 2.4.7c. Additionally, the SP-CAM composite of 50 events does not show a consistent low-level divergence pattern after Day +10 when compared to statistically significant divergence values in ERA-40.

In nature and in the model, boundary layer convergence prior to deep convection is primarily associated with the meridional component (Figs. 2.4.7b and 2.4.7e, respectively). This shallow convergence layer develops as early as Day -20 and counteracts weak zonal divergence as seen in the reanalysis composite (Fig. 2.4.7a).

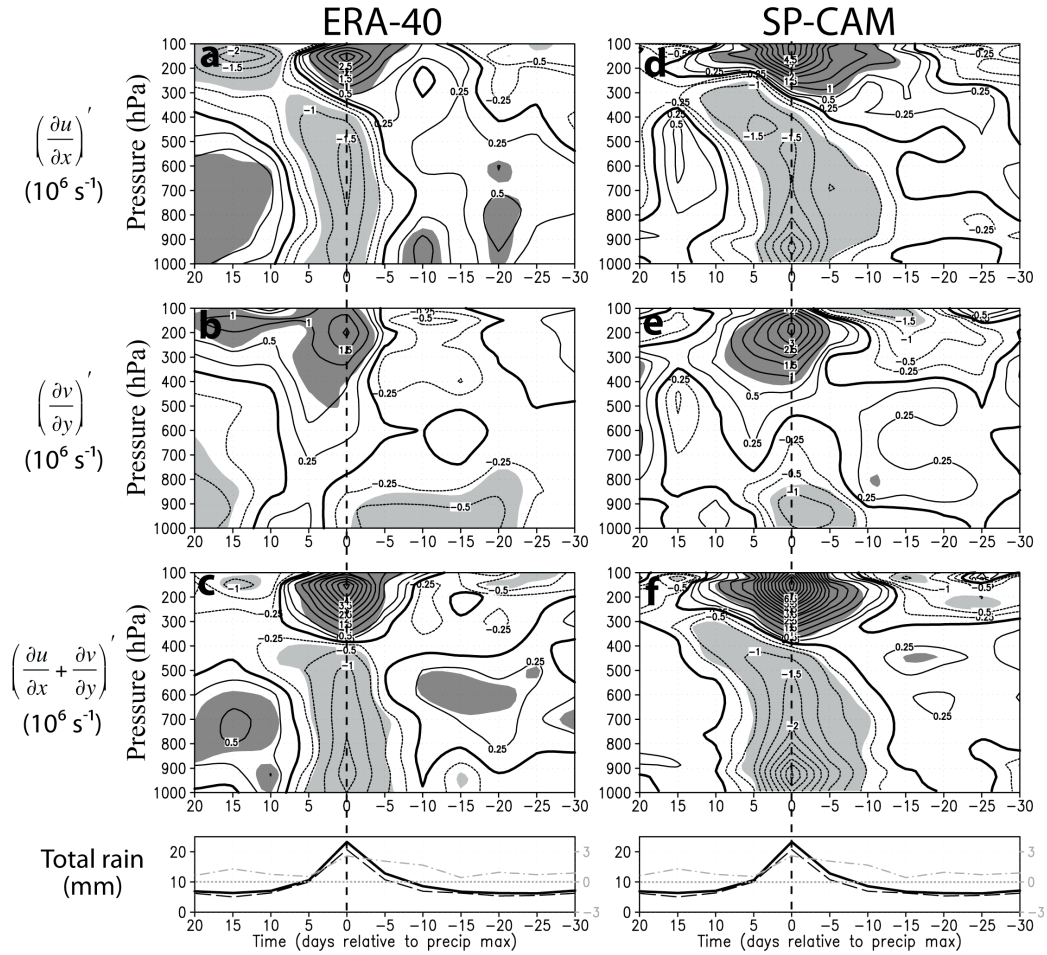


Fig. 2.4.7. As in Fig. 2.4.3, but for zonal divergence, meridional divergence, and total horizontal divergence.

Boundary layer convergence extending well ahead of mature MJO convective disturbances is described by the “frictional convergence feedback.” This mechanism has

been well-documented in numerous studies and is thought to play an important role in preparing the atmosphere for deep convection via destabilization (Wang 1988, Salby et al. 1994, Maloney and Hartmann 1998).

Displayed in the top row of Fig. 2.4.7, deep-layer zonal convergence from the surface to 350 hPa is accomplished by a rapid deceleration of easterly (westerly) zonal winds preceding (following) MJO-related deep convection near Day 0 (see Fig. 2.4.3). Lingering zonal convergence above 500 hPa between Days +5 and +10 reflects the transition from convective to stratiform cloud processes, with mid-level convergence sandwiched between divergent (or less convergent) layers above and below. Insufficient (or inconsistent, from event to event) simulated zonal divergence, noted in Fig. 2.4.7d between the surface and 500 hPa after Day +10, can be traced back to the premature weakening of low-level westerly anomalies in the SP-CAM relative to reanalysis (Figs. 2.4.3e and 2.4.3a, respectively). Additionally, weaker low-level zonal divergence in the model prior to deep convection (Fig. 2.4.7a) is linked to suppressed-phase easterlies that are too extensive and fairly uniform in magnitude (c.f. Figs. 2.4.3e and 2.4.3a).

Figure 2.4.8 presents the total horizontal components of the advective form of the moisture budget equation². As demonstrated by Arakawa (2004), components of the moisture budget equation in *advective* form more directly and accurately represent temporal changes in q . The plots of total horizontal moisture advection indicate that deep-layer moistening occurs prior to the onset of the MJO wet phase. At this time (Days –20 to –10), advective moistening within the boundary layer is achieved by the zonal

² Condensation (C) and evaporation (E) are not explicitly analyzed because they are not available as reanalysis products and are, in practice, difficult to measure.

component while meridional moisture convergence is noted in the free troposphere (not shown). Vertical moisture transport (not shown) dominates between Days -10 and $+5$ and, because Q_1' is positive and non-negligible at this time, this moistening by large-scale vertical advection is likely a manifestation of widespread deep convection and its associated detrainment on subgrid scales. In both the model and observations, large-scale horizontal advective drying commences just before heaviest precipitation and is maximized between Days 0 and $+5$ at 650 hPa (Fig. 2.4.8). Although the moisture budget on Day 0 is dominated by moistening from the vertical component, the rapid decrease in

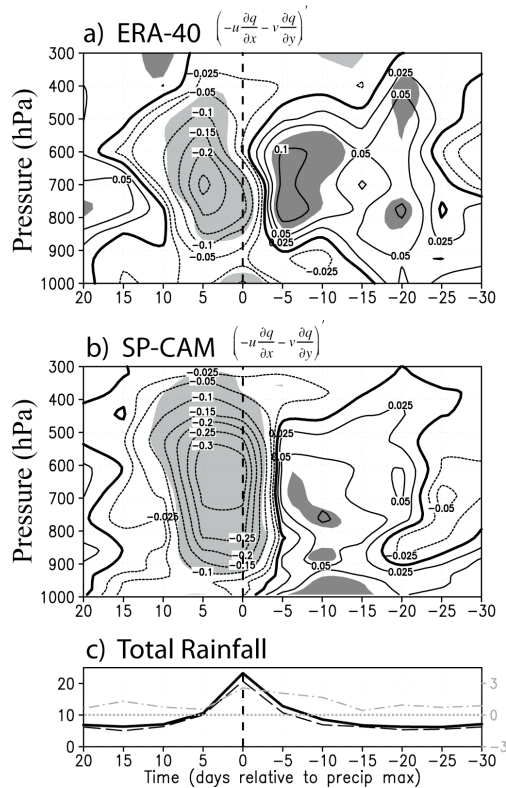


Fig. 2.4.8. As in Fig. 2.4.4, but for horizontal moisture transport.

q' between Days 0 and $+5$ can be mostly attributed to horizontal advective drying because $[-\omega(\partial q/\partial p)]'$ remains positive through Day $+5$ (not shown). Lower tropospheric drying linked to horizontal advection following the MJO has been discussed in previous studies (e.g., Maloney 2009, Benedict and Randall 2007). Overall, the SP-CAM composites compare very favorably with those of ERA-40, accurately capturing key large-scale advective features throughout the MJO life cycle. We note that our analysis of pentad data restricts our

ability to investigate the role of humidity advection by small-scale eddies, a potentially important aspect of the MJO moisture budget (Maloney et al. 2009).

2.4.e. Longitudinal dependence of MJO structure

Our compositing technique pinpoints the time and longitude of maximum unfiltered rainfall during an MJO disturbance. Owing to this procedure, we can subset the list of all MJO events by categorizing them based on their tagged longitudes. This subsetting allows us to examine the differences in dynamic and thermodynamic structure of the MJO as a function of the longitude at which each event reaches its peak intensity.

Table 2.4.1. The number of MJO events recorded in each longitudinal sector. The event location is defined as the longitude at which the MJO disturbance’s maximum rainfall occurred. “Observations” here refers to the ERA-40 dataset.

	Observations 1984-2002	Model 1985-2004
Indian Ocean MJO events (50°E-100°E)	15	13
Maritime Continent MJO events (100°E-145°E)	14	22
West Pacific MJO events (145°E-170°W)	17	15
Total	46	50

Table 2.4.1 gives the number of MJO events for each longitudinal sector. Time-height composites of u' for each sector are displayed in Fig. 2.4.9. The SP-CAM captures the longitudinal-dependent timing and vertical structure of westerly anomalies remarkably well. In the Indian Ocean sector, anomalous low-level easterlies transition to

westerlies only one to two days prior to maximum rainfall in the reanalysis composite (Fig. 2.4.9a). This transition is uniform with height from the surface to 500 hPa, and the maximum westerlies occur about one pentad following peak rainfall (Fig. 2.4.9c). A similar transition is noted in the SP-CAM Indian Ocean composite (Fig. 2.4.9b), although somewhat greater inconsistency among events in the westerly onset is reflected by the

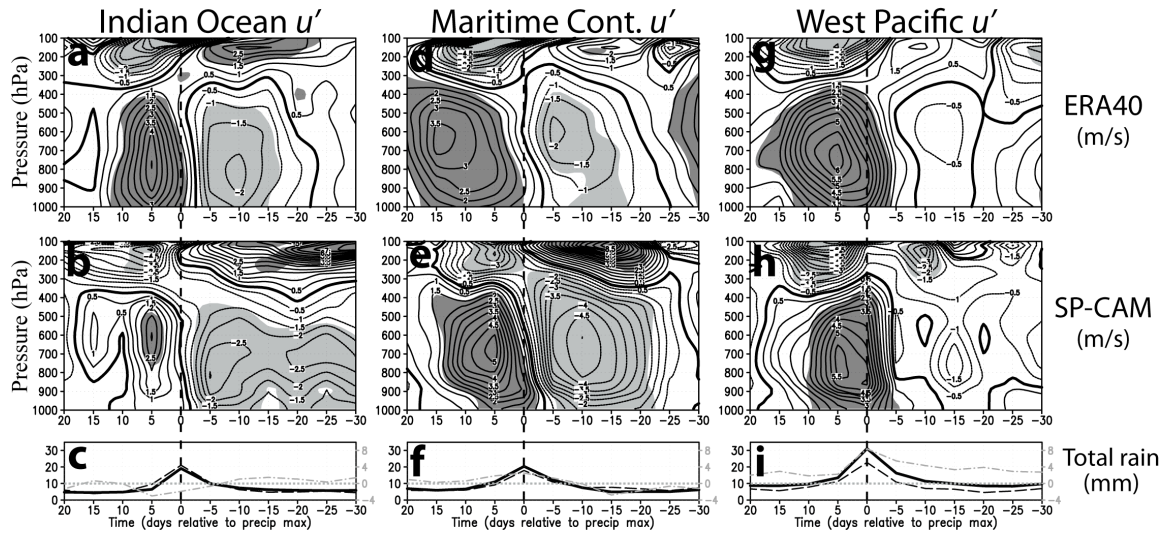


Fig. 2.4.9. A comparison between ERA-40 (top row) and SP-CAM (middle row) composite anomalous zonal wind u' for the Indian (50°E - 100°E ; left column), Maritime Continent (100°E - 145°E ; middle column), and West Pacific sectors (145°E - 170°W ; right column). Composites are based on any identified MJO events that have their maximum intensity in the indicated longitudinal sector. Thin solid (thin dashed, thick solid) lines display the positive (negative, zero) contours, and dark (light) shading indicates areas of statistical significance greater than 90% for positive (negative) anomalies. Composite timeseries (bottom) of rainfall corresponding to the indicated longitudinal sector are shown, including GPCP (dashed black), SP-CAM (thick solid black) and their difference (SP-CAM—GPCP; dot-dash gray).

lower significance values. Simulated and observed MJO disturbances in the Maritime Continent sector both indicate a slightly earlier onset of low-level westerlies (3-4 days before peak rainfall) and a more pronounced vertical tilting (Figs. 2.4.9d and 2.4.9e, respectively). MJO events in the West Pacific tend to have an even earlier onset of westerlies relative to maximum rainfall. In both model and reanalysis (Figs. 2.4.9h and

2.4.9g, respectively), westerly onset within a deep layer from the surface to 400 hPa occurs 5-6 days before intense rainfall for West Pacific events. While there are noted differences between the wind structures of the SP-CAM and ERA-40 (e.g., the magnitudes of low-level Indian Ocean westerlies), the general character of the easterly-to-westerly transition in the model compares favorably with nature.

Figure 2.4.10 displays more clearly the consistent behavior of low-level (925 hPa) westerly wind onset between the SP-CAM and reanalysis composites. For events with peak convective intensities in the Indian Ocean sector, both the model and reanalysis (thick solid gray and thick dashed gray

lines in Fig. 2.4.10, respectively) indicate that total (not shown) and anomalous low-level winds are decidedly easterly on Day -5 and weakly westerly on Day 0. For MJO events farther east in the Maritime Continent sector, we can infer that this transition is slightly earlier in nature

and the SP-CAM (dashed and solid

dark gray lines in Fig. 2.4.10, respectively). The earliest onset of low-level westerly wind anomalies is noted for West Pacific events, with the strongest westerlies nearly coincident with maximum rainfall for the reanalysis and simulation composites (thin dashed black and thin solid black lines, respectively). This shift in maximum surface westerlies—from

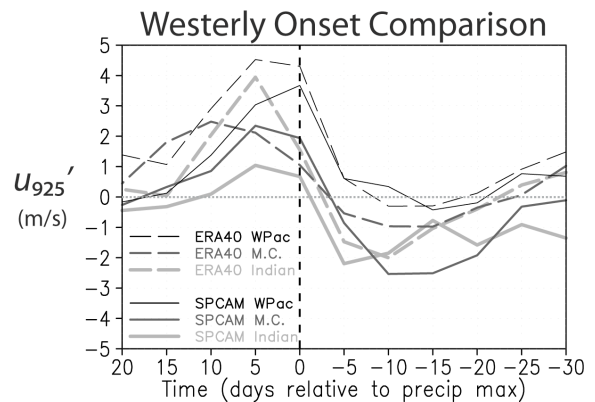


Fig. 2.4.10. A comparison between ERA-40 (dashed lines) and SP-CAM (solid lines) anomalous zonal winds at 925 hPa for the longitudinal sectors examined in Fig. 2.4.9.

several days after heaviest precipitation to being coincident with it—has been extensively documented using *in situ* measurements (e.g., Zhang and McPhaden 2000).

2.4.f. Composite maps

Figures 2.4.11 and 2.4.12 present the spatial structure of MJO disturbances with maximum rainfall centers in the eastern Indian and West Pacific sectors, respectively. We

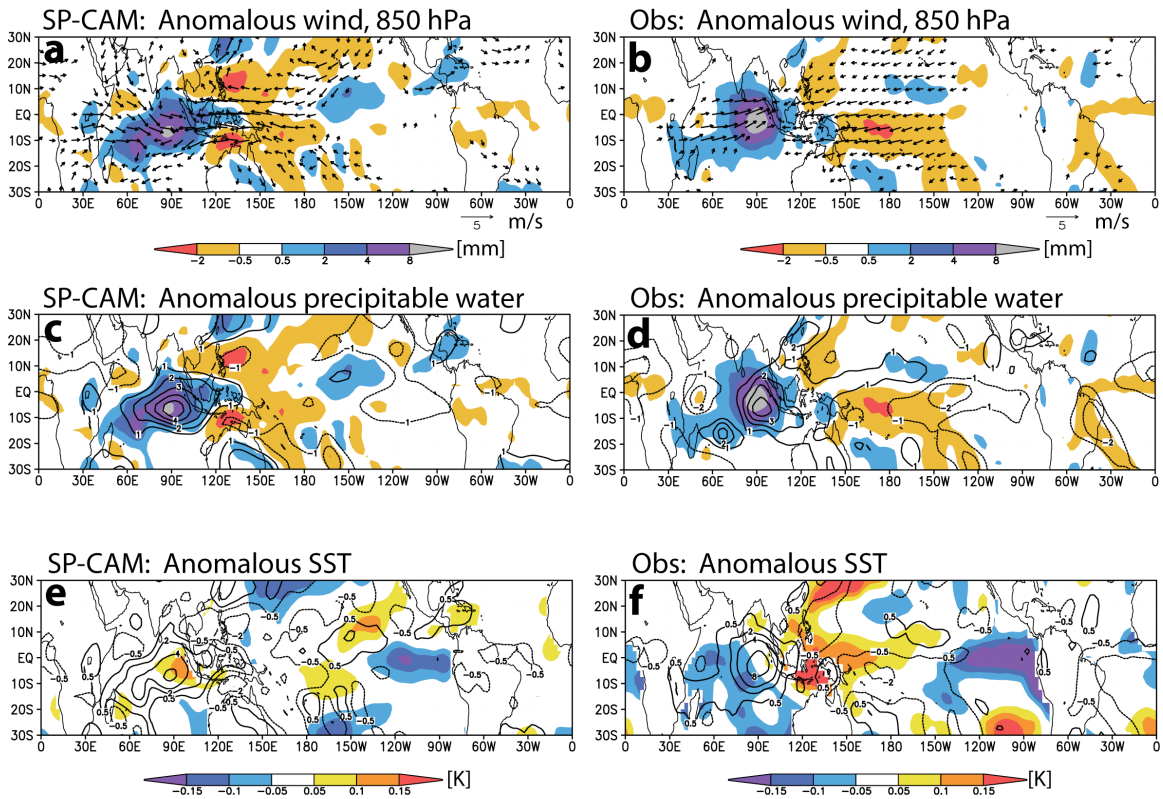


Fig. 2.4.11. Composite plots of anomalous 850 hPa wind (top), precipitable water (middle), and SST (bottom) for simulated (left) and observed (right) MJO events with rainfall maxima at 90°E. Rainfall anomalies are shaded in the top two rows, and contoured in the bottom row. Anomalies are based on departures from the long-term boreal winter mean. Shading and contours correspond to significance levels above 90% in the Tropics. Approximately 40 MJO disturbances contribute to each composite.

follow a similar procedure used to produce Fig. 2.4.6 (see Section 2.4d), but now construct composites in longitude-latitude rather than pressure-longitude space. Overall,

the simulated spatial composites exhibit consistency with observations. Owing to the chosen seasonal range, precipitation centers occur as a single maximum just south of the Equator and are flanked by negative rainfall anomalies to the east and west (shading in Figs. 2.4.11a,b and 2.4.12a,b). The spatial scale of the rainfall anomalies in the SP-CAM compares well with that in the GPCP-based composite. The 850 hPa anomalous horizontal wind fields are similar, with westerly anomalies concurrent and to the west of the 90°E rainfall center but leading the 160°E rainfall center (vectors in Figs. 2.4.11a,b

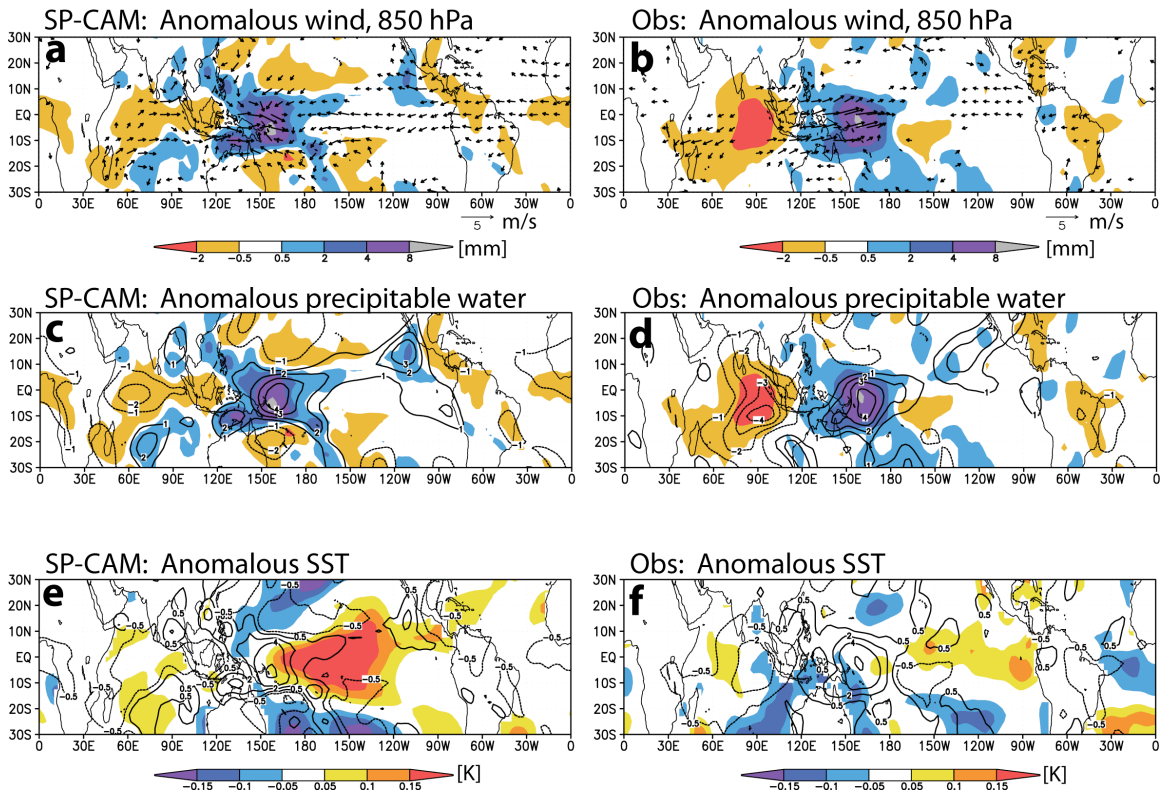


Fig. 2.4.12. As in Fig. 2.4.11, but for MJO events with rainfall maxima at 160°E.

and 2.4.12a,b). Easterly anomalies to the east of the disturbance are stronger when the rainfall center is in the Indian Ocean. In both the model and observations, maximum

positive precipitable water anomalies occur just ahead of the rain centers and are of comparable magnitude (Figs. 2.4.11c,d and 2.4.12c,d). Additional analyses (not shown) reveal that other well-documented features of the MJO are seen in the SP-CAM spatial composites: (1) low-level positive moisture anomalies, convergence, and rising motion occur well ahead of the disturbance where rainfall anomalies are still negative, (2) low-level divergence and subsidence are noted in the wake of the disturbance (Maloney and Hartmann 1998), and (3) anomalous surface latent heat fluxes tend to be negative (positive) before (within and after) the rain center (Jones and Weare 1996).

Several differences between the spatial composites of the simulation and observations must be addressed. Possibly arising from the greater magnitude of equatorward flow from the drier subtropics (Figs. 2.4.11a,b and 2.4.12a,b), bands of more substantial negative rain anomalies straddle the Equator ahead of the rain centers in the SP-CAM, particularly for the Indian Ocean composite. Greater meridional flow in the model is also noted at upper levels (not shown), where Rossby gyres are stronger and shifted equatorward compared to observations. Consistent with the rainfall timeseries of Fig. 2.4.9, simulated peak rain anomalies are weaker (stronger) for the Indian Ocean (West Pacific) composites. Additionally, the redevelopment of easterly anomalies in the West Indian Ocean is delayed in the model (cf. Figs. 2.4.12a,b), possibly suggesting a slower re-emergence of the next MJO event. Perhaps the most notable discrepancy, as previously discussed in Section 2.4.c, is the significantly weaker atmospheric drying in the wake of simulated MJO disturbances. In the Indian Ocean, trailing rainfall anomalies to the southwest of the rain center are more positive in the model and trailing negative

moisture anomalies are shifted northward off the Equator (Figs. 2.4.11c,d). Insufficient atmospheric drying in the model is clearer for West Pacific events (Figs. 2.4.12c,d). In this region, simulated negative anomalies of rainfall and moisture in the MJO wake are weaker and shifted westward by 30° to the West Indian Ocean. The absence of strong drying following heavy rains in the SP-CAM could be partially tied to the model's prescribed SSTs. In Figs. 2.4.11e,f and 2.4.12e,f, warm SSTs³ lead heavy rains, but the substantial cooling seen in nature following the precipitation maximum is non-existent in the AMIP simulation. Consistent with this lack of ocean surface cooling, negative anomalies of low-level q and θ_e are weaker and surface flux anomalies are higher in the model (not shown). A more detailed discussion of the atmosphere-ocean feedbacks in relation to the simulated MJO is presented next.

2.5. Discussion and Conclusions

2.5.a. The West Pacific MJO intensity bias

We have demonstrated that the convective intensity of the all-event composite MJO is greater in the SP-CAM than in observations. A closer examination indicates that such biases are relatively small for events in the Indian Ocean and much larger for West Pacific (WP) events. For example, root-mean-square errors of total precipitation over the composite MJO life cycle are 1.4, 1.5, and 4.1 mm d⁻¹ for events in the Indian, Maritime

³ Although SST in the model is prescribed using observations from 1985-2004, we can treat these data as we would any other variable and form composites based on simulated maximum rainfall.

Continent, and WP sectors, respectively (e.g., bottom panels of Fig. 2.4.9). Additional metrics based on other atmospheric variables (not shown) also reveal the overestimated intensity of WP MJO events. Although a more detailed and definitive explanation is beyond the scope of this study, we will mention several factors that may contribute toward the positive intensity bias of simulated WP MJO disturbances.

Possible origins of the intense WP MJO events may be linked to the lower boundary conditions when such disturbances are active. Figure 2.5.1 displays the behavior of several boundary layer variables during the MJO life cycle for events in the Indian and WP sectors. Composite timeseries of SST' (Figs. 2.5.1a,b) indicate that simulated MJO disturbances tend to have their maximum rainfall rates in the WP when SSTs there are warmer than climatology, while SST' values for events farther west are more similar to observations. The tendency of the model to produce WP MJO events when prescribed SST values in that region are warm—in combination with other factors [e.g., substantially stronger surface fluxes (cf. Fig. 2.5.1c,d) and a more developed moisture convergence signal (see Fig. 3.5.2)]—would contribute toward an increased likelihood and intensity of simulated deep convection (Maloney and Hartmann 1998, Wang and Xie 1998). These processes linking anomalously warm SSTs, overestimated air-sea energy exchange, and enhanced moisture convergence may help to explain the model's tendency to favor the development of organized convection of greater intensity in the WP region. We also note that three (of 15 total) events in the SP-CAM WP composite occurred after the end of the selected observational data range and at a time when SSTs were above their long-term average.

In nature, tropical convective intensity is regulated by downdrafts that inject cooler and drier air into the boundary layer, generally resulting in increased surface

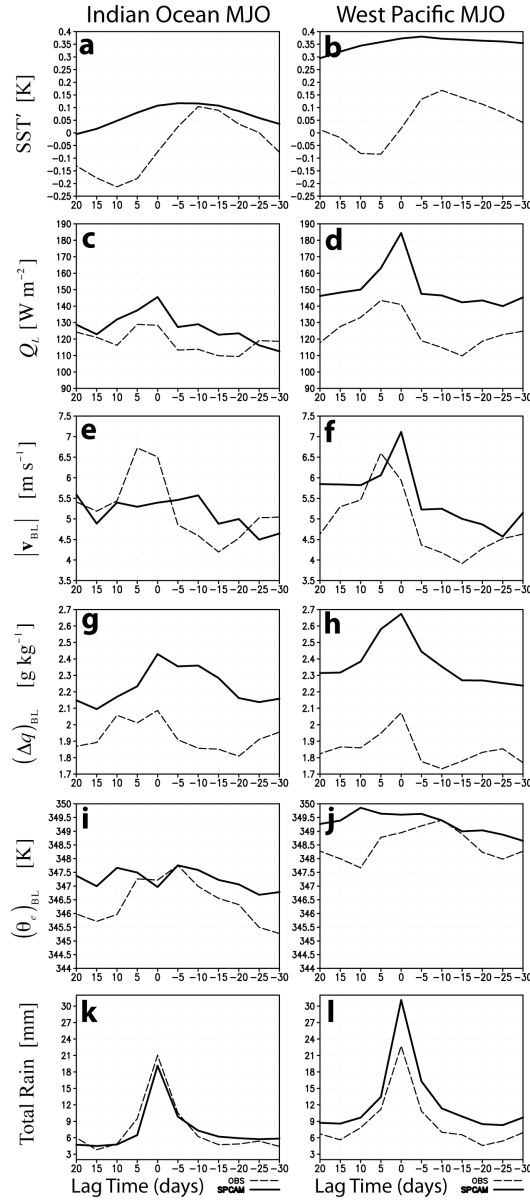


Fig. 2.5.1. Composite timeseries of boundary layer fields during the life cycle of MJO disturbances in the Indian Ocean (left) and West Pacific (right). Displayed from top to bottom are SST anomaly, total surface latent heat flux Q_L , boundary-layer-averaged [“BL”; (992 hPa + 925 hPa)/2] wind magnitude $|\mathbf{v}_{BL}|$, BL difference (992–925 hPa) of specific humidity $(\Delta q)_{BL}$, BL total equivalent potential temperature $(\theta_e)_{BL}$, and total rainfall for observations (dashed) and SP-CAM (solid). Domain boundaries are listed in the Fig. 2.4.9 caption. ERA-40 are used as observed fields for all but SST' (OISST2) and rainfall (GPCP).

gustiness, enhanced evaporative fluxes, and cooler SSTs (Zipser 1969, Houze 1982, Lin and Johnson 1996a, Zheng et al. 2004; dashed lines in our Figs. 2.5.1f,d,b, respectively). Although downdrafts and robust convectively generated cold pools exist in the SP-CAM (e.g., Fig. 2.4.3g), the feedback connection is incomplete because the prescribed SSTs are unaffected by the surface energy fluxes (solid lines in Figs. 2.5.1a,b). In the model, the combination of enhanced, convectively driven surface fluxes and unmodulated SSTs could maintain or more rapidly restore boundary layer θ_e and lead to an increased probability of future convection (e.g., Raymond 1995). Additional factors such as the “recycling” of small-scale convective systems across the periodic CRM boundary may also contribute to this problem, termed the “convection-wind-evaporation feedback.” Adaptations of this theory, originally proposed by Emanuel (1987) and Neelin et al. (1987), have been shown to play an important role in organized tropical convection on many scales, as seen in observations (e.g., Hendon and Glick 1997), conventional GCM simulations (Zhang 1996, Maloney and Sobel 2004), GCM simulations using superparameterization (Luo and Stephens 2006), or CRM simulations (Wang et al. 1996).

To further investigate the potential role that convection-wind-evaporation feedback may play regarding WP MJO biases in the SP-CAM, we examine the components of surface latent heat flux during the MJO life cycle (Fig. 2.5.1). We have established that, compared to Indian Ocean events, simulated MJO disturbances in the WP have higher SST' (Figs. 2.5.1a,b) and consistently heavier rains (Figs. 2.5.1k,l). In this region, near-surface (992 hPa) q is considerably higher in the model compared to observations (not shown) and contributes to a sharper vertical gradient of q within the

boundary layer (Fig. 2.5.1h). This, combined with generally stronger boundary layer winds (Fig. 2.5.1f; Thayer-Calder and Randall 2009), is linked to substantially larger simulated surface evaporative fluxes (25-30% greater than ERA-40; Fig. 2.5.1d) throughout the lifetime of the simulated WP MJO disturbance. An investigation of which of these two terms—near-surface moisture gradient or wind speed—contributes more strongly to the surface evaporative flux is an interesting question but is beyond the scope of the current analysis. The ERA-40 total surface latent heat flux composite values in the active and suppressed MJO phases closely match composite *in situ* measurements presented in Zhang (2005), signaling that the SP-CAM is indeed overestimating surface fluxes for MJO disturbances in the WP. Shinoda et al. (1998) show that SST behavior during the life cycle of MJO events in the West Pacific acts to reduce surface flux anomalies, a result that suggests that surface fluxes may be effectively reduced in the SP-CAM by the inclusion of a slab ocean model. A distinguishing feature of simulated WP MJO events involves boundary layer θ_e . Large vertical gradients of θ_e within the boundary layer are seen in the SP-CAM (not shown)—particularly during the heaviest rains—and are the result of warmer near-surface θ_e (relative to reanalysis) and cooler θ_e near the upper boundary layer. As in any observed MJO event, θ_e at 992 hPa and 925 hPa for simulated Indian Ocean events decreases as heavy MJO rains develop near Day -5 (e.g., Fig. 2.5.1i), implying the emergence of mechanisms that act dissipate deep convection as discussed previously. In stark contrast, the reduction of boundary layer θ_e during heavy rains is nonexistent for simulated WP MJO events (Fig. 2.5.1j), with θ_e at 992 hPa steadily *increasing* between Days -15 and +10 (not shown). Simulated Indian

Ocean MJO events generally have less rainfall (Fig. 2.15k) and weaker near-surface winds (Fig. 2.5.1e), boundary layer moisture gradients (Fig. 2.5.1g), and surface fluxes (Fig. 2.5.1c) compared to WP events. Additionally, climatological low-level westerlies are weaker in over the Indian Ocean and may contribute to the weaker MJO intensity there. The convection-wind-evaporation feedback and its interaction with elevated SST' appear to play a role in the WP MJO bias of the SP-CAM.

Differences in topography may also contribute to the biases of simulated WP MJO events. In nature, MJO events tend to weaken and become disorganized over the Maritime Continent region in association with altered air-sea interactions and a disruption of the low-level wind field (e.g., Maloney and Hartmann 1998, Inness and Slingo 2006). Our results support these findings and indicate reductions in peak rainfall amounts and maximum convective heating rates for observed MJO events over the Maritime Continent (see Fig. 2.4.9 for rainfall comparison; heating rates not shown). We find, however, that MJO events in the SP-CAM do not weaken as they cross the Maritime Continent. Though simulated intraseasonal disturbances are weaker than observed events in the Indian Ocean region, both show a tendency of increased heating magnitudes as the disturbances propagate eastward. Observed MJO events then weaken as they encounter Indonesia, while MJO intensity is maintained or slightly elevated in the SP-CAM. The sustained heating for simulated Maritime Continent MJO events generates a more vigorous dynamical response (Figs. 2.4.9d,e) and is associated with an environment more favorable for MJO intensification over the WP region. For example, comparing observed and simulated MJO disturbances with rainfall centers over the Maritime Continent

(120°E), lower tropospheric convergence over the WP is two to three times stronger in the SP-CAM (not shown). The lack of MJO weakening over the Maritime Continent and sustained low-level convergence ahead of the disturbance may be yet another factor related to the WP MJO bias.

Differences between simulated and observed boreal winter mean states must also be considered. In the equatorial WP region, climatological precipitation (surface evaporative fluxes) is overestimated by 2-4 mm d⁻¹ (20-35 W m⁻², or 20%) in the SP-CAM (see Figs. 2.4.1a-c and 3.4.5). In the equatorial eastern Indian Ocean, mean rainfall and evaporative fluxes are *underestimated* by ~1-2 mm d⁻¹ and 5-10 W m⁻², respectively. Precipitation biases in the mean state are often associated with biases of the same sign in intraseasonal precipitation variability (Slingo et al. 1996, Kim et al. 2009). We will demonstrate in Chapter 3 that this association between the mean state and intraseasonal variability appears to be occurring in the SP-CAM. Simulated boreal winter mean vertical wind shear is also significantly weaker in the Indian Ocean region compared to observations, whereas slightly positive WP vertical shear biases exist in the model (see Fig. 3.4.6). Additionally, positive (negative) mean 850 hPa zonal wind biases occur over the Maritime Continent and West Pacific (Indian Ocean). The structure of climatological low-level westerlies and the resulting interaction of perturbation and mean winds and surface energy fluxes have been shown to strongly impact the MJO (e.g., Inness and Slingo 2003) and may be contributing to the MJO intensity biases seen in the SP-CAM.

Biases in WP intraseasonal convection may also be related to the treatment of momentum feedbacks in the SP-CAM. The SP-CAM simulation used in this study

neglects convective momentum transport (CMT; see Khairoutdinov et al. 2005), which has been shown to have a considerable impact on the large-scale wind field (Mapes and Wu 2001). Khairoutdinov et al. (2005) demonstrated that excessive boreal summer precipitation is remedied in the West Pacific by including CMT in a version of the SP-CAM that used a 3D CRM configuration. Although those authors did not report whether there was improvement in the MJO representation, it is plausible to infer that accounting for “cumulus friction” in the SP-CAM could reduce West Pacific mean precipitation during boreal winter and perhaps mitigate the West Pacific MJO intensity bias.

We conclude that a combination of factors—unrealistic convection-wind-evaporation feedbacks in the boundary layer, topographic effects, mean state biases, and the lack of convective momentum transport in the SP-CAM—contribute toward the SP-CAM’s MJO intensity bias in the West Pacific region.

2.5.b. Summary

In this study we conduct a detailed comparison of the space-time structure of MJO disturbances between the superparameterized Community Atmosphere Model version 3.0 (SP-CAM) and observation-based data sets. Tropical intraseasonal variability is unrealistically weak in many GCMs (Lin et al. 2006), but the newly developed approach of embedding a collection of cloud-resolving models into each GCM grid cell in order to explicitly simulate subgrid-scale cloud processes gives a realistic depiction of the MJO (KDR08). Whereas previous studies have only done a limited analysis of intraseasonal variability in the SP-CAM using spectral characteristics and simple

measures of variance (e.g., Khairoutdinov et al. 2005, KDR08), our work examines in much greater detail the composite MJO structure and the fundamental convective, advective, and boundary layer processes that affect it.

Our analysis demonstrates that the AMIP-style simulation examined here compares favorably with observation-based data sets regarding many aspects of the composite MJO life cycle. A similar vertical progression of increased moisture and warmth from the boundary layer to the tropopause during deep convective development is seen in the model and observations. The magnitude, timing, and vertical structure of westerly wind onset as well as the magnitude and timing of maximum westerlies following intense convection are well simulated. In both the SP-CAM and reanalysis, there is evidence of low-level convective heating preceding deep convective heating. Meridional convergence within the boundary layer leads deep-layer zonal convergence and intense rainfall in the model and in nature. Additionally, the simulated horizontal advective drying that works to reduce q immediately following the heaviest rains matches the corresponding drying structure in ERA-40.

Several deficiencies of the SP-CAM are apparent from our analysis as well. Many of these biases stem from the overestimation of convective intensity for MJO disturbances with maximum rainfall centers in the West Pacific region. Such an overestimation of MJO variability was initially noted in KDR08 and is confirmed here in greater detail. In the Indian Ocean and Maritime Continent sectors, MJO structural and intensity biases are generally smaller, with the SP-CAM underestimating convective intensity over the Indian Ocean. We will demonstrate in Chapter 3 that this weak bias of

intraseasonal convection in the Indian Ocean is partially alleviated through the implementation of a slab ocean model coupled to the SP-CAM. Compared to observations, the simulated atmosphere at the time of maximum rainfall for MJO events outside of the Indian Ocean involves more robust boundary layer cold pools; stronger vertical motion; a warmer, moister middle troposphere; greater convective heating; and less OLR. We hypothesize that several factors contribute to the overestimated MJO convective intensity in the West Pacific, including unrealistic boundary layer interactions, the lack of weakening of simulated MJO disturbances over the Maritime Continent, differences in the boreal winter mean state, and the neglect of cumulus friction in the SP-CAM configuration. To investigate the impact that prescribed SSTs have on boundary layer processes and surface evaporative fluxes in the context of the MJO, we must utilize a more realistic representation of air-sea energy exchanges. Implementation of a more sophisticated coupling between the atmosphere and ocean surface and the impacts this approach has on MJO representation in the SP-CAM is the subject of Chapter 3.

Chapter 3

MODIFICATIONS TO THE MJO IN A COUPLED VERSION OF THE SP-CAM

The detailed space-time structures of the MJO in the 19-year SP-CAM¹ simulation forced by observed monthly mean SSTs presented in Chapter 2 indicate a considerable improvement over the MJO depiction of the standard CAM and a close resemblance to observed intraseasonal convective disturbances. However, several deficiencies in the SP-CAM's MJO representation are apparent, including disturbances that appear too weak in the eastern Indian Ocean sector, and unrealistically strong convective intensity of West Pacific MJO events. It is well known that air-sea interactions can substantially influence the MJO by modulating its amplitude, structure, and propagation characteristics (e.g., Flatau et al. 1997, Waliser et al. 1999, Rajendran and Kitoh 2006). In this chapter, we investigate the impact of coupling the SP-CAM to an idealized slab ocean model that allows more realistic air-sea interactions. We examine the structure and propagation properties of MJO disturbances from a five-year simulation using the coupled SP-CAM, and compare these results to the MJO representation in the uncoupled SP-CAM.

¹ A list of selected acronyms appears in Appendix A.

3.1. Introduction: Air-sea Interaction and the MJO

3.1.a. Observations

One of the first observational studies to highlight the importance of air-sea interactions and their role in modulating MJO deep convection was reported by Krishnamurti et al. (1988). Those authors examined data from the Monsoon Experiment (MONEX; Greenfield and Krishnamurti 1979) and the First Global Atmospheric Research Program (GARP) Global Experiment (FGGE; Fleming et al. 1979 and references therein) to discover that the ocean supplies the atmosphere with moisture for sustained cumulus heating primarily through surface latent heat flux that is regulated by boundary layer wind fluctuations on intraseasonal time scales. Krishnamurti et al. (1988) also contended that air-sea coupling would be a necessary component of future GCMs if a full understanding of the MJO is to be achieved.

The development of an advanced ocean-atmosphere observing system as part of the Tropical Ocean-Global Atmosphere (TOGA) Tropical Atmosphere-Ocean (TAO) buoy array program in the tropical Pacific (Hayes et al. 1991) between 1985-1990 provided the opportunity to examine Warm Pool surface heat fluxes over extensive space-time scales. Detailed relationships between surface atmospheric conditions, turbulent fluxes, and SSTs emerged from the TAO data. Zhang and McPhaden (1995) investigated the simple relationships among SSTs, surface winds, and latent heat fluxes in the Pacific to discover a 10-day lag between atmospheric forcing from surface wind fluctuations and the oceanic response. Zhang (1996) combined TOA buoy data with ECMWF reanalysis

and satellite retrievals to describe the large degree of variability of many dynamic and thermodynamic variables over the Warm Pool on intraseasonal time scales.

Atmospheric and oceanic measurements of high temporal resolution and extended duration obtained during the TOGA Coupled Ocean-Atmosphere Response Experiment (TOGA COARE; Webster and Lukas 1992) from November 1992 to March 1993 shed new light on the behavior of air-sea interactions from diurnal to intraseasonal time scales in the tropical West Pacific. Weller and Anderson (1996) detailed the interactions between surface fluxes and different atmospheric regimes, including westerly wind bursts, that accompany the MJO. Lau and Sui (1997) used TOGA COARE data to examine the interactions among convection, surface shortwave and latent heat fluxes, and low-level winds. Those authors show that intraseasonal shortwave radiative fluxes at the surface, modulated by deep convection, interact with evaporative fluxes both constructively and destructively depending on the MJO phase.

Gridded datasets have also been used to investigate the lagged relationships between surface latent heat fluxes and MJO convection. Jones and Weare (1996) used ECMWF surface analyses and ISCCP brightness temperatures to conclude that the coherent eastward propagation of MJO convection is associated with low-level moisture convergence to the east of the convective center. Surface evaporation anomalies are strongest (weakest) to the west (east) of the convective center. The observed paradigm of anomalously weak evaporative fluxes leading deep convection opposed the original wind-evaporation feedback theory of MJO development and propagation (see Section 3.1.b, Emanuel 1987, Neelin et al. 1987). Further investigation revealed that strong

evaporative fluxes lag deep convection (minima in surface insolation) by only a few days in the West Pacific, while the lag can be more than a week over the Maritime Continent and Indian Ocean (Zhang 1996, Hendon and Glick 1997, Shinoda et al. 1998, Woolnough et al. 2000). Fluctuations of surface shortwave radiation were found to be dominant over evaporative fluxes for the surface energy balance in the Indian Ocean, with the two components contributing equally in the West Pacific (Shinoda et al. 1998). The combined effects of insolation and surface latent heat flux drive intraseasonal SST fluctuations of about 0.2-0.3°C (e.g., Lau and Sui 1997, Shinoda et al. 1998).

The Mirai Indian Ocean Cruise for the Study of the Madden-Julian Oscillation Convection Onset (MISMO) was conducted to measure a host of atmospheric and oceanic variables during October and November of 2006 (Yoneyama et al. 2008). Preliminary results from this field campaign highlight the complex interactions between the atmosphere and ocean mixed layers that occur during the developmental stages of intraseasonal convection. Research utilizing the MISMO data is ongoing and will undoubtedly help solidify our understanding of exactly how air-sea interactions combine with other dynamic and thermodynamic processes in the initiation of MJO disturbances in the Indian Ocean (Yoneyama et al. 2008).

Summarizing the cumulative observational evidence (see reviews in Zhang 2005 and Hendon 2005), the current paradigm of intraseasonal air-sea interactions over the equatorial Indian and West Pacific regions suggests that strong insolation and weak evaporative fluxes occur during the convectively suppressed MJO phase due to widespread clear skies and easterly wind stress anomalies that oppose the westerly mean state

flow. The cumulative effect of total surface flux into the ocean and shoaling of the oceanic mixed layer results in peak SST values approximately 10 days prior to maximum convective intensity. As SSTs peak and the atmosphere becomes unstable, developing cumuli begin to decrease insolation. Incident shortwave radiation reaches a minimum, low-level winds become stronger, and SSTs decline rapidly around the time of maximum MJO precipitation. Two to eight days later, boundary layer wind speeds and westerly wind stress anomalies are most intense, followed soon after by the strongest evaporative fluxes. SSTs reach a minimum about 10 days after deep convection due to the combined effects of strong evaporative fluxes, minimal insolation, and a deepening oceanic mixed layer that entrains cooler subsurface waters. The return of positive insolation anomalies and calm winds gradually warms SSTs and shallows the oceanic mixed layer, signaling the beginning of the next intraseasonal convective episode.

3.1.b. Theoretical modeling studies

A number of theoretical modeling studies have been conducted to investigate the role that air-sea interactions play in the representation of the MJO. One early theory asserts that intraseasonal instabilities could be driven by wind-induced surface latent heat fluxes, the so-called WISHE mechanism (Emanuel 1987, Neelin et al. 1987). As a brief review, the growth and maintenance of organized tropical convective systems like the MJO involve the generation of eddy available potential energy (EAPE) and its conversion to eddy kinetic energy (EKE) driven by a positive correlation between heating and temperature (i.e., $\overline{Q'T'} > 0$; Lorenz 1955). The tropical atmosphere in which the MJO oper-

ates resembles a quasi-equilibrium system, where convective available potential energy (CAPE) is rapidly consumed by the convection itself. Early theoretical studies of the MJO likened it to a convectively-coupled Kelvin wave. For such disturbances in a strict quasi-equilibrium system, warm tropospheric anomalies lead deep heating by 1/4 cycle such that instabilities and wave growth by EAPE generation cannot occur. The WISHE theory states that the Gill-type response (Gill 1980) to an equatorial heat source would generate enhanced (weakened) evaporative fluxes to the east (west) of the initial heating given a background low-level easterly flow regime. The enhanced air-sea fluxes ahead of the main heating would increase low-level moist entropy, which would then be redistributed through the troposphere via developing convection. In this way, deep convective heating would be shifted toward warm anomalies, thus generating EAPE and wave instability (Emanuel et al. 1994). There are serious limitations to the WISHE mechanism, however. The original theory requires a low-level easterly background flow to operate, but climatological low-level winds are westerly in the tropical Indian and West Pacific regions throughout most of the year. Measurements of intraseasonal evaporative fluxes have since revealed that the strongest latent heat fluxes are located to the west of the convective center in the westerly wind regime rather than to the east, as mandated by linear WISHE theory. Additionally, the spectral and propagation characteristics of the MJO differ considerably from convectively-coupled Kelvin waves (Wheeler and Kiladis 1999). Modified versions of WISHE have revealed that this mechanism may be important to the MJO in a nonlinear sense, however (e.g., Maloney and Sobel 2004). In particular, the positive covariance between precipitation and latent heat flux appears necessary to desta-

bilize the MJO in some GCMs (Sobel et al. 2008, Maloney et al. 2009), and this destabilization can must occur in a low-level westerly regime, as observed.

Wang and Xie (1998) used a simple model to investigate how oceanic mixed layer processes and ocean-atmosphere coupling can generate unstable growth of planetary-scale atmospheric modes. Their model produced a Kelvin-like dynamical response including many features that resemble the observed MJO structure: warm SSTs, weak evaporative fluxes and strong insolation leading maximum convection, with anomalies of opposite sign lagging the peak rainfall (e.g., Woolnough et al. 2000). The resulting moist Kelvin mode favors the generation of EAPE and its conversion to kinetic energy via two mechanisms. The first involves an overlap of low-level heating (convective precipitation processes, condensation associated with moisture convergence) with positive temperature anomalies, while the second requires a coincidence of positive SST and low-level temperature anomalies. Wang and Xie (1998) demonstrate that the first mechanism alone cannot produce unstable growth of the Kelvin mode, and that the covariance between warm SSTs and lower tropospheric temperatures (lower surface pressures) is necessary for strengthening of the disturbance. The exact mechanism of disturbance strengthening is unclear, and the degree of application to the MJO remains somewhat unanswered considering the differences between moist Kelvin modes and the MJO.

3.1.c. Numerical modeling studies

More recently, many studies have utilized complex GCMs to examine the impact of air-sea coupling on the behavior of the MJO. Up until the mid 1990s, most theories

with proposed mechanisms for the maintenance and eastward propagation of the MJO focused on atmospheric processes and involved fixed SSTs (Emanuel 1987, Lau et al. 1989, Hu and Randall 1994). One of the first studies to use a GCM to explicitly address the role that air-sea interactions have on the MJO was conducted by Flatau et al. (1997). Flatau et al. (1997) examined how convectively generated longitudinal SST gradients impact the phase speed of intraseasonal disturbances. Those authors develop the air-sea convective intraseasonal interaction (ASCII) mechanism which suggests that the combination of weak easterlies and evaporative fluxes and strong insolation ahead of the convective center warm SSTs and thus provide the increased surface moist entropy required to fuel new convection to the east, resulting in more coherent eastward propagation. Their model results indicate that by adding simple air-sea coupling to an aquaplanet GCM, slower and more robust intraseasonal convective disturbances develop. Flatau et al. (1997) assert that the MJO is a coupled atmosphere-ocean phenomenon but fall short of fully explaining how interactions among convection, radiation, evaporation, and SSTs improve the MJO depiction in their model.

The study by Waliser et al. (1999) greatly advanced the scope and understanding of whether the MJO should be considered an instability of the atmosphere alone or a coupled phenomenon. Two simulations were compared, one in which specified annual cycle SSTs forced the model (“control” model), and another that was identical to the first except that the SSTs were allowed to deviate slightly their specified values in the presence of surface flux anomalies (“coupled” model). The coupled simulation employed a slab ocean mixed layer model that computed SST anomalies that were applied to the pre-

scribed SST values equatorward of 24° . Waliser et al. (1999) discovered considerable differences in the depiction of the MJO between the two models, despite very similar mean states. They found that SST changes driven by interactions in the coupled atmosphere-ocean system promoted an enhancement of meridional moisture convergence associated with the frictional wave-CISK (conditional instability of the second kind; e.g., Wang 1988, Lau et al. 1989) to the east of the main convective center. The increased boundary layer moisture ahead of the convective center helps to generate instability, which intensifies the disturbance and/or maintains it against dissipation while promoting eastward propagation (Waliser et al. 1999).

Additional insights into the detailed nature of air-sea interactions and their relationship with intraseasonal convection have been uncovered through extensive research based on a host of GCMs. The inclusion of even simple air-sea coupling tends to improve the depiction of the MJO in climate models, although additional factors such as the model's ability to correctly simulate the mean state are also important (Hendon 2000, Kemball-Cook et al. 2002). Sperber et al. (1997) examined two atmospheric GCMs (AGCMs) forced by prescribed SSTs and concluded that the inability of the models to simulate the transition of MJO convection from the Indian Ocean into the West Pacific was tied to the lack of an interactive ocean and the absence of warm (cool) SSTs leading (lagging) the convective center. Maloney and Sobel (2004) illustrated that by adding an idealized slab ocean to the Community Atmosphere Model version 2.0.1, MJO convection in the West Pacific improved (20% amplitude increase), with the largest convective variance coinciding with an oceanic mixed layer depth close to the observed value in that

region (20 m). Those authors also hypothesized that a type of nonlinear WISHE mechanism—one that involved low-level moisture originating from strong evaporative fluxes within the convective region being advected ahead of the rainfall center—appeared to be active in CAM2.0.1. Sperber (2004) demonstrated that eastward-propagating intraseasonal convective disturbances could be obtained in version 2 of the Community Coupled System Model (CCSM2; Kiehl and Gent 2004), in contrast to the atmospheric component of that model forced by observed SSTs (CAM2) in which intraseasonal convection was unrealistically weak and propagated westward. Sperber (2004) illustrated that the CCSM2, despite its poor mean state depiction, produced an eastward propagating signal due to a more realistic SST gradient and surface heat flux profile in longitude, which propagate eastward with the convection.

Comparison of coupled and uncoupled versions of the Hadley Centre GCM [HadCM3 and HadAM3, respectively (see Collins et al. 2001)] revealed a more coherent signal and more organized eastward propagation of the MJO across the Indian Ocean in HadCM3 (Inness and Slingo 2003). MJO disturbances in HadCM3 weakened considerably over the Maritime Continent, and this dissipation was tied to the absence of low-level climatological westerlies extending into the West Pacific (Inness and Slingo 2003). It was found that the Kelvin wave response reinforced the biased climatological low-level easterlies in the West Pacific, which increased surface heat fluxes, cooled SSTs, and caused convection to weaken (Inness and Slingo 2003). When flux adjustment procedures were applied to the coupled model to obtain a more realistic SST and low-level

wind climatology, MJO disturbances propagated farther east into the West Pacific (Inness et al. 2003), emphasizing the importance of a correct mean state.

The MJO signal can also be improved in atmospheric GCMs that already have a fair representation of its structure and propagation characteristics even without realistic air-sea coupling (e.g., Sperber et al. 2005). Studies utilizing the European Centre Hamburg Model (ECHAM4) AGCM (Roeckner et al. 1996) coupled to a variety of ocean models show a more coherent MJO signal in that model (Kimball-Cook et al. 2002, Sperber et al. 2005). Kimball-Cook et al. (2002) demonstrate that coupling improves the intensity and organization of MJO convection through the development of more realistic structures of low-level wind and moisture convergence, despite a worsened mean state. Based on their results, those authors contend that air-sea coupling is not critical for the existence of the MJO but positively impacts its organization and intensity. Sperber et al. (2005) assessed the MJO signals of several simulations in which the ECHAM4 AGCM is coupled to four different ocean models, two of which are flux adjusted and two of which are not. Their findings suggest that the representation of the mean state is as important as the inclusion of air-sea coupling regarding the model's ability to accurately depict the MJO. Additionally, Sperber et al. (2005) show that while all of the models examined correctly simulate the region of warm (cool) SST that precedes (follows) the convective center, they differ in the partitioning of the total flux components that generate such ocean anomalies, suggesting that the details of radiative transfer and cloud parameterizations may need to be reexamined. A detailed study by Rajendran and Kitoh (2006) shows that air-sea coupling positively impacts the Meteorological Research Institute (MRI) GCM

(Yukimoto et al. 2001), producing a more coherent and long-lasting MJO signal due to an improvement in the phasing of precipitation, surface fluxes, and SSTs. An examination of four pairs of coupled and uncoupled GCMs by Zhang et al. (2006) illustrates the importance of accurately simulating mean state variables such as precipitation and low-level zonal wind and moisture convergence. Those authors caution that, although air-sea coupling generally improved MJO representation in their analyses, inconsistencies between simulations indicate that coupling may not improve intraseasonal variability in every model. Marshall et al. (2008) apply an adapted version of the slab ocean model configuration of Waliser et al. (1999) to the Australian Bureau of Meteorology Centre's atmospheric GCM version 3.0 (BAM3; Colman et al. 2005) and find a more realistic MJO period and spatial structure. Marshall et al. (2008) contend that these improvements arise due to an enhanced moisture convergence-evaporation feedback in which warm SSTs ahead of the convective center offset weakened evaporative fluxes, increase boundary layer moisture due to air-sea humidity differences, and promote shallow convection which drives moisture convergence and further increases boundary layer moisture.

Evidence from many numerical modeling studies strongly suggests that, while not critical for the existence of intraseasonal convective disturbances, air-sea coupling tends to beneficially impact MJO spatial patterns; propagation and spectral characteristics; and the phasing of convection, dynamics, and surface fluxes. Such improvements have clearly been shown to result from a more realistic interaction between the atmosphere and ocean on both seasonal and intraseasonal space-time scales.

3.2. Data Sources

We analyze two five-year time segments from two SP-CAM simulations to investigate the effects of simplified ocean-atmosphere coupling. The first five-year time segment is taken from the end of the AMIP-style simulation that is forced by prescribed (observed) SSTs, as discussed in Chapter 2. Thus, there is no influence of the atmosphere on the ocean due to surface fluxes. This first simulation dataset spans 1 September 1999 to 31 August 2004 and will be referred to as the “control” run (CTL). The second simulation is identical to the first but with a new treatment of tropical SSTs. A highly simplified mixed-layer ocean model is used to calculate prognostic SST anomalies that are coupled to the atmosphere. This second simulation is referred to as the “slab ocean model” run (SOM). SSTs in the SOM simulation are allowed to deviate slightly from their prescribed (observed) values if anomalous surface fluxes exist. Unlike the CTL simulation, the ocean in the SOM can now respond to anomalous surface fluxes in a more natural manner. For example, strong westerly winds following the passage of an MJO disturbance result in a cooling of SSTs; in the CTL simulation, these anomalous surface fluxes had no effect on the SST.

The idealized ocean mixed-layer model implemented in SOM is an adaptation of Equation 1 in Waliser et al. (1999):

$$\frac{dT'}{dt} = \frac{F'}{\rho CH} - \gamma T'. \quad (3.1)$$

Here, T' is the SST departure from the monthly mean (linearly interpolated to daily mean) observed SST, F' the departure of the total net surface flux from its climatological value, ρ the water density, C the specific heat of water, H the climatological oceanic mixed-layer depth, and γ the damping coefficient. Climatological values of H and net surface flux represent smoothed seasonal cycles at daily temporal resolution. Net surface flux climatological values used in Eq. 3.1 are computed directly from the CTL simulation and smoothed by retaining only the mean and first three harmonics of the seasonal cycle. Although Waliser et al. (1999) set the value of H to 50 m for all ocean grid points, in Eq. 3.1 the mixed-layer depth is space and time dependent as described by Monterey and Levitus (1997). We use only the mean and first three harmonics of the mixed-layer depth seasonal cycle. Additionally, a temporal 1-2-1 filter is applied to the smoothed seasonal cycle of H to prevent negative values where rapid shoaling occurs. The γ parameter represents the timescale for SST perturbations to return to zero or, alternatively, the timescale for SSTs to return to their prescribed (observed) value. As in Waliser et al. (1999), we set $\gamma=(50 \text{ d})^{-1}$ in the SOM simulation to match the approximate decorrelation timescale of tropical intraseasonal phenomena (Hendon and Salby 1994). The γ parameter also maintains similar model climatologies and accounts for planetary-scale oceanic mixing and advection.

The MJO has a strong sensitivity to the mean state, such that small changes in background conditions within which the MJO is active can have an impact on the intensity and structure of the disturbance itself (Hendon and Salby 1994, Inness and Slingo 2003). It is important therefore to limit differences in the climatological states between

the CTL and SOM simulations so that changes in the MJO structure between the two runs can be more directly attributed to air-sea interactions on MJO space and time scales. The SST fluctuations caused by strong surface fluxes at middle and high latitudes can be large and may potentially alter the climatological dynamical fields. Because we are interested in the effects of air-sea interactions on the MJO and wish not to significantly alter the mean state of the model, we only apply the slab ocean model equatorward of 26° . A Hann weighting function is applied from 12° (1.0 weight) to 26° (0.0 weight), and the slab ocean model is fully active within 12° of the Equator. Poleward of 26° , there is no impact of anomalous surface fluxes on SSTs.

We compare the simulation results to several observation-based datasets. To facilitate comparison, all simulated and observed data sources are daily averaged and linearly interpolated to a spatial grid of 2.5° resolution in the horizontal and 27 levels in the vertical (25 hPa resolution between 1000-750 hPa, 50 hPa resolution between 750-250 hPa, and 25 hPa resolution between 250-100 hPa). This differs from the previous analyses described in Chapter 2 in which pentad-averaged datasets are used. Except for precipitation, OLR, precipitable water, and SSTs, all dynamic, thermodynamic, and radiation fields are obtained from the European Centre for Medium-Range Weather Forecasts (ECMWF) Reanalysis-Interim dataset (ERA-Interim, hereafter abbreviated “ERA-Interim”; Berisford et al. 2009). Like its predecessor ERA-40 (see description in Chapter 2), ERA-Interim is a byproduct of surface and satellite measurements blended with short-term model forecasts. ERA-Interim benefits from full data coverage in space and time, but is subject to the same deficiencies as ERA-40—namely, a strong dependence on model physics and parameteri-

zations where measurements are sparse. We use ERAI in this analysis because it covers the selected time range (1999-2004) and exhibits several notable improvements over the ERA-40 dataset (Berrisford et al. 2009). ERAI draws upon an advanced implementation of 4-dimensional variational analysis, increased spatial resolution, and improved model physics of the forecast model component; improved handling of observational biases and inputs; and new sources of satellite observations. As a result, the hydrologic cycle and stratospheric circulations are better represented in ERAI relative to ERA-40 (Simmons et al. 2006). Overall, the ECMWF reanalysis datasets are well-suited in the study of meso-scale to planetary scale weather features (Lin and Johnson 1996a; Straub and Kiladis 2003; Sperber 2003; Kiladis et al. 2005; Benedict and Randall 2007; Benedict and Randall 2009).

Observed rainfall data is taken from the Global Precipitation Climatology Project (GPCP; Adler et al. 2003) and OLR data are derived from the National Oceanic and Atmospheric Administration's (NOAA) suite of polar orbiting satellites (Liebmann and Smith 1996). We use total column water vapor from the Tropical Rainfall Measurement Mission (TRMM) Microwave Imager (TMI; Kummerow et al. 1998). We use version 2 of NOAA's Optimal Interpolation SST (OISST2; Reynolds et al. 2002) dataset for ocean surface temperatures. We note that the OISST2 product may not fully capture the amplitude of high-frequency SST fluctuations due to its weekly time resolution.

3.3. Methodology

We employ a number of statistical analysis methods to highlight variability on intraseasonal space and time scales, clarify relationships between convection and dynamics, and display physical structures of the MJO. Unlike the results shown in Sections 2.4, which are based on composites of many MJO events, the limited time span of the SOM simulation (1825 days) requires an alternative analysis approach to ensure that results are statistically robust and meaningful. In this section, we use a multi-step analysis approach based on statistical methods of increasing complexity. Outlined below are the primary methods used to examine the impacts of air-sea coupling on the SP-CAM.

3.3.a. Climatological total and filtered variance

Two elemental measurements of climate model performance include the model's ability to capture the correct mean state and level of variance. Total variance indicates the magnitude of fluctuations of a particular variable on all space and time scales. We utilize the standard diagnostics package from the U.S. Climate Variability and Predictability Program (CLIVAR) MJO Working Group (Kim et al. 2009) to compute the variance of data that has been filtered to include only those features on 20-100 day time scales, such as the MJO. The diagnostics package uses a Lanczos filter to isolate the 20-100-day signals.

3.3.b. Decile averaging

We assess the most basic relationships between convection (as measured by precipitation) and other fields by constructing decile histograms. These plots are generated by first ranking precipitation values for all space and time points within a specified domain. We choose a domain that includes ocean-only points within the region in which the MJO is most active— 60°E - 180° , 10°S - 10°N —as well as the full time range (1825 days). The ranked precipitation values are then divided into 10 bins (deciles). Other selected variables can then be averaged based on these precipitation deciles. For example, one can calculate the averaged SST value corresponding to the driest 10% of rainfall occurrences, the wettest 10% of rainfall occurrences, and so on. The decile histograms in our analysis only indicate simple associations between convection and other variables and contain no information regarding time or space dependencies.

3.3.c. Zonal wavenumber-frequency analysis

It is often useful to partition the total variability of a selected field into its zonal wavenumber and frequency components. We utilize this statistical approach, advanced by Wheeler and Kiladis (1999), to compare several features of the CTL and SOM simulations and observations. Zonal wavenumber-frequency analysis effectively highlights the spectral power for different wave types—that is, the magnitude of variability contained within specific zonal wavenumbers and frequencies relative to a background variability—as well as the ratio of westward- to eastward-propagating wave features. We use such methods to determine differences between the MJO spectral signal between the CTL and

SOM simulations. A detailed discussion of spectral analysis can be found in Wheeler and Kiladis (1999).

3.3.d. Longitude-time analysis

Though simple to construct, longitude-time plots (“Hovmöller” diagrams) reveal abundant information regarding tropical wave propagation behavior in space and time. Several types of equatorial atmospheric waves whose space-time scales are greater than the mesoscale (equatorial Rossby waves, Kelvin waves, the MJO, etc.) propagate primarily in the zonal direction. Therefore, there is little information lost during the meridional averaging used to construct Hovmöller diagrams. We compare the CTL, SOM, and observations in terms of their propagation characteristics of many wave types.

3.3.e. Lag correlation

We use lag correlation methods to deduce the strength and direction of linear relationships between two variables in time and/or space. The lag correlation technique indicates the extent to which two variables are linearly related but provides no information regarding (a) how amplitude changes in the two variables are linearly related and (b) the relationship between variables in a nonlinear context. Lag correlation is helpful in understanding basic physical tendencies between two variables. For example, this technique can be used to show that MJO-filtered SST anomalies in nature tend to be positive several days prior to positive MJO-filtered anomalies in precipitation, thus yielding a posi-

tive correlation at a time lag. Statistical significance of the correlation between the two variables is computed using the t test,

$$t = \frac{r\sqrt{N^* - 2}}{1 - r^2}, \quad (3.2)$$

where the effective sample size is taken from Eq. 31 of Bretherton et al. (1999),

$$N^* = N \frac{1 - r_1 r_2}{1 + r_1 r_2}. \quad (3.3)$$

In Eq. 3.2, r is the correlation coefficient between the two variables. In Eq. 3.3, N^* is the effective sample size, N is the total number of time steps in the dataset and r_1 and r_2 are the lag-one autocorrelations of the first and second variables, respectively.

3.3.f. Linear regression

While correlation indicates the robustness of a linear relationship, regression techniques denote the relationship between fluctuations in one variable and changes in another. In our analyses of the CTL and SOM simulations, we utilize linear regression techniques to compare the time-lagged association of one variable to another. We use the term “association” rather than “response” because causality cannot be directly determined from regression statistics. Many of the plots shown in Section 3.4.h display the linear, time-lagged association of a dependent variable to an index designed to capture convective fluctuations of the MJO. We choose this index to be 20-100-day filtered precipitation that has been standardized. Statistical significance of the time-lagged regression

values is computed using the corresponding correlation coefficients and t test statistics from Eq. 3.2.

3.3.g. Compositing

We also construct cross sections of the space-time MJO structure using composite analysis techniques. Spectrally filtered and meridionally averaged precipitation defines an index upon which other variables are composited. This index will be defined in Section 3.4.i. We use the index to locate individual MJO events and subsequently composite multiple events into a single, representative MJO disturbance. The resulting composite cross sections highlight important structures of the MJO in time-height space and complement lag regression analyses.

3.4. Results

3.4.a. Energy budget

Changes made to the configuration of a GCM have the potential to strongly impact fluxes of heat and energy on global scales (Kiehl et al. 1998). We examine the energy budgets at the Earth's surface (SFC) and top of the atmosphere (TOA) for three versions of the CAM: (a) CAM3.0, the SP-CAM's host GCM that employs conventional parameterizations; (b) the uncoupled SP-CAM (CTL) forced by prescribed SSTs; and (c) the coupled SP-CAM (SOM), identical to (b) except for a different treatment of tropical SSTs in which ocean surface temperatures are allowed to deviate slightly from their pre-

scribed values through the use of a simple slab ocean model. In nature, we would expect the globally averaged energy budget at the TOA and SFC to be very close to zero over a multi-year time span and in the absence of significant climate events such as volcanic eruptions. It is important to confirm that net TOA and SFC energy budgets in the three GCMs are reasonably close to zero. By ensuring this, we have confidence that the overall distribution and flow of energy on planetary scales are realistic.

Table 3.1. Global mean energy budgets at the top of the atmosphere (TOA) and Earth surface (SFC) for the standard Community Atmosphere Model version 3.0 (CAM), the control SP-CAM simulation (CTL), the slab-ocean SP-CAM simulation (SOM), and the best current observational estimates from Trenberth et al. (2009). Net flux components are also shown, including shortwave (SW) and longwave (LW) radiation, surface latent heat flux (LH), and surface sensible heat flux (SH). Flux sign conventions are those of the CAM. Global mean precipitation appears on the bottom row, with observed values representing the 1999-2004 GPCP mean. Units are W m^{-2} for fluxes and mm d^{-1} for precipitation.

	CAM	CTL	SOM	OBS
Time Range	1986-1999	1999-2004	1999-2004	2000-2004
SFC				
Net SW	+158.7	+158.5	+154.6	+161.2
Net LH	-82.0	-81.5	-80.2	-80.0
Net LW	-56.3	-56.0	-53.9	-63.0
Net SH	-19.7	-22.9	-23.0	-17.0
NET SFC	+0.7	-1.9	-2.5	-0.9
TOA				
Net SW	+236.8	+237.4	+233.8	+239.4
Net LW	-233.6	-237.4	-234.3	238.5
NET TOA	+3.2	0.0	-0.5	+0.9
TOA-SFC	+2.5	+1.9	+2.0	0.0
Total Precipitation	2.830	2.814	2.768	2.612

Table 3.1 displays global mean energy budgets and precipitation rates for the three GCMs and observations. Estimates of the observed global mean energy budgets are taken from Trenberth et al. (2009). Flux sign conventions follow those used in the CAM. The five-year average of net TOA and SFC energy budgets for both versions of the SP-CAM are less than 3 W m^{-2} from zero, in accordance with the same measures from a 14-yr average of the CAM. The larger negative SFC net flux value noted in the SOM appears to stem from less positive net shortwave (SW) fluxes and may be linked to increased mean cloudiness in the Tropics and Subtropics (not shown). All three versions of the CAM have weak net atmospheric heating of $\sim 2 \text{ W m}^{-2}$, which presumably could rectify discretization errors in the model. Globally averaged precipitation rates are also similar, with the SOM being closest to observations. Table 3.1 demonstrates that the global energy budgets at the TOA and SFC for all three versions of the CAM are similar to each other and close to the observed value of zero.

3.4.b. Climatology: Mean state

Five-year (1999-2004) climatological 850 hPa zonal winds based on means for (a) all months and (b) December-February (DJF) only are shown in Fig. 3.4.1. The similarities of the annual mean 850 hPa zonal wind pattern between the CTL and SOM simulations shown in Fig. 3.4.1a are very strong, with differences usually less than 1 m s^{-1} . We utilize two measurements to assess quantitative differences between climatological CTL and SOM fields: normalized root-mean-square error (NRMSE) and pattern correlation. Root-mean-square errors are normalized by a domain-averaged standard deviation from

the CTL simulation (average of square root of temporal variance at each spatial point in selected domain) and capture cumulative biases between the CTL and SOM means. Pat-

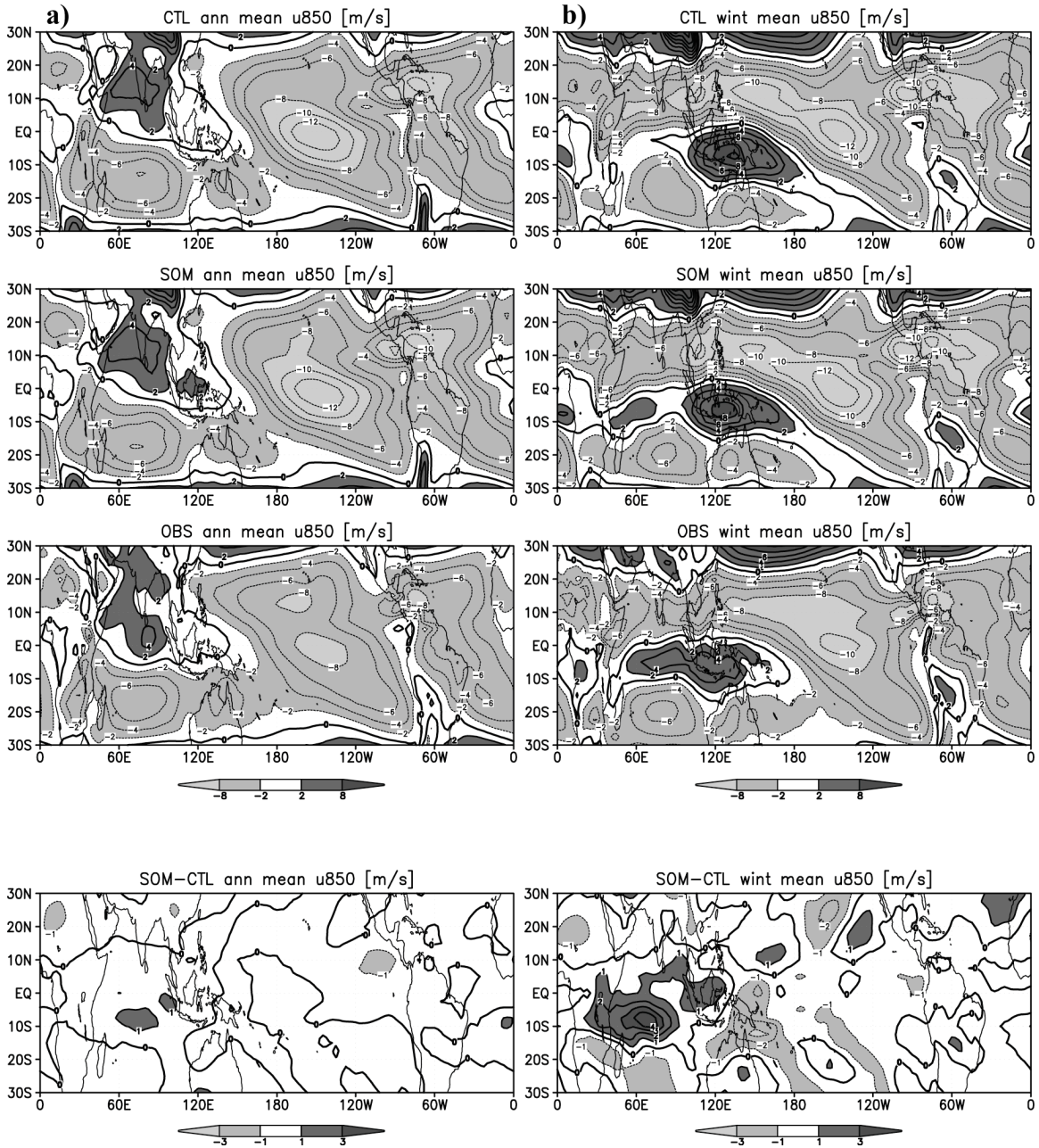


Fig. 3.4.1. Mean zonal wind at 850 hPa for all months (a, left column) and winter months (Dec-Feb; b, right column). Plots based on data from the control simulation (CTL), the slab-ocean simulation (SOM), observations (OBS), and the SOM-CTL difference are displayed from top to bottom.

tern correlation measures the similarity of spatial distributions within a chosen domain. We select the domain (20°S-20°N, 60°E-100°W) to encompass regions that are directly impacted by MJO convection and dynamics. The pattern correlation between the CTL and SOM 850 hPa zonal wind annual means is 0.99. The NRMSE between the two mean states is 0.08, signifying that local differences in low-level winds between the CTL and SOM fields are typically less than 10% of a representative CTL standard deviation. The overestimated strength of easterly trade winds in the central Pacific and Caribbean Sea seen in both versions of the SP-CAM is likely dynamically linked to excessive precipitation to the west of these two regions (c.f. Fig. 3.4.2). The MJO is particularly active during the Northern Hemisphere winter months (Salby and Hendon 1994). Mean state differences between the two models are notably larger during this season, although the smaller sample size is likely a contributing factor. Key differences between the CTL and SOM winter mean 850 hPa winds (Fig. 3.4.1b) include stronger westerlies along 5°-10°S in the Indian Ocean, enhanced easterlies in the Southern Hemisphere subtropics of the Indian Ocean, and reduced westerlies near the Coral Sea in the SOM. These changes represent a slight improvement of the SOM climatology over the CTL. MJO intensity and structure have a dependence on the climatological magnitude and direction of low-level winds within regions in which the MJO operates (Salby and Hendon 1994, Inness et al. 2003, Sperber et al. 2005). The increased 850 hPa westerlies in the equatorial Indian Ocean in the SOM, in particular the change of direction from easterlies to westerlies in the western Indian Ocean, may have a subtle yet positive impact on the representation of the MJO in the SOM compared to CTL. Lower tropospheric westerlies have been shown

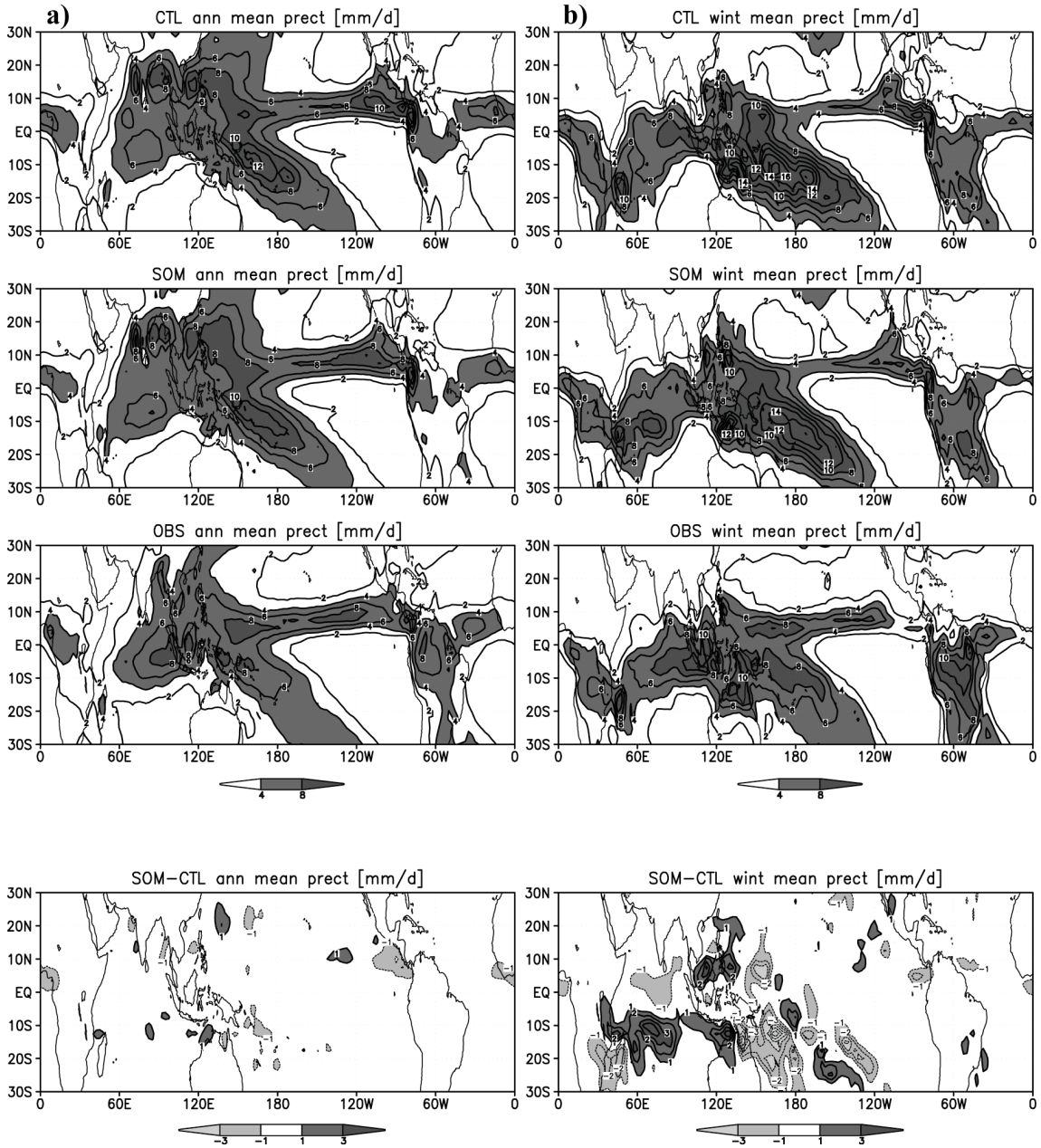


Fig. 3.4.2. As in Fig. 3.4.1, but for precipitation.

in some models to play a critical role in the eastward propagation of the MJO (e.g., Maloney et al. 2009).

Annual mean precipitation patterns of the CTL and SOM simulations are very similar (Fig. 3.4.2a). Model differences are sporadic with magnitudes generally less than

$\sim 1 \text{ mm d}^{-1}$. The pattern correlation and NRMSE between CTL and SOM for annual mean precipitation are 0.98 and 0.06, respectively. The SOM shows slightly reduced rainfall over the West Pacific Warm Pool and the East Pacific intertropical convergence zone (ITCZ), both of which represent model improvement. However, the SOM erroneously overestimates annual mean precipitation immediately northwest of Australia and northeast of the Philippines. In both versions of the SP-CAM, excessive precipitation is noted over India, the West Pacific Warm Pool, and the East Pacific ITCZ relative to GPCP measurements (Fig. 3.4.2a). The largest differences in mean winter precipitation between the CTL and SOM (Fig. 3.4.2b) are generally confined to where the slab ocean model is active and SSTs are relatively warm. The SOM has reduced rainfall in the West Pacific Warm Pool, which is an improvement over the CTL simulation. The SOM also indicates increased precipitation along 10°S in the Indian Ocean compared to CTL. Both the CTL and SOM have too little precipitation over the eastern Indian Ocean and too much over the West Pacific Warm Pool and SPCZ. Kim et al. (2009) suggest that high mean precipitation over the West Pacific generally results in an eastward extension of winter-time climatological 850 hPa westerlies, and this appears to be true for both uncoupled and coupled versions of the SP-CAM (Figs. 3.4.1b and 3.4.2b).

Annual and winter mean SSTs are displayed in Figs. 3.4.3a and 3.4.3b, respectively. By construction, CTL SSTs are nearly identical to observations because the CTL SST forcing file is derived from the OISST2 dataset. Overall, SST patterns between the CTL and SOM simulations match up reasonably well, especially in open-ocean areas. The pattern correlation of annual mean SSTs between the CTL and SOM is 0.99, and the

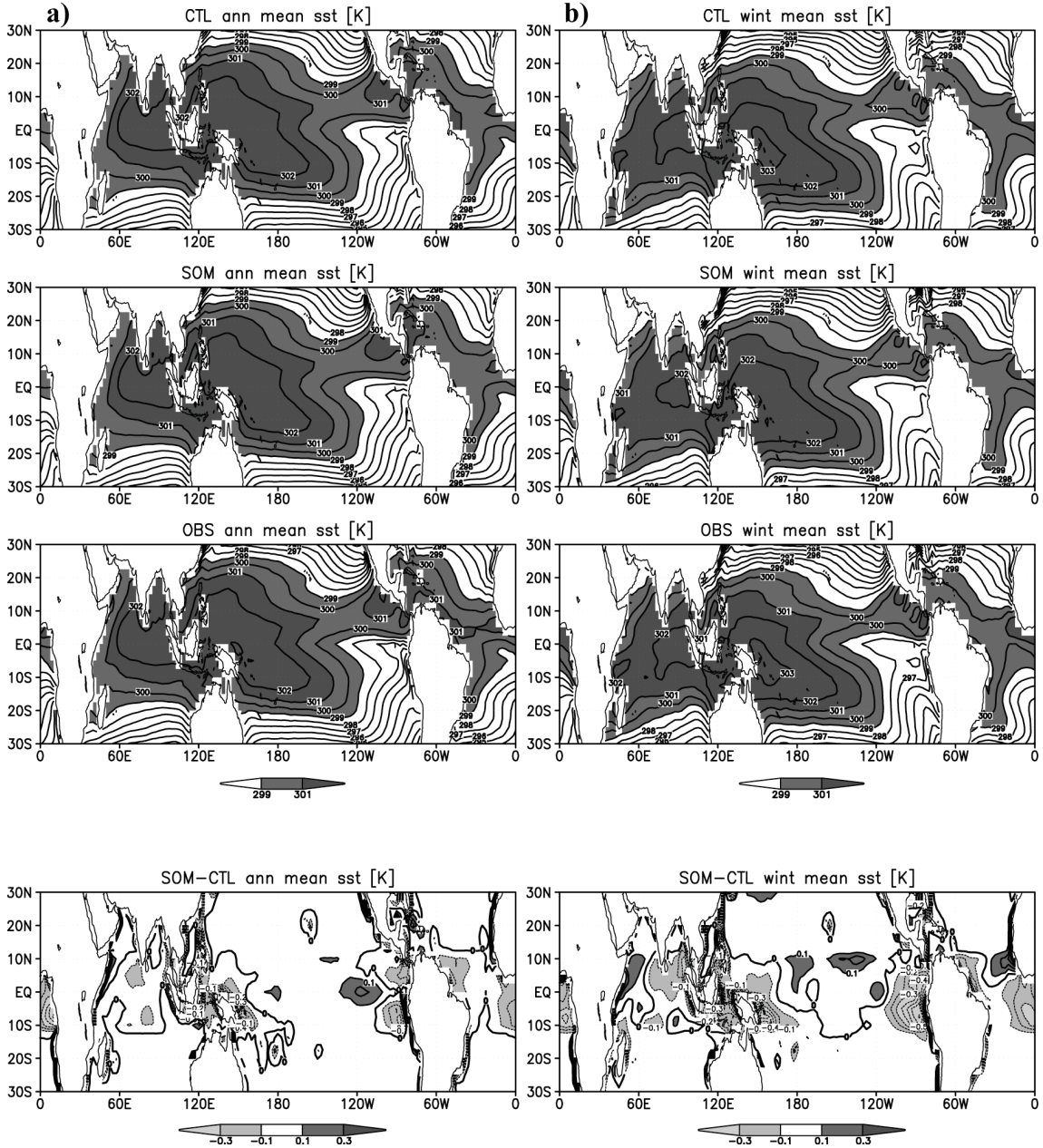


Fig. 3.4.3. As in Fig. 3.4.1, but for SST.

NRMSE is 0.18. That the two models have comparable climatological SST patterns is an important result given that SSTs act as the model forcing and the SOM allows SSTs to deviate from their prescribed values. Local SST differences do exist, however. The SOM annual mean values are cooler by 0.1-0.2 K near the Maritime Continent. Given

that mean SLHFs and surface westerlies are weaker over the eastern Maritime Continent (Fig. 3.4.5a), the cooler SSTs there are likely associated with a widespread 5% increase in high cloudiness and the related reduction of surface insolation over the Indian Ocean and

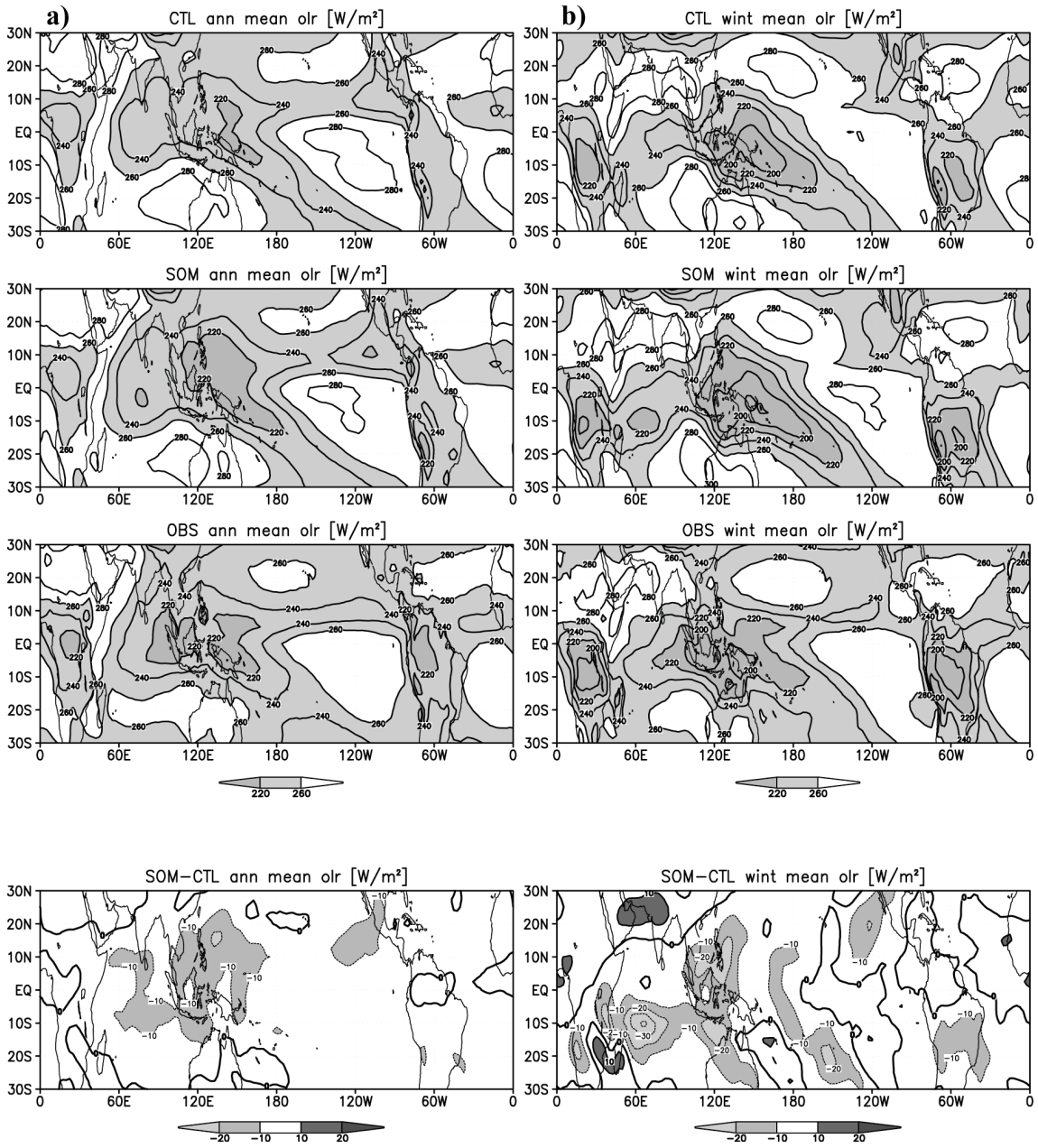


Fig. 3.4.4. As in Fig. 3.4.1, but for OLR.

Maritime Continent (not shown). SOM SSTs are also slightly cooler in the equatorial Indian Ocean, but typically by less than 0.1 K. A similar pattern is noted for winter mean SSTs (Fig. 3.4.3b).

Despite a strong pattern correlation (0.99), the SOM has slightly reduced annual mean OLR values in the Indian and West Pacific regions compared to CTL (Fig. 3.4.4a). This widespread bias results in a higher NRMSE of 0.21. The decreased OLR and slightly increased high cloud amount (not shown) in the SOM appear to be related to increases in climatological precipitation (c.f. Fig. 3.4.2a), although the correspondence is not perfect (e.g., note the reduced SOM rainfall and increased OLR east of Australia, relative to CTL). Winter mean OLR patterns (Fig. 3.4.4b) appear to have a better correspondence with rainfall biases between the CTL and SOM simulations.

We present climatological surface fluxes in Fig. 3.4.5. Annual mean flux values are lower (less evaporation) in SOM compared to CTL over most of the equatorial Indian and Pacific Oceans, but the pattern correlation is 0.99 and the NRMSE is 0.12. The flux reductions are likely a combined result of lower SSTs and weaker low-level easterlies in the SOM (Figs. 3.4.3a and 3.4.1a, respectively). Comparison of winter mean fluxes (Fig. 3.4.5b), SSTs (Fig. 3.4.3b), and 850 hPa zonal winds (Fig. 3.4.1b) clarifies this hypothesis. The decreased West Pacific surface fluxes in the SOM represent an improvement in the model. However, implementation of the slab ocean model makes the surface flux climatology slightly worse in the Indian Ocean due to cooler SSTs there.

Climatological vertical wind shear, defined as the difference between the zonal winds at 850 hPa and 200 hPa, is shown in Fig. 3.4.6. Similar patterns are noted between

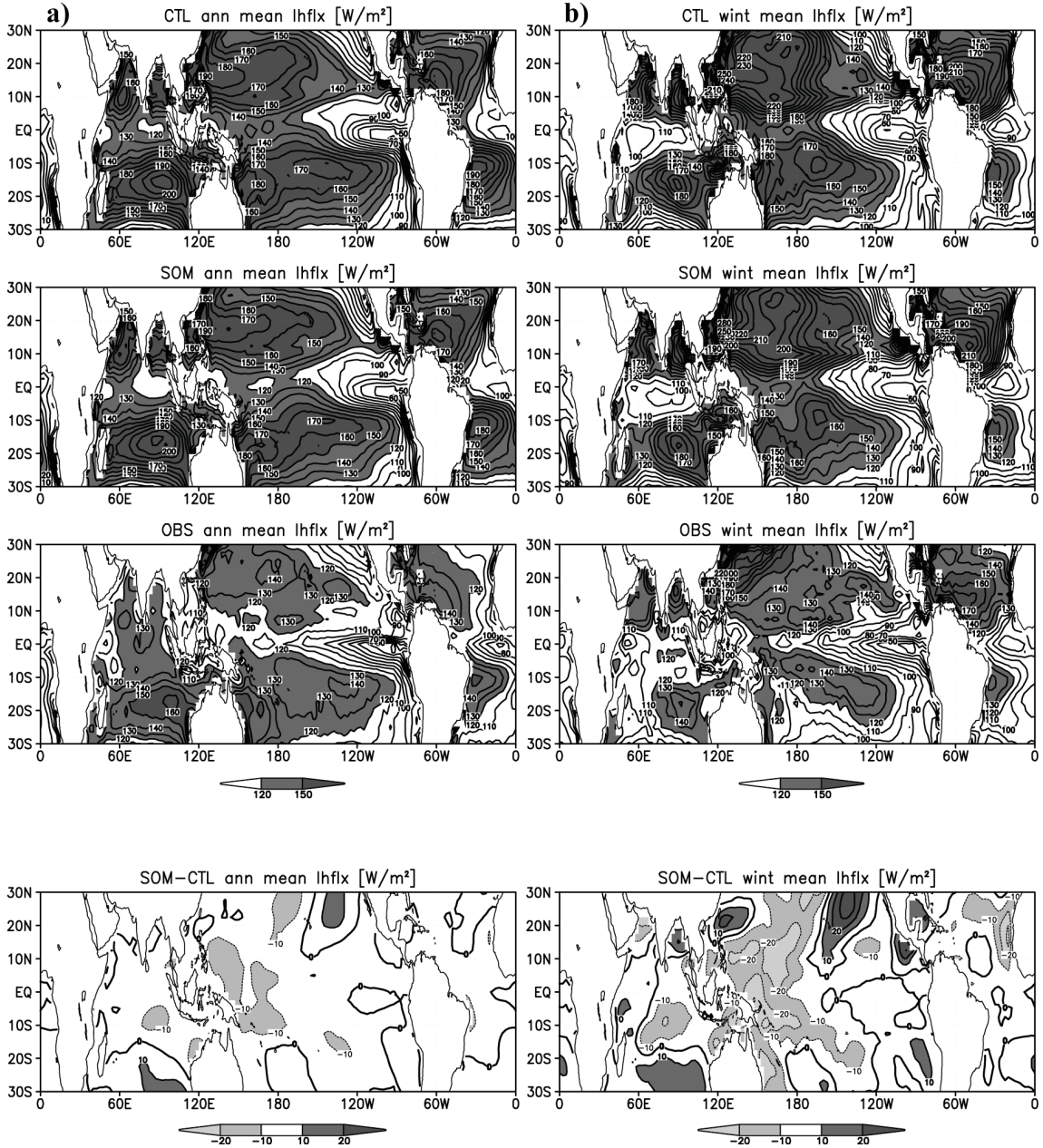


Fig. 3.4.5. As in Fig. 3.4.1, but for surface latent heat flux. Data are not plotted over land masses.

the CTL and SOM in the annual mean (Fig. 3.4.6a), but SOM indicates an increased shear magnitude over the Indian Ocean and Maritime Continent by $\sim 3 \text{ m s}^{-1}$. Climatological shear in the CTL is markedly weaker than in nature over the Indian Ocean but matches observations in the West Pacific. The increased shear over the Indian Ocean in

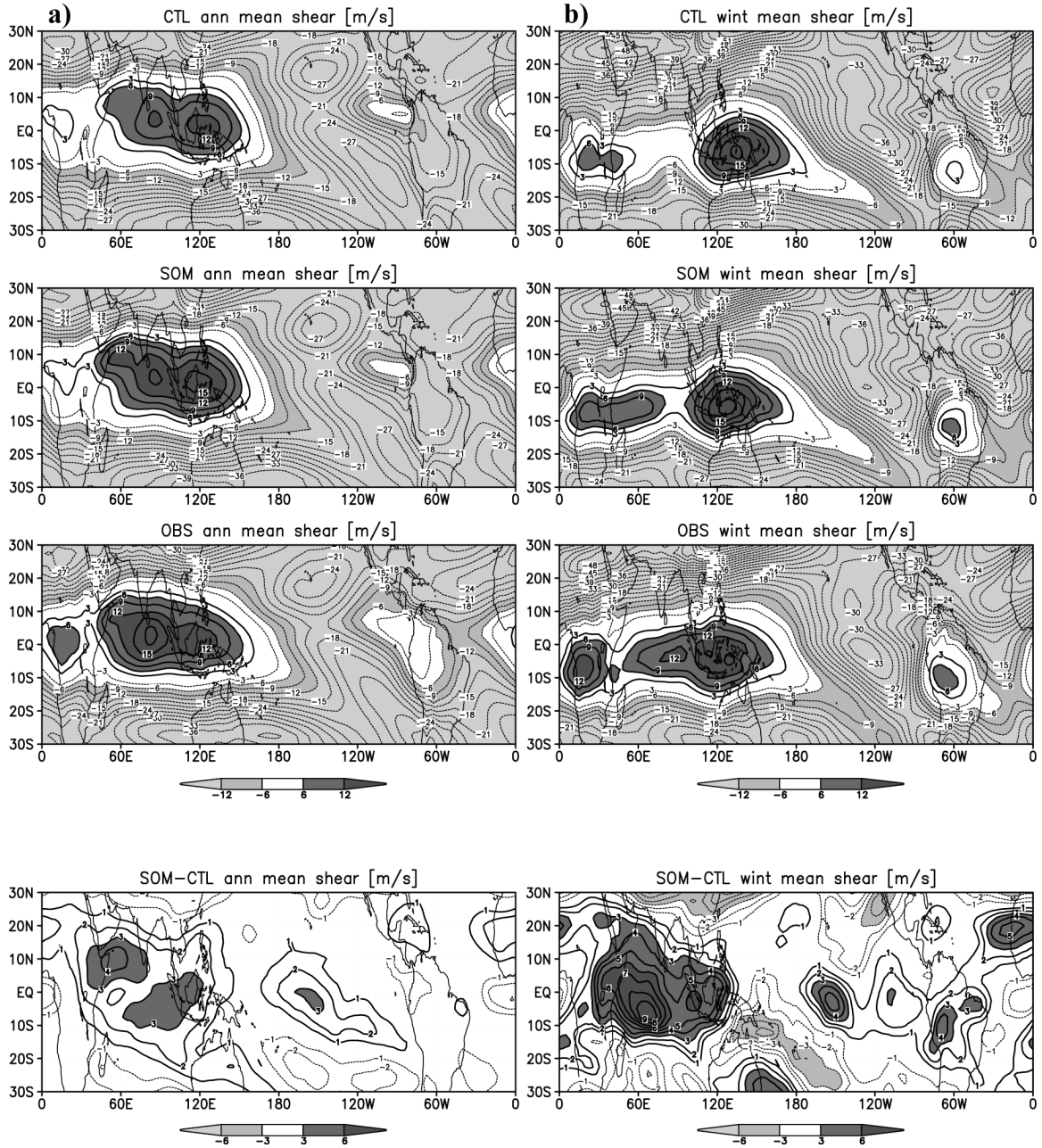


Fig. 3.4.6. As in Fig. 3.4.1, but for vertical wind shear, defined as the difference between zonal wind at 850 hPa and 200 hPa (U850-U200).

the SOM therefore pushes the model closer to observations and establishes a vertical wind profile that is more similar to nature. Improved patterns of vertical shear in the SOM are also evident in the winter mean plots (Fig. 3.4.6b) and, over the Indian Ocean, result from increased magnitudes of low-level westerlies (Fig. 3.4.1b) and upper-level

easterlies (not shown). It is unclear if and to what extent the north-south CRM orientation affects the climatological shear.

Several studies have highlighted the interactions between the MJO and the climatological state in which it operates (Salby and Hendon 1994, Slingo et al. 1996, Inness et al. 2003, Zhang et al. 2006). We have shown that the differences between the annual mean states of the CTL and SOM simulations are small. Pattern correlations between annual mean climatologies of all variables examined are at or above 0.98 and statistically significant above the 99% level. Normalized root-mean-square errors, which measure the cumulative difference in local magnitudes between two fields within a selected spatial domain, are less than ~20% of the domain-averaged standard deviation of the CTL simulation. We can therefore infer that changes in MJO structure and intensity between the two models are not a result of changes in the simulated mean states and any associated MJO-mean state interactions.

3.4.c. Climatology: Variance

Maps of total and filtered boreal winter (DJF) variance for 850 hPa zonal wind (U850) are displayed in Fig. 3.4.7. Total (20-100-day filtered) winter variance is shown in the top (middle) row, and the percent of total winter variance captured by the 20-100-day filtered winter variance (hereafter called “percent of total”) appears in the bottom row of each column. Results from the CTL, SOM, and observations are shown in columns (a), (b), and (c), respectively. We choose to focus on the boreal winter season because the MJO is most intense during this time (Salby and Hendon 1994). We mask out

variance values poleward of 20° due to the strong influence of midlatitude weather systems there. Fig. 3.4.7 indicates that the SOM generally has reduced total U850 variance

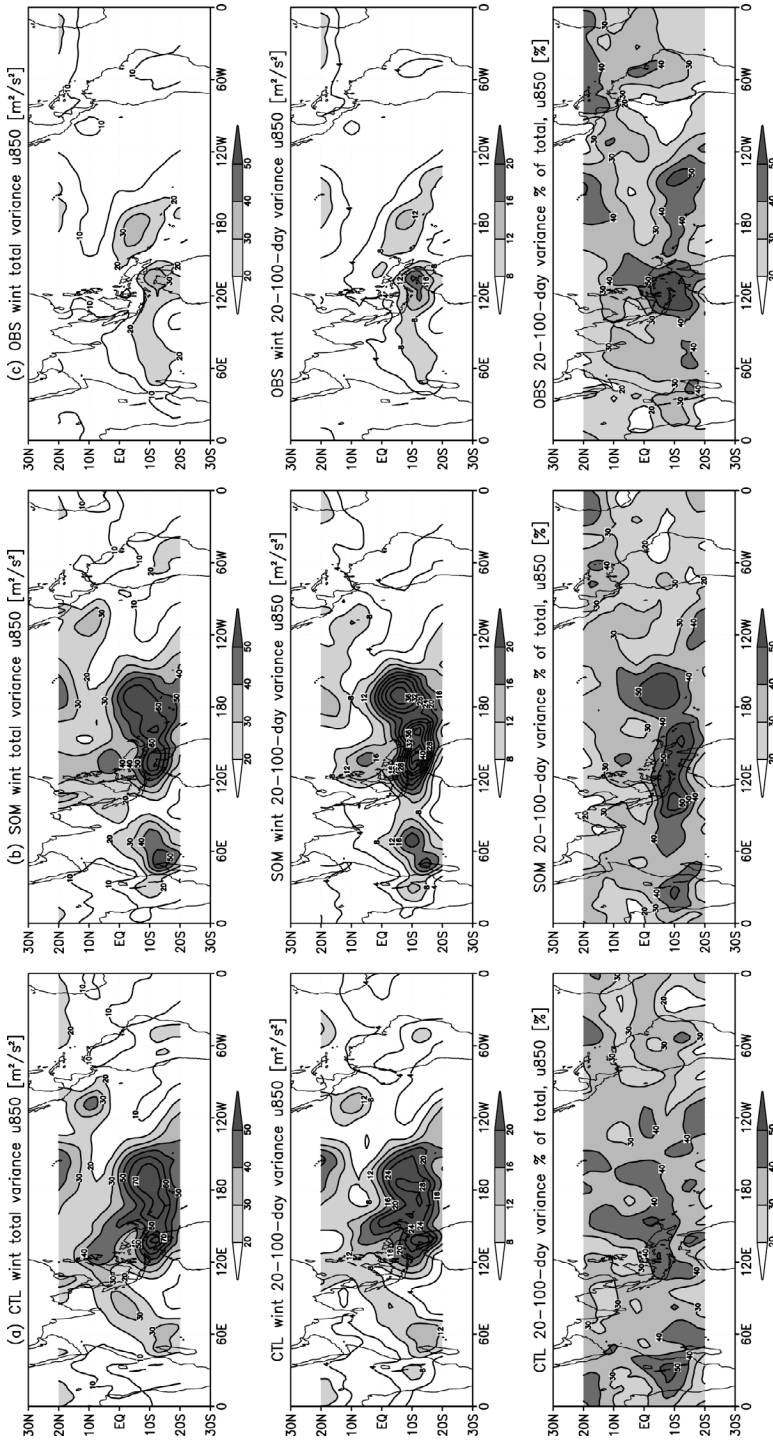


Fig. 3.4.7. 850 hPa zonal wind total winter variance (top), 20-100-day filtered winter variance (middle), and the 20-100-day winter variance as a percent of total winter variance (bottom) for the control simulation (CTL; a), slab-ocean simulation (SOM; b), and observations (OBS; c). Winter is defined as December-February. Variance values poleward of 20° are omitted.

over the West Pacific and southern Maritime Continent compared to CTL, but larger total variance in the western Indian Ocean. MJO-filtered (hereafter referring to the 20-100-day filter) U850 variance in both the Pacific and Indian regions is substantially higher in the SOM, representing an increase in the variance bias that already exists in the SPCAM. We note that, in the Indian Ocean, the zonally confined (5° - 15° S) pattern of MJO-filtered U850 variance in observations is reasonably well replicated in the SOM, but the CTL has more of a southwest-northeast pattern of MJO-filtered U850 variance. Fig. 3.4.7a indicates that intraseasonal U850 variance accounts for approximately 45% of the total U850 variance over the southern Maritime Continent in the CTL, while the SOM suggests a value of about 55%. In nature, intraseasonal wintertime U850 variance accounts for about 50% of the total variance in this region. Overall, the SP-CAM dramatically overestimates boreal winter total and MJO-filtered U850 variance across much of the Indian and West Pacific Oceans.

SOM total and filtered winter precipitation in the SPCZ is reduced relative to the CTL (Fig. 3.4.8). It is unclear exactly why MJO-filtered precipitation is smaller but filtered U850 is larger in the West Pacific for the SOM simulation. The spurious maximum of total and filtered rainfall variance seen in the CTL near 5° N, 160° E is also markedly diminished in the SOM. The SOM has slightly higher total and filtered winter precipitation variance in the Indian Ocean corresponding to similar increases of MJO-filtered variances of U850 (Fig. 3.4.7), OLR (Fig. 3.4.9), and SST (Fig. 3.4.10). Intraseasonal variance accounts for about 25% (20-25%, \sim 20%) of the total winter precipitation variance in basins where the MJO is active for the CTL (SOM, observations). Our results

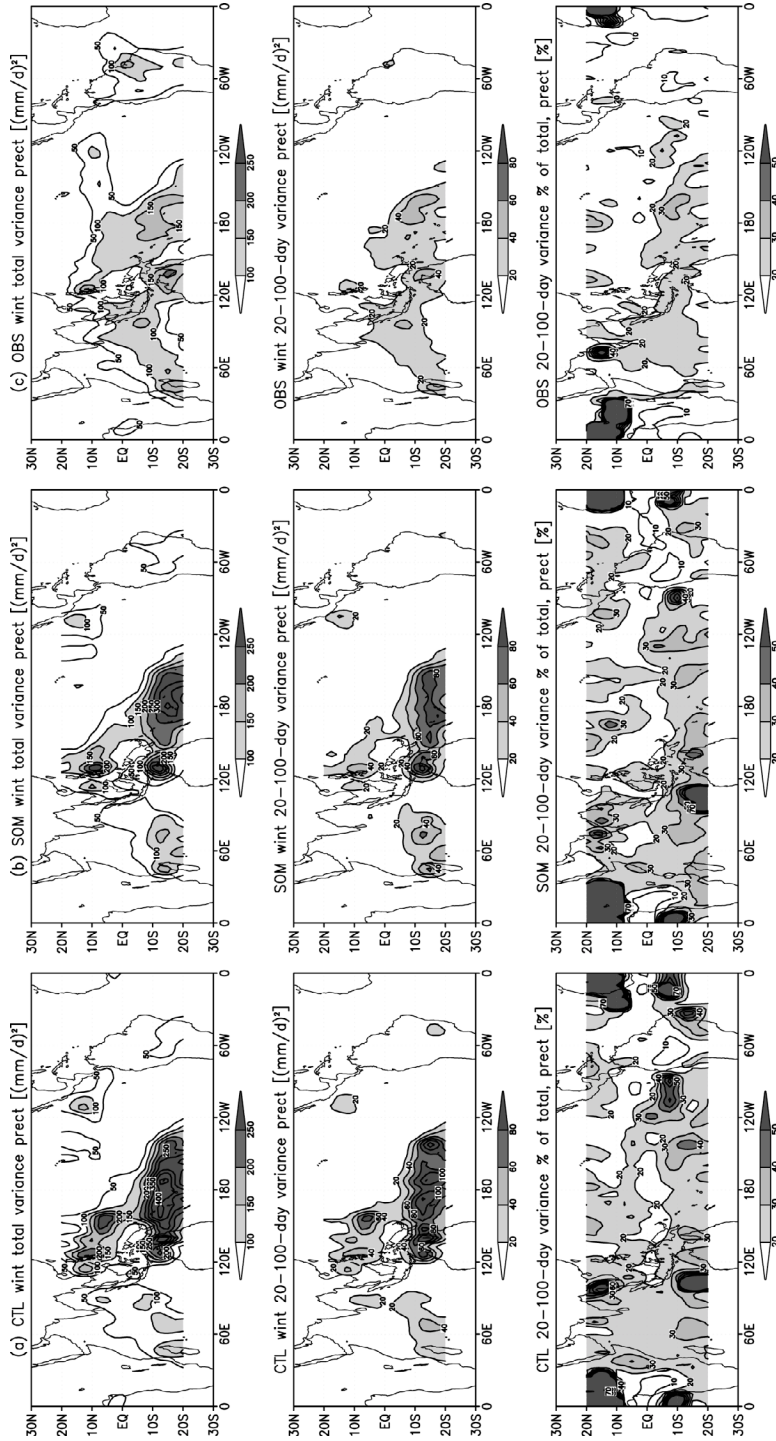


Fig. 3.4.8. As in Fig. 3.4.7, but for precipitation.

agree with previous studies of the SP-CAM which found that the model possesses substantially higher MJO-filtered winter precipitation variance compared to observations north of Australia and into the West Pacific (KDR08).

We present total and filtered winter SST variances in Fig. 3.4.9. We note that the CTL simulation uses observed monthly mean SSTs that are linearly interpolated to daily

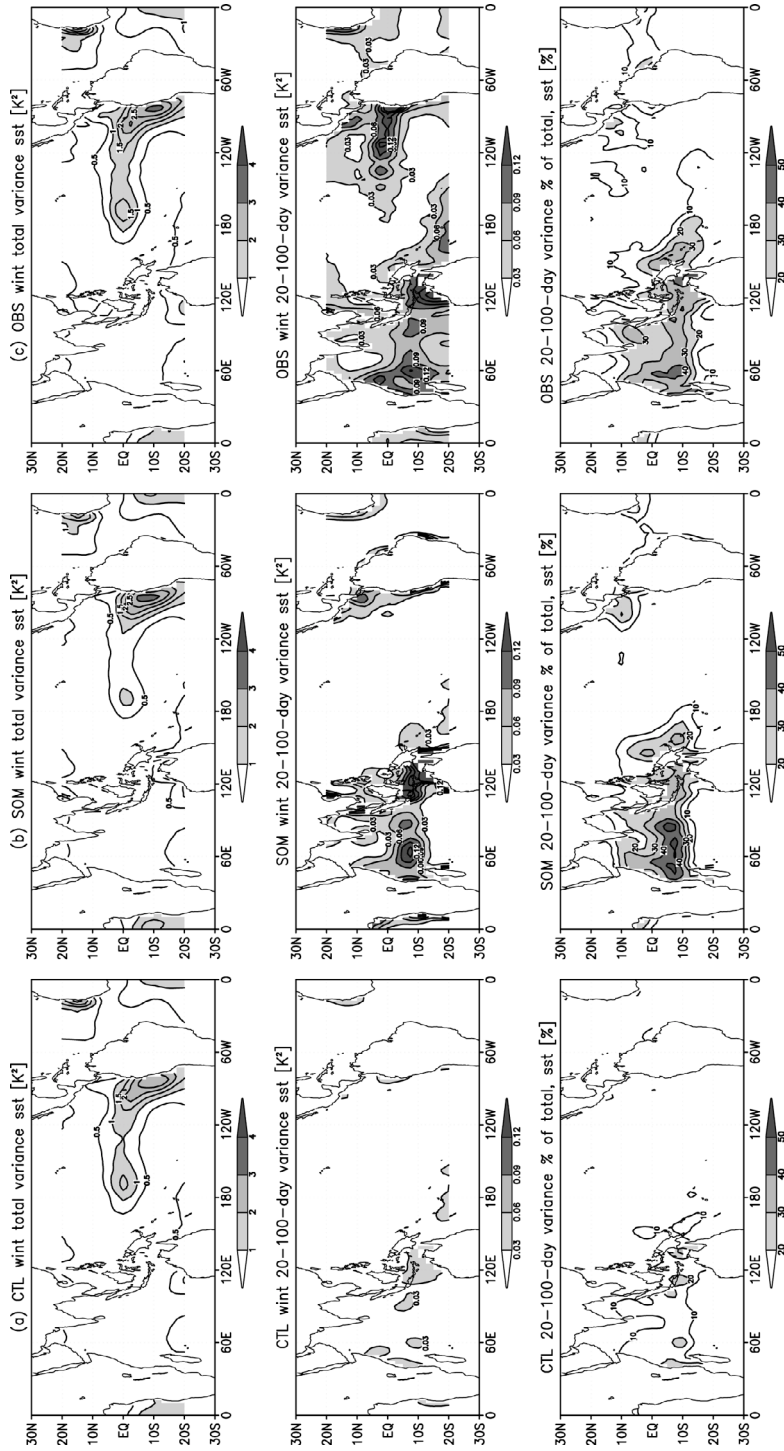


Fig. 3.4.9. As in Fig. 3.4.7, but for SST.

means for the prescribed forcing. The SOM is forced by the same linearly interpolated SSTs with the exception that the SSTs are allowed to deviate slightly from their prescribed values due to surface flux perturbations. While total winter SST variances are roughly the same for the two models, MJO-filtered SST variance is much higher in the SOM and more closely matches observations (derived from weekly data) in the equatorial Indian and West Pacific Oceans. The largest improvement in MJO-filtered SST variance is mainly within the latitude band where the slab ocean model is fully active (12°S - 12°N). The lack of SST variance on MJO space-time scales in the CTL is likely related to the monthly resolution (and linear interpolation) of the SSTs that force the model. Regardless of this caveat, SSTs in the SOM are behaving in a more natural manner and therefore we should expect more realistic air-sea interactions in the SOM. It is interesting to note that, despite its improvements in the Eastern Hemisphere, the SOM does not capture the high MJO-filtered SST variance in the cold tongue region. This deficiency likely arises because ocean dynamics, which are a strong contributor to SSTs in the eastern Pacific, are not fully captured in either the CTL or SOM (e.g., Maloney and Kiehl 2002). The observed MJO-filtered winter SST variance accounts for 30-40% of the total variance in the warm-ocean Indian and West Pacific areas, with a slightly higher percentage in the SOM and a substantially lower percentage in the CTL.

Overall, total winter OLR variance in the SOM is about the same or slightly higher than that seen in the CTL (Fig. 3.4.10), particularly over the Indian Ocean. MJO-filtered winter OLR variance tends to be larger in many areas of the SOM as well, with the exception of the region near and east of the Philippines. It is unclear why the SOM

shows increased MJO-filtered OLR variance but decreased filtered precipitation variance.

The positive winter OLR variance bias in the SOM is associated with lower mean OLR

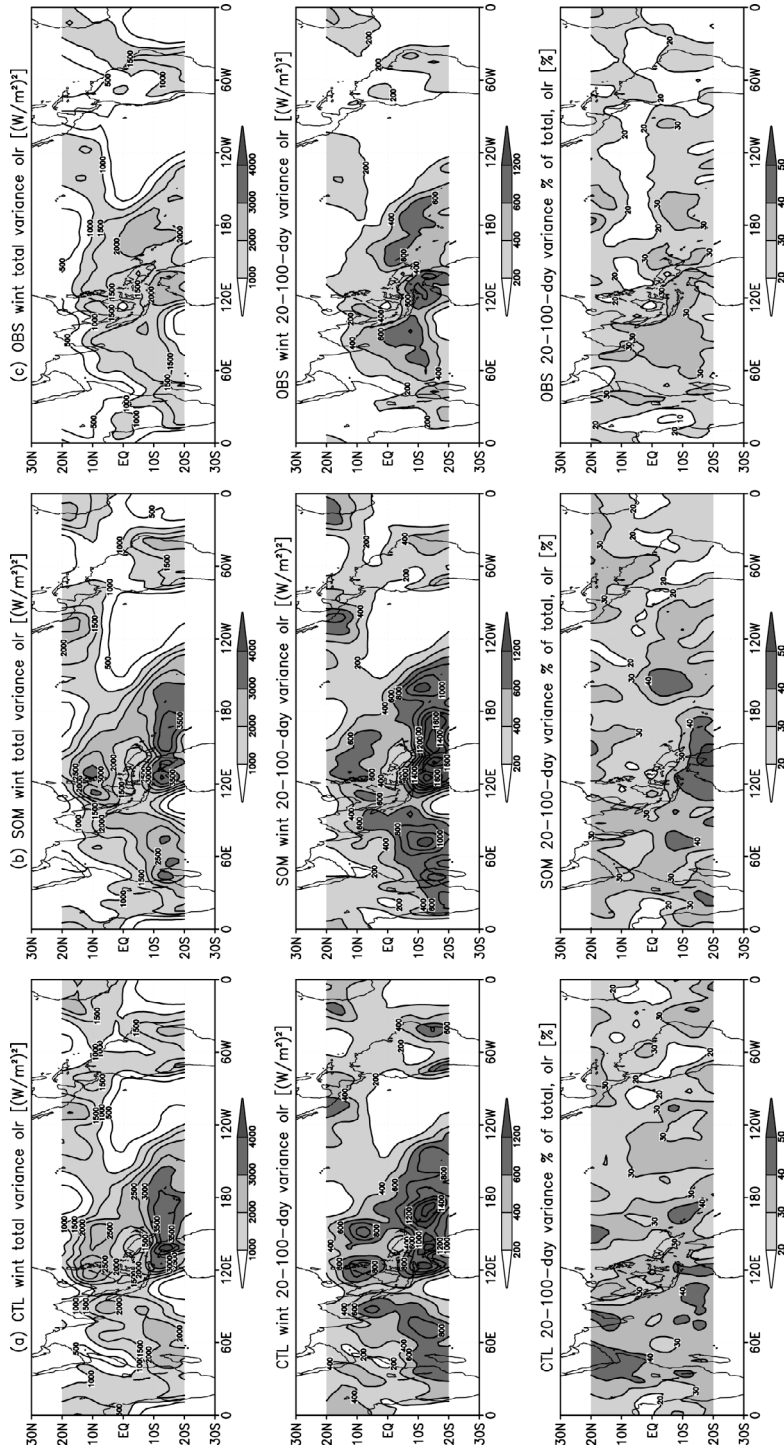


Fig 3.4.10. As in Fig. 3.4.7, but for OLR.

values in that model (Fig. 3.4.4), a correspondence common to many GCMs (e.g., Slingo et al. 1996, Kim et al. 2009). The increase in MJO-filtered winter OLR variance over the eastern Indian Ocean in the SOM represents an improvement over the CTL. In both versions of the SP-CAM, MJO-filtered OLR variance accounts for 35-40% of total OLR variance, with the observed percentage slightly lower.

Patterns of wintertime surface latent heat flux (SLHF; Fig. 3.4.11) variance are captured reasonably well by the CTL and SOM within 10° of the Equator, but the two models overestimate variances poleward of this zone. The SOM tends to have reduced total and MJO-filtered SLHF variance in both the equatorial Indian Ocean, revealing a slight worsening compared to the CTL, and the tropical West Pacific, indicative of an improvement to the model. Overestimation of the SLHF mean and variance in the West Pacific by the CTL (Fig. 3.4.11a) may be contributing to that model's excessive MJO convection (see Fig. 2.5.1 and related discussion), and so the weakened SLHFs in the SOM are an encouraging result. As was the case for OLR, reductions of SLHF variance in the SOM (Fig. 3.4.11b) are linked to decreases in the mean SLHF (Fig. 3.4.5b) in that model.

Overall, the analysis of total and MJO-filtered variance yields mixed results with regard to the impact of SP-CAM air-sea coupling and the depiction of intraseasonal variability. With the exception of SLHF, for which the SOM generally has a widespread but weak reduction, all other variables suggest that the SOM has larger intraseasonal variance in the Indian Ocean compared to the CTL. In the West Pacific and southern Maritime Continent, the SOM displays increased intraseasonal winter variance for all variables except precipitation and SLHF. We will demonstrate in Section 3.4.i that such differences

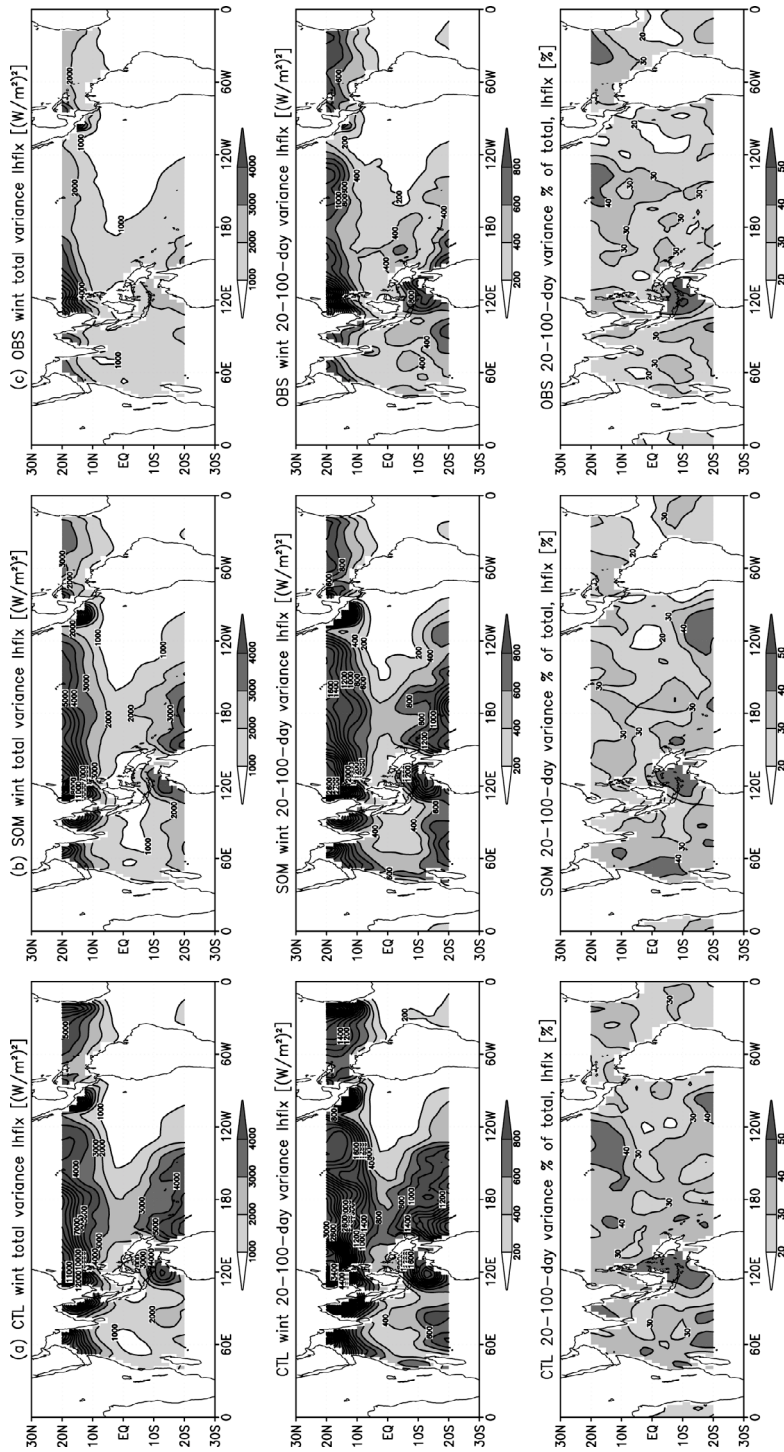


Fig. 3.4.11. As in Fig. 3.4.7, but for surface latent heat flux.

in intraseasonal variability are strongly tied to MJO convective and dynamic processes. Aside from SSTs, both versions of the SP-CAM overestimate total and filtered variances relative to observations.

3.4.d. Decile averages

Histograms based on decile averages highlight simple relationships between a selected dependent variable—in this case precipitation—and other fields. Figure 3.4.12 displays decile averages of (a) total precipitation, (b) SST, (c) SLHF, and (d) boundary layer mean wind magnitude based on an index of total precipitation. Computation of the

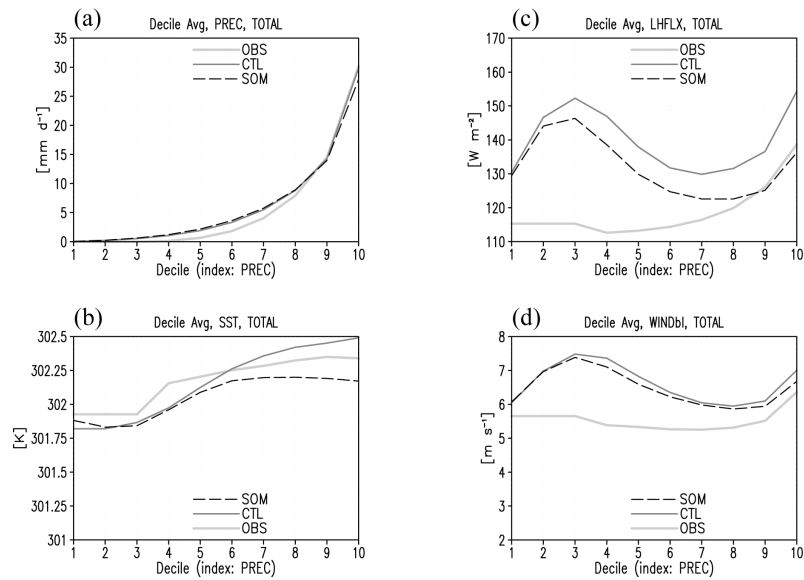


Fig. 3.4.12. Total (a) precipitation, (b) SST, (c) surface latent heat flux, and (d) boundary layer wind magnitude binned based on deciles of total precipitation for all ocean grid points within the region 60°E-180° and 10°S-10°N, for all seasons. Decile 1 (10) corresponds to the average of the driest (wettest) 10% of rainfall values. Values from the slab-ocean simulation (SOM; dashed black), control simulation (CTL; solid, dark gray), and observations (OBS; solid, light gray) are displayed.

boundary layer mean simply involves a non-weighted averaging of wind speeds at 1000, 975, 950, and 925 hPa. We use all available days and ocean-only spatial points within the domain (10°S-10°N, 60°E-180°E) to construct the plots. Index rain rates increase from left (decile 1) to right (decile 10). Low and moderate rain rates (deciles 3-7) are much more common in the CTL (solid dark gray line) and SOM (dashed black line) compared

to observations (solid light gray line; Fig. 3.4.12a). It is not particularly surprising that the SP-CAM has more instances of very light rain rates relative to GPCP given the difficulty for satellite-based sensors to detect drizzle from shallow cumuli (Petty 1999) which are ubiquitous in the Tropics (Stevens et al. 2003). “Dry” days—those in which no rainfall occurs—are prevalent in the GPCP measurements and entirely fill deciles 1-3. Heavy rain occurrences are slightly less common in the SOM compared to the CTL. In total, the rainfall decile profiles of the CTL, SOM, and observations are sufficiently similar to conduct comparisons of other variables using a precipitation-based index.

Decile averages of SSTs indicate cooler (warmer) ocean surface temperatures during periods of light (heavy) rain (Fig. 3.4.12b). We note that observed SST values in deciles 1-3 have been averaged together because all observed rainfall values in these bins are zero. We have not applied any such adjustments to the SP-CAM profiles because rain values vary within the first three deciles. For light rain rates, SSTs in the CTL and SOM are similar to each other and cooler than the observed value. Once rain rates exceed ~ 3 mm d^{-1} (decile 5), the model profiles diverge as SSTs in the CTL steadily increase but those in the SOM climb slightly and then level off and weakly decrease during periods of very heavy rainfall. Observed SSTs level off during periods of heavy rain, suggesting that certain processes linked to the deep convection regulate ocean surface temperatures. This basic interaction does not appear in the CTL simulation.

Figure 3.4.12c displays binned profiles of SLHF. Simulated SLHFs are clearly different from observations that depict a steady rise in fluxes with increasing rain rate. Both the CTL and SOM show a moderate overestimation (15-25%) of SLHF for most

rain rates but especially during periods of light precipitation. The excessive SLHF values also appear in the climatological mean (Fig. 3.4.5) and are directly tied to increased boundary layer winds (Fig. 3.4.12d) in the model. SLHFs in the SOM are generally reduced by 5-10 W m^{-2} , especially during heavy rain periods when the SOM and observations match up very well (Fig. 3.4.12c). This reduction may be associated with lower SSTs under heavy rain conditions (Fig. 3.4.12b). Both SLHFs and SSTs (Fig. 3.4.12b) simultaneously and steadily increase during heavy rains in the CTL but not in the SOM or observations, suggesting that the simple relationships between convection, surface evaporation, and SSTs are more unrealistic in the CTL simulation.

We present decile average profiles of boundary layer wind magnitudes in Fig. 3.4.12d. The boundary layer mean is found by averaging wind magnitudes within the 1000-925 hPa layer. Simulated boundary layer wind behavior is similar to SLHF, showing dual maxima at light (decile 3) and heavy (decile 10) rain rates and widespread overestimation in both versions of the SP-CAM. This model wind bias appears to be related to biases in the mean state wind fields (Fig. 3.4.1). These positive model biases are lower in the SOM. Except for a modest increase during periods of heavy rains, little variability is seen in observed winds.

We examine the relationships between 20-100-day filtered precipitation and other variables in Fig. 3.4.13. As in Fig. 3.4.12, precipitation acts as the index upon which other variables are binned with the exception that all variables involved are filtered to retain only features on intraseasonal time scales. We caution that only limited interpretation of the decile profiles in the context of the MJO is possible because the plots do not

contain any information regarding space or time dependencies. For example, we can assume that deciles 1-2 (9-10) correspond to the MJO phase in which convection is strongly suppressed (active) but the relationship for intermediate deciles is less clear. We cannot be sure whether the average of decile 5 is associated with moderate rainfall rates that precede or follow MJO deep convection, a critical piece of information for variables such as SST and SLHF that are temporally asymmetric with regard to the MJO wet phase. Fig. 3.4.13a highlights the flawed relationship between convection and SSTs in the CTL as discussed previously. SSTs in the CTL increase steadily with increasing rain rates, while the opposite is true for both SOM and observations. The SOM appears overly sensitive to rain rate changes, with warmer (cooler) SSTs during periods of very light (heavy) precipitation.

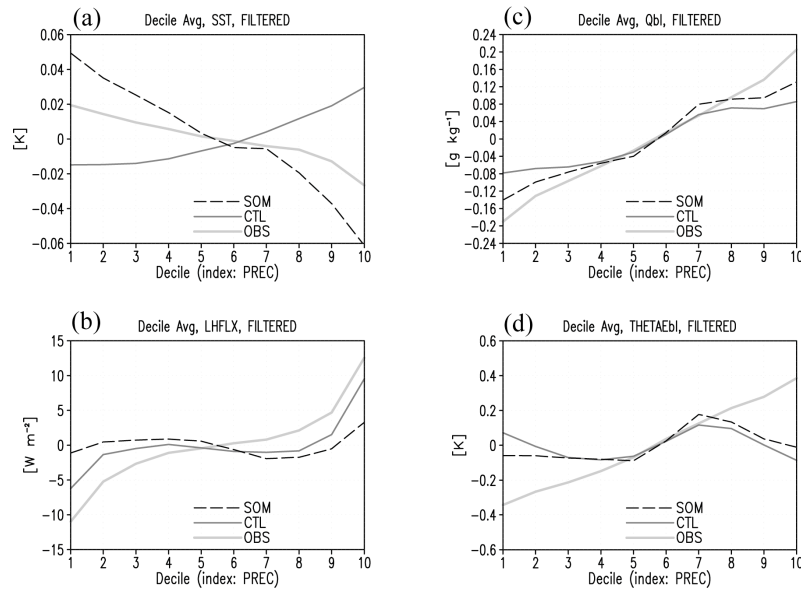


Fig. 3.4.13. 20-100-day filtered (a) SST, (b) surface latent heat flux, (c) boundary layer specific humidity, and (d) boundary layer equivalent potential temperature binned based on deciles of 20-100-day filtered precipitation for all ocean grid points within the region 60°E-180° and 10°S-10°N, for all seasons. Values from the slab-ocean simulation (SOM; dashed black), control simulation (CTL; solid, dark gray), and observations (OBS; solid, light gray) are displayed. Decile 1 (10) corresponds to the average of the driest (wettest) 10% of rainfall values.

Decile profiles of intraseasonal SLHF (Fig. 3.4.13b) indicate that the models do a fair job at capturing the relative minimum (maximum) of SLHF at low (high) rain rates. The SOM has only a weak SLHF sensitivity to rain rate. Specific humidity gradients within the lowest two model levels are better represented in the SOM (not shown), and we can therefore conclude that the poorer depiction of SLHF in the SOM is mainly due to the stronger (weaker) near-surface wind magnitudes during periods of low (high) precipitation compared to the CTL (not shown).

We present decile profiles of boundary layer specific humidity in Fig. 3.4.13c. The boundary layer mean is found by averaging specific humidity values over the four levels within the 1000-925 hPa layer. Between deciles 4-7, both versions of the SP-CAM resemble observations, with a positive correlation between boundary layer moisture and rain rate. The SOM captures the behavior of low-level moisture better than the CTL for very light and heavy rain periods. The CTL is too dry during heavy rains and not dry enough during periods of suppressed convection. We will show in Sections 3.4.i and 3.5.b that these smaller biases seen in SOM boundary layer moisture are directly related to the more coherent signal of the MJO in the SOM.

Boundary layer averaged equivalent potential temperature, $\theta_{e,bl}$, is displayed in Fig. 3.4.13d. For moderate rain rates, the models and observations match up well, but errors are noted during the suppressed and active phases of the MJO. In the dry MJO phase (deciles 1-2), the observed atmosphere is stable, convection is suppressed, and the boundary layer is cool and dry resulting in a minimum of $\theta_{e,bl}$ (solid light gray line in Fig. 3.4.13d). The CTL and SOM do not show this relationship; in fact, $\theta_{e,bl}$ increases during

periods of light rain. Around the times that the MJO is in its wet phase, deep convection is abundant and the boundary layer is warm and moist corresponding to a maximum in $\theta_{e,bl}$ (solid light gray line in Fig. 3.4.13d). In contrast, the CTL and SOM suggest a local minimum of $\theta_{e,bl}$ for the heaviest rain rates. We have previously demonstrated that the decrease in MJO-filtered $\theta_{e,bl}$ during the MJO wet phase is mainly linked to unrealistically intense boundary layer cold pools in the CTL (Fig. 2.4.3), and this appears to be true for the SOM as well (Fig. 3.4.13d).

Cross sections for height-dependent variables are also binned based on deciles of precipitation. Figure 3.4.14 represents differences (SOM–CTL) of the decile average of (a) anomalous longwave heating rate Q_{LW} and (b) anomalous apparent convective moisture sink, $-Q_2$, at each pressure level. Anomalies are defined as departures from a smoothed calendar-day mean value. We use smoothed calendar-day means due to the limited five-year time range being analyzed. During heavy rain periods, the longwave radiation anomaly difference (Fig. 3.4.14a) is slightly negative in the lower and middle troposphere, positive near 300 hPa, and negative near the tropopause. Because there is typically deep longwave heating from the surface to 200 hPa and cooling above for high rain rates (not shown), Fig. 3.4.14a indicates that the SOM has weaker longwave heating in the lower troposphere, stronger heating between 450-200 hPa, and stronger cooling above.

A vertical dipole of opposite sign is noted in longwave radiation anomalies at upper levels during light rain rates (Fig. 3.4.14a). We hypothesize that differences in anomalous cloud amount contribute toward this vertical dipole. It is unclear why cloud

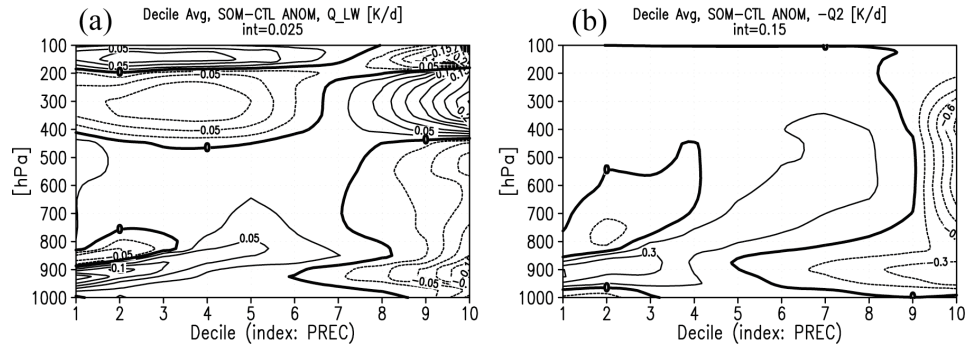


Fig. 3.4.14. Cross section differences of anomalous (a) longwave heating and (b) apparent convective moisture sink between the slab-ocean (SOM) and control simulation (CTL), binned based on deciles of anomalous precipitation for all ocean grid points within the region 60°E - 180° and 10°S - 10°N , for all seasons. Differences are defined as SOM-CTL. Decile 1 (10) corresponds to the average of the driest (wettest) 10% of rainfall values. Positive (negative, zero) contours are displayed as thin black (dashed, thick black) lines.

amount is greater below 400 hPa and above 250 hPa in the SOM compared to the CTL (not shown), but this difference is linked to cloud-radiative interaction that could be a contributing factor toward the differences in longwave radiation cross sections. An interesting feature in the longwave radiation anomaly differences is seen below 700 hPa during light to moderate rain rates (Fig. 3.4.14a). During dry periods, the SOM has greater longwave heating in the boundary layer (below 900 hPa) and stronger longwave cooling in a thin layer above. As rain rates increase (deciles 2-3), the heating-under-cooling dipole gradually shifts upwards. The heating signature loses its overlying cooling counterpart but continues its upward movement, reaching ~ 800 hPa by decile 5 when total precipitation rates are 2-3 mm d^{-1} . The longwave heating-cooling dipole and its gradual lofting with increasing rain rate complement similar behavior seen in many other variables (e.g., convective heating and moistening, equivalent potential temperature θ_e , and cloud amount), strongly indicating that the SOM has more suppressed-phase shallow cumuli. More importantly, these difference profiles might imply that the transition be-

tween shallow cumuli, cumulus congestus, and cumulonimbi—a critical feature of the MJO and one that GCMs have difficulty simulating (Johnson et al. 1999, Inness et al. 2001)—is better represented in the SOM compared to the CTL. We caution, however, that interpretation of data in the middle deciles is less clear in the context of the MJO because we cannot be sure whether the middle deciles represent the growing or declining MJO wet phase. In either case, we are confident that deciles 1-3 accurately capture the phase of the MJO when convection is suppressed.

The SOM has weaker convective condensational heating ($-Q_2$) compared to CTL during deep periods of heavy rains (Fig. 3.4.14b). Although convective heating in the CTL and SOM is directly available from the CRMs, we use the bulk formula of $-Q_2$ from Lin and Johnson (1996b) for equal comparison with the ERAI data:

$$-Q_2 = L \left[\frac{\partial q}{\partial t} + \mathbf{v}_h \cdot \nabla_h q + \omega \frac{\partial q}{\partial p} \right] \quad (4.1)$$

Because the CTL has a strong positive bias in convective heating and drying compare to observations (not shown), this weakening of convective drying throughout the troposphere during heavy rains generally represents an improvement of the SOM over the CTL. The weakened convective drying in the SOM simply reflects less precipitation during periods of heavy rain (c.f. Fig. 3.4.12a). The more coherent transition between the suppressed and active phases of the MJO indicated by the gradual rise of positive convective heating anomalies rooted in the boundary layer is also seen (Fig. 3.4.14b).

Overall, the decile plots exhibit the SP-CAM’s tendency to overestimate the difference between dry and wet periods. During periods of heavy rain, both the CTL and

SOM display unrealistically strong convective intensity compared to observations. The simulations have more vigorous upward motion, greater convective heating and drying, and a warmer and moister environment relative to the observed fields. In the dry phase, simulated subsidence, low-level divergence, and mid-tropospheric radiative cooling are stronger than observed, and the atmosphere is drier. The SOM results indicate that the contrasts between wet and dry periods are generally less intense compared to the CTL simulation, suggesting that the inclusion of a slab ocean model weakly but realistically regulates convection and thus improves the SP-CAM.

3.4.e. Zonal wavenumber-frequency analysis

Diagrams of fields decomposed into their zonal wavenumber and frequency components reveal distinct wave patterns within the Tropics (Wheeler and Kiladis 1999). We present the zonal wavenumber-frequency diagrams for 850 hPa zonal wind in Fig. 3.4.15. The top (bottom) row displays spectral power divided by a smoothed background power for tropical wave features that are antisymmetric (symmetric) about the Equator for (a) CTL, (b) SOM, and (c) observations. Corresponding dispersion curves for shallow water equation equivalent depths of 12, 25, and 50 m are also shown (thick black lines). Representative wave types are labeled red in (a) as a reference. The MJO spectral signal is the leading mode of observed intraseasonal variability in the Tropics and is captured very well in both the uncoupled and coupled versions of the SP-CAM. This is in stark contrast to CAM3.0, which has virtually no MJO spectral signal (Zhu et al. 2009). For zonal winds, the MJO spectral power is confined to zonal wavenumbers one and two and peri-

ods 20-90 days, reflecting the large zonal extent of the MJO's dynamical response. Both the CTL and SOM have a slightly weaker spectral signal (relative to their respective

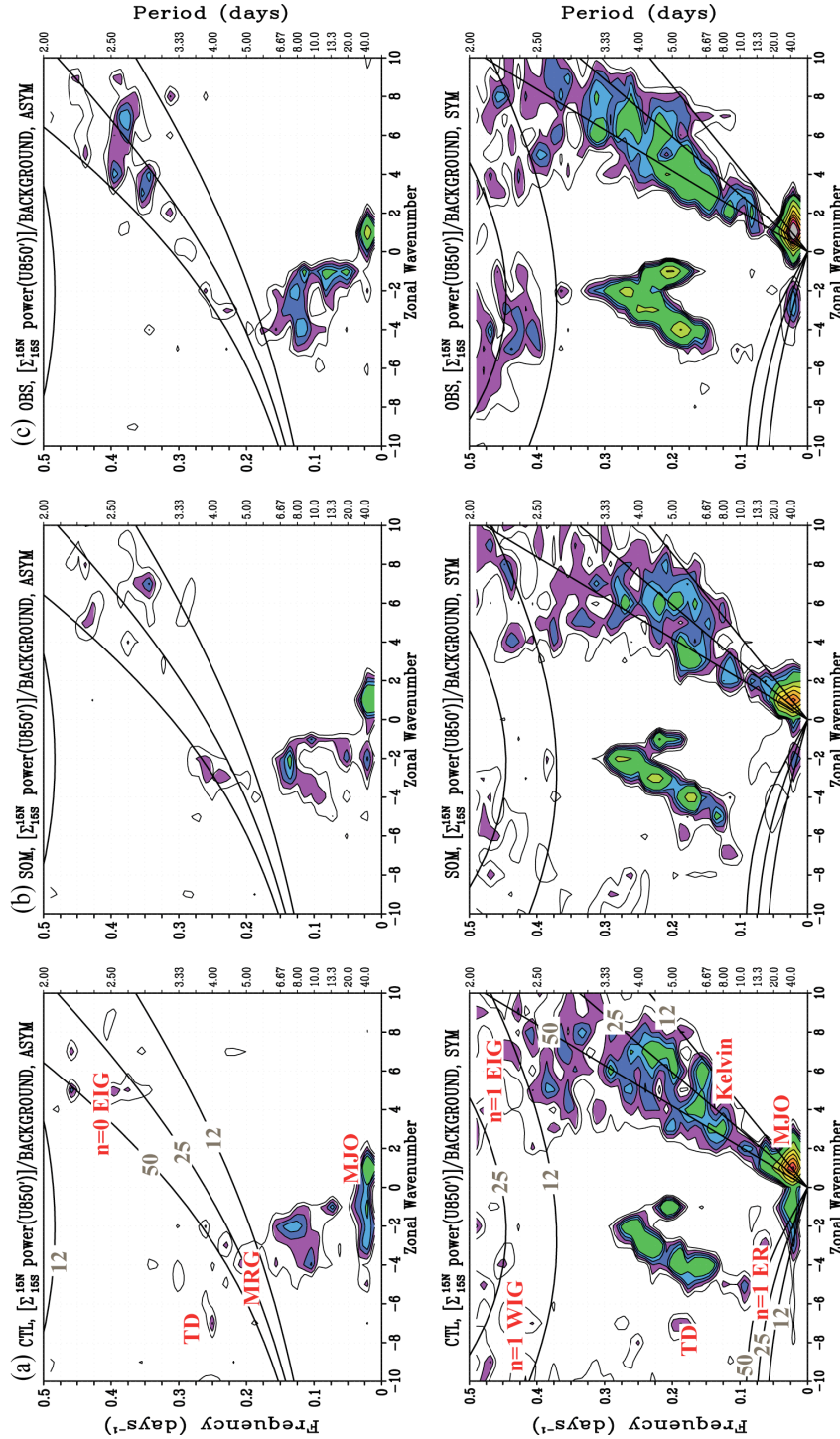


Fig. 3.4.15. Ratios of antisymmetric (top) and symmetric (bottom) spectral power to a smoothed background power for zonal wind at 850 hPa. Displayed are results for the control simulation (CTL; a), slab-ocean simulation (SOM; b), and observations (OBS; c). Power contour interval (thin black) is 0.1 between 1.1 and 1.5 and 0.5 above 1.5. Values above 1.2 are shaded. Dispersion curves of the linear shallow water equations (thick black) for equivalent depths of 12, 25, and 50 m are superimposed on each plot. Representative wave types are shown in red in (a). Negative (positive) zonal wavenumbers correspond to westward- (eastward-) propagating waves. Frequency spectral bandwidth is 1/96 cycles per day.

background spectra) for Kelvin waves and the antisymmetric component of the MJO, with a more substantially negative model bias in the symmetric MJO component (Fig. 3.4.15). In contrast, the raw spectra (not shown) reveal that both the CTL and SOM *overestimate* U850 variance in the MJO spectral region, with the positive bias in the SOM less than the CTL. This indicates that the MJO signal in the SPCAM is not as distinct from the spectral background as in nature and is a result of larger overall low-frequency variability in the SPCAM (not shown).

The SOM shows a modest improvement compared to the CTL in the spectral signal of precipitation (relative to its background signal) for several wave types including the MJO (Fig. 3.4.16). In nature and the models, significant spectral power of low-frequency (>30 days) precipitation extend beyond wavenumbers one and two. This is because the convective signals for the MJO and equatorial Rossby waves are of smaller spatial scale relative to zonal wind (c.f. Fig. 3.4.15) and are generally confined to the Eastern Hemisphere, thus projecting onto a mixture of zonal wavenumbers (Salby and Hendon 1994). The SOM antisymmetric wave components indicate a low-frequency signal that is less extensive across zonal wavenumbers (top row of Fig. 3.4.16). For symmetric components, low-frequency power (above the background signal) in the CTL is spread evenly across many zonal wavenumbers, but in nature the MJO and equatorial Rossby wave signals are relatively more distinct. The SOM displays improved distinctions between symmetric, low-frequency wave types compared to the CTL—including a stronger equatorial Rossby wave signal in the correct spectral region—and has slightly more robust Kelvin wave and MJO signals. We hypothesize that the Kelvin and Rossby

signal improvement in the SOM must be related to the more realistic depiction of the MJO, which can modulate both Kelvin and Rossby modes. The raw power spectra (not

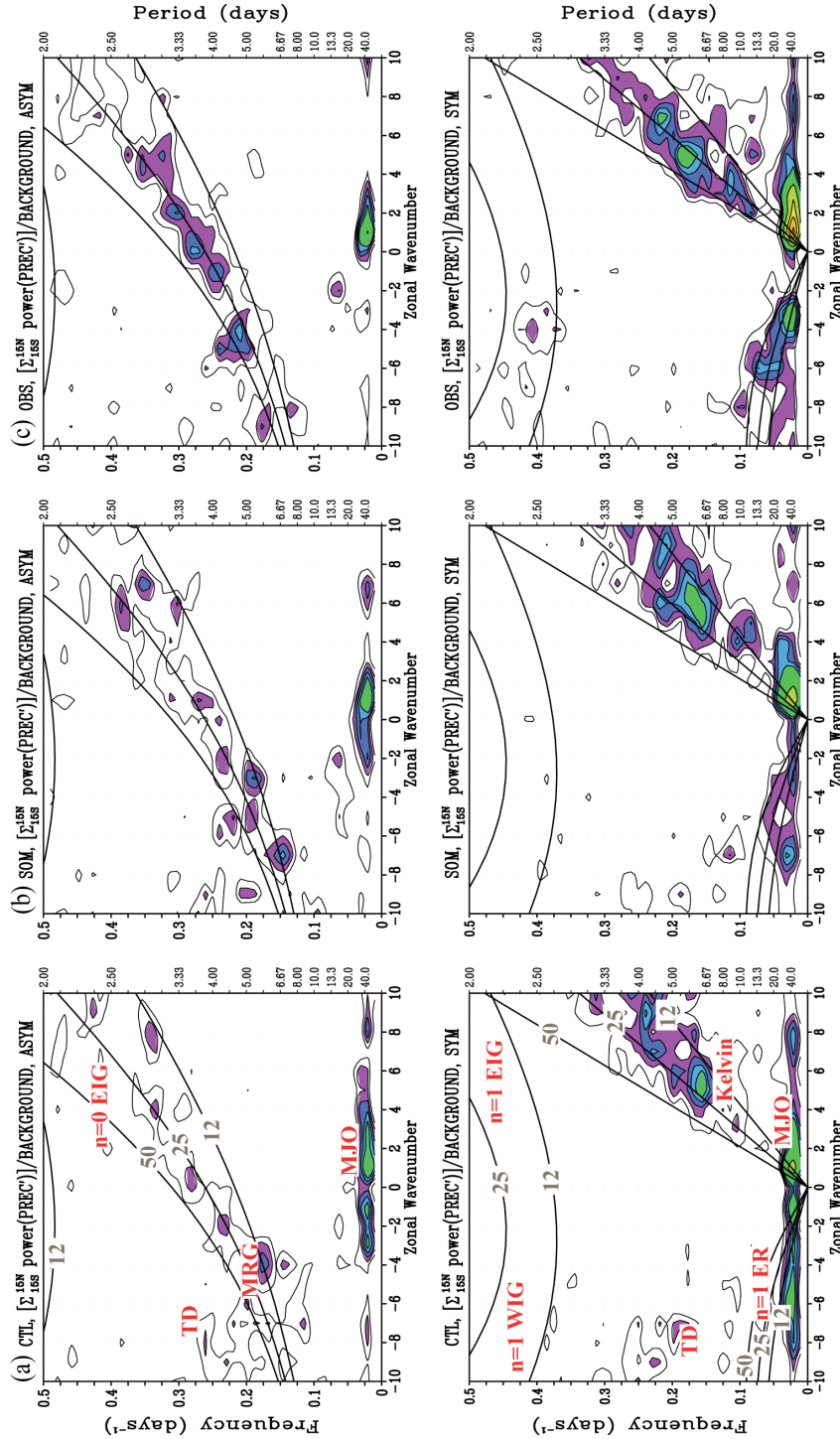


Fig. 3.4.16. As in Fig. 3.4.15, but for precipitation.

shown) indicate that both versions of the SPCAM weakly underestimate the symmetric component of the MJO signal, similar to the results of the 850 hPa zonal wind spectral analysis above.

We display zonal wavenumber-frequency diagrams of OLR in Fig. 3.4.17. Similar to the results for precipitation (Fig. 3.4.16), the SOM appears to more closely resemble observations for several wave types including equatorial Rossby waves and the anti-symmetric and symmetric components of the MJO. The SOM results indicate a robust spectral density consolidated around zonal wavenumbers 1-2 as seen in nature, whereas the CTL depicts a weaker MJO signal (relative to background) extending out to wavenumber 3 for eastward-propagating disturbances (positive wavenumbers). Raw OLR spectra (not shown) indicate that both versions of the SPCAM have very similar power values in the MJO region for symmetric components compared to the observed spectra.

An important diagnostic related to MJO spectral analysis involves the ratio of raw power values between westward- and eastward-propagating features (Lin et al. 2006, Kim et al. 2009). Coherent wave signals have significant spectral power within a specific range of frequencies and zonal wavenumbers. If similar raw power (background not removed) is noted at the same frequencies for matching positive and negative zonal wavenumbers, the wave feature may have a large standing oscillation component and will not display clear propagation in physical space (Hayashi 1979). Most GCMs have difficulty in accurately capturing the correct east-west power ratio of the MJO signal (Lin et al. 2006), but the SP-CAM has a ratio that is comparatively closer to observations (Kim et al. 2009). We compare east-west spectral power ratios of several key variables for the

CTL, the SOM, and observations in Table 3.2. For OLR and precipitation, we compare the eastward MJO signal (zonal wavenumbers +1 and +2) to its westward counterpart

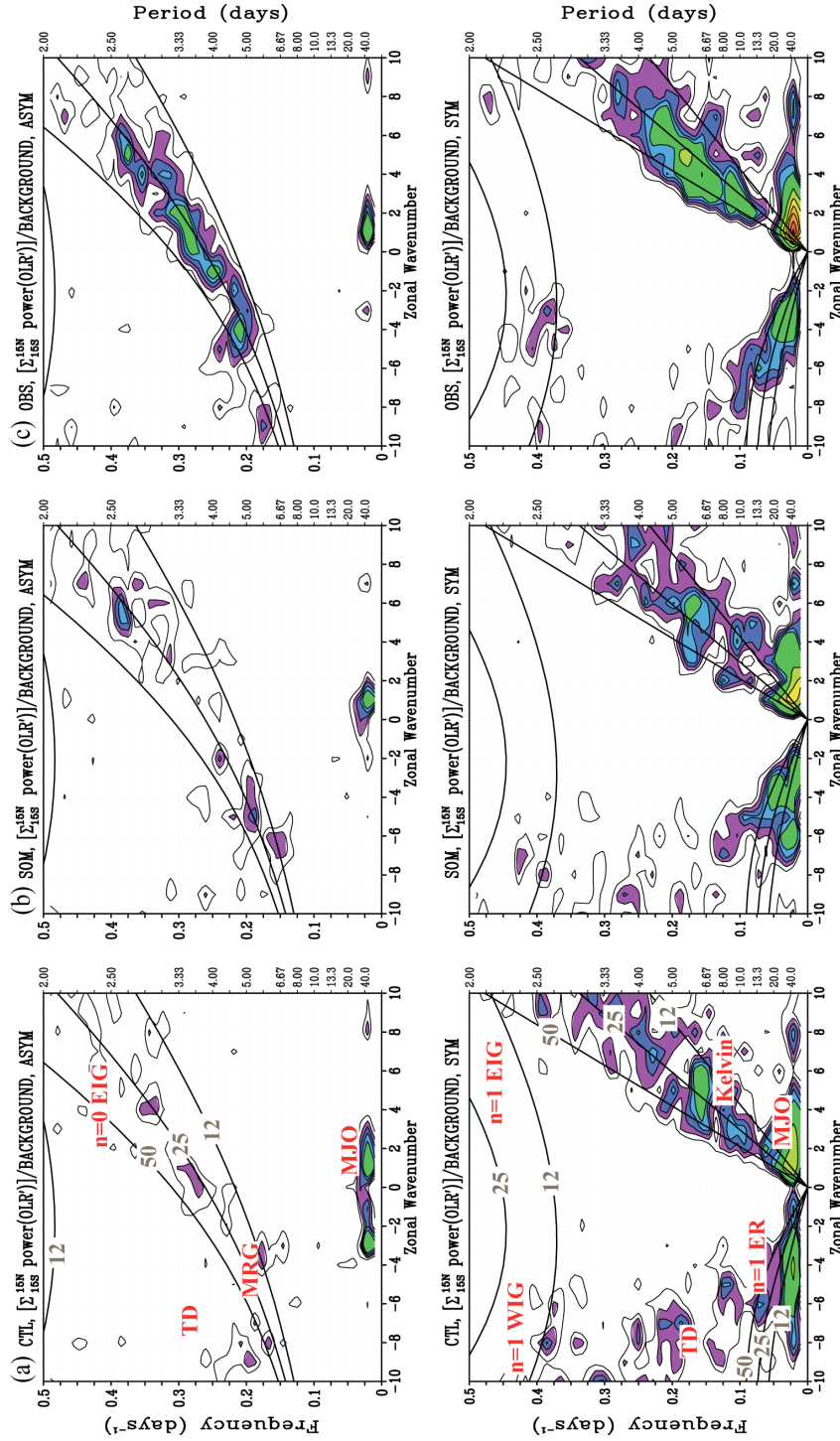


Fig. 3.4.17. As in Fig. 3.4.15, but for OLR.

(zonal wavenumbers -1 and -2) for periods of 32-96 days. For zonal winds, the ratio is between zonal wavenumber $+1$ (eastward propagation) and -1 (westward propagation)

Table 3.2. Ratios of eastward to westward MJO spectral power for the control SP-CAM simulation (CTL), the SP-CAM with slab ocean (SOM), and observations (OBS). Zonal wavenumbers of -2 , -1 , $+1$, and $+2$ are used to compute east-west ratios for OLR and precipitation, but only zonal wavenumbers -1 and $+1$ are used for 850 hPa and 200 hPa winds (U850 and U200, respectively). A period range of 32-96 days is used for all ratio calculations.

	Precipitation	OLR	U850	U200
CTL	1.3	1.7	2.6	3.7
SOM	1.7	2.1	3.5	4.0
Observations	2.7	3.1	5.9	7.4

for the same frequency range. Although it still falls short of the observed ratio values, the SOM shows an increased east-west power ratio for the convective and dynamic variables compared to the CTL. This demonstrates that the implementation of the slab ocean model in the SP-CAM is associated with clearer eastward MJO propagation and likely a reduced standing wave signal. We will soon illustrate that the improved east-west power ratio of the MJO signal in the SOM is not just a spectral artifact but is also manifested in the physical structure of the MJO disturbances.

3.4.f. Longitude-time analysis

Figure 3.4.18 displays the tropical wave propagation characteristics in longitude-time space. This figure shows anomalies of precipitation—defined as departures from a smoothed calendar-day mean—averaged from 12.5°S - 12.5°N for all longitudes (shading), as well as MJO-filtered (20-100 days, eastward-propagating zonal wavenumbers 1-

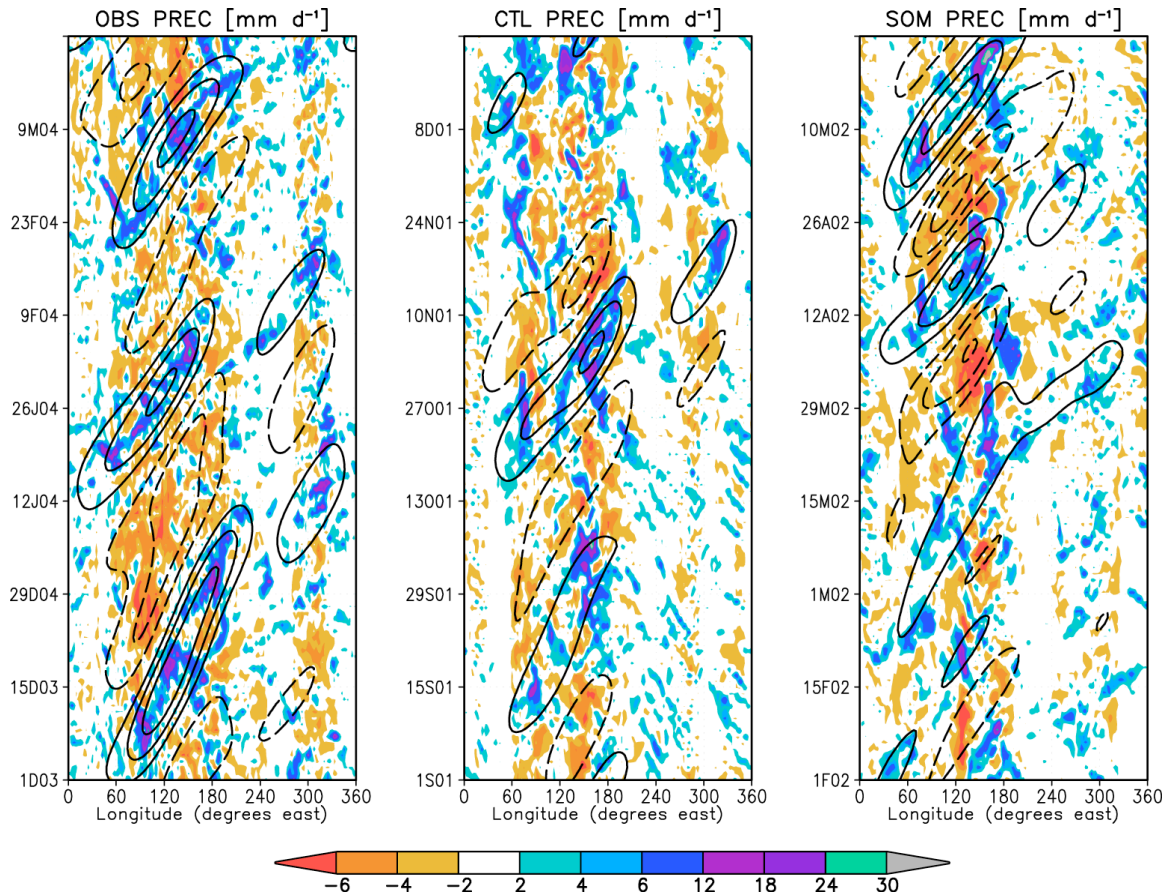


Fig. 3.4.18. Longitude-time plots of anomalous total (shaded) and filtered (contour) precipitation from observations (OBS; left), the control simulation (CTL; middle), and the slab-ocean simulation (SOM; right). Filtered data corresponds to eastward-propagating waves with zonal wavenumbers 1-6 and periods 20-100 days. Data are averaged from 12.5°S-12.5°N. Date format is d(d)myy where, for example, 12 Jan 2004 is 12J04. The contour interval is 1.0, positive (negative) contours are solid (dashed), and there is no zero contour.

6) precipitation averaged over the same latitudinal span (line contours). Negative anomalies appear as warm colors (dashed contours) and positive anomalies are represented by cool colors (solid contours). Each column presents a four-month time segment in which the MJO was particularly active in the observations (left), CTL (middle), or SOM (right). The plots are only meant to portray the typical modulation of rainfall by the MJO and the ability of space-time filtering to capture such modulations. We note that

the start and end times for each temporal segment are different; however, each panel captures the common behavior of the MJO for its respective data source.

Figure 3.4.18 indicates that both the CTL and SOM have intraseasonal convective disturbances with qualitatively similar amplitudes and phase speeds close to those seen in observations. In all three columns, the disturbances develop in the western Indian Ocean and dissipate near the International Date Line. Closer examination reveals some differences between the simulated and observed MJO. The observed MJO embodies a coherent, nearly uninterrupted region of enhanced precipitation from its onset to its dissipation, but the MJO-related convective signal in the CTL and SOM appears to be more episodic and irregular (for example, compare the CTL MJO outlined by the solid contour beginning near 7 September 2001 with the observed MJO beginning near 12 January 2004). In particular, the CTL tends to have a greater degree of local convective intensification at 90°E and $120^{\circ}\text{--}130^{\circ}\text{E}$ with no clear propagating convective signal—even anomalies of opposite sign—in between (Fig. 3.4.18, middle column). This problem appears to be slightly alleviated in the SOM (Fig. 3.4.18, right column), which displays a more coherent convective signal and fewer disruptions to the heavy rainfall (for example, compare the SOM MJO event beginning around 5 April 2002 with the CTL event starting at 15 October 2001). This difference in convective behavior suggests that allowing the atmosphere and ocean surface to interact in a more natural manner results in improved coherence and propagation characteristics of MJO disturbances in the SP-CAM.

3.4.g. Lag correlations

Improved coherence in the MJO signal of the SOM can also be seen through lag correlation analysis. Figure 3.4.19 displays 20-100-day (“MJO”-) filtered OLR, averaged

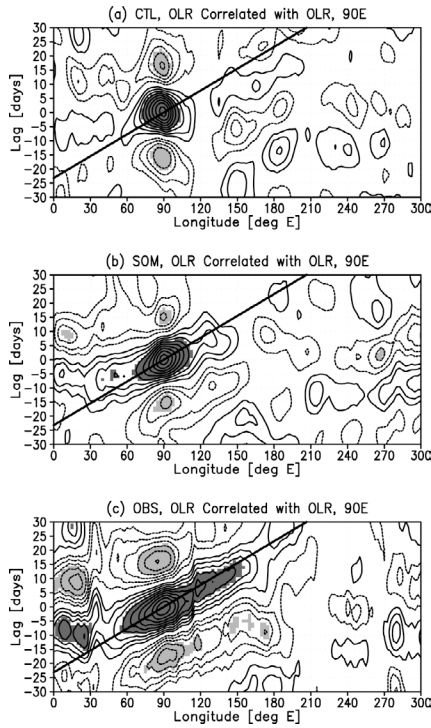


Fig. 3.4.19. Lag autocorrelation of 20-100-day filtered OLR at 90°E, averaged between 10°S-5°N, for (a) the control simulation (CTL), (b) slab-ocean simulation (SOM), and (c) observations. Contour interval is 0.1, positive (negative) contours are solid (dashed), and no zero contour is shown. Dark (light) shading represents autocorrelations above the 95% significance level for positive (negative) values. A 5 m s⁻¹ phase speed line (thick black) is also shown.

between 10°S-5°N, lag correlated with an index timeseries at 90°E. For this figure, the index is defined by MJO-filtered OLR averaged between 10°S-10°N, and thus Fig. 3.4.19 approximates a lag autocorrelation of OLR on MJO space-time scales. Time increases from bottom to top in each panel, and negative (positive) lag days correspond to days before (after) minimum OLR. Positive (negative) correlation magnitudes greater than the 95% statistical significance level are shaded dark (light) gray. In nature (Fig. 3.4.19c), OLR is significantly lag correlated with its 90°E value from the West Indian to the West Pacific Ocean. We can infer a clear east-

ward propagation of the observed MJO signal with a phase speed of approximately 5 m s⁻¹ (thick black line; Fig. 3.4.19c). Examination of the OLR lag autocorrelation in the CTL reveals a large stationary signal in the MJO with weak, limited eastward propagation

(Fig. 3.4.19a). The CTL indicates a nearly zero correlation of OLR at 90°E and OLR between 110°-140°E for all lag days. The SOM shows an improved MJO signal as measured by OLR lag autocorrelation, with positive correlations from the West Indian Ocean through to at least the Maritime Continent (Fig. 3.4.19b).

We present lag correlations of 850 hPa zonal wind (U850) with an index time-series based on precipitation at 90°E (Fig. 3.4.20) and 150°E (Fig. 3.4.21). As in Fig. 3.4.19, all data sets are filtered to MJO time scales (20-100-day periods) and meridionally averaged. Observed patterns of U850 indicate a strong coupling of easterly followed by westerly anomalies as the maximum MJO-related rainfall passes. Centers of robust dynamical response in the East Indian and West Pacific Oceans correspond to more vigorous intraseasonal precipitation in these regions (e.g., Salby and Hendon 1994). As convection moves into the central Pacific Ocean, it becomes decoupled from the dynamical signal and the MJO propagates as a faster, “dry” Kelvin wave into the Western Hemisphere as evidenced by the increase phase speed of the easterly-westerly couplet in Figs. 3.4.20c and 3.4.21c (compare to the 5 m s^{-1} phase speed line; Matthews 2000). The CTL results show a weaker and more limited extent of the easterly-westerly coupling for precipitation indices at both 90°E and 150°E (Figs. 3.4.20a and 3.4.21a). The propagation of statistically significant positive correlation values that lag precipitation—representing trailing westerlies—is also limited in the CTL. Although the MJO signal in the SOM remains notably weaker than that observed, it shows improvement in MJO signal coherence over the CTL, mainly in the greater longitudinal extent of significant leading negative and trailing positive correlations (Figs. 3.4.20b and 3.4.21b). The SOM also performs

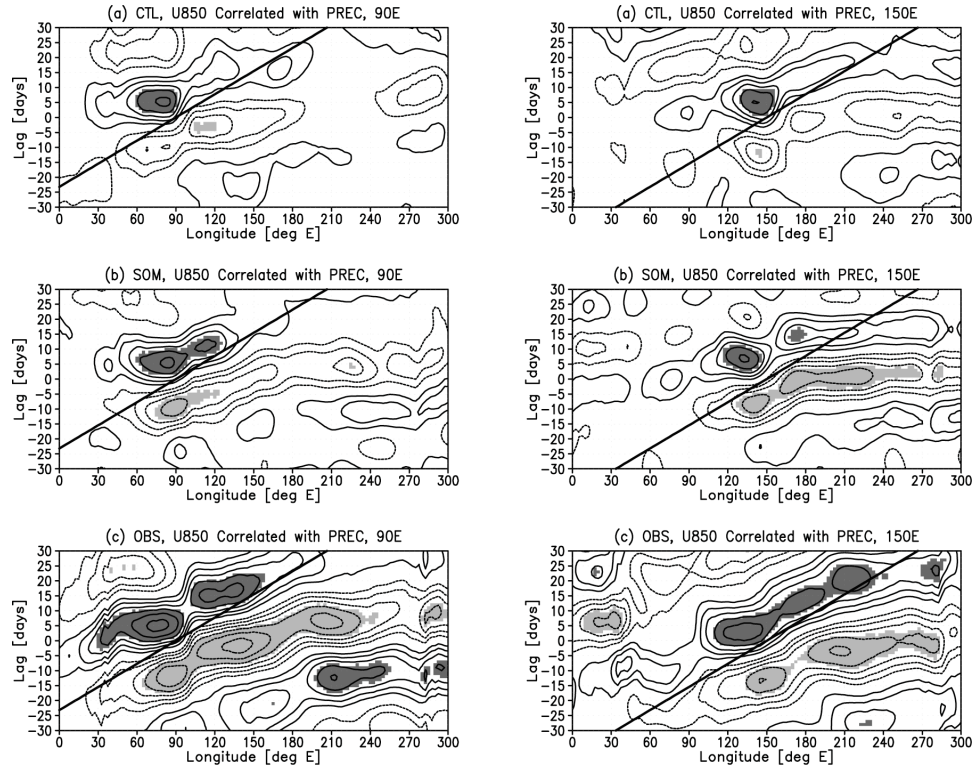


Fig. 3.4.20 (left). Lag correlation of 20-100-day filtered 850 hPa zonal wind with 20-100-day filtered precipitation at 90°E, averaged between 10°S-5°N, for (a) the control simulation (CTL), (b) slab-ocean simulation (SOM), and (c) observations. Contours and shading are identical to Fig. 3.4.19. A 5 m s⁻¹ phase speed line (thick black) is also shown.

Fig. 3.4.21 (right). As in Fig. 3.4.20, but for a base longitude of 150°E.

better at capturing the rapid increase in the propagation speed of easterly anomalies across the Pacific Ocean as seen in the negative correlations of Fig. 3.4.21b. Overall, Figs. 3.4.20 and 3.4.21 indicate a stronger, more coherent relationship between convection and dynamics in the SOM relative to the CTL.

We also construct lag correlations based on an index timeseries at each longitude rather than the index timeseries at a single longitude as depicted in Figs. 3.4.20 and 3.4.21. Figures 3.4.22-3.4.25 display lag correlations of SST, U850, SLHF, and 925 hPa equivalent potential temperature $\theta_{e,925}$ (respectively) with a precipitation index at each longitude. As in Fig. 3.4.20, all variables are filtered to MJO time scales and meridion-

ally averaged. The plots in Figs. 3.4.22-3.4.25 are designed to illustrate phase differences between convection and other variables as the MJO propagates from the central Indian Ocean east to the Date Line. Lag correlations of precipitation and SST (Fig. 3.4.22) clearly exhibit the substantial differences between the CTL (panel a) and SOM (panel b) simulations. In nature, warm SSTs represented by positive lag correlations and dark gray shading lead MJO precipitation maxima by approximately 10 days in both the Indian and West Pacific regions (Fig. 3.4.22c; Kawamura 1988, Inness and Slingo 2003). Cool SSTs are observed to lag the heaviest rainfall by about one week. A strong resemblance to this

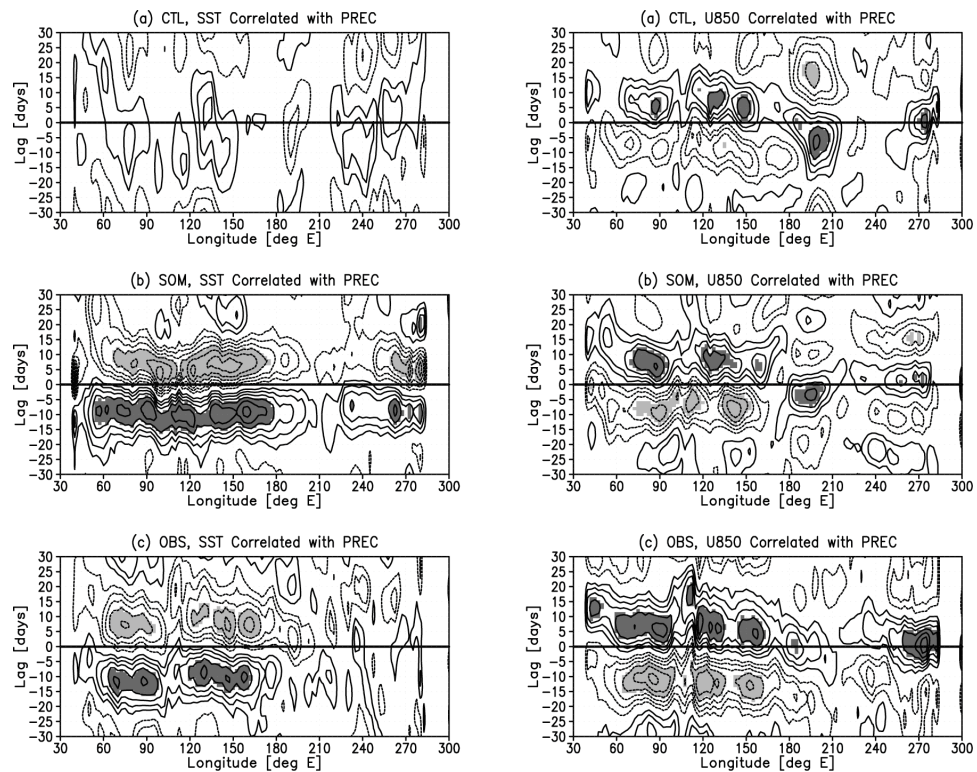


Fig. 3.4.22 (left). Lag correlation of 20-100-day filtered SST with 20-100-day filtered precipitation, averaged between 10°S-5°N, for (a) the control simulation (CTL), (b) slab-ocean simulation (SOM), and (c) observations. Contours and shading are identical to Fig. 3.4.19.

Fig. 3.4.23 (right). As in Fig.3.4.22, but for 20-100-day filtered 850 hPa zonal wind lag correlated with 20-100-day filtered precipitation.

pattern is seen in the SOM results (Fig. 3.4.22b) with the exception that the time between the leading maximum and trailing minimum correlations is shorter in the SOM relative to nature, particularly near the Maritime Continent where shallow oceanic mixed layer depths may allow more rapid cooling of SSTs. No significant correlations or coherent patterns between precipitation and SSTs are noted in the CTL simulation (Fig. 3.4.22a).

Lag correlations of U850 with precipitation (Fig. 3.4.23) show the phase relationship between MJO convection and dynamics. As MJO disturbances traverse the Indian and West Pacific Oceans, the rainfall maximum lags anomalous easterlies (negative correlations) by 1-2 weeks but leads anomalous westerlies (positive correlations) by 5-10 days (Fig. 3.4.23c; Woolnough et al. 2000). We note an interesting trend in the relationship between observed precipitation and the trailing westerlies. As convection initially develops but remains weak in the far western Indian Ocean, trailing westerlies are delayed more than 10 days following rainfall maxima. Convection and its associated equatorial Rossby wave gyres strengthen over the Indian Ocean, and the westerlies migrate closer to the precipitation maximum. The convection becomes disrupted over the Maritime Continent likely weakening the Rossby wave response, and the intense westerlies recede toward a later lag. With the reorganization of convection in the West Pacific, equatorial Rossby waves likely restrengthen and the trailing westerlies again migrate back toward the precipitation maximum, eventually overtaking it near the Date Line as the MJO convection and dynamics decouple. Additional discussions of the complex phase relationships between convection and winds can be found in several previous studies (e.g., Salby and Hendon 1994, Inness and Slingo 2003). Both the CTL and SOM in-

indicate a similar pattern of leading easterlies and trailing westerlies relative to precipitation (Figs. 3.4.23a,b, respectively). The migration of trailing westerlies toward the rainfall maximum is qualitatively depicted by both models as well. However, relative to the CTL, the SOM generally displays a more consistent and statistically significant easterly-westerly couplet, particularly in the Indian Ocean.

We present lag correlations between SLHF and precipitation in Figure 3.4.24. The interactions of convection, the mean state low-level winds, and perturbation low-level winds and SLHFs have a substantial impact on MJO structure and intensity (Salby

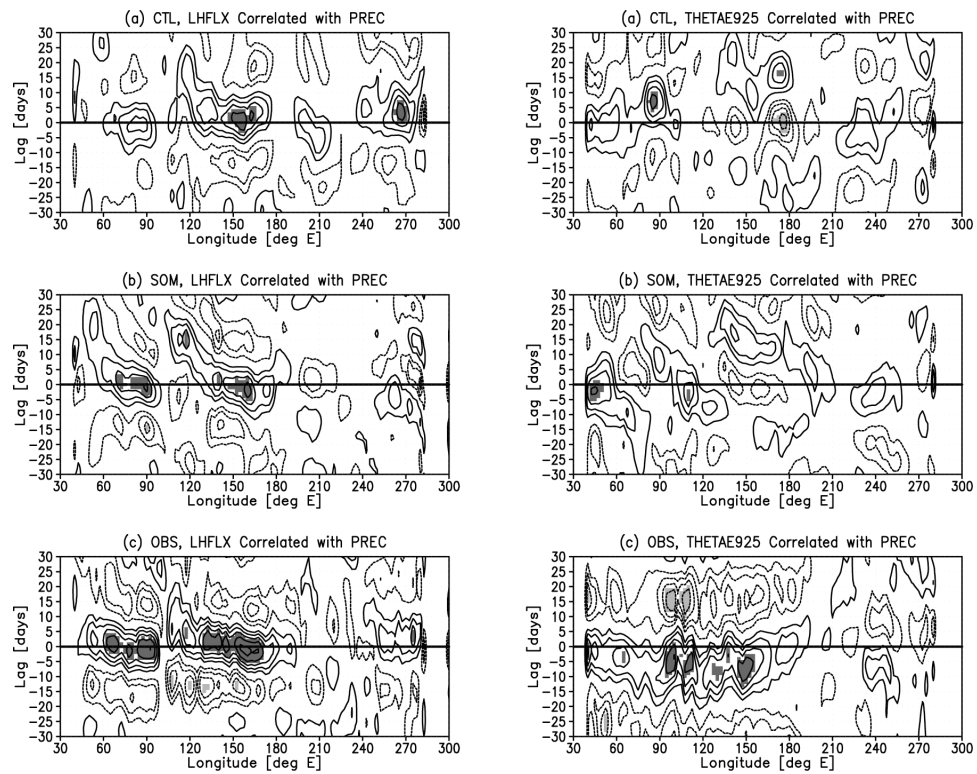


Fig. 3.4.24 (left). As in Fig.3.4.22, but for 20-100-day filtered surface latent heat flux lag correlated with 20-100-day filtered precipitation.

Fig. 3.4.25 (right). As in Fig. 3.4.22, but for 20-100-day filtered 925 hPa equivalent potential temperature lag correlated with 20-100-day filtered precipitation.

and Hendon 1994, Jones and Weare 1996). Correctly depicting such relationships in GCMs is critical for an accurate representation of the MJO (Inness et al. 2003, Zhang et al. 2006). The correlation fields of observed SLHF lag correlations are noisier, but it is still apparent that weaker evaporation precedes maximum precipitation and strong SLHFs by roughly two weeks in nature (Fig. 3.4.24c). There is also evidence that, like U850 (c.f. Fig. 3.4.23), trailing SLHF maxima (strong evaporation) tend to migrate toward the rainfall center and with time become nearly collocated with it. The SLHF depiction is very similar in the West Pacific between the CTL and SOM (Figs. 3.4.24a and b, respectively), but the SOM displays a much improved SLHF-rainfall relationship in the Indian Ocean. Additionally, the SOM even weakly captures the overtaking of the heavy precipitation centers by trailing SLHF maxima in both the Indian and West Pacific regions.

We display Fig. 3.4.25 to illustrate that, although the SP-CAM has a more accurate depiction of the MJO relative to many other GCMs that utilize conventional parameterizations (Kim et al. 2009), several key deficiencies related to the MJO still exist in the model. One such deficiency involves the phasing between MJO convection and low-level θ_e . Figure 3.4.25c shows that positive MJO-filtered $\theta_{e,925}$ anomalies lead rainfall maxima by 3-10 days in nature. Correlation values and their associated significance of the $\theta_{e,925}$ field are notably weaker than other analyzed variables (c.f. U850 in Fig. 3.4.23c), but we note the fairly robust and longitudinally extensive consistency of the pattern. Following deep convection, $\theta_{e,925}$ is reduced and reaches a minimum approximately 10-20 days after the peak in precipitation. Neither the CTL (Fig. 3.4.25a) nor the SOM (Fig. 3.4.25b) display a $\theta_{e,925}$ correlation similar to observations. The model results show

no pattern consistency across longitudes. In the East Indian Ocean, the CTL exhibits weak negative (positive) $\theta_{e,925}$ anomalies leading (following) heavy rainfall, which opposes observations in that region (Fig. 3.4.25c). Because the phasing between convection, SSTs, and SLHFs in the SOM (Figs. 3.4.22b and 3.4.24b) closely resembles the observed phasing, processes other than air-sea interaction are likely contributing to that model's $\theta_{e,925}$ bias. We analyze this model deficiency further and discuss potential sources of error in Section 3.5.c.

3.4.h. Lagged linear regression analysis

We primarily use the lagged linear regression technique to evaluate the space-time MJO structure in the CTL and SOM. We focus on this method rather than a composite analysis of many MJO events (c.f. Section 2.4) due to the limited time range of the SOM simulation (5 years). The reduced number of MJO events in the 5-yr period makes the assessment of statistically robust features more difficult. Despite this restriction, limited composite analysis results will be displayed in Section 3.4.i.

Figures 3.4.26-3.4.28 show the spatial patterns of OLR and 850 hPa winds from lag days -20 (a) through $+15$ (h) for observations, the CTL simulation, and the SOM simulation, respectively. These patterns represent lagged linear regressions of the selected fields onto a standardized precipitation index timeseries at 90°E . Filtered (20-100-day periods), meridionally averaged (10°S - 10°N), and standardized precipitation at 90°E defines the index upon which other 20-100-day filtered variables are regressed. As for all regression plots in this dissertation, the regressed data are scaled to a one standard devia-

OBSERVED OLR & 850 HPA WIND, 90E

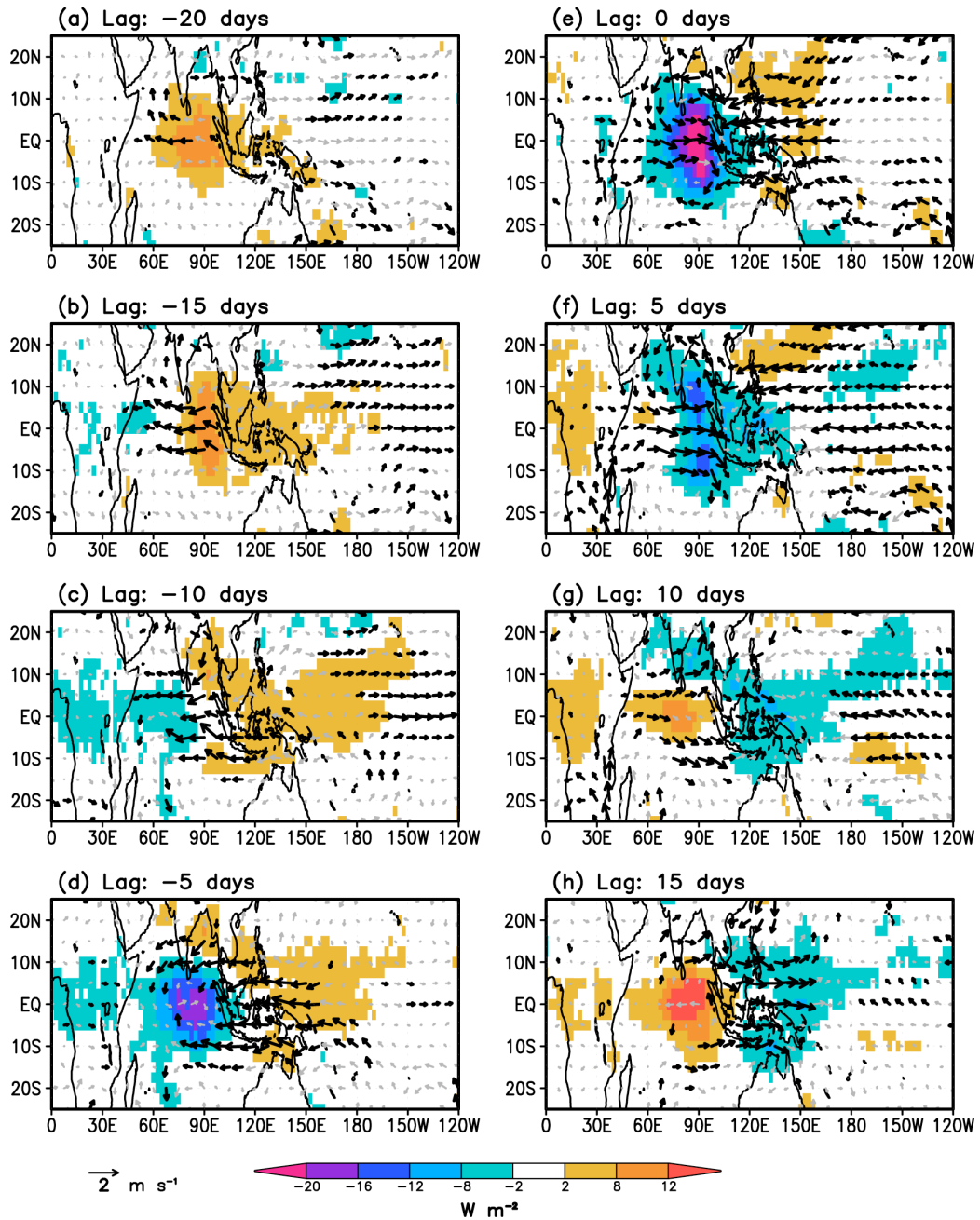


Fig. 3.4.26. Lag regressions of observed 20-100-day filtered OLR and 20-100-day filtered 850 hPa winds onto a base timeseries of 20-100-day filtered precipitation at 90°E. The base precipitation time series is averaged between 10°S-10°N. OLR values are colored and wind vectors emboldened where local regressions are significant above the 95% level. Reference wind vector appears at bottom left. Lag days relative to the maximum in the precipitation index are plotted from (a) -20 days to (h) +15 days.

tion value of the precipitation index. Two to three weeks prior to the MJO convective maximum at 90°E, positive anomalies of observed OLR exist over the Indian Ocean and

Maritime Continent with weak 850 hPa easterlies in the western and central Indian Ocean (Fig. 3.4.26). Over the next 20 days, negative OLR anomalies develop in the western In-

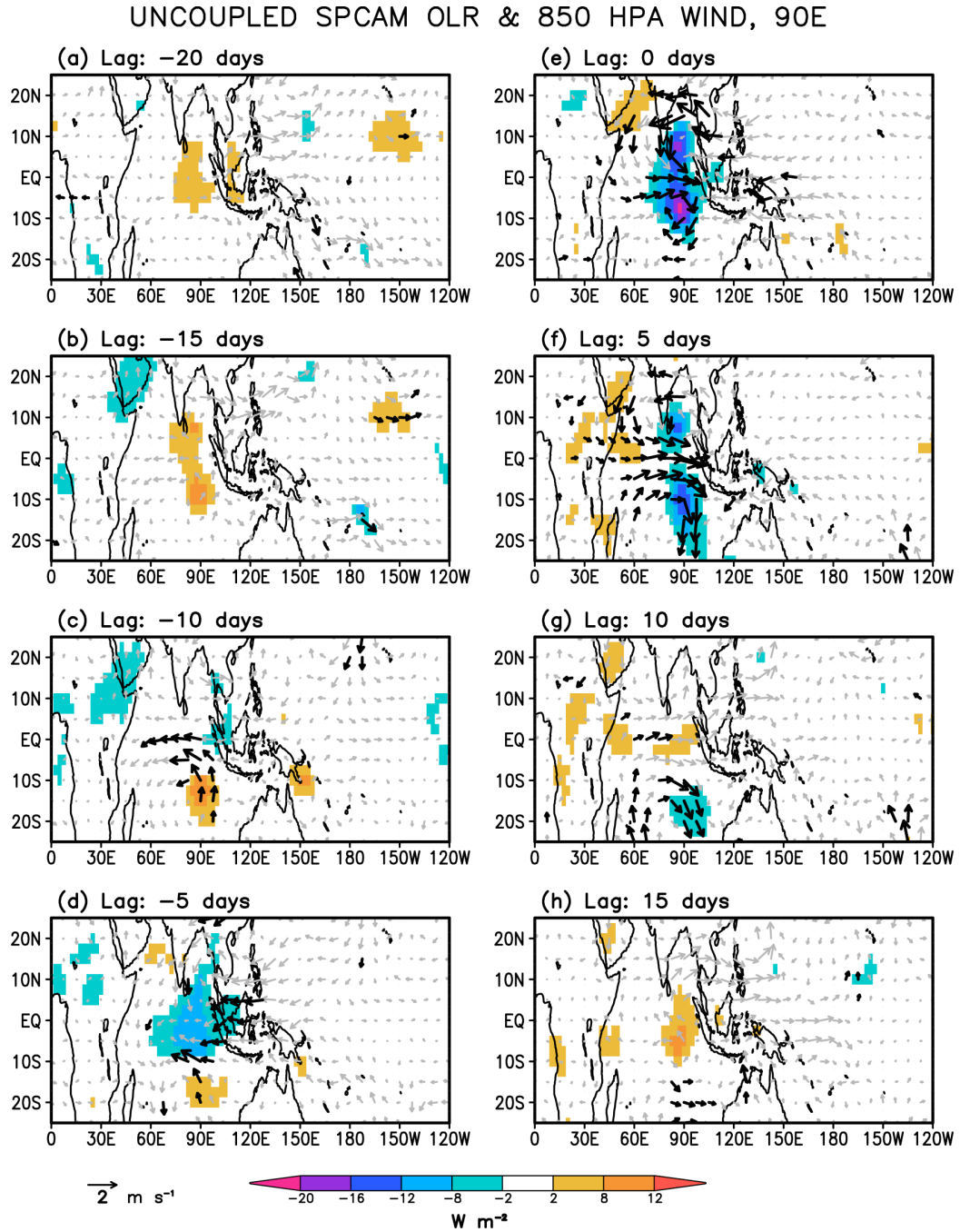


Fig. 3.4.27. As in Fig. 3.4.26, but for the control simulation (CTL).

dian Ocean and propagate to 90°E where they reach a minimum of about -25 W m^{-2} . This minimum OLR value is expected to be weaker than the typical -40 W m^{-2} departure computed using MJO composite analysis (e.g., Section 2.4, Kiladis et al. 2005) because the lag regression technique accounts for all variability on the 20-100-day time scale and likely includes weaker MJO events. Westerly anomalies develop and strengthen in the Indian Ocean between lags -5 and 0 as strong easterlies continue ahead of the convection over the Maritime Continent and West Pacific (Figs. 3.4.26d,e). By lag day $+15$ the main area of convection has moved to about 150°E and is nearly collocated with strong low-level westerlies, while positive OLR anomalies and weak easterlies have redeveloped over the Indian Ocean (Fig. 3.4.26h).

The CTL appears to have some difficulty replicating the observed features (Fig. 3.4.27). The propagation of convection across the Indian Ocean is less clear in the CTL, even when viewed on a daily lag basis (not shown). Rather than continuing to propagate eastward into the West Pacific, the main area of convection in the CTL is split along the Equator at 90°E between lag days -5 and 0 , a deficiency that is common in many GCMs (Zhang et al. 2006). The longitudinal span of significant leading easterly wind anomalies is lacking in the CTL as well, and almost no significant OLR anomalies develop or propagate into the West Pacific region (Fig. 3.4.27).

The SOM results (Fig. 3.4.28) show substantial improvement regarding many of the biases noted in the CTL. Significant 850 hPa easterlies develop much earlier in the Indian Ocean compared to the CTL (c.f. lag day -15 in Fig. 3.4.27 and 3.4.28). Eastward propagation of convection across the Indian Ocean is more apparent in the SOM relative

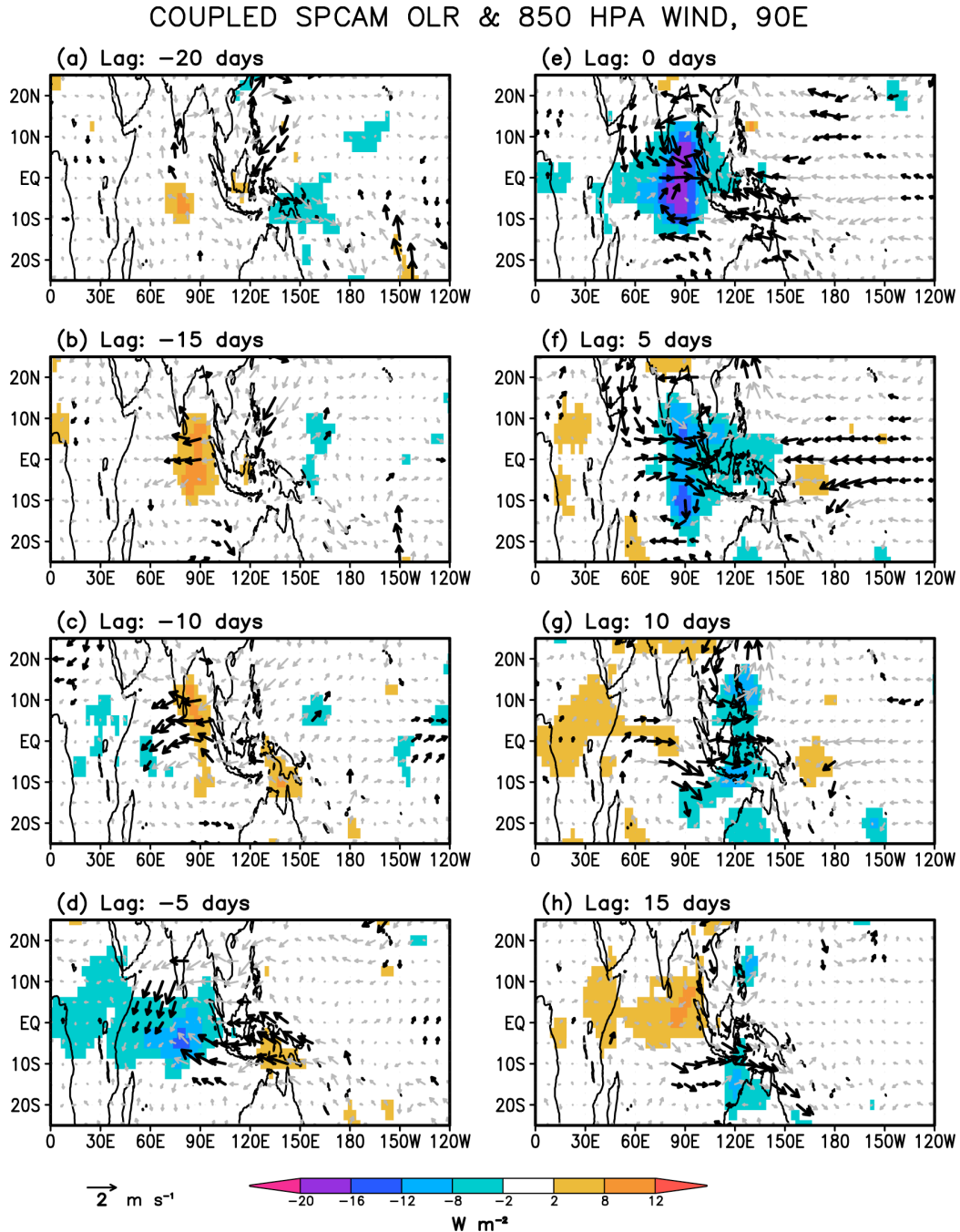


Fig. 3.4.28. As in Fig. 3.4.26, but for the slab-ocean simulation (SOM).

to the CTL, especially when viewed on a daily lag basis (not shown), and the convective center does not split into separate regions on each side of the Equator at 90°E. The MJO in the SOM exhibits a much broader longitudinal extent of significant OLR and low-level

wind anomalies that is lacking in the CTL. For example, comparison of the CTL and SOM on lag day +5 illustrates that significant negative OLR anomalies reach into the West Pacific and equatorial easterlies extend well into the Central Pacific in the SOM plot (Fig. 3.4.28f) while the corresponding CTL results (Fig. 3.4.27f) show no such structures.

Linear regressions of boundary layer average wind speed anomalies and SSTs for the observations, the CTL, the SOM are displayed in Figs. 3.4.29-3.4.31, respectively. The index timeseries at 90°E is identical to that used in the OLR-U850 analysis (e.g., Fig. 3.4.26). Between lag days -20 and -10 in Fig. 3.4.29, observed SSTs in the Indian Ocean are anomalously warm and boundary layer winds are light due to the superposition of low-level westerly mean flow (Fig. 3.4.1) and low-level easterly anomalies (Fig. 3.4.26). Observed West Pacific SSTs are generally cool during this period. Once convection develops around lag day -10, Indian Ocean SSTs begin to cool as boundary layer wind speeds strengthen and surface insolation decreases. Initial increases in boundary layer wind speeds appear to develop at about 10°S where the Kelvin wave response to convection in the central Indian Ocean drives low-level easterly anomalies (Fig. 3.4.26) that are coincident with a background easterly flow (Fig. 3.4.1). As convection moves into the eastern Indian Ocean, enhanced boundary layer winds are associated with Rossby wave-induced low-level westerly anomalies (Fig. 3.4.26) superimposed on a westerly mean state (Fig. 3.4.1). A clear SST dipole is observed between lag days 0 and +10, with cool (warm) ocean surface temperatures in the Indian (West Pacific) Ocean (Fig. 3.4.29). Indian Ocean SSTs reach a minimum about a week after peak convection at 90°E as strong

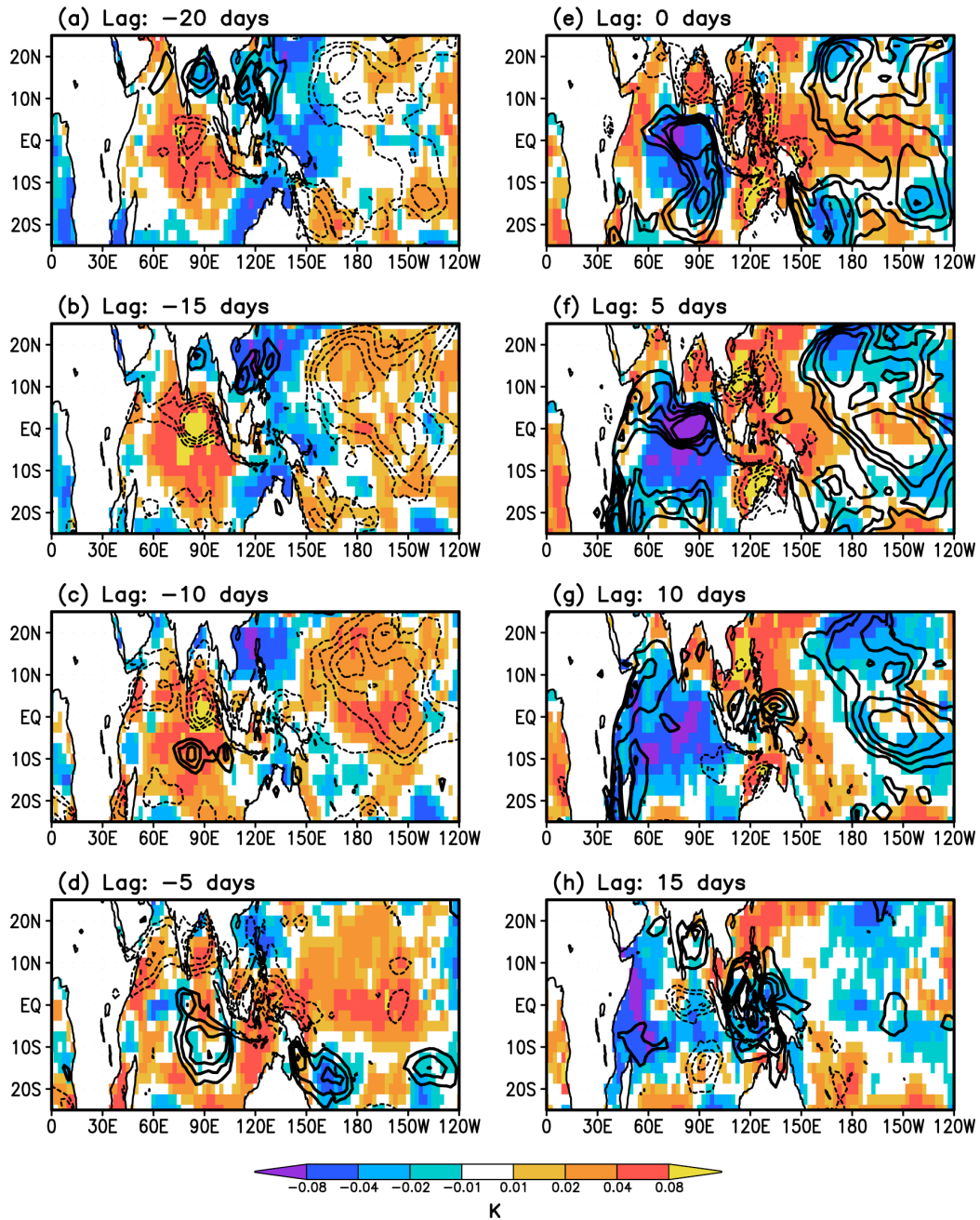
OBSERVED SST & $|\text{WIND}_{\text{BL}}|$, 90E

Fig. 3.4.29. Lag regressions of observed 20-100-day filtered SSTs (shaded) and 20-100-day filtered boundary layer averaged wind speed (contours) onto a base timeseries of 20-100-day filtered precipitation at 90°E. The base precipitation time series is averaged between 10°S-10°N. Contour interval is 0.1 m s⁻¹, starting at 0.2 m s⁻¹, and positive (negative) contours are solid (dashed). Wind speeds greater than approximately 0.3 m s⁻¹ are locally significant above the 95% level. No significance is assigned to SSTs due to their long decorrelation time scale. Lag days relative to the maximum in the precipitation index are plotted from (a) -20 days to (h) +15 days.

boundary westerlies begin to subside. As convection moves into the West Pacific at lag

day +15 (Fig. 3.4.29h), SSTs around the Maritime Continent are at their lowest while SST anomalies in the Indian Ocean return toward zero. The West Pacific convection drives low-level easterly anomalies linked to Kelvin wave dynamics to the east, and these

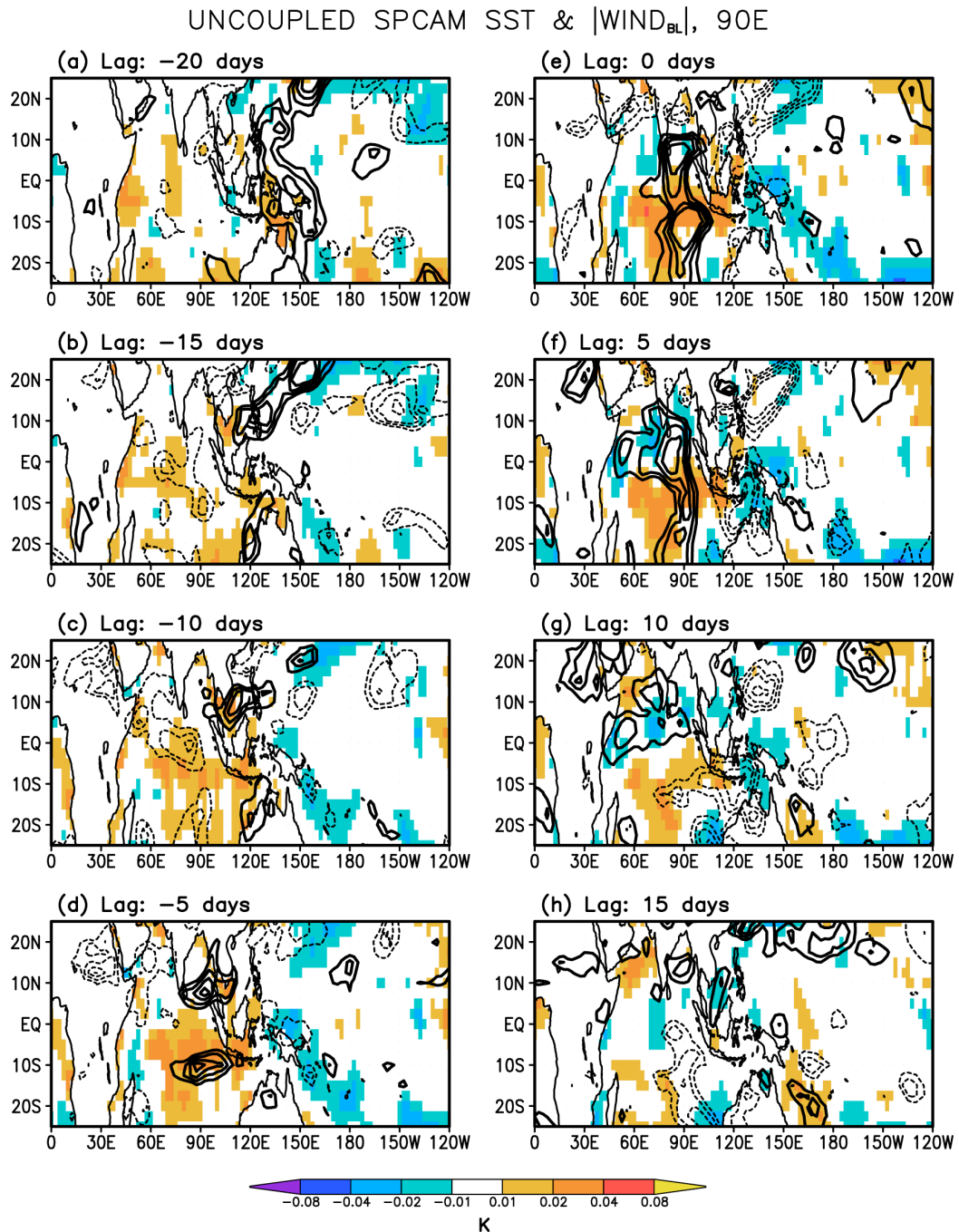


Fig. 3.4.30. As in Fig. 3.4.29, but for the control simulation (CTL).

easterly anomalies match an easterly mean state to increase boundary wind speeds and SLHFs and lower SSTs in the central Pacific. The interplay of mean and convectively-driven anomalous low-level winds and their impact on surface evaporation, SSTs, and the convection itself is an important component of the MJO (Inness and Slingo 2003, Zhang et al. 2006, Marshall et al. 2008), and Fig. 3.4.29 clearly illustrates these complexities.

The relationship between MJO convection, boundary layer wind speeds, and SSTs is much weaker in the CTL simulation (Fig. 3.4.30), consistent with the lag correlation results of Fig. 3.4.22. This result should not be surprising because SSTs in the CTL simulation are prescribed and so surface energy fluxes cannot affect the ocean surface conditions. Although boundary layer winds are light and SSTs are slightly warm in the Indian Ocean prior to the development of deep convection (lag days -20 to -10), SSTs are not relatively cooler during periods of increased boundary layer wind speeds following peak convective intensity at 90°E (c.f. SST patterns in Figs. 3.4.29f and 3.4.30f). The CTL also does not capture the development of relatively warm SSTs in the West Pacific Ocean ahead of MJO convection around lag days 0 to +5.

Substantially improved phasing of MJO convection, boundary layer wind speeds, and SSTs is exhibited by the SOM (Fig. 3.4.31). The pattern of anomalously weak boundary layer winds and warm SSTs in the Indian Ocean prior to the onset of MJO deep convection in the SOM (Fig. 3.4.31) is remarkably similar to the observed pattern (Fig. 3.4.29). As convective intensity peaks at 90°E on lag day 0 in the SOM, strengthened low-level westerlies increase SLHFs that quickly help to reduce Indian Ocean SSTs, as seen in nature. Easterly low-level wind anomalies (Fig. 3.4.28e,f) ahead of MJO convec-

COUPLED SPCAM SST & $|\text{WIND}_{\text{BL}}|$, 90E

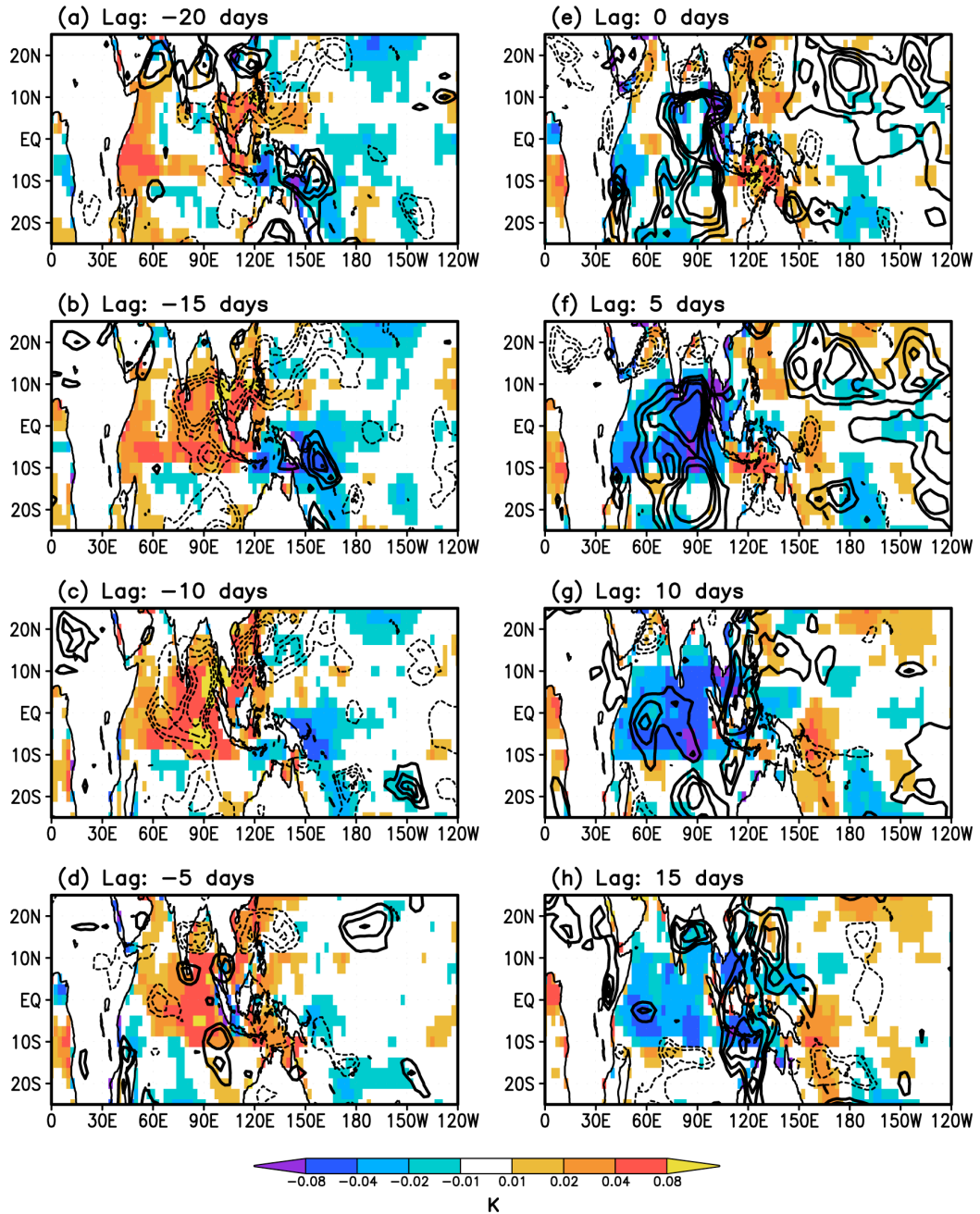


Fig. 3.4.31. As in Fig. 3.4.29, but for the slab-ocean simulation (SOM).

tion on lag days 0 and +5 weaken boundary layer winds slightly in the West Pacific and allow SSTs to warm moderately in that region (Fig. 3.4.31e,f). The pattern of warmer West Pacific SSTs ahead of MJO convection in the SOM illustrates a substantial im-

provement in the phasing of convection and SSTs in the SP-CAM with the implementation of the slab ocean model. The SOM more accurately captures the complex interactions between the mean state and anomalous wind speeds, SSTs, and MJO convection.

Fluctuations in the amount of downwelling shortwave radiation at the surface are related to changes in cloud coverage and thickness and have an important impact on the net surface energy budget and ocean surface temperatures (Lau and Sui 1997). Because the MJO modulates cloud characteristics on intraseasonal time scales (Johnson 1995), the assessment and accurate depiction of downwelling surface shortwave radiation is essential. Additionally, surface pressure fluctuations are linked to convergent and divergent flows in the Tropics. In the lower troposphere, these different flow patterns can cause moisture to accumulate or become diluted within the boundary layer and are therefore related to convective instability (Wang and Xie 1998). We present lag regressions of anomalous downwelling surface shortwave radiation (Q_{sw} ; color shading) and surface pressure (line contours) in Figures 3.4.32-3.4.34. We use the same precipitation-based index in these figures that we employed in all previous lag regression plots. All colors correspond to regression values that are greater than the 95% significance level locally. Pressure contours greater than about $|25 \text{ Pa}|$ are above the 95% significance level.

Two to three weeks prior to the peak of MJO convection at 90°E , observed Q_{sw} is strongly positive in the eastern Indian Ocean and surface pressures are above normal across both basins (Figs. 3.4.32a,b). Between lag days -10 and -5 , organized convection develops and moves eastward across the Indian Ocean, reducing Q_{sw} and surface pressures in that region (Figs. 3.4.32c,d). The minimum in Q_{sw} is collocated with the convec-

OBSERVED SFC Q_{sw} & SFC PRES, 90E

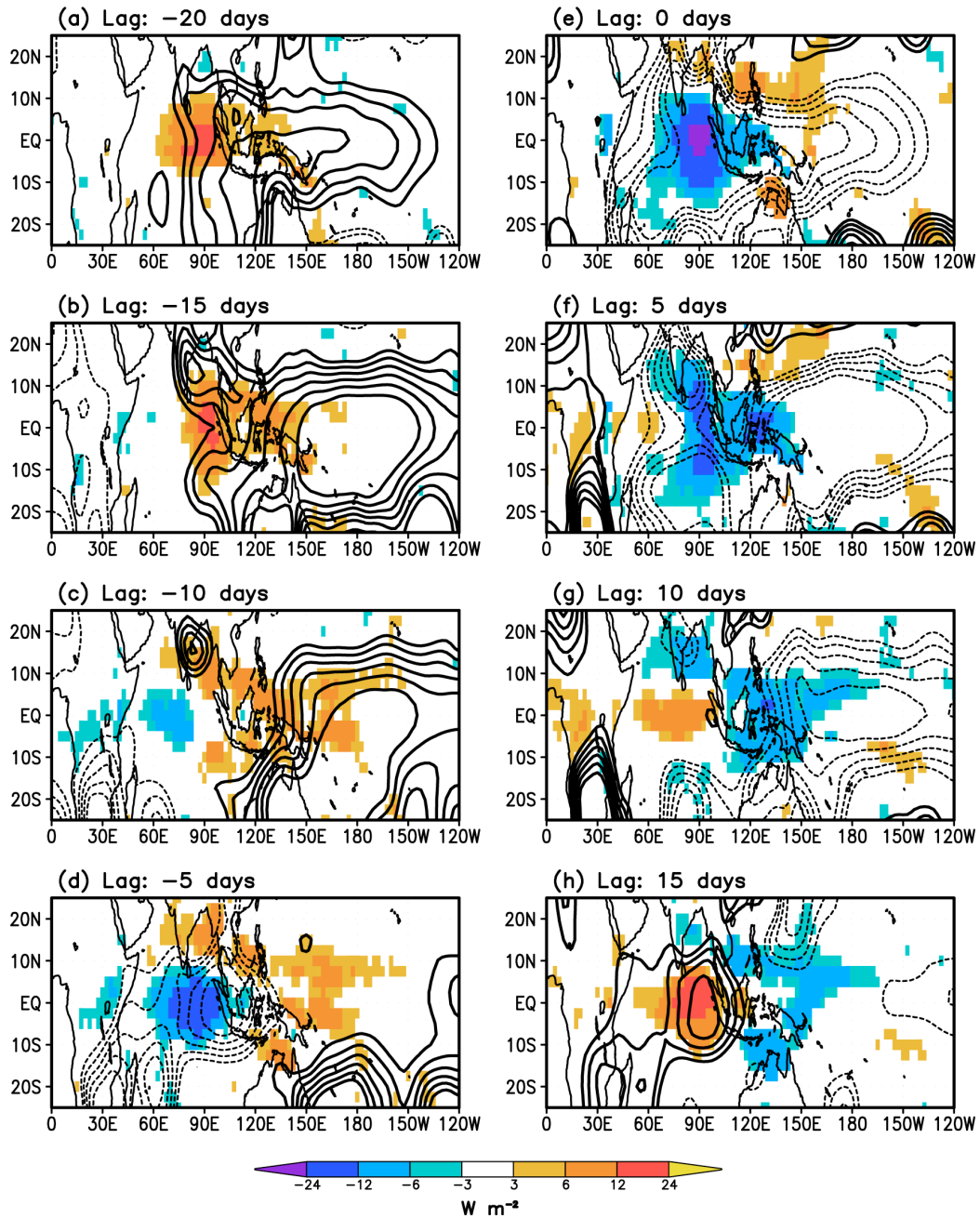


Fig. 3.4.32. Lag regressions of observed 20-100-day filtered downward surface shortwave radiation (shaded) and 20-100-day filtered surface air pressure onto a base timeseries of 20-100-day filtered precipitation at 90°E. The base precipitation time series is averaged between 10°S-10°N. Pressure contour interval is 5 Pa, starting at 15 Pa, and positive (negative) contours are solid (dashed). Near-equatorial pressure contours greater than $\sim|25 Pa|$ are locally significant above the 95% level. Radiation values are colored where local regressions are significant above the 95% level. Lag days relative to the maximum in the precipitation index are plotted from (a) -20 days to (h) +15 days.

tion maximum on lag day 0 at 90°E, but negative Q_{sw} anomalies are observed over a wide

longitudinal range from the central Indian Ocean into the West Pacific at this time. Surface pressure decreases rapidly to the east of the main convective center due to the Kelvin wave response (Heckley and Gill 1984). As abundant cloud cover and heavy MJO rains enter into the West Pacific, Q_{sw} becomes positive again in the Indian Ocean around lag day +10 as skies clear (Fig. 3.4.32g). The return to positive Q_{sw} anomalies in the Indian Ocean leads positive SST (Fig. 3.4.29) and surface pressure anomalies by several days. The interactions among radiation, convection, and the dynamical response (e.g., in the form of surface pressure fluctuations and the implied low-level convergence) are critical elements of the MJO and have been shown to impact its structure (Woolnough et al. 2000, Marshall et al. 2008).

The CTL simulation captures the main radiative and surface pressure features but has problems accurately depicting the longitudinal extent and propagation of the anomalies (Fig. 3.4.33). Positive Q_{sw} values are noted over the eastern Indian Ocean before deep convective development (Figs. 3.4.33a,b). However, the eastward propagation of negative Q_{sw} anomalies into the 90°E region is not clear and reductions in Q_{sw} appear to develop *in situ* (c.f. Figs. 3.4.33b,c,d). In addition, the axis of surface pressure minimum that extends well into the Pacific basin on lag days 0 and +5 in observations (Figs. 3.4.32e,f) is absent in the CTL simulation (Figs. 3.4.33e,f), hinting that low-level convergence ahead of MJO deep convection is also spatially limited. The phasing of positive Q_{sw} and surface pressure anomalies following deep MJO convection in the East Indian Ocean appears to be captured well by the uncoupled model, however (Figs. 3.4.33g,h).

More realistic behavior of intraseasonal Q_{sw} and surface pressure anomalies is noted in the SOM (Fig. 3.4.34). Between lag days -10 and -5 , a developing area of negative Q_{sw} anomalies propagates across the Indian Ocean toward 90°E (Figs. 3.4.34c,d).

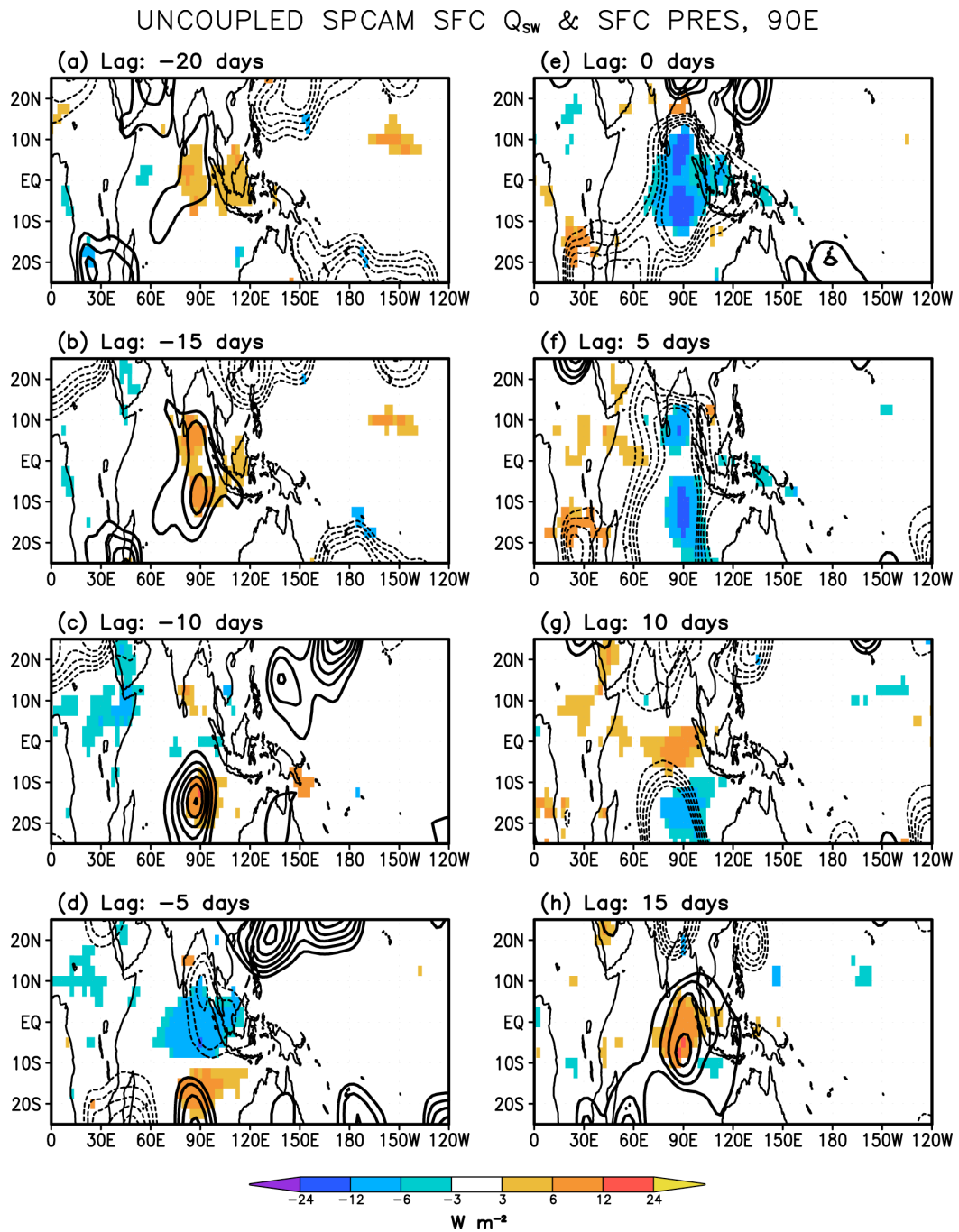


Fig. 3.4.33. As in Fig. 3.4.32, but for the control simulation (CTL).

Similar to observations, the minimum in Q_{sw} on lag day 0 in the SOM simulation is fairly consolidated around the Equator, and a coherent region of negative Q_{sw} values covers the longitudes 60°E-140°E (Fig. 3.4.34e). The SOM results show a substantial improvement

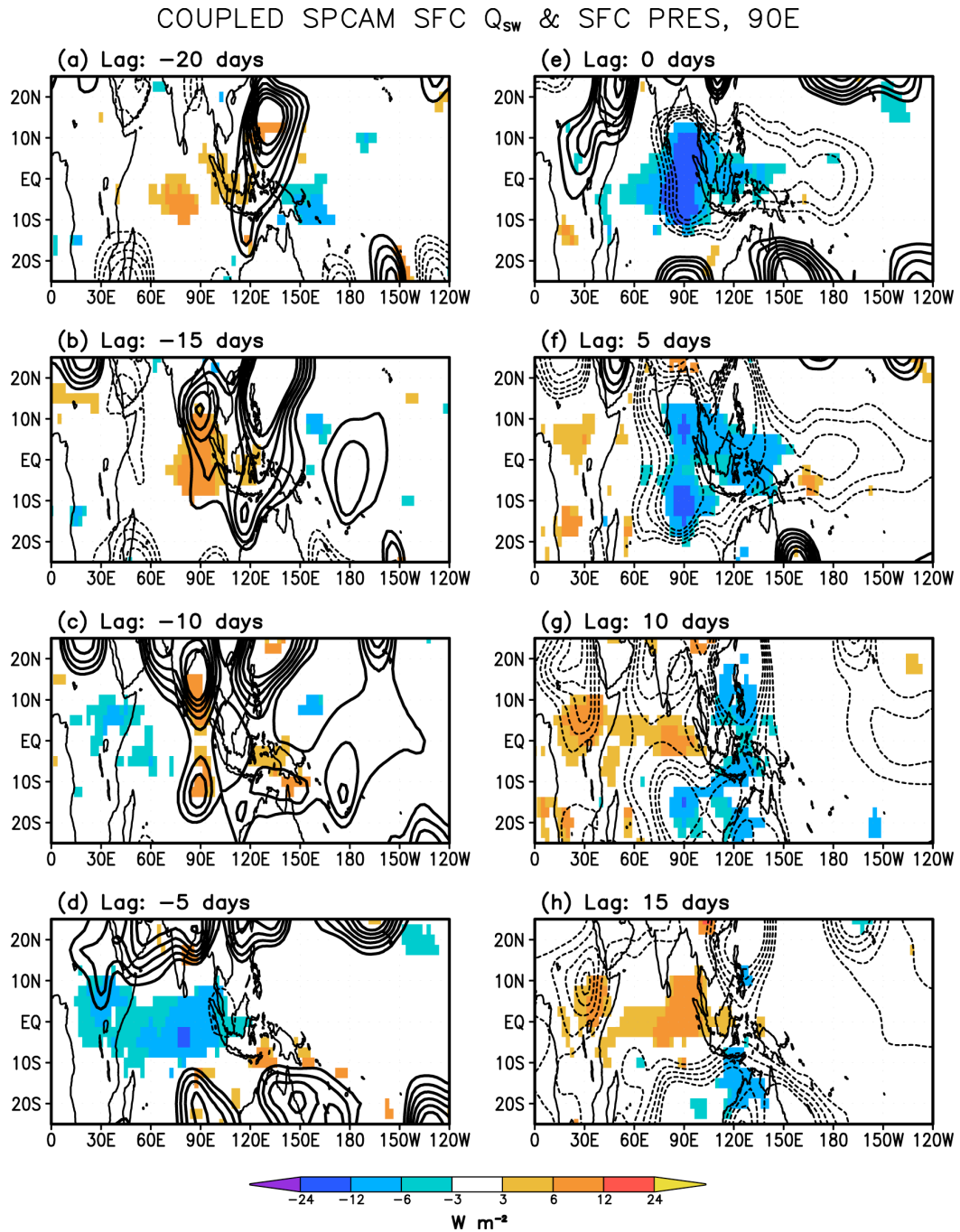


Fig. 3.4.34. As in Fig. 3.4.32, but for the slab-ocean simulation (SOM).

in the depiction of surface pressure falls well ahead (east) of deep convection as it exits the Indian Ocean and crosses the Maritime Continent (c.f. Figs. 3.4.34e,f with 3.4.33e,f). These improvements suggest that the processes linking radiation, convection, and the dynamical response to convection (here, in the form of surface pressure fluctuations and the implied low-level convergence) are more realistic in the coupled simulation.

Linear regressions of surface latent heat fluxes (SLHF) and boundary layer averaged (BL) winds for the observations, the CTL simulation, and the SOM simulation are displayed in Figs. 3.4.35-3.4.37, respectively. The BL mean is found by averaging winds within the 1000-925 hPa layer. The SLHF and wind fields are regressed onto the same precipitation index that we used in previous lag regression plots. Only lag days that capture the salient features of SLHF and BL wind behavior in the context of the MJO are shown. Seventeen days before the MJO reaches its peak intensity at 90°E, the Indian Ocean atmosphere is dry and stable in the wake of the previous MJO disturbance. Anomalous easterly BL winds and weak SLHFs dominate the Indian Ocean at this time in nature (Fig. 3.4.35a). Equatorial SLHFs remain weak at lag day -12 even as anomalous BL easterlies strengthen because these easterly anomalies generally occur in a region of mean low-level westerlies (see Fig. 3.4.1). The weak SLHFs (Fig. 3.4.35b) and strong surface Q_{sw} (Fig. 3.4.32b) contribute to the warming of SSTs (Fig. 3.4.29b), atmospheric destabilization, and the subsequent development of convection (Figs. 3.4.26b,c) in the Indian Ocean one to two weeks prior to heaviest MJO rainfall in the eastern Indian Ocean. As convective heating in the central and eastern Indian Ocean intensifies around

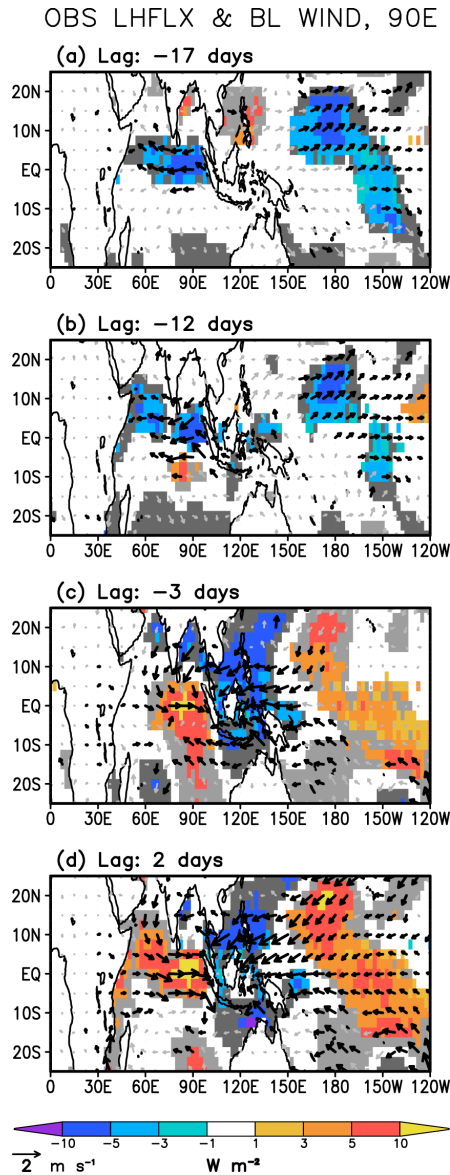


Fig. 3.4.35. Lag regressions of observed 20-100-day filtered surface latent heat fluxes (shaded) and 20-100-day filtered boundary layer averaged winds onto a base timeseries of 20-100-day filtered precipitation at 90°E. The base precipitation time series is averaged between 10°S-10°N. Flux values are colored and wind vectors emboldened where local regressions are significant above the 95% level. Additional flux values greater than 2 $W m^{-2}$ (less than -2 $W m^{-2}$) are shaded light (dark) gray to help viewing. Reference wind vector appears at bottom left. Lag days relative to the maximum in the rain index are plotted from (a) -17 days to (d) +2 days.

lag day -3, the associated Rossby wave response generates BL westerly anomalies that, when combined with a weak mean westerly flow at low levels, rapidly increase BL wind speeds and SLHFs (Fig. 3.4.35c). With heavy MJO rains at 90°E, BL easterly wind anomalies to the east extend well into the Pacific Ocean and correspond to negative SLHF anomalies (where BL mean winds are westerly) and positive SLHF anomalies (where BL mean winds are easterly).

Similar but weaker patterns of SLHF and BL winds are noted in the CTL and SOM results (Figs. 3.4.36 and 3.4.37). Several differences between the two versions of the SP-CAM exist, however. The SOM more closely resembles the observed

pattern of SLHFs and BL wind anomalies in the Indian Ocean on lag day -17 (c.f. panel a

in Figs. 3.4.35-3.4.37). Anomalous easterly BL winds and negative SLHF perturbations are significant in the SOM, but these features are much weaker in the CTL. A more robust signal of BL easterlies (westerlies) and negative (positive) departures of SLHF in the SOM is also seen in the Indian Ocean on lag day -12 (-3) compared to the CTL (c.f. Figs. 3.4.36b,c and 3.4.37b,c). The large zonal scale of significant BL wind perturbations displayed in the observational results (Fig. 3.4.35d), particularly the signal of BL easterlies extending well into the Pacific, is matched reasonably well in the SOM results but nearly absent in the CTL (c.f., Figs. 3.4.36d and 3.4.37d).

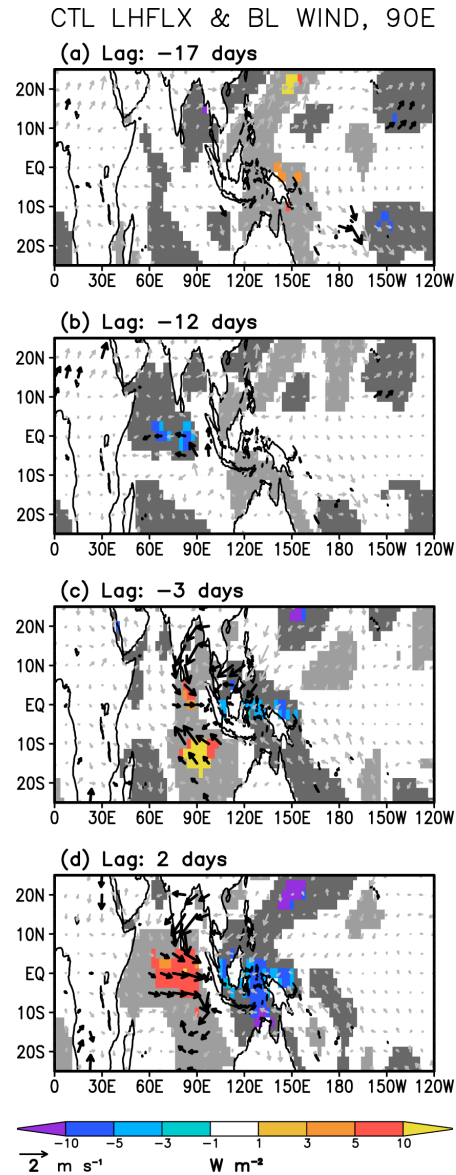


Fig. 3.4.36. As in Fig. 3.4.35, but for the control simulation (CTL).

We examine the vertical structure of the intraseasonal convective disturbances using longitude-pressure cross sections of lag linear regressions (Figs. 3.4.38-3.4.42). To construct such plots we regress the selected variable onto the same precipitation index used to generate the longitude-latitude regression composites—that is, 20-100-day fil-

tered precipitation anomalies that have been averaged between 10°S-10°N at either 90°E

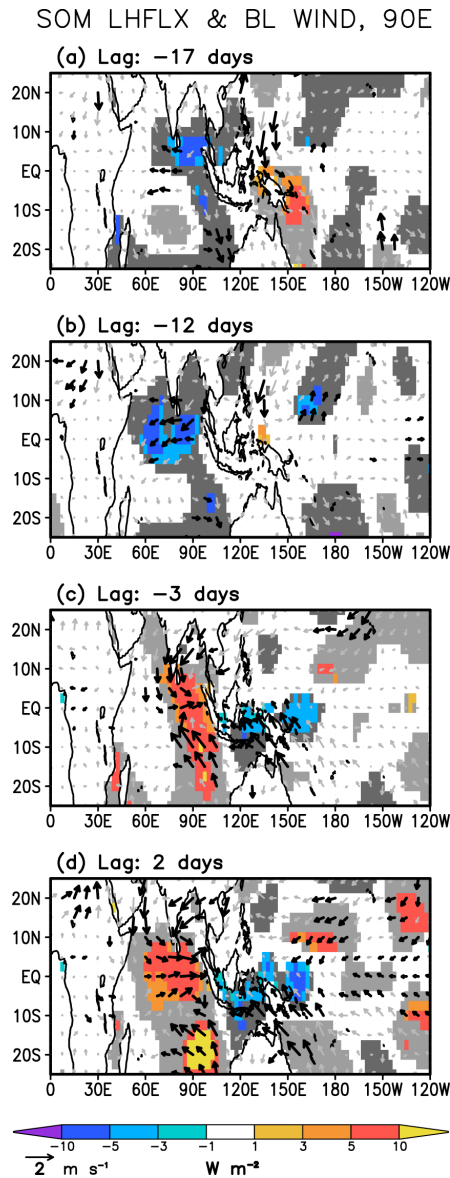


Fig. 3.4.37. As in Fig. 3.4.35, but for the slab-ocean simulation (SOM).

or 150°E and then standardized. All regressed variables are 20-100-day filtered anomalies and are averaged between 5°S-5°N. The regressed fields correspond to a zero lag, when maxima in MJO precipitation occur at 90°E (or 150°E, where indicated). When observed MJO precipitation is at its peak intensity in the eastern Indian Ocean (marked by a thin vertical line at 90°E in Fig. 3.4.38c), there is strong convergence in a deep layer from the surface to 400 hPa and vigorous divergence aloft coincident with the deep convection. Ahead of the disturbance, consistent low-level convergence is observed eastward to ~150°E with weak divergence above.

The observed convergence-divergence structure is tilted westward with height such that maximum convergence occurs in the lower troposphere before (east of) deep convection

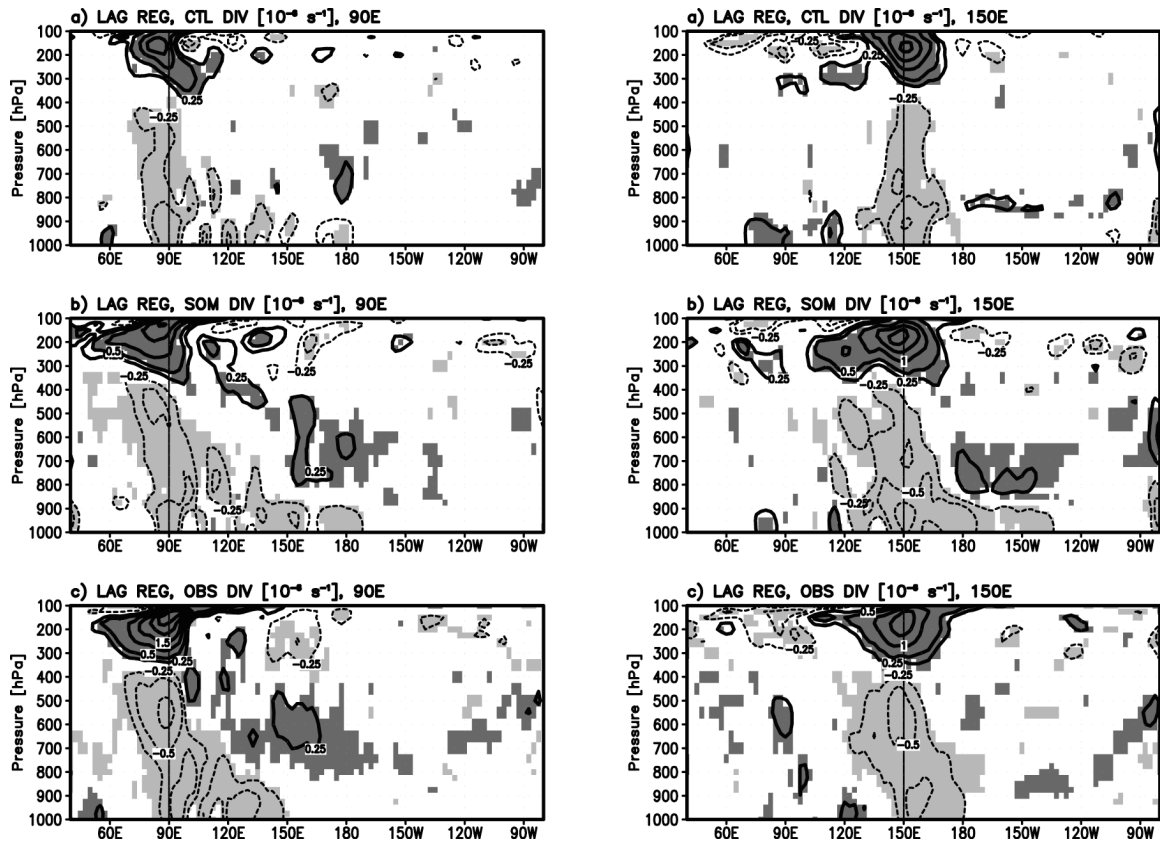


Fig. 3.4.38 (left). Lagged linear regressions of 20-100-day filtered anomalous horizontal divergence onto an index timeseries of 20-100-day filtered anomalous precipitation at 90°E for (a) the control simulation (CTL), (b) slab-ocean simulation (SOM), and (c) observations (OBS). The precipitation index is averaged between 10°S-10°N, and the regressed fields are averaged between 5°S-5°N. Solid (dashed) contours correspond to positive (negative) regression values, and dark (light) gray shading is applied where regression values are statistically significant above the 95% level. Thin vertical lines mark the longitude of the precipitation index. The contour interval is $0.5 \times 10^{-6} \text{ s}^{-1}$, with the first positive (negative) contour $+0.25 \times 10^{-6} \text{ s}^{-1}$ ($-0.25 \times 10^{-6} \text{ s}^{-1}$), and no zero contour is drawn.

Fig. 3.4.39 (right). As in Fig. 3.4.38, but for the precipitation index timeseries at 150°E.

and is gradually displaced upwards as the main rainfall center approaches. This tilted structure represents a deepening of the convective layer, the transition from shallow cumuli to congesti to cumulonimbi (Johnson et al. 1999), and the preconditioning of the free troposphere (Kemball-Cook and Weare 2001). The CTL and SOM capture the general pattern of low-level convergence leading deep-layer convergence, but the SOM shows some improvement in the signal (Figs. 3.4.38a,b). Compared to the CTL, the

SOM exhibits a more robust low-level convergence pattern over the Maritime Continent ($\sim 100^\circ\text{-}130^\circ\text{E}$) and clearer divergence signal (dark shading) above the convergent layer. Additionally, the magnitude of mid-tropospheric convergence at 90°E is closer to the observed value. When MJO convection is centered in the West Pacific Ocean at 150°E (Fig. 3.4.39c), the main area of convergence clearly tilts westward with height. Although the SOM overestimates boundary layer convergence east of the Date Line (Fig. 3.4.39b), the pattern of convergence in that model displays a coherent tilt that is lacking in the CTL profile (Fig. 3.4.39a). Leading boundary layer convergence has been shown to play a fundamental role in the maintenance and realistic propagation of the MJO, and correctly simulating this feature contributes toward an improved depiction of the MJO in several GCMs (Wang and Xie 1998, Waliser et al. 1999, Kemball-Cook et al. 2002, Zhang et al. 2006).

Cross sections of regressed convective heating rate Q_1 highlight the wider longitudinal span of MJO thermodynamic features in the SOM relative to the CTL (Figs. 3.4.40 and 3.4.41). The observed Q_1 cross section associated with maximum MJO rainfall at 90°E indicates shallow convective heating below 700 hPa and (radiative) cooling aloft at the leading (eastern) edge of the disturbance ($\sim 150^\circ\text{E}$; Fig. 3.4.40c). The low-level heating reflects the presence of shallow cumuli which warm the lower troposphere while eroding the dry middle troposphere, preconditioning the atmosphere for future deep convection (Kemball-Cook and Weare 2001, Benedict and Randall 2007). The maximum in convective heating progresses upwards toward the west, reaching 600 hPa near 120°E (Fig. 3.4.40c). Over the Maritime Continent, the MJO heating signal is comparatively

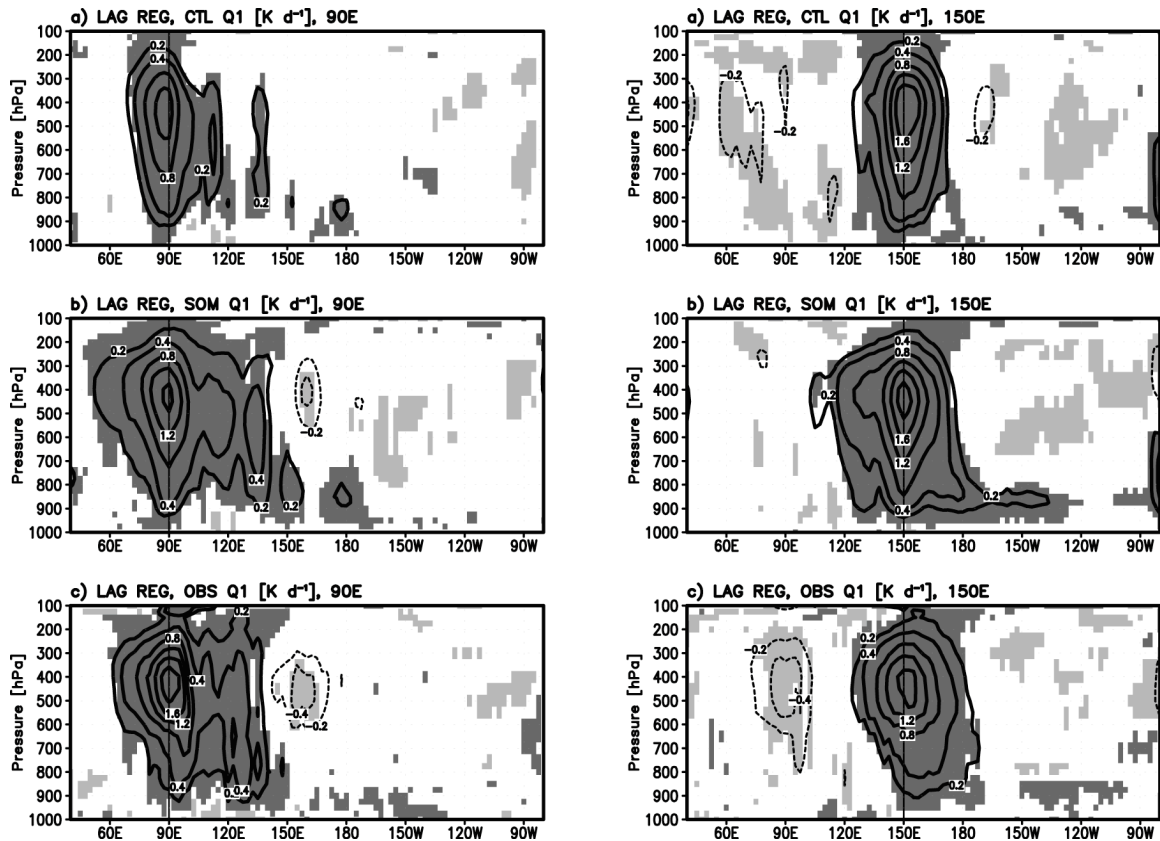


Fig. 3.4.40 (left). As in Fig. 3.4.38, but for 20-100-day filtered anomalous convective heating regressed onto the precipitation index at 90°E. The contour interval is 0.8 K d⁻¹, with the first positive (negative) contour +0.2 K d⁻¹ (-0.2 K d⁻¹), and no zero contour is drawn.

Fig. 3.4.41 (right). As in Fig. 3.4.40, but for the precipitation index timeseries at 150°E.

weak. This may be due to the more isolated nature of cumulonimbi in this region of the MJO disturbance which would dilute the heating signal over a GCM grid cell. The weakened signal also likely reflects the disruption of the 20-100-day disturbance due to strong diurnal heating of Maritime Continent land masses (Inness and Slingo 2006). The strongest deep convective heating is coincident with maximum precipitation, with a peak value of 2.1 K d⁻¹ near 450 hPa (Fig. 3.4.40c). Less intense but distinct convective heating above 600 hPa extends westward to nearly 60°E.

The pattern and peak magnitude of MJO Q_1 in the SOM simulation resembles nature more closely than the CTL (Fig. 3.4.40). The SOM exhibits evidence of the shallow-to-deep heating profile between 130°-150°E, including the mid-tropospheric cooling above the shallow heating; consistent but weak heating between 100°-130°E; more robust deep heating at 90°E; and an improved signal in the trailing upper-level heating into the western Indian Ocean (Fig. 3.4.40b). All of these features are weaker or absent in the CTL simulations (Fig. 3.4.40a).

When MJO precipitation is a maximum in the West Pacific (thin vertical lines in Fig. 3.4.41), the tilted heating structure manifested by leading shallow heating and trailing upper-level heating is again seen in the observed field (Fig. 3.4.41c). Negative Q_1 anomalies exist over the Indian Ocean and denote radiative cooling of the convectively suppressed MJO phase. The SOM exhibits improved tilting of the convective heating signal relative to the CTL, particularly in the depiction of shallow heating near 180° (Fig. 3.4.41b). However, we note that several biases in the convective heating cross section of the SOM simulation exist as well. The SOM has a maximum mid-tropospheric heating rate that is greater than both the CTL and observed values (Fig. 3.4.41b). Where low-level convective heating anomalies are near zero or slightly negative immediately to the west of the MJO rainfall center in nature (Fig. 3.4.41c), the CTL has weakly positive heating and the SOM has robust heating in that region (130°-140°E; Figs. 3.4.41a,b). It is unclear exactly why the SOM low-level heating bias in the MJO wake is worse than the CTL. The prolonged persistence of low-level convective heating is associated with a redevelopment of positive boundary layer θ_e anomalies and will be the focus of discus-

sion in Section 3.5.c. Additionally, the region of negative Q_1 anomalies over the Indian Ocean is weaker and displaced westward in the CTL compared to observations, and is entirely absent in the SOM. Overall, the SOM displays an improved MJO convective heating signal in the Indian Ocean region and an improved tilted structure in the West Pacific compared to the CTL, but overestimates the peak heating rate in that region.

Lag regressed specific humidity profiles corresponding to an MJO convective center in the East Indian Ocean are displayed in Fig. 3.4.42. A similar tilted structure as seen in the convective heating cross sections is also observed in the humidity profiles. In

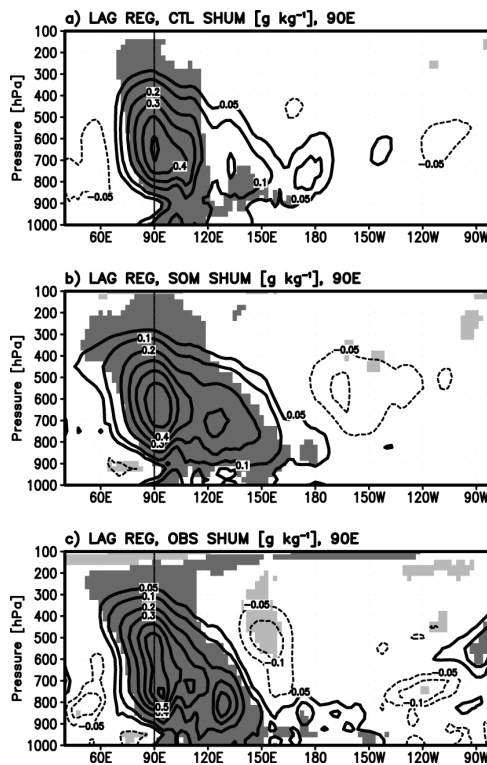


Fig. 3.4.42. As in Fig. 3.4.38, but for 20-100-day filtered anomalous specific humidity regressed onto the precipitation index at 90°E. The contour interval is 0.1 g kg⁻¹, with the first positive (negative) contour +0.05 g kg⁻¹ (-0.05 g kg⁻¹), and no zero contour is drawn.

nature (Fig. 3.4.42c), the atmosphere is initially moistened within the boundary layer well east of the main convective center as the middle and upper troposphere remain anomalously dry. Closer to the rain center, positive specific humidity anomalies gradually extend upward as detrained vapor and liquid evaporation from deepening cumulus clouds moisten the middle troposphere. Moisture anomalies peak over a deep layer just to the east of heaviest rainfall. In the wake of the MJO disturbance, drying occurs

first within the boundary layer and later in the lower and middle troposphere as moisture in the form of cirrus clouds lingers aloft (Fig. 3.4.42c).

Both the CTL and SOM capture the tilted moisture structure, but the SOM has a more robust signal of low-level moistening leading the MJO convective center, particularly east of 120°E (Figs. 3.4.42a,b). The magnitude of peak specific humidity near 90°E is greater than that seen in the CTL and closer to the observed value. Additionally, an improved signal of boundary layer drying and lingering moisture aloft is noted in the SOM results relative to the CTL.

3.4.i. Composite analysis of filtered fields

We average together several individual MJO disturbances to make a single, representative event. To locate the disturbances, we first compute anomalies of the data (departures from the smoothed calendar-day mean) and then apply a spectral filter that retains only positive zonal wavenumbers 1-6, representing eastward-propagating waves, and periods of 20-100 days. We meridionally average the MJO-filtered data from 12.5°S-12.5°N. MJO disturbances are selected based on the following thresholds applied to the full timeseries of meridionally averaged and MJO-filtered precipitation at a chosen longitude: (1) the precipitation must exceed one standard deviation for 10 or more consecutive days, and (2) the precipitation must exceed two standard deviations at any point during the 10+ day event. We then visually inspect each disturbance using longitude-time plots of unfiltered precipitation to ensure that the selected disturbances show com-

mon MJO features. For each event, the day of precipitation maximum defines the zero lag day upon which other variables are composited.

Composite time-height cross sections of MJO events based on a precipitation timeseries at 90°E are displayed in Fig. 3.4.43 for observations (top row), the CTL (second row), the SOM (third row), and the SOM–CTL difference (bottom row). Positive (negative) contours are solid (dashed) and labeled, with the zero contour solid and thicker. Dark (light) shading corresponds to composited values that are 95% significant based on a zero-anomaly null hypothesis. The composites shown in Fig. 3.4.43 are based on 10 (10, 11) MJO events for the observations (CTL, SOM). Plots of filtered and composited horizontal divergence anomalies [i.e., $(\partial u/\partial x + \partial v/\partial y)'$] for MJO disturbances in the eastern Indian Ocean indicate a tilted structure with height in the observations and simulations such that low-level convergence leads upper-level convergence (Fig. 3.4.43). In nature below 300 hPa, the convergence signal has a primary maximum exceeding $-0.6 \times 10^{-6} \text{ s}^{-1}$ at 550 hPa on lag day 0 and a secondary maximum near the boundary layer at approximately lag day -4 . The lower tropospheric-upper tropospheric couplet of convergence and divergence around lag day 0 is too weak in the CTL but stronger and closer to the observed intensity in the SOM (Fig. 3.4.43, second and third rows of the left column). Additionally, the low-level signal of convergence during lag days -5 to 0 and divergence during lag days $+5$ to $+20$ is more robust in the SOM compared to the CTL as evidenced by the difference plot (Fig. 3.4.43, bottom row of left column).

An increased amplitude of the composited specific humidity signal in the SOM is also seen (Fig. 3.4.43 middle column). The weaker CTL composite signal indicates that

positive moisture anomalies develop simultaneously from the surface to 700 hPa around lag day -10 , while in observations and the SOM the onset of moistening occurs first below about 800 hPa. Dry anomalies ahead of the rain center appear too weak in the SOM relative to either the CTL or observations. The frequency of wet and dry anomalies ap-

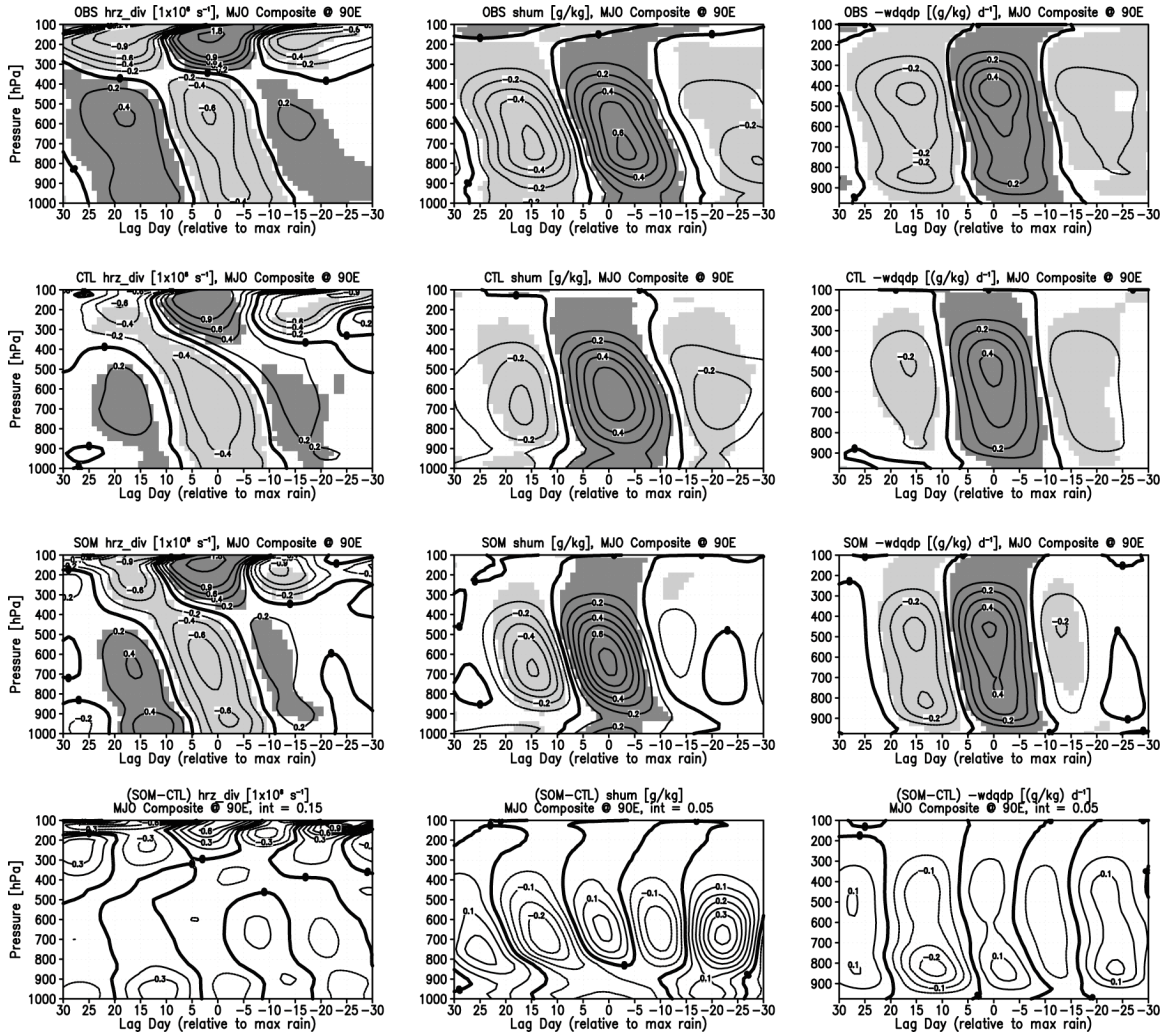


Fig. 3.4.43. MJO composite timeseries of anomalous filtered horizontal divergence (left column), specific humidity (middle column), and vertical moisture transport (right column) at 90°E . All data are filtered for periods of 20-100 days and eastward propagating zonal wavenumbers 1-6. Composites based on observations, the CTL simulation, the SOM simulation, and the (SOM-CTL) difference are shown from top to bottom and are based on anomalous filtered precipitation, with lag day 0 representing the day of maximum rainfall. Positive (negative, zero) contours are thin solid (dashed, thick solid) lines. Dark (light) shading corresponds to anomalies that are 95% significant based on a zero-anomaly null hypothesis. Positive (negative) lag days precede (follow) the maximum precipitation.

appears too high in the SOM, such that the time duration of either anomaly is too short. Both the CTL and SOM display the low-level wet bias following the precipitation maximum (see Fig. 2.4.3), particularly near lag days +5 to +10 when the observations suggest a dry boundary layer (Fig. 3.4.43, top row of middle column).

Large-scale vertical moisture transport in an MJO context [i.e., $(-\omega \partial q / \partial p)'$] can be linked to vertical lofting of moisture by convection given that the corresponding signature of convective heating (Q_1) is non-negligible (confirmed but not shown). In the right column of Fig. 3.4.43, composites of large-scale vertical moisture transport indicate similar moistening structures during lag days -10 to $+5$ between the observations, CTL, and SOM. Subtle differences include a slightly better tilting structure with height in the SOM compared to the CTL (where the SOM has clearer low-level moistening preceding mid-tropospheric moistening), and an improved depiction of subsidence drying in the MJO wake. Both models and observations show that the initial increase of q' in the lower troposphere occurs at a time when vertical moisture transport is near zero. In both ocean basins examined, horizontal moisture advection is weak ($\sim 0.1 \text{ g kg}^{-1} \text{ d}^{-1}$) but statistically significant in the lower troposphere between lag days -10 and -15 and contributes toward the initial increase of q' at this time (not shown).

We display composite time-height cross sections of MJO events at 150°E in Fig. 3.4.44. These composites are based on 14 (7, 8) MJO events for the observations (CTL, SOM). Overall, the SOM shows a markedly improved vertically tilted structure with height relative to the CTL (Fig. 3.4.44). Although the phasing and amplitude of mid-

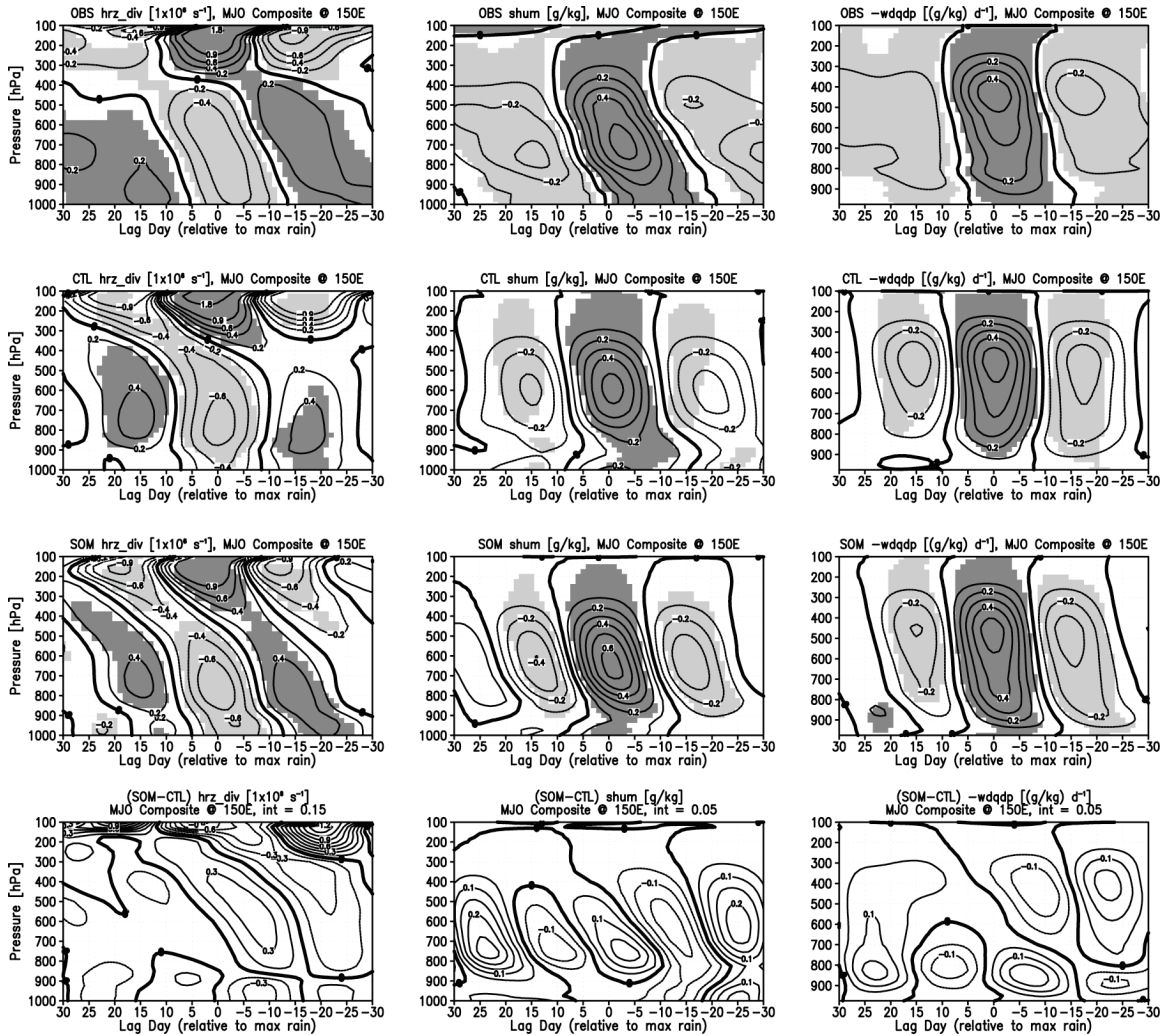


Fig. 3.4.44. As in Fig. 3.4.43, but for a base longitude of 150°E.

tropospheric maxima and minima are relatively similar between the two versions of the model, considerable differences between the CTL and SOM composites occur below about 700 hPa. We note that there are differences with the depiction of simulated boundary layer q' seen in both versions of the SP-CAM compared to the observed moisture structure, namely involving the delayed initiation (decline) of near-surface positive moisture anomalies at the beginning (end) of the MJO wet phase. These model biases will be discussed in greater detail in Section 3.5 below. The inclusion of the slab ocean model

appears to positively affect the depiction of the MJO in the West Pacific regarding the vertical tilt of the disturbance. We hypothesize that the improved air-sea interactions modulate the West Pacific disturbances in such a way that the *phasing* between low-level and mid-level horizontal convergence, anomalous moisture amount, and vertical moisture transport is more realistic in the SOM. For example, the SOM indicates a more realistic development of low-level convergence and upward moisture transport at lag day -10 , followed by mid- to upper-level convergence and upward moisture transport at lag day 0 (Fig. 3.4.44). The relationships among SSTs, the relative phasing of dynamic and radiation anomalies in the lower and middle levels, and the vertically tilted structure are signature features of the MJO and have been shown to play a role in the development, maintenance, and propagation of the intraseasonal convective disturbances (Bladé and Hartmann 1993, Kemball-Cook and Weare 2001, Kiladis et al. 2005).

3.5. Discussion and Conclusions

3.5.a. Overview: CTL-SOM comparison

By including more realistic air-sea interactions through the implementation of an idealized slab ocean model in the SP-CAM, considerable changes to the character of the MJO have been produced. Our analysis of the uncoupled (CTL) and coupled (SOM) versions of the SP-CAM reveals that the annual mean states of the two five-year simulations are very similar. Changes in the SOM boreal winter mean patterns relative to the CTL winter means—e.g., stronger low-level westerlies over the Indian Ocean; reduced West

Pacific rainfall and surface evaporative fluxes—are generally limited but reflect a more realistic climatology in the SOM. The mean state has been shown to affect the characteristics of the MJO (e.g., Inness and Slingo 2003). We display the similarities between the simulated mean states in order to demonstrate that changes in the MJO structure are more closely related to intraseasonal air-sea interactions rather than mean state differences.

We have implemented a suite of diagnostics to quantitatively compare MJO disturbances between the CTL and SOM simulations. Overall, our metrics reveal considerable improvement to the depiction of the MJO in the SOM relative to the CTL. Decile histogram plots (Figs. 3.4.12-3.4.14) indicate that the SOM displays more realistic feedbacks between convection, surface evaporative fluxes, and SSTs. For example, the intraseasonal behavior of SSTs in observations and in the SOM shows that ocean surface temperatures cool during heavy rains, but SSTs increase monotonically with rain rate in the CTL (Fig. 3.4.13a). The decile plots also indicate a more robust and coherent transition from the MJO dry phase to the wet phase as evidenced by the gradual deepening of longwave warming and convective drying out of the boundary layer, signaling the vertical growth of shallow cumuli (Fig. 3.4.14). Accurately capturing this transition of cloud regime is vital to the simulation of the MJO (Inness et al. 2001). We use zonal wavenumber-frequency diagrams to illustrate that the SOM more accurately distinguishes intraseasonal wave types—both equatorial Rossby waves and the MJO—compared to the CTL (Figs. 3.4.15-3.4.17). In particular, the east-west power ratios derived from the spectral analysis indicate clearer eastward MJO propagation in the SOM relative to the

CTL. The lack of dominance of eastward spectral power (low east-west power ratio) is a deficiency common to many current GCMs (Lin et al. 2005, Kim et al. 2009).

We use longitude-time diagrams and lag correlation, lag regression, and composite analyses to display improvements of the MJO signal coherence, eastward propagation, and vertical and horizontal structure in the SOM compared to the CTL. These analyses indicate that the SOM more accurately captures the complex interactions between mean and perturbations low-level winds, SSTs, and MJO convection. More importantly, the SOM shows improvement over the CTL because the coupled model displays robust, coherent, and realistic space-time relationships among MJO convection, the Rossby and Kelvin wave dynamical response to MJO convection, SSTs, surface evaporative fluxes, surface pressure perturbations, surface insolation anomalies, low-level convergence, vertical moisture structure, and convective heating. For example, the SOM displays greater consistency and a stronger signal of leading (trailing) easterlies (westerlies; Fig. 3.4.23), a more realistic spatial extent of dynamic and radiation anomalies (Figs. 3.4.28 and 3.4.31, respectively), and more coherent low-level convergence leading the convective center (Figs. 3.4.38-3.4.39). The relationships and phasing among the variables mentioned have a substantial impact on the generation, maintenance, and propagation of MJO convective disturbances and play a fundamental role in the representation of the MJO in GCMs (Salby and Hendon 1994, Sperber 2003, Lin et al. 2006, Zhang et al. 2006).

Eastward propagation is apparent in both models and the observations (Figs. 3.4.20 and 3.4.21). The calculation of propagation speed is less clear, in part due to limited spatial coverage of statistically significant values resulting from a reduced sample

size. There is no standard method and no accepted variable used for computing propagation speed in the literature, with studies using velocity potential, zonal wind, or OLR (e.g., Waliser et al. 1999, Zhang et al. 2006). We define propagation speed as the time required for the onset of 850 hPa westerly wind anomalies (defined by the zero node between westerlies to the west and easterlies to the east, which is located near the maximum MJO convection) to travel 60° in longitude. We use daily lag linear regression maps (e.g., Fig. 3.4.26) and, because propagation speed may change slightly with longitude in MJO-active regions, we chose two 60° longitude zones (90°E - 150°E and 120°E - 180°) and average the phase speeds together from each zone. Overall, the speeds are very similar between the SP-CAM simulations and the observations. Our results indicate that eastward propagation for the SOM is slightly faster (5.5 m s^{-1}) than either the CTL (5.35 m s^{-1}) or the observed MJO (5.3 m s^{-1}).

3.5.b. Mechanisms: Why has the MJO in the coupled model changed?

Implementation of the slab ocean model in the SP-CAM does not affect the characteristics of intraseasonal convective disturbances equally across all longitudes. In the eastern Indian Ocean region, the MJO eastward propagation is clearer and more robust, the intensity of convection and its dynamical response is greater, and spatial patterns are more realistic in the SOM relative to the CTL. Some GCMs have difficulty in representing the transition of MJO convection from the Indian Ocean into the West Pacific (e.g., Inness and Slingo 2003). The lag autocorrelation of OLR (Fig. 3.4.19) suggests that the

CTL suffers from this deficiency, but the eastward transition of convection is smoother and more coherent in the SOM.

To investigate possible mechanisms related to changes in MJO properties between the CTL and SOM simulations, we display timeseries of lagged regression values of several variables for Indian Ocean MJO events (Fig. 3.5.1). In this figure, time is plotted from right to left to mimic a zonal cross section such that negative lag days correspond to positions east of deep convection. The variables are regressed onto the same precipitation index time series of Fig. 3.4.26 and are averaged over a $10^{\circ}\times 10^{\circ}$ box centered on the Equator and selected longitude (90°E in Fig. 3.5.1). Because we are examining the sign, phasing, and relative magnitudes of the variables, all regression values are plotted on a unified ordinate axis. Thicker line segments represent values that are statistically significant above the 95% level. Variables that display the fundamental thermodynamic, dynamic, and radiative properties of MJO disturbances centered at 90°E appear in the left column. It is immediately clear that both versions of the SP-CAM qualitatively capture the relative magnitude and phasing between boundary layer and upper level divergence (DIVbl and DIV200, respectively), precipitable water (PW), and OLR (Figs. 3.5.1a,b) seen in the observations (Fig. 3.5.1d). In all three profile plots (Figs. 3.5.1a,b,d), positive OLR anomalies are noted around lag days -20 to -15 , followed by low-level convergence (negative divergence; lag days -5 to -2), maximum PW (lag days -3 to -1), maximum upper-level divergence (lag days -2 to 0), and minimum OLR (lag day 0). The SOM-CTL difference plot (Fig. 3.5.1c, left column) suggests that Indian Ocean MJO convec-

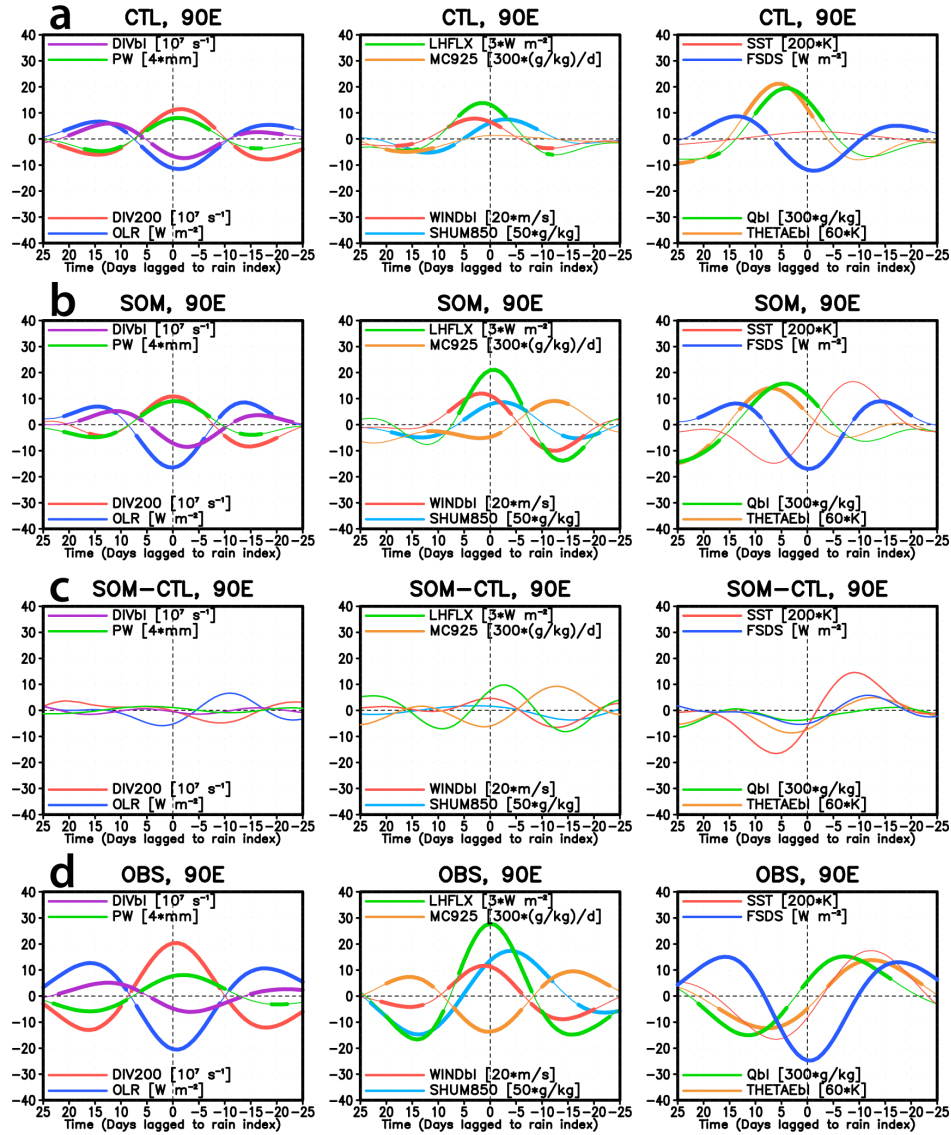


Fig. 3.5.1. Timeseries of lagged regression values based on a one standard deviation change in an index timeseries of precipitation at 90°E. Both index and regressed variables are filtered in time (20-100 days) and averaged over a 10°x10° box centered at (0°N, 90°E). Values of OLR, 200 hPa horizontal divergence (DIV200), boundary layer averaged (“BL”) horizontal divergence (DIVbl), precipitable water (PW), 850 hPa specific humidity (SHUM850), BL wind magnitude (WINDbl), surface latent heat flux (LHFLX), 925 hPa moisture convergence (MC925), BL equivalent potential temperature (THETAEBI), SST, and surface insolation (FSDS) are shown for (a) the CTL, (b) the SOM, (c) the SOM-CTL difference, and (d) observations. Negative (positive) time values along the x-axis precede (follow) the maximum in the precipitation index. Emboldened line segments represent regression values above the 95% significance level. Assessment of statistical significance is not applied to the difference plots (third row) because samples come from different populations.

tion is slightly more intense in the SOM—as evidenced by lower lag-zero OLR (~8 W m⁻²)

in that model—and is representative of an improvement of MJO depiction in the SOM.

We examine timeseries of lower tropospheric variables in the middle and right columns of Fig. 3.5.1 to find more substantial differences between the CTL and SOM simulations. In nature (Fig. 3.5.1d, middle column), evaporative fluxes (SLHF) and boundary layer winds (WINDbl) are weak, near-surface moisture differences are small (not shown), anomalous 850 hPa specific humidity (SHUM850) is negative, and low-level moisture convergence (MC925) is fairly robust prior to lag day -9 . In this same time period, the CTL profile (Fig. 3.5.1a, middle column) indicates almost no significant relationships between low-level winds, evaporative fluxes, and low-level moisture amount while the SOM displays robust, coherent relationships. Most importantly, there is considerable boundary layer moisture convergence one to more than two weeks prior to deep convection in both the SOM and observed profiles, but the mean signal is inconsistent and near zero in the CTL. Many studies have illustrated that an accurate representation of low-level moisture convergence is required for a realistic MJO simulation (Maloney and Hartmann 1998, Waliser et al. 1999), citing its role in generating EAPE and destabilizing the atmosphere ahead of the approaching convective center (Wang and Xie 1998). Observed evaporative fluxes are strongest near lag day zero, followed soon after by maximum low-level westerly anomalies and a dry lower troposphere (Fig. 3.5.1, middle column). The SOM results capture the observed amplitude and phasing reasonably well, while the CTL profiles generally indicate an underestimation of the amplitude and poorer phasing.

Examining the right column of Fig. 3.5.1, time profiles of both SSTs (red) and surface insolation (blue) appear more realistic in the SOM simulation compared to the

CTL. In both versions of the SP-CAM, we note that there are large errors in the phasing of boundary layer equivalent potential temperature (THETAEBL) and specific humidity (QBL). Further discussion of these errors can be found in Section 3.5.c. We note that although no SST regression values are statistically significant according to the criteria used in this study (largely due to the smaller sample size and large lag-one autocorrelation; Bretherton et al. 1999), the SST behavior shown in Fig. 3.5.1d is thoroughly documented in numerous studies (Krishnamurti et al. 1988, Hendon and Glick 1997, Hendon 2005). In both the observations and the SOM simulation, strong surface insolation (FSDS) occurs one to more than three weeks before the heaviest MJO rainfall, with the peak in SST following maximum surface insolation by about five days (Figs. 3.5.1b,d, right column). Additionally, the surface insolation minimum is coincident with the convection maximum, while a distinct SST minimum follows approximately one week later (Figs. 3.5.1b,d, right column). In the CTL, the amplitude of surface insolation is noticeably weaker and SST fluctuations are nearly zero (Fig. 3.5.1a, right column). At least for the Indian Ocean region, the improved amplitude and phasing of intraseasonal boundary layer winds; low-level moisture; surface insolation, evaporative fluxes; net surface heat fluxes (not shown); SSTs; and low-level moisture convergence/divergence displayed by the SOM are associated with more realistic depiction of the MJO. Of particular importance is the more realistic representation of moisture convergence ahead of the MJO in the SOM simulation, which many studies have illustrated is the primary driver of atmospheric destabilization and disturbance intensification in nature (Hendon and Salby 1994, Jones and Weare 1996) and in theoretical and numerical models (Wang and Rui 1990,

Wang and Xie 1998, Waliser et al. 1999, Rajendran and Kitoh 2006, Zhang et al. 2006, Marshall et al. 2008). The refined phasing allows the fundamental components of the MJO—convection, radiation, dynamics, and thermodynamics—to interact in a more natural manner. With proper phasing, the atmosphere is destabilized ahead of the main convective center allowing cumulus growth that warms the lower levels and moistens the dry middle troposphere, thus preconditioning the environment for future deep convection (Bladé and Hartmann 1993, Kemball-Cook and Weare 2001, Sperber 2003). In the MJO disturbance wake, proper phasing results in an environment that is unfavorable for deep convection because SSTs are cooled, divergence dominates the boundary layer, the middle and lower troposphere becomes cool and dry, and surface insolation is reduced (Maloney and Hartmann 1998, Matthews 2000). We conclude that the improved phasing of variables—in particular, the more realistic representation of low-level moisture convergence, surface insolation, and SSTs ahead of deep convection—promotes more robust and coherent eastward propagation and a more realistic intensity of Indian Ocean MJO disturbances in the SOM compared to the CTL.

Figure 3.5.2 displays timeseries of lagged regression values of several variables for MJO disturbances centered at 150°E (West Pacific). Plot details are identical to Fig. 3.5.1 except for the change in selected longitude. The profiles in the left column of Fig. 3.5.2 indicate that the phasing and amplitudes of the fundamental dynamic, thermodynamic, and convective variables in both versions of the SP-CAM are similar to the observed profiles (Fig. 3.5.2d). We note, however, that these regression profiles suggest that the MJO intensity—as measured by minimum OLR, maximum upper (lower) level

divergence (convergence), maximum PW, and peak rainfall (not shown)—is weakly overestimated in the CTL and slightly more so in the SOM simulation. This overestimation is qualitatively consistent with other metrics of MJO intensity as illustrated in Sections 2.4 and 3.4. Given the similarities in MJO intensity between the CTL and SOM, we will focus on mechanisms that might explain the improved vertical tilting structure of MJO disturbances in the SOM simulation as noted in Figs. 3.4.38-3.4.44.

We display timeseries of lower tropospheric variables for West Pacific MJO disturbances in the middle and right columns of Fig. 3.5.2. Within two weeks leading up to deep convection, vigorous low-level moisture convergence (orange, MC925) counteracts strongly negative evaporative flux anomalies (green, LHFLX; representing very weak evaporation) in the CTL profile (Fig. 3.5.2a, middle row), but both the SOM and observations indicate smaller amplitudes of these two profiles (Figs. 3.5.2b,d, middle row). Despite its strong moisture convergence, low-level moisture amounts (light blue, SHUM850) in the CTL within 10 days before maximum rainfall are still slightly underestimated presumably due to the lack of surface evaporation. In the right column of Figure 3.5.2, both versions of the SP-CAM display large errors in the phase of boundary layer moisture (green; Qbl) and equivalent potential temperature (orange, THETAEBL; hereafter $\theta_{e,bl}$), where maxima of these variables occur about one to two weeks *after* deep convection while in nature their maxima occur three to seven days *before* deep convection. These errors will be discussed further in Section 3.5.c. Despite these errors in the model, the SOM exhibits increased boundary layer moisture and $\theta_{e,bl}$ prior to deep convection, as evidenced in the difference plot (Fig. 3.5.2, right column). Like MJO disturbances in the

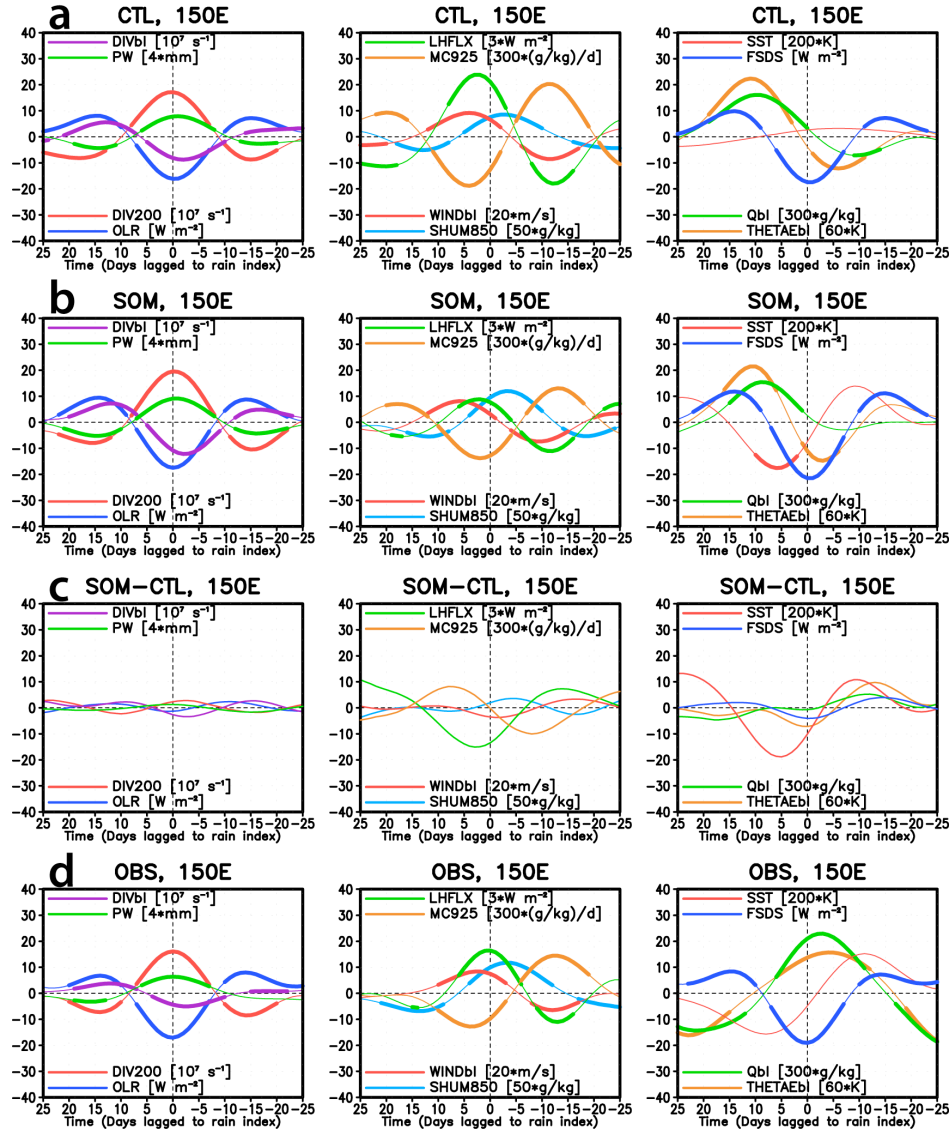


Fig. 3.5.2. As in Fig. 3.5.1, but for a base longitude of 150°E.

Indian Ocean, the SOM SST profile (red) is very similar to the observed timeseries, with warm (cool) SSTs leading (following) maximum convection by approximately 10-15 days (5-10 days). This contrasts the CTL SST profile, which displays very weak warming before day 0 and a considerably delayed and weak cooling afterward. Although surface insolation anomalies are larger for the SOM, surface heat flux anomalies (here, the sum of the two dominant terms, net surface solar radiation and surface latent heat flux)

are similar between the CTL and SOM (not shown). Both the CTL and SOM indicate positive surface heat flux anomalies one to three weeks ahead of deep convection (not shown), but the warming SST response only occurs in the SOM.

We conclude that the SOM's improved vertical structure and tilting of the West Pacific MJO suggested by regression and composite analyses of Figs. 3.4.38-3.4.44 is due to increased low-level moisture and $\theta_{e,bl}$ one to two weeks before peak convection. Fig. 3.5.2 suggests that the enhanced moisture in the SOM is not a result of stronger moisture convergence, but rather appears to be related to comparatively stronger evaporative fluxes and warmer SSTs in that model (i.e., the magnitude of negative flux anomalies are less negative in the SOM, as was noted in Shinoda et al. 1998). Increased low-level warmth and moisture during the MJO approach contribute to a destabilization of the atmosphere because the middle and upper troposphere remain cool and dry during this time (e.g., Fig. 3.4.44). This destabilization (a) generates cumulus development and deepening; (b) moistens the troposphere to the east of the deep convective center, preconditioning it for more vigorous convection (the exact mechanism of this moistening remains somewhat unclear but is likely related to cumulus detrainment, as in Johnson et al. 1999); and (c) promotes coherent eastward propagation of the MJO disturbance. The mechanism described here related to the improved vertical structure of West Pacific MJO disturbances is similar to that proposed by Marshall et al. (2008), who unified and advanced earlier theories of air-sea interaction and its ties to the MJO (Flatau et al. 1997, Wang and Xie 1998, Waliser et al. 1999). Marshall et al. (2008) compare an uncoupled and coupled version of BAM3 and find that composite surface evaporative flux and zonal wind

anomalies are less negative (close to zero or even slightly positive) east of MJO disturbances centered at 100°E. They assert that the more realistic, warmer SSTs east of the disturbance act to mitigate the decreased evaporation, increase boundary layer warmth and moisture, hydrostatically reduce surface pressures, and ultimately drive enhanced low-level moisture convergence which further elevates boundary layer moisture levels. Key elements of the mechanism proposed by Marshall et al. (2008)—comparatively stronger evaporative fluxes, warmer SSTs, increased boundary layer warmth and moisture, reduction in surface pressures (c.f. Figs. 3.4.33 and 3.4.34) in the SOM—are evident in our analyses of West Pacific MJO disturbances. Low-level moisture convergence is moderately stronger in the CTL simulation, and so we contend that it is the *combination* of factors mentioned above (moisture convergence included) that ultimately contributes to the improved vertical structure of West Pacific MJO events in the SOM relative to the CTL.

3.5.c. Comments on the simulated boundary layer heat and moisture biases

Large biases in the phasing of boundary layer averaged (hereafter denoted “BL”) q_{bl} and $\theta_{e,bl}$ are evident in Figures 3.5.1 and 3.5.2 (right columns, green and orange lines, respectively). The BL mean is found by averaging selected variables over the 1000-925 hPa layer. In nature, q_{bl} and $\theta_{e,bl}$ anomalies steadily increase and become positive about three weeks prior to deep convection, reaching a maximum anywhere from a few days to two weeks before the most intense rainfall (Figs. 3.5.1d and 3.5.2d, right column). Dur-

ing this period, the atmosphere is destabilized and cumuli develop and deepen. The onset of deep convection typically occurs from a few days to a week before the peak convective intensity (Kemball-Cook and Weare 2001). As discussed in Section 2.5.a, the reduction of q_{bl} and $\theta_{e,bl}$ due to convection can be seen in Figs. 3.5.1d and 3.5.2d (right column). One to three weeks following peak convection, q_{bl} and $\theta_{e,bl}$ reach a minimum due to the cumulative effects of reduced SSTs and insolation as well as convective and meso-scale downdrafts (Lau and Sui 1997, Zipser 1969, Houze 1982).

The q_{bl} and $\theta_{e,bl}$ profiles are less realistic in the SP-CAM. When deep convection is centered in the eastern Indian Ocean, leading q_{bl} and $\theta_{e,bl}$ anomalies are weakly negative and reach a minimum at about lag day -10 (Figs. 3.5.1a,b, right column). Maxima in q_{bl} and $\theta_{e,bl}$ occur at about lag day $+5$. Similar biases are noted for West Pacific MJO events, except for a slight shift in phasing such that minima (maxima) occur near lag day -5 ($+10$; Figs. 3.5.2a,b, right column). These patterns are nearly out of phase with observations (Figs. 3.5.1d and 3.5.2d, right column).

In Figs. 3.5.3 and 3.5.4, we display temporal cross sections of lag-regressed lower-tropospheric q , T , and θ_e for MJO disturbances at 90°E and 150°E , respectively. The same precipitation index from Figs. 3.5.1-3.5.2 is used here. Observed thermodynamic features discussed above are apparent in Figs. 3.5.3 and 3.5.4 (top row of each figure), with positive (negative) q and θ_e anomalies leading (trailing) maximum convection. The behavior of observed q , T , and θ_e is qualitatively similar to the radiosonde-based

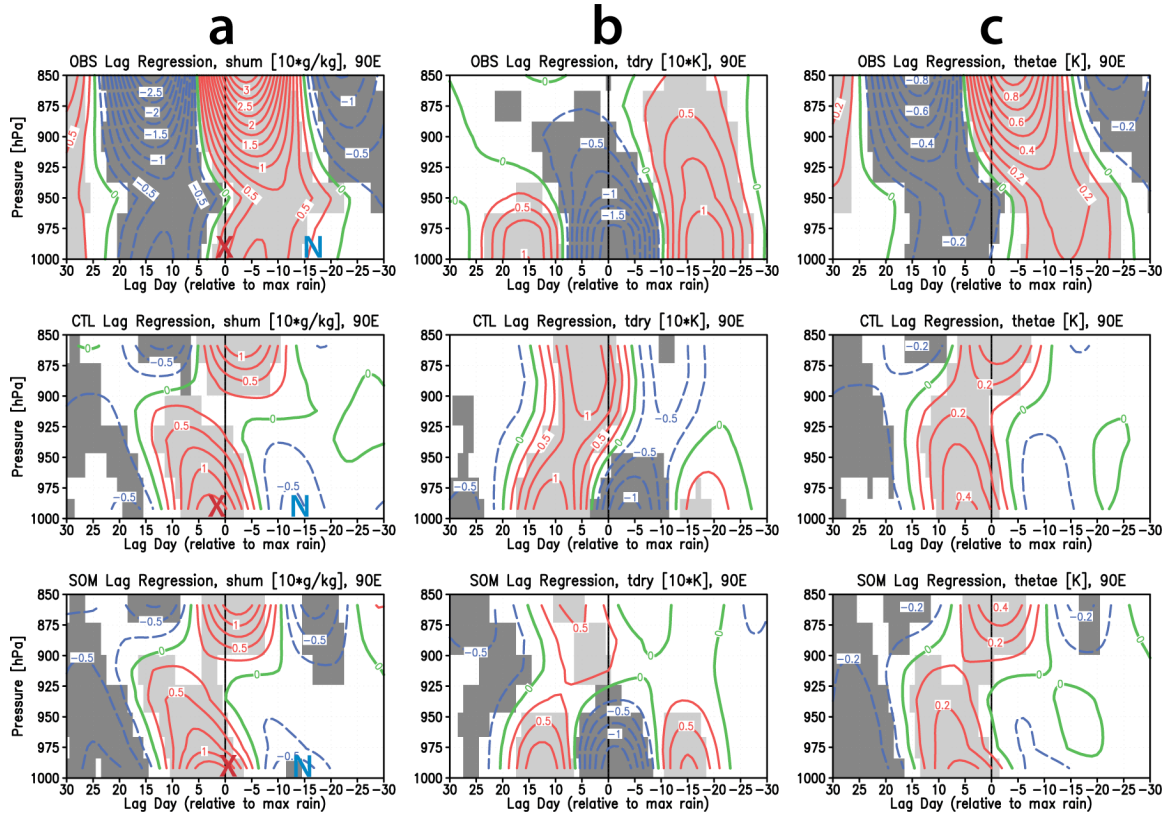


Fig. 3.5.3. Temporal cross sections of (a) specific humidity, (b) temperature, and (c) equivalent potential temperature linearly regression onto an index timeseries of precipitation at 90°E. Both index and regressed variables are filtered in time (20-100 days) and averaged over a 10°x10° box centered at (0°N, 90°E). Regression values correspond to a one standard deviation change in the index and for observations (top), the CTL (middle), and the SOM (bottom). Negative (positive) time values along the x-axis precede (follow) the maximum in the precipitation index. Dark (light) gray shading represents positive (negative) regression values that are statistically significant above the 95% level.

MJO composites of KSH05. Several conclusions can be drawn from Figs. 3.5.3-3.5.4 and additional analyses (not shown) regarding the model biases:

1. Similar errors appear in both the uncoupled and coupled simulations, suggesting that the bias is not related to atmosphere-ocean coupling.
2. Phase errors in the model are most apparent in the lower boundary layer (below about 950 hPa) and smallest above 875 hPa.

3. Phase errors in simulated θ_e are primarily associated with biases in q rather than T .
4. Model biases are not associated with large-scale advection (not shown)—there is large-scale moistening (drying) in the boundary layer leading (trailing) maximum rainfall, in accordance with the observed structure.

Our examination of simulated boundary layer biases will focus on errors in moisture rather than temperature owing to Point (3) above. In Figs. 3.5.3a-3.5.4a, minimum and maximum SLHFs are marked by an “N” and “X,” respectively. It is clear that the amount of water vapor within the boundary layer (which we define as the layer from the surface to 925 hPa) is overly sensitive to surface evaporative fluxes in the SP-CAM, with extrema in SLHF corresponding closely to near-surface q extrema of the same sign. In nature, surface evaporative flux extrema are closer to the nodes of near-surface q anomalies (top row of Figs. 3.5.3a-3.5.4a).

Points (1)-(4) above suggest that physical processes that regulate boundary layer moisture are too weak in the model, and that these processes are occurring on spatial scales similar to the CRM grid size or smaller. These processes may include the flux of moisture across the boundary layer top by shallow cumuli, which are ubiquitous in the observed Tropics (Stevens et al. 2003). One could imagine how an underrepresentation of shallow cumuli in the SP-CAM could result in the noted biases in Figs. 3.5.3a and 3.5.4a. In general, the SP-CAM’s boundary layer moisture biases are less extreme ahead

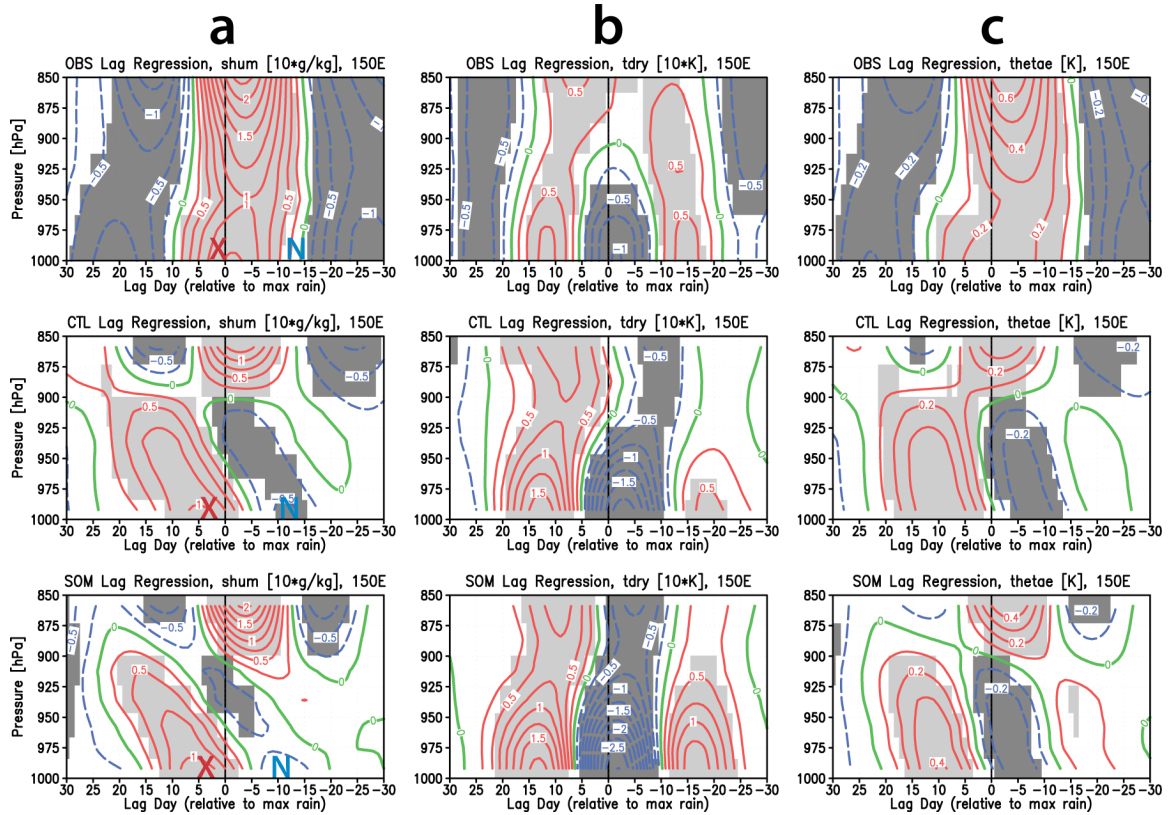


Fig. 3.5.4. As in Fig. 3.5.4, but for a base longitude of 150°E.

(east) of the convective center, perhaps due to increased moisture fluxes by larger convective cells that may be resolved on the CRM grid scale. In the MJO wake to the west of the convective center, deep cumuli have dissipated leaving behind mid- to upper-tropospheric stratus clouds and shallow cumuli. In nature, these shallow cumuli partake in an important vertical redistribution of moisture. Lin and Johnson (1996a,b) examined thermodynamic processes during TOGA COARE and found for periods of high surface winds (i.e., in the MJO wake), convective moistening peaked near the upper boundary layer despite a minimum in boundary layer relative humidity. Those authors presumed that the convective moistening was directly related to shallow cumuli. The shallow cumuli in the MJO wake are associated with a vertical moisture flux within the boundary layer, where excess

moisture from strong surface evaporation is transported upward out of the boundary layer and free tropospheric dry air is injected into the boundary layer. This, combined with dry advection on the large scales [see Fig. 2.4.8 and Fig. 5 in Benedict and Randall (2007)], drives q_{bl} toward a minimum. We hypothesize that, following MJO deep convection, the underrepresentation of shallow cumuli in the SP-CAM leads to an unrealistically weak low-level vertical moisture flux and the excessive accumulation of water vapor within the boundary layer seen in Figs. 3.5.3a-3.4.5a.

The underrepresentation of shallow cumuli in the SP-CAM may be related to the CRM grid resolution. The horizontal and vertical extent of shallow cumuli can be considerably smaller than the resolved scales on the CRM grid (4 km horizontally), forcing the CRM to rely heavily on subgrid-scale parameterizations. Given that individual shallow cumuli make up only a small percentage of the grid cell area, their contribution to the vertical moisture flux on the CRM scale may be underestimated. Additionally, cloud formation on the CRM grid would be delayed until the layer becomes fully saturated, which may not even occur in a shallow cumuli regime. Without cloud formation on the CRM grid, moisture fluxes would presumably remain weaker than if a cloud and its associated latent heat release had developed. Improvement of CRM boundary layer turbulence parameterizations and subgrid-scale condensation schemes has been shown to positively impact shallow convection representation (Firl 2009).

Although further investigation is beyond the scope of this project, we will now briefly discuss some implications regarding the boundary layer moisture biases and CRM grid resolution. To test whether our hypothesis stated above is correct, we could change

the CRM grid resolution. We speculate that the SP-CAM moisture bias would get worse if CRM grid size was increased (coarser horizontal resolution) because the representation of shallow cumuli and their associated moisture fluxes would be poorer. With higher CRM grid resolutions, shallow cumuli—at least a greater fraction of their size spectrum—may be better represented resulting in more realistic boundary layer moisture fluxes and a reduced bias. We again point out that recent work by Firl (2009) has shown that shallow convection representation in a CRM is improved with more sophisticated CRM boundary layer turbulence parameterizations. We also note that the SP-CAM produces eastward propagating MJO disturbances, which is not trivial considering that the maxima in q_{bl} and $\theta_{e,bl}$ occur to the *west* of the convective center. GCMs with cloud parameterizations tied to convective available potential energy (CAPE; see review in Arakawa 2004)—which is strongly affected by boundary layer heat and moisture—would tend to develop new convection to the west of the convective center given the moisture bias described above. This would plausibly result in an MJO that propagates westward. Considering that both versions of the SP-CAM show eastward MJO propagation despite the boundary layer moisture bias, it is unclear if or how this bias impacts the SP-CAM's representation of the MJO or if remedying it might improve the MJO in the model. The performance of the SP-CAM in depicting a fairly realistic MJO suggests that moisture structures in the free troposphere (rather than the boundary layer) may contribute significantly to MJO representation.

Chapter 4

CONCLUSIONS

To the casual observer, the simple essence of the Madden-Julian Oscillation is prolonged alternating periods of active and suppressed cloudiness and precipitation over the equatorial Indo-Pacific region. A closer look at the MJO reveals its almost overwhelming number of complex processes: moist convection on multiple space-time scales interacting with large-scale wave dynamics, exchanges of energy between the atmospheric and oceanic mixed layers, a transition of cloud regimes as the disturbance approaches, topographical impacts on the low-level flow and disturbance intensity near the Maritime Continent, and interactions between the equatorial convection and extratropics. Our understanding of the MJO is far from satisfactory, and our ability to simulate all of the above processes with considerable accuracy has yet to be realized. These challenges result in a poor representation of the MJO in many current GCMs, with the most common deficiency being an underestimation of intraseasonal variability and convective intensity. A modified version of the NCAR CAM3.0, the so-called Superparameterized CAM (SP-CAM), shows a marked increase in intraseasonal convective intensity and variability, suggesting that the substitution of several cloud, turbulence, and boundary layer parameterizations with cloud-resolving models can improve MJO representation in a GCM (KDR08). Previous studies have examined only basic features of SP-CAM intraseasonal tropical convection such as spectral power and

the spatial distribution of total and filtered variance (Khairoutdinov et al. 2005, KDR08). Additionally, these studies analyzed MJO representation in an SP-CAM simulation that was forced by observed monthly-mean SSTs. Such model configurations do not allow SSTs to respond to anomalous energy fluxes associated with the intraseasonal convection and winds, however.

The goal of this project is to analyze in detail the space-time structure of the MJO in two versions of the SP-CAM. In the first simulation, we utilize an uncoupled version of the SP-CAM that is forced by observed monthly-mean SSTs. The second simulation is identical to the first but with a new treatment of tropical SSTs in which a highly simplified mixed-layer ocean model is used to compute prognostic SST anomalies that are coupled to the atmosphere. Compared to the standard CAM, both versions of the SP-CAM exhibit substantially more robust and realistic intraseasonal variability (Zhu et al. 2009).

Many aspects of the MJO are captured in the uncoupled SP-CAM simulation. The vertical progression of enhanced moisture and warmth from the boundary layer to the upper troposphere is qualitatively similar between the model and observations. The uncoupled SP-CAM depicts the magnitude, timing, and vertical structure of anomalous westerly wind onset and its migration into the region of heavy rainfall as the disturbance propagates eastward, a classic feature of MJO dynamics (Hendon and Salby 1994). Other fundamental features of the observed MJO—e.g., lower-level heating and boundary layer meridional convergence leading deep heating and heavy precipitation, the reduction

in tropospheric moisture in the wake of the MJO occurring first by horizontal advection and later by subsidence—are also found in the uncoupled SP-CAM.

Overall, the implementation of the slab ocean model in the coupled version of the SP-CAM (SOM) improves many aspects of the MJO compared to the uncoupled SP-CAM (CTL). Although propagation speeds are similar between the two simulations, the SOM simulation exhibits more realistic feedbacks between convection, surface evaporative fluxes, and SSTs on climatological space-time scales (Figs. 3.4.12 and 3.4.13). There is a more robust and coherent transition between the MJO dry and wet phases, as evidenced by the gradual deepening of longwave warming and convective drying out of the boundary layer which signals the vertical growth of shallow cumuli (Fig. 3.4.14). Spectral, correlation, and linear lag regression analyses indicate that the SOM shows more realistic MJO eastward propagation, signal coherence and vertical and horizontal structure relative to the uncoupled SP-CAM (e.g., Figs. 3.4.15, 3.4.19, and 3.4.28). In general, the SOM shows improvement over the CTL because the coupled version displays robust, coherent, and realistic space-time relationships among MJO convection, the Rossby and Kelvin wave dynamical response to MJO convection, SSTs, surface evaporative fluxes, surface pressure perturbations, surface insolation anomalies, low-level convergence, vertical moisture structure, and convective heating. Much of this improvement is apparent in the increased intensity of MJO disturbances in the eastern Indian Ocean region. We assert that the improved phasing of variables—in particular, the more realistic representation of low-level moisture convergence, surface insolation, and SSTs ahead of deep convection—promotes more robust and coherent eastward

propagation and a more realistic intensity of Indian Ocean MJO disturbances in the SOM compared to the CTL. In the West Pacific region, both versions of the SP-CAM overestimate MJO convection intensity, with the SOM having a slightly larger intensity bias. However, improved vertical heating and moisture structures that display a westward tilt with height and that closely resemble the observed structure are noted in the SOM simulation (Figs. 3.4.38-3.4.45). We conclude that the SOM's improved vertical tilted structure of the West Pacific MJO disturbances is due to a combination of factors including:

- (a) comparatively stronger evaporative fluxes, warmer SSTs, increased boundary layer warmth and moisture, reduced surface pressures ahead of the main convection (c.f. Figs. 3.4.33 and 3.4.34)
- (b) realistic low-level moisture convergence east of the convective center, and, most importantly
- (c) increased low-level moisture and $\theta_{e,bl}$ one to two weeks before peak convection.

These factors may also contribute to the larger convection intensity bias in the SOM, however.

Our analysis has also highlighted several biases, related to the depiction of intraseasonal convective activity in the SP-CAM, that do not appear to be related to or alleviated by the implementation of the slab ocean model. We have established that MJO convection intensity is too strong in the West Pacific region for both versions of the SP-CAM analyzed. While a detailed investigation into the source of this error is beyond the

scope of this study, we will mention several factors that might contribute toward the positive intensity bias of simulated WP MJO disturbances. Although the results from the uncoupled SP-CAM simulation suggest that the model produces MJO events more readily compare to nature when SST anomalies are positive, the results of the coupled simulation indicate that MJO convection in the West Pacific remains overly intense even if the SST profile is more realistic (Fig. 3.5.2). Another possibility discussed in Chapter 2 is that an unrealistically intense convection-wind-evaporation feedback might be active in the SP-CAM. This problem involves mesoscale convective systems that generate enhanced boundary layer winds and surface evaporative fluxes which positively feed back to promote new or sustained convection. The error is exacerbated by the CRM periodic boundary conditions and if SSTs are prescribed (such that regulation by evaporative fluxes is not possible). It is possible that convection-wind-evaporation feedback driven by the CRM periodic boundary conditions is contributing to the SP-CAM West Pacific MJO intensity bias. However, our analysis suggests that the main cause of the error is not related to the prescribed SSTs because the coupled SP-CAM exhibits reasonable estimates of boundary layer winds and surface fluxes but still overestimates West Pacific intraseasonal convection strength (Fig. 3.5.2).

Topographical effects might also play a role in the West Pacific MJO intensity bias. In nature, MJO disturbances weaken and become disorganized when they interact with Maritime Continent land masses. This disruption in convection may weaken the dynamical response in the West Pacific, reduce friction-induced moisture convergence there, and ultimately weaken West Pacific MJO disturbances relative to a hypothetical

world in which the Maritime Continent did not exist. Due to the coarser horizontal resolution in the SP-CAM, the topography in this region is muted, allowing a slow but continued strengthening of MJO disturbances as they propagate across Indonesia (Fig. 3.4.10) and perhaps resulting in the overly intense convection in the West Pacific.

In light of our results from Chapters 2 and 3, we contend that biases in the mean state strongly contribute to biases in the intensity of simulated MJO disturbances in the West Pacific region. Numerous studies have highlighted the mutual interactions between the MJO and the mean state in which it operates (Salby and Hendon 1994, Slingo et al. 1996, Inness et al. 2003, Zhang et al. 2006). Kim et al. (2009) reviewed several GCM simulations and found that high mean precipitation over the West Pacific generally results in an eastward extension of winter-time climatological 850 hPa westerlies, and this appears to be true for both uncoupled and coupled versions of the SP-CAM (Figs. 3.4.1b and 3.4.2b). Inness et al. (2003) report that by forcing basic state westerlies to extend farther into the West Pacific in a coupled GCM through the use of flux adjustment techniques, MJO events become more robust and propagate farther eastward compared to a similar GCM lacking an eastward extension of mean state westerlies in the Pacific region. Low-level westerlies in the SP-CAM extend farther eastward than in nature, even beyond 170°W, and this may be contributing to the notable biases of convection intensity. Additionally, regions where there is a stronger signal of convection (precipitation, OLR) in the annual average typically display larger amplitudes of intraseasonal convection in GCMs (Slingo et al. 1996, Kim et al. 2009). This relationship is also seen in our results (Figs. 3.4.1b, 3.4.2b, and 3.4.4b). We hypothesize that this relationship emerges because

both the mean state and MJO resemble a Walker circulation of similar spatial scale (see Fig. 4.1). When the transient Walker cell associated with the MJO projects strongly onto the basic state Walker cell (i.e., when deep convection occurs in the West Pacific; Fig. 4.1a), the components of the MJO—rising motion, convective heating, moisture convergence—are enhanced and MJO intensifies. This intensification in the West Pacific

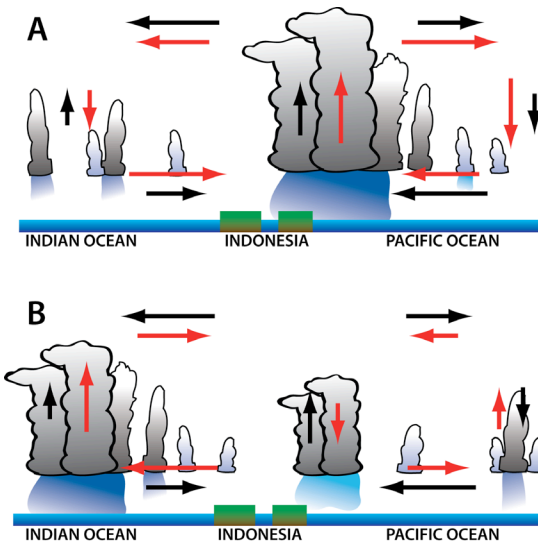


Fig. 4.1. Longitudinal cross section of the interaction between MJO structure and basic state circulation when the MJO convective center is over the (a) West Pacific and (b) Indian Ocean. Convective intensity is indicated by the cloud size, with heavier rainfall having dark blue coloring. Climatological (MJO) circulation is represented by black (red) arrows. Arrow length represents the qualitative wind intensity.

is magnified in the SP-CAM because its basic state convection in that region is already positively biased, particularly during the boreal winter (e.g., Figs. 3.4.1b, 3.4.2b, 3.4.4b). Similarly, when the MJO transient Walker cell projects weakly or negatively onto the basic state Walker cell (Fig. 4.1b), MJO convective intensity may be reduced if biases in the mean state already exist. This appears to most applicable to the uncoupled SP-CAM simulation, which displays unrealistically weak convection both in the mean state and on

intraseasonal time scales in the central and eastern Indian Ocean (Figs. 2.4.1 and 3.4.40). Although many additional factors are likely involved, we emphasize that the depiction of the basic state can strongly impact the representation of MJO disturbances.

Excessive simulated mean precipitation in the West Pacific may also be related to the treatment of momentum feedbacks between the CRM and CAM. Convective momentum transport (CMT), or “cumulus friction,” can have a considerable impact on the large-scale wind field (Mapes and Wu 2001) as well as the intensity and spatial distribution of precipitation (Khairoutdinov et al. 2005). However, the effects of cumulus friction are neglected in the 2D CRM configuration used in the present study (see KDR08). When CMT effects are included in an SP-CAM simulation using a 3D CRM configuration, excessive boreal summer precipitation in the West Pacific is reduced (Khairoutdinov et al. 2005). It is possible that CMT effects might also reduce the SP-CAM’s boreal winter precipitation and MJO intensity biases in the West Pacific, although implementation of a 3D CRM configuration in a 15-20-year SP-CAM simulation would be computationally prohibitive at this time.

We conclude that several factors contribute to the SP-CAM’s MJO intensity bias in the West Pacific region. These factors include an unrealistic convection-wind-evaporation feedback in the boundary layer, unresolved topographical features that allow the simulated MJO to remain organized over the Maritime Continent, biases in the mean state, and the lack of convective momentum transport in the SP-CAM simulation analyzed.

SP-CAM errors are also noted in the behavior of boundary layer moisture and equivalent potential temperature, especially immediately following MJO deep convection. We hypothesize that the excessive moisture noted in the MJO wake is related to an underrepresentation of shallow cumuli and an unrealistically weak vertical moisture flux within the boundary layer.

The results of this project contribute substantially to our understanding of the MJO and its representation in GCMs. This study is the first to conduct a simulation with the SP-CAM coupled to an idealized slab ocean model, and one of the first to examine the effects of air-sea interactions in a coupled version of any superparameterized GCM. The results presented in Chapter 2 confirm that the improved depiction of intraseasonal convection reported by Khairoutdinov et al. (2005) and KDR08 goes well beyond power spectra and variance distributions and is associated with a very realistic representation of the physical MJO structure and the mechanisms that modulate it. We have also demonstrated that the physical mechanisms associated with improvements to the MJO representation in the coupled SP-CAM have a longitudinal dependence and are related to a combination of factors, including more realistic phasing among near-surface variables and a clearer transition of cumulus regime ahead of the MJO convection. No other study to date has examined the physical mechanisms related to changes in MJO representation between an uncoupled and coupled version of a superparameterized GCM. Our results strongly suggest that air-sea coupling modifies the SP-CAM's MJO in a beneficial way. Given that the basic states between the uncoupled and coupled SP-CAM simulations are qualitatively similar, we assert that future simulations using the SP-CAM aimed at

investigating the MJO should utilize a representation of air-sea interaction at least as sophisticated as the scheme used in this study. Such an approach has certain limitations in that the slab ocean model framework does not capture oceanic advection and dynamics well. We hypothesize that an increase in the CRM grid resolution or improved CRM parameterizations might result in an improved representation of shallow cumuli and their associated vertical moisture fluxes, potentially reducing the boundary layer moisture biases in the SP-CAM.

Despite nearly four full decades of research, many questions about the MJO remain unanswered. What are the triggering mechanisms that govern the emergence of the disturbance in the western Indian Ocean? What are the destabilization and propagation mechanisms of the MJO? What role do tropical-extratropical interactions play in the development, maintenance, and dissipation of intraseasonal convection? Will simulations using grids of higher spatial and temporal resolution improve the MJO representation, and if so through what mechanisms? What observational data are needed most to produce more accurate weather and climate forecasts of the MJO? Will such predictions impact our understanding and outlook of global climate change? Continuing studies of the MJO, rooted in observational analyses, theoretical approaches, and numerical simulations, will further improve our understanding of this important tropical phenomenon.

Appendix A

LIST OF SELECTED ACRONYMS

2D: two-dimensional

3D: three-dimensional

AGCM: atmospheric general circulation model

AMIP: Atmospheric Model Intercomparison Project

BL: boundary layer (or, in this study, “boundary layer averaged”)

CAM: Community Atmosphere Model

CISK: conditional instability of the second kind

CMT: convective momentum transport

CTL: control simulation using monthly-mean observed SSTs

COARE: Coupled Ocean-Atmosphere Response Experiment

CRM: cloud resolving model

DJF: time period of December, January, and February

EAPE: eddy available potential energy

ECHAM: European Centre Hamburg Model

ECMWF: European Centre for Medium Range Weather Forecasts

EKE: eddy kinetic energy

ERA-40: ECMWF 40-year reanalysis dataset

ERA-Interim: ECMWF reanalysis “interim” dataset

GCM: general circulation model, or global climate model

GPCP: Global Precipitation Climatology Project

IO: Indian Ocean

ISO: intraseasonal oscillation

ISCCP: International Satellite Cloud Climatology Project

ITCZ: intertropical convergence zone

KDR08: Khairoutdinov et al. (2008)

MJO: Madden-Julian Oscillation

NASA: National Aeronautical and Space Administration

NCAR: National Center for Atmospheric Research

NRMSE: normalized root-mean-square error

NVAP: NASA Water Vapor Project

OLR: outgoing longwave radiation

PW: precipitable water

SFC: (Earth’s) surface

SLHF: surface latent heat flux

SOM: SP-CAM simulation using slab ocean model

SST: sea-surface temperature

SP: superparameterized

SPCZ: South Pacific convergence zone

TAO: Tropical Atmosphere-Ocean buoy array

TMI: TRMM Microwave Imager

TOA: top of atmosphere

TOGA: Tropical Ocean Global Atmosphere project

TRMM: Tropical Rainfall Measurement Mission

WISHE: wind-induced surface heat exchange

WP: (equatorial) West Pacific

Appendix B

COUPLING BETWEEN THE CRM AND GCM

Although all results from the SP-CAM simulations shown in this dissertation involve variables that are averaged to the GCM spatial scale, mutual interactions between the subgrid-scale processes captured by the CRM and the large-scale environment of the GCM play a critical role. It is useful, therefore, to outline mathematically the coupling between the host GCM and the CRM.

In stepping from time n to $n+1$, a provisional value of the GCM variable is first computed as

$$\tilde{q}_G^{n+1} = q_G^n + B_G \Delta t_{LS}. \quad (\text{B1})$$

Here, subscript G denotes GCM variables, Δt_{LS} is the GCM time step, q_G represents any prognostic variable except precipitating water, and B involves all large-scale, non-CRM effects (mainly advection). The CRM variables are updated using CRM advection, CRM physics, and a relaxation term involving \tilde{q}^{n+1} as obtained from (B1):

$$\frac{q_C^{m+1} - q_C^m}{\Delta t_{CRM}} = B_C + S_C + \left(\frac{\tilde{q}_G^{n+1} - \langle q_C^0 \rangle}{\Delta t_{LS}} \right). \quad (\text{B2})$$

In (B2), subscript C denotes CRM variables, Δt_{CRM} is the CRM time step, S is the source/sink term, and $\langle \bullet \rangle$ denotes a CRM-domain average. It is important to note here that the CRM is not re-initialized on each GCM time step. Rather, the CRM time stepping involves a continuous series of subcycles, integrations that take place *within* each GCM time step, from $m=0$ to $m=M$. The CRM field at the end of subcycle α is identical to the CRM field at the beginning of subcycle $\alpha+1$, such that $(q_C^M)_\alpha = (q_C^0)_{\alpha+1}$. The GCM's only influence on the CRM is through the relaxation term in (B2), updated at each GCM time step. GCM variables are then updated according to

$$\frac{q_G^{n+1} - q_G^n}{\Delta t_{LS}} = B_G + \left(\frac{\langle q_C^{n+1} \rangle - \tilde{q}_G^{n+1}}{\Delta t_{LS}} \right), \quad (\text{B3})$$

where the second term on the RHS of (B3) represents the influence of the CRM on the GCM.

REFERENCES

- Adler, R. F., and Coauthors, 2003: The Version-2 Global Precipitation Climatology Project (GPCP) Monthly Precipitation Analysis (1979-Present). *J. Hydrol.*, **4**, 1147-1167.
- Arakawa, A., 2004: The Cumulus Parameterization Problem: Past, Present, and Future. *J. Climate*, **17**, 2493-2525.
- Benedict, J. J., and D. A. Randall, 2007: Observed Characteristics of the MJO Relative to Maximum Rainfall. *J. Atmos. Sci.*, **64**, 2332-2354.
- , and ———, 2009: Structure of the Madden-Julian Oscillation in the Superparameterized CAM. *J. Atmos. Sci.*, **66**, 3277-3296.
- Berrisford, P., and Coauthors, 2009: The ERA-Interim Archive. ERA Report Series No. 1, 20 pp. Online at <http://www.ecmwf.int/publications/>
- Bladé, I., and D. L. Hartmann, 1993: Tropical Intraseasonal Oscillations in a Simple Non-linear Model. *J. Atmos. Sci.*, **50**, 2922-2939.
- Bretherton, C. S., M. Widmann, V. P. Dymnikov, J. M. Wallace, and I. Bladé, 1999: The Effective Number of Spatial Degrees of Freedom of a Time-Varying Field. *J. Climate*, **12**, 1990-2009.

- Collins, M., S. F. B. Tett, and C. Cooper, 2001: The Internal Climate Variability of HadCM3, a Version of the Hadley Centre Coupled Model without Flux Adjustments. *Climate Dynamics*, **17**, 61-81.
- Collins, W. D., and Coauthors, 2006: The Formulation and Atmospheric Simulation of the Community Atmosphere Model Version 3 (CAM3). *J. Climate*, **19**, 2144-2161.
- Colman, R., and Coauthors, 2005: BMRC Atmospheric Model (BAM) version 3.0: Comparison with Mean Climatology, BMRC Research Report No. 108, 66 pp.
- ECMWF, cited 2003: IFS documentation CY28r1 —Part IV: Physical processes. ECMWF, 175 pp. [Available online at [http://www.ecmwf.int/research/ifsdocs/.](http://www.ecmwf.int/research/ifsdocs/)]
- Emanuel, K. A., 1987: An Air-Sea Interaction Model of Intraseasonal Oscillations in the Tropics. *J. Atmos. Sci.*, **44**, 2324-2340.
- , 1994: *Atmospheric Convection*. Oxford University Press, 580 pp.
- Firl, G., 2009: Development of a Third-Order Closure Turbulence Model with Subgrid-Scale Condensation. M.S. Thesis, Department of Atmospheric Science, Colorado State University, 224 pp.
- Flatau, M., P. J. Flatau, P. Phoebus, and P. P. Niiler, 1997: The Feedback between Equatorial Convection and Local Radiative and Evaporative Processes: The Implications for Intraseasonal Oscillations. *J. Atmos. Sci.*, **54**, 2373-2386.
- Fleming, R. J., T. M. Kaneshige, and W. E. McGovern, 1979: The Global Weather Experiment 1. The Observational Phase Through the First Special Observing Period. *Bull. Amer. Meteor. Soc.*, **60**, 649-661.

- Gates, W. L., 1992: AMIP: The Atmospheric Model Intercomparison Project. *Bull. Amer. Meteor. Soc.*, **73**, 1962-1970.
- Gill, A. E., 1980: Some Simple Solutions for Heat-induced Tropical Circulation. *Quarterly Journal of the Royal Meteorological Society*, **106**, 447-462.
- Grabowski, W. W., 2001: Coupling Cloud Processes with the Large-Scale Dynamics Using the Cloud-Resolving Convection Parameterization (CRCP). *J. Atmos. Sci.*, **58**, 978-997.
- , and P. K. Smolarkiewicz, 1999: CRCP: A Cloud Resolving Convection Parameterization for Modeling the Tropical Convecting Atmosphere. *Physica D: Nonlinear Phenomena*, **133**, 171-178.
- Greenfield, R. S., and T. N. Krishnamurti, 1979: Winter Monsoon Experiment – Report of December 1978 Field Phase. *Bull. Amer. Meteor. Soc.*, **60**, 439-444.
- Gruber, A., 1974: The Wavenumber-Frequency Spectra of Satellite-Measured Brightness in the Tropics. *J. Atmos. Sci.*, **31**, 1675-1680.
- Hayashi, Y., 1970: A Theory of Large-Scale Equatorial Waves Generated by Condensation Heat and Accelerating the Zonal Wind. *J. Meteor. Soc. Japan*, **48**, 140-160.
- , 1979: A Generalized Method of Resolving Transient Disturbances into Standing and Traveling Waves by Space-Time Spectral Analysis. *J. Atmos. Sci.*, **36**, 1017-1029.
- Hayes, S. P., L. J. Mangum, J. Picaut, A. Sumi, and K. Takeuchi, 1991: TOGA-TAO: A Moored Array for Real-time Measurements in the Tropical Pacific Ocean. *Bull. Amer. Meteor. Soc.*, **72**, 339-347.

- Heckley, W. A., and A. E. Gill, 1984: Some Simple Analytical Solutions to the Problem of Forced Equatorial Long Waves. *Quarterly Journal of the Royal Meteorological Society*, **110**, 203-217.
- Hendon, H. H., 2000: Impact of Air-Sea Coupling on the Madden-Julian Oscillation in a General Circulation Model. *J. Atmos. Sci.*, **57**, 3939-3952.
- , 2005: Air-sea Interaction, Chapter 7. *Intraseasonal Variability in the Atmosphere-Ocean Climate System*, W. K. Lau, and D. E. Waliser, Eds., Praxis-Springer, 474.
- , and J. Glick, 1997: Intraseasonal Air-Sea Interaction in the Tropical Indian and Pacific Oceans. *J. Climate*, **10**, 647-661.
- , and M. L. Salby, 1994: The Life Cycle of the Madden-Julian Oscillation. *J. Atmos. Sci.*, **51**, 2225-2237.
- Houze, R. A., Jr., 1982: Cloud Clusters and Large-Scale Vertical Motion in the Tropics. *J. Meteor. Soc. Japan*, **60**, 396-410.
- Hu, Q., and D. A. Randall, 1994: Low-Frequency Oscillations in Radiative-Convective Systems. *J. Atmos. Sci.*, **51**, 1089-1099.
- Hurrell, J. W., J. J. Hack, D. Shea, J. M. Caron, and J. Rosinski, 2008: A New Sea Surface Temperature and Sea Ice Boundary Dataset for the Community Atmosphere Model. *J. Climate*, **21**, 5145-5153.
- Inness, P. M., and J. M. Slingo, 2003: Simulation of the Madden-Julian Oscillation in a Coupled General Circulation Model. Part I: Comparison with Observations and an Atmosphere-Only GCM. *J. Climate*, **16**, 345-364.

- , and J. M. Slingo, 2006: The Interaction of the Madden-Julian Oscillation with the Maritime Continent in a GCM. *Quarterly Journal of the Royal Meteorological Society*, **132**, 1645-1667.
- , J. M. Slingo, E. Guilyardi, and J. Cole, 2003: Simulation of the Madden-Julian Oscillation in a Coupled General Circulation Model. Part II: The Role of the Basic State. *J. Climate*, **16**, 365-382.
- , J. M. Slingo, S. J. Woolnough, R. B. Neale, and V. D. Pope, 2001: Organization of Tropical Convection in a GCM with Varying Vertical Resolution; Implications for the Simulation of the Madden-Julian Oscillation. *Climate Dynamics*, **17**, 777-793.
- Johnson, R., 1995: Variability of Clouds and Precipitation During TOGA COARE. *Proceedings from the International Science Conference on the Tropical Ocean Global Atmosphere Program*, Melbourne, Australia, World Meteorological Organization, 552-556.
- , T. M. Rickenbach, S. A. Rutledge, P. E. Ciesielski, and W. H. Schubert, 1999: Tri-modal Characteristics of Tropical Convection. *J. Climate*, **12**, 2397-2418.
- Jones, C., L. M. V. Carvalho, R. Wayne Higgins, D. E. Waliser, and J. K. E. Schemm, 2004: Climatology of Tropical Intraseasonal Convective Anomalies: 1979-2002. *J. Climate*, **17**, 523-539.
- , and B. C. Weare, 1996: The Role of Low-Level Moisture Convergence and Ocean Latent Heat Fluxes in the Madden and Julian Oscillation: An Observational Analysis Using ISCCP Data and ECMWF Analyses. *J. Climate*, **9**, 3086-3104.

- Kawamura, R., 1988: Intraseasonal Variability of Sea Surface Temperature Over the Tropical West Pacific. *Journal of the Meteorological Society of Japan*, **66**, 1007-1012.
- Kemball-Cook, S., and B. C. Weare, 2001: The Onset of Convection in the Madden-Julian Oscillation. *J. Climate*, **14**, 780-793.
- , B. Wang, and X. Fu, 2002: Simulation of the Intraseasonal Oscillation in the ECHAM-4 Model: The Impact of Coupling with an Ocean Model. *J. Atmos. Sci.*, **59**, 1433-1453.
- Khairoutdinov, M., 2003: Cloud Resolving Modeling of the ARM Summer 1997 IOP: Model Formulation, Results, Uncertainties, and Sensitivities. *J. Atmos. Sci.*, **60**, 607-625.
- , C. DeMott, and D. Randall, 2008: Evaluation of the Simulated Interannual and Subseasonal Variability in an AMIP-Style Simulation Using the CSU Multiscale Modeling Framework. *J. Climate*, **21**, 413-431.
- , and D. A. Randall, 2001: A Cloud Resolving Model as a Cloud Parameterization in the NCAR Community Climate System Model: Preliminary Results. *Geophys. Res. Lett.*, **28**, 3617-3620.
- , D. Randall, and C. DeMott, 2005: Simulations of the Atmospheric General Circulation Using a Cloud-Resolving Model as a Superparameterization of Physical Processes. *J. Atmos. Sci.*, **62**, 2136-2154.
- Kiehl, J. T., and P. R. Gent, 2004: The Community Climate System Model, Version 2. *J. Climate*, **17**, 3666-3682.

- , J. J. Hack, and J. W. Hurrell, 1998: The Energy Budget of the NCAR Community Climate Model: CCM3. *J. Climate*, **11**, 1151-1178.
- Kiladis, G. N., K. H. Straub, and P. T. Haertel, 2005: Zonal and Vertical Structure of the Madden-Julian Oscillation. *J. Atmos. Sci.*, **62**, 2790-2809.
- Kim, D., and Coauthors, 2009: Application of MJO Simulation Diagnostics to Climate Models. *J. Climate*, in press.
- Krishnamurti, T. N., D. K. Oosterhof, and A. V. Mehta, 1988: Air-Sea Interaction on the Time Scale of 30 to 50 Days. *J. Atmos. Sci.*, **45**, 1304-1322.
- Kummerow, C., W. Barnes, T. Kozu, J. Shiue, and J. Simpson, 1998: The Tropical Rainfall Measuring Mission (TRMM) Sensor Package. *Journal of Atmospheric and Oceanic Technology*, **15**, 809-817.
- Lau, K. M., and C. H. Sui, 1997: Mechanisms of Short-Term Sea Surface Temperature Regulation: Observations during TOGA COARE. *J. Climate*, **10**, 465-472.
- , and L. Peng, C. H. Sui, and T. Nakazawa, 1989: Dynamics of Super Cloud Clusters, Westerly Wind Bursts, 30-60 Day Oscillations, and ENSO: A Unified View. *Journal of the Meteorological Society of Japan*, **67**, 205-219.
- Liebmann, B., and C. A. Smith, 1996: Description of a complete (interpolated) outgoing longwave radiation dataset. *Bull. Amer. Meteor. Soc.*, **77**, 1275-1277.
- Lin, J.-L., B. Mapes, M. Zhang, and M. Newman, 2004: Stratiform Precipitation, Vertical Heating Profiles, and the Madden-Julian Oscillation. *J. Atmos. Sci.*, **61**, 296-309.
- , and Coauthors, 2006: Tropical Intraseasonal Variability in 14 IPCC AR4 Climate Models. Part I: Convective Signals. *J. Climate*, **19**, 2665-2690.

- Lin, X., and R. H. Johnson, 1996a: Kinematic and Thermodynamic Characteristics of the Flow over the Western Pacific Warm Pool during TOGA COARE. *J. Atmos. Sci.*, **53**, 695-715.
- , and ———, 1996b: Heating, Moistening, and Rainfall over the Western Pacific Warm Pool during TOGA COARE. *J. Atmos. Sci.*, **53**, 3367-3383.
- Lindzen, R. S., 1974: Wave-CISK in the Tropics. *J. Atmos. Sci.*, **31**, 156-179.
- Lorenz, E. N., 1955: Available Potential Energy and the Maintenance of the General Circulation. *Tellus*, **7**, 157-167.
- Luo, Z., and G. L. Stephens, 2006: An enhanced convection-wind-evaporation feedback in a superparameterization GCM (SP-GCM) depiction of the Asian summer monsoon. *Geophys. Res. Lett.*, **33**.
- Madden, R. A., and P. R. Julian, 2005: Historical Perspective, Chapter 1. *Intraseasonal Variability in the Atmosphere-Ocean Climate System*, W. K. Lau, and D. E. Waliser, Eds., Praxis-Springer, 474.
- , 1971: Detection of a 40-50 Day Oscillation in the Zonal Wind in the Tropical Pacific. *J. Atmos. Sci.*, **28**, 702-708.
- , 1972: Description of Global-Scale Circulation Cells in the Tropics with a 40-50 Day Period. *J. Atmos. Sci.*, **29**, 1109-1123.
- Maloney, E. D., 2009: The Moist Static Energy Budget of a Composite Tropical Intraseasonal Oscillation in a Climate Model. *J. Climate*, **22**, 711-729.
- , and D. L. Hartmann, 1998: Frictional Moisture Convergence in a Composite Life Cycle of the Madden-Julian Oscillation. *J. Climate*, **11**, 2387-2403.

- , and J. T. Kiehl, 2002: Intraseasonal Eastern Pacific Precipitation and SST Variations in a GCM Coupled to a Slab Ocean Model. *J. Climate*, **15**, 2989-3007.
- , and A. H. Sobel, 2004: Surface Fluxes and Ocean Coupling in the Tropical Intraseasonal Oscillation. *J. Climate*, **17**, 4368-4386.
- , A. H. Sobel, and W. M. Hannah, 2009: Intraseasonal Variability in an Aquaplanet General Circulation Model. *J. Adv. Model. Earth Sys.*, submitted.
- Mapes, B. E., 2000: Convective Inhibition, Subgrid-Scale Triggering Energy, and Strati-
form Instability in a Toy Tropical Wave Model. *J. Atmos. Sci.*, **57**, 1515-1535.
- , and X. Wu, 2001: NOTES AND CORRESPONDENCE Convective Eddy Momen-
tum Tendencies in Long Cloud-Resolving Model Simulations. *J. Atmos. Sci.*, **58**,
517-526.
- Marshall, A. G., O. Alves, and H. H. Hendon, 2008: An Enhanced Moisture
Convergence-Evaporation Feedback Mechanism for MJO Air-Sea Interaction. *J.*
Atmos. Sci., **65**, 970-986.
- Matsuno, T., 1966: Quasi-geostrophic Motions in the Equatorial Area. *Journal of the Me-
teorological Society of Japan*, **44**, 25-43.
- Matthews, A. J., 2000: Propagation Mechanisms for the Madden-Julian Oscillation.
Quarterly Journal of the Royal Meteorological Society, **126**, 2637-2651.
- Miura, H., M. Satoh, T. Nasuno, A. T. Noda, and K. Oouchi, 2007: A Madden-Julian Os-
cillation Event Realistically Simulated by a Global Cloud-Resolving Model. *Sci-
ence*, **318**, 1763-1765.

- Monterey, G., and S. Levitus, 1997: Seasonal Variability of Mixed Layer Depth for the World Ocean. NOAA Atlas NESDIS, U.S. Government Printing Office, Washington, D.C., **14**, 96 pp.
- Myers, D. S., and D. E. Waliser, 2003: Three-Dimensional Water Vapor and Cloud Variations Associated with the Madden-Julian Oscillation during Northern Hemisphere Winter. *J. Climate*, **16**, 929-950.
- Nakazawa, T., 1988: Tropical Super Clusters within Intraseasonal Variations over the Western Pacific. *Journal of the Meteorological Society of Japan*, **66**, 823-828.
- Neelin, J. D., I. M. Held, and K. H. Cook, 1987: Evaporation-Wind Feedback and Low-Frequency Variability in the Tropical Atmosphere. *J. Atmos. Sci.*, **44**, 2341-2348.
- Petty, G. W., 1999: Prevalence of Precipitation from Warm-Topped Clouds over Eastern Asia and the Western Pacific. *J. Climate*, **12**, 220-229.
- Rajendran, K., and A. Kitoh, 2006: Modulation of Tropical Intraseasonal Oscillations by Ocean-Atmosphere Coupling. *J. Climate*, **19**, 366-391.
- Randall, D., M. Khairoutdinov, A. Arakawa, and W. Grabowski, 2003: Breaking the Cloud Parameterization Deadlock. *Bull. Amer. Meteor. Soc.*, **84**, 1547-1564.
- Randel, D. L., T. J. Greenwald, T. H. Vonder Haar, G. L. Stephens, M. A. Ringerud, and C. L. Combs, 1996: A New Global Water Vapor Dataset. *Bull. Amer. Meteor. Soc.*, **77**, 1233-1246.
- Raymond, D. J., 1995: Regulation of Moist Convection over the West Pacific Warm Pool. *J. Atmos. Sci.*, **52**, 3945-3959.

- Reynolds, R. W., N. A. Rayner, T. M. Smith, D. C. Stokes, and W. Wang, 2002: An Improved In Situ and Satellite SST Analysis for Climate. *J. Climate*, **15**, 1609-1625.
- Roeckner, E., and Coauthors, 1996: The Atmospheric General Circulation Model ECHAM-4: Model Description and Simulation of Present-Day Climate. Max Planck Institut für Meteorologie Rep. 218, 90 pp.
- Salby, M. L., and H. H. Hendon, 1994: Intraseasonal Behavior of Clouds, Temperature, and Motion in the Tropics. *J. Atmos. Sci.*, **51**, 2207-2224.
- , R. R. Garcia, and H. H. Hendon, 1994: Planetary-Scale Circulations in the Presence of Climatological and Wave-Induced Heating. *J. Atmos. Sci.*, **51**, 2344-2367.
- Shinoda, T., H. H. Hendon, and J. Glick, 1998: Intraseasonal Variability of Surface Fluxes and Sea Surface Temperature in the Tropical Western Pacific and Indian Oceans. *J. Climate*, **11**, 1685-1702.
- Simmons, A. J., and S. Uppala, D. Dee, S. Kobayashi, 2006: ERA-Interim: New ECMWF Reanalysis Products from 1989 Onwards. ECMWF Newsletter No. 110, 11 pp. Online at <http://www.ecmwf.int/publications/>
- Slingo, J. M., and P. M. Inness, K. R. Sperber, 2005: Modeling, Chapter 11. *Intraseasonal Variability in the Atmosphere-Ocean Climate System*, W. K. Lau, and D. E. Waliser, Eds., Praxis-Springer, 474 pp.
- , and Coauthors, 1996: Intraseasonal Oscillations in 15 Atmospheric General Circulation Models: Results from an AMIP Diagnostic Subproject. *Climate Dynamics*, **12**, 325-357.

- Sobel, A. H., and E. D. Maloney, G. Bellon, and D. M. Frierson, 2008: The Role of Surface Heat Fluxes in Tropical Intraseasonal Oscillations. *Nature Geoscience*, **1**, 653-657.
- , and E. D. Maloney, G. Bellon, and D. M. Frierson, 2009: Surface Fluxes and Tropical Intraseasonal Variability: A Reassessment. *J. Adv. Model. Earth Sys.*, in press.
- Sperber, K. R., 2003: Propagation and the Vertical Structure of the Madden-Julian Oscillation. *Mon. Wea. Rev.*, **131**, 3018-3037.
- , 2004: Madden-Julian Variability in NCAR CAM2.0 and CCSM2.0. *Climate Dynamics*, **23**, 259-278.
- , S. Gualdi, S. Legutke, and V. Gayler, 2005: The Madden-Julian Oscillation in ECHAM4 Coupled and Uncoupled General Circulation Models. *Climate Dynamics*, **25**, 117-140.
- , J. M. Slingo, P. M. Inness, and W. K. M. Lau, 1997: On the Maintenance and Initiation of the Intraseasonal Oscillation in the NCEP/NCAR Reanalysis and in the GLA and UKMO AMIP Simulations. *Climate Dynamics*, **13**, 769-795.
- Stephens, G. L., P. J. Webster, R. H. Johnson, R. Engelen, and T. L'Ecuyer, 2004: Observational Evidence for the Mutual Regulation of the Tropical Hydrological Cycle and Tropical Sea Surface Temperatures. *J. Climate*, **17**, 2213-2224.
- Stevens, B., and Coauthors, 2003: Dynamics and Chemistry of Marine Stratocumulus—DYCOMS-II. *Bull. Amer. Meteor. Soc.*, **84**, 579-593.

- Straub, K. H., and G. N. Kiladis, 2003: The Observed Structure of Convectively Coupled Kelvin Waves: Comparison with Simple Models of Coupled Wave Instability. *J. Atmos. Sci.*, **60**, 1655-1668.
- Thayer-Calder, K., and D. A. Randall, 2009: The Role of Convective Moistening in the Madden-Julian Oscillation. *J. Atmos. Sci.*, **66**, 3297-3312.
- Trenberth, K. E., J. T. Fasullo, and J. Kiehl, 2009: Earth's Global Energy Budget. *Bull. Amer. Meteor. Soc.*, **90**, 311-323.
- Uppala, S. M., and Coauthors, 2005: The ERA-40 Re-analysis. *Quarterly Journal of the Royal Meteorological Society*, **131**, 2961-3012.
- Waliser, D. E., K. M. Lau, and J.-H. Kim, 1999: The Influence of Coupled Sea Surface Temperatures on the Madden-Julian Oscillation: A Model Perturbation Experiment. *J. Atmos. Sci.*, **56**, 333-358.
- Wang, B., 1988: Dynamics of Tropical Low-Frequency Waves: An Analysis of the Moist Kelvin Wave. *J. Atmos. Sci.*, **45**, 2051-2065.
- , and H. Rui, 1990: Dynamics of the Coupled Moist Kelvin-Rossby Wave on an Equatorial β -Plane. *J. Atmos. Sci.*, **47**, 397-413.
- , and X. Xie, 1998: Coupled Modes of the Warm Pool Climate System. Part I: The Role of Air-Sea Interaction in Maintaining Madden-Julian Oscillation. *J. Climate*, **11**, 2116-2135.
- Wang, Y., W.-K. Tao, and J. Simpson, 1996: The Impact of Ocean Surface Fluxes on a TOGA COARE Convective System. *Mon. Wea. Rev.*, **124**, 2753-2763.

- Webster, P. J., and R. Lukas, 1992: TOGA COARE: The Coupled Ocean–Atmosphere Response Experiment. *Bull. Amer. Meteor. Soc.*, **73**, 1377-1416.
- Weller, R. A., and S. P. Anderson, 1996: Surface Meteorology and Air-Sea Fluxes in the Western Equatorial Pacific Warm Pool during the TOGA Coupled Ocean-Atmosphere Response Experiment. *J. Climate*, **9**, 1959-1990.
- Wheeler, M., and G. N. Kiladis, 1999: Convectively Coupled Equatorial Waves: Analysis of Clouds and Temperature in the Wavenumber-Frequency Domain. *J. Atmos. Sci.*, **56**, 374-399.
- , G. N. Kiladis, and P. J. Webster, 2000: Large-Scale Dynamical Fields Associated with Convectively Coupled Equatorial Waves. *J. Atmos. Sci.*, **57**, 613-640.
- Woolnough, S. J., J. M. Slingo, and B. J. Hoskins, 2000: The Relationship between Convection and Sea Surface Temperature on Intraseasonal Timescales. *J. Climate*, **13**, 2086-2104.
- Yoneyama, K., and Coauthors, 2008: MISMO Field Experiment in the Equatorial Indian Ocean. *Bull. Amer. Meteor. Soc.*, **89**, 1889-1903.
- Yukimoto, S., and Coauthors, 2001: The New Meteorological Research Institute Coupled GCM (MRI-CGCM2) Model Climate and Variability. *Papers in Meteorology and Geophysics*, **51**, 47-88.
- Zhang, C., 1996: Atmospheric Intraseasonal Variability at the Surface in the Tropical Western Pacific Ocean. *J. Atmos. Sci.*, **53**, 739-758.
- , 2005: Madden-Julian Oscillation. *Rev. Geophys.*, **43**.

- , and M. J. McPhaden, 2000: Intraseasonal Surface Cooling in the Equatorial Western Pacific*. *J. Climate*, **13**, 2261-2276.
- , and Coauthors, 2006: Simulations of the Madden–Julian Oscillation in Four Pairs of Coupled and Uncoupled Global Models. *Climate Dynamics*, **27**, 573-592.
- Zhang, G. J., and M. J. McPhaden, 1995: The Relationship between Sea Surface Temperature and Latent Heat Flux in the Equatorial Pacific. *J. Climate*, **8**, 589-605.
- Zhang, M. H., 1996: Impact of the Convection-wind-evaporation Feedback on Surface Climate Simulation in General Circulation Models. *Climate Dynamics*, **12**, 299-312.
- Zhang, Y., W. B. Rossow, A. A. Lacis, V. Oinas, and M. I. Mishchenko, 2004: Calculation of Radiative Fluxes from the Surface to Top of Atmosphere Based on ISCCP and Other Global Data Sets: Refinements of the Radiative Transfer Model and the Input Data. *J. Geophys. Res.*, **109**.
- Zheng, Y., D. E. Waliser, W. F. Stern, and C. Jones, 2004: The Role of Coupled Sea Surface Temperatures in the Simulation of the Tropical Intraseasonal Oscillation. *J. Climate*, **17**, 4109-4134.
- Zhu, H., H. Hendon, and C. Jakob, 2009: Convection in a Parameterized and Superparameterized Model and Its Role in the Representation of the MJO. *J. Atmos. Sci.*, **66**, 2796-2811.
- Zipser, E. J., 1969: The Role of Organized Unsaturated Convective Downdrafts in the Structure and Rapid Decay of an Equatorial Disturbance. *J. Appl. Meteor.*, **8**, 799-814.